ULF Waves Driven By Recently-Injected Energetic Particle Populations

Matthew Knight James

Radio and Space Plasma Physics Group

Department of Physics and Astronomy

University of Leicester

A thesis submitted for the degree of

Doctor of Philosophy

September 2014

Abstract

Matthew Knight James
ULF Waves Driven By Recently-Injected Energetic Particle Populations

This thesis studies the characteristics of ultra low frequency (ULF) waves driven by recently-injected energetic particle populations gradient-curvature drifting azimuthally around the Earth.

A statistical study of 83 separate substorm-driven ULF waves is undertaken in order to determine if the spatial proximity to the driving substorm affects the characteristics of the observed waves, as suggested by *Yeoman et al.* (2010). Waves were observed using Super Dual Auroral Radar Network (SuperDARN) radars and substorms identified using the Far Ultraviolet Imager (FUV) on-board the IMAGE spacecraft alongside a list of substorms provided by *Frey et al.* (2004). Azimuthal wave numbers, m, ranged in magnitude from 2 - 60 corresponding to particle energies, W, of ~1 - 70 keV. Phase propagation was always directed away from the location of the substorm and predicted particle energies were highest when closest to the substorm location in azimuth.

This thesis also includes the study of three individual substorms, each with associated observations of multiple ULF waves using different SuperDARN radars. It is demonstrated that individual substorms are capable of driving a number of wave events characterised by different azimuthal scale lengths and wave periods, associated with different energies in the driving particle population. Similar trends in m and W are found to exist for multiple wave events with a single substorm as was seen in the single wave events of the statistical study.

A recent case study event is included where substorm triggered ULF wave activity observed by two SuperDARN radars and observations of the particle populations responsible for driving the waves were observed using

in-situ magnetospheric data from the Van Allen Probes. This conjunction of the recently-injected cloud of energetic ions with the probes allowed the study of the ion distribution functions which could then be compared to particle energies estimated using the characteristics of the waves.

Declaration

The following paper has been has been produced during the studies for this thesis, based on the work in Chapter 5:

James, M. K., T. K. Yeoman, P. N. Mager, and D. Y. Klimushkin (2013), The spatio-temporal characteristics of ULF waves driven by substorm injected particles, J. Geophys. Res. Space Physics, 118, 1737âĂŞ1749, doi:10.1002/jgra.50131.

To my son,
Jacob Matthew James

Acknowledgements

I am very grateful to have been given the opportunity to study for my PhD as part of the Radio and Space Plasma Physics Group. Firstly, and most of all, I would like to thank my supervisor, Tim Yeoman, for offering me support and guidance over the last three years and helping me create this thesis. Writing is certainly not my strong point - I can't imagine how painful it was for him to try and decipher the original drafts of this thesis. I would also like to thank him for helping me to spend my enormous travel budget by sending me all over the place to fun conferences and meetings.

The Radio and Space Plasma Physics Group in general deserve my gratitude, especially those who have tried to teach me over the years; if it were not for the lecture courses taught by Stan Cowley, Mark Lester and Steve Milan - I probably would not have been interested in space plasmas in the first place. Also my office mates, Gabby Provan and Tim Booth, have been brilliant in putting up with me over the last few years. I am very grateful to Steve Milan and Rob Fear for leading the charge to Babelas and introducing me to Mr Timothy Taylor and his friends, who I would also like to thank for helping me get through some of the more stressful times. A special thanks must be given to those who have provided me with vital supplies such as tea (Tom, Jasmine, Ben), crosswords (Calum, John, Greg) and samosas (me, Tim). I'm still waiting for a regular instalment of beer club though, Jasmine...

The last few months of my PhD have been the most stressful and difficult months of my entire life. I would like to extend my thanks to Michaela, who has stuck by me when I have been struggling, and pushed me when I felt lazy!

Cheers.

Contents

List of Figures

List of Tables

Chapter 1

Introduction

Solar-terrestrial physics has its origins in the observation of the aurora and the discovery of the geomagnetic field. The magnetic and auroral activity were first discovered to be related in 1741 by Olef Hiorter, though it wasn't until Kristian Birkland's third expedition to northern Norway in the early 1900's that the aurora had been associated with currents flowing along magnetic field lines. We now know that perturbations in the magnetic field are often due to currents driven by electric fields flowing in the ionosphere. Solar-terrestrial physics forms a part of the larger subject of space plasma physics where the main concern is the complex interaction of energetic charged particles with electric and magnetic fields. The complexity of this interaction arises from the fact that the electric and magnetic fields which affect the motion of these particles are in turn affected by the motion of the charged particles.

This thesis focuses on the pulsations in the Earth's magnetic field that are driven by populations of these energetic charged particles as they drift azimuthally around the planet. These pulsations are called ultra low frequency (ULF) waves, which have a typical range of frequencies of 1 mHz - 1 Hz. ULF waves are an important mechanism in space plasma physics as they are responsible for transporting energy, momentum and information around magnetised planets. At the Earth, ULF waves may be driven by forces external to the magnetosphere directly related to the solar wind such as the rippling at the magnetopause caused by a Kelvin-Helmholtz instability driving a field line resonance deeper in the magnetosphere. Also, ULF waves driven indirectly by the solar wind, by processes internal to the magnetosphere, are common at Earth and are the mechanism to be studied in this thesis.

The remainder of this chapter will give a brief description of some of the important systems involved in the study of solar-terrestrial physics. A brief description of the Sun and the importance of the solar wind will be discussed. This will be followed by an overview of the Earth's magnetosphere. Finally there will be an introduction to the ionosphere and its structure.

1.1 The Sun and the Solar Wind

The Sun is a ball of mostly ionised hydrogen (~90%) and helium (~10%) gas held together by its own gravity. It has a radius of ~109 R_E (696,000 km) and is about 330,000 times as massive as the Earth at 2×10^{30} kg. The centre of the Sun is hot enough to fuse hydrogen into helium, further adding to the heat. The heat created by the Sun is seen in the photosphere, the light emitting part of the Sun's atmosphere, at temperatures of about 4200 K. This temperature increases out through the chromosphere and the corona to around 2×10^6 K at 75,000 km (*Erdélyi and Ballai*, 2007). The effective black body temperature of the Sun is approximately 5,785 K (*Hanslmeier*, 2007) where, during active periods, there may be enhancements in the x-ray or the radio wave end of the electromagnetic spectrum.

It is important to remember that most of the activity seen at Earth is powered by our Sun. The Sun supplies energy to the Earth's plasma environment through the photoionisation of gases in the upper atmosphere and by coupling with the solar wind.

Due to the high temperatures present in the Sun's corona, the hydrogen and helium present can become completely ionised. This completely ionised gas experiences pressures that are too high for gravity to contain it, causing it to stream out away from the Sun, forming the solar wind. The solar wind's properties are controlled by solar activity and is a medium by which the solar activity can be transmitted to other objects in the solar system such as comets and planets.

The solar wind is a hot, tenuous plasma which flows at highly supersonic speeds which typically range from 200 km s^{-1} to greater than 1000 km s^{-1} at 1 Astronomical Unit (~1.5×10^8 km). The electron and ion densities observed at 1 AU from the Sun are typically about ~7 cm^{-3} each with an IMF field magnitude of approximately 7 nT.

Due to the high degree of ionisation, the solar wind is a highly conductive plasma. The conductivity is high enough for the diffusion of the magnetic field to be negligible.

This results in the Sun's magnetic field becoming bound to the plasma and is known as the 'frozen-in-flux' theorem which will be discussed further in Chapter 2. Because the magnetic field generated by the Sun is frozen in to the plasma, and the plasma is streaming away from the sun, the magnetic field is dragged along with the solar wind forming the interplanetary magnetic field (IMF).

Figure 1.1 shows what happens when the IMF is bound to the solar wind as it streams away radially from the Sun. If a parcel of plasma were emitted from the Sun and were to travel away from the Sun radially then, as the Sun rotates, the magnetic flux tube which the plasma exists on becomes twisted causing the IMF to become more azimuthal as it gets farther from the Sun. This is known as the Parker Spiral as it was predicted by *Parker* (1958).

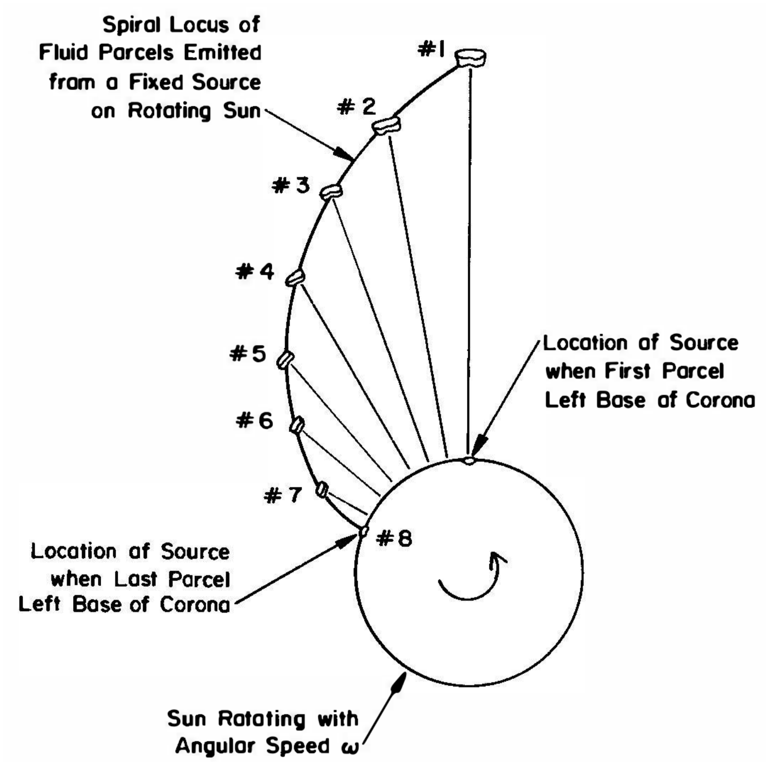

Figure 1.1: Spiral emission of solar wind plasma - Diagram showing the twisting of a flux tube while several parcels of plasma are emitted from the Sun as it rotates. Figure taken from *Kivelson and Russell* (1995).

As the solar wind drags the Sun's magnetic field outward, this leads to the IMF being almost parallel to the Earth's ecliptic plane when measured close to the ecliptic plane. The field lines that have a footprint in the northern hemisphere of the Sun are anti-parallel to those with a footprint in the southern hemisphere of the Sun, thus forming an interplanetary current sheet. The current sheet forms a 'ballerina skirt' shape like that shown in Figure 1.2 due to the complex nature of the Sun's magnetic field structure and its offset from the rotational dipole.

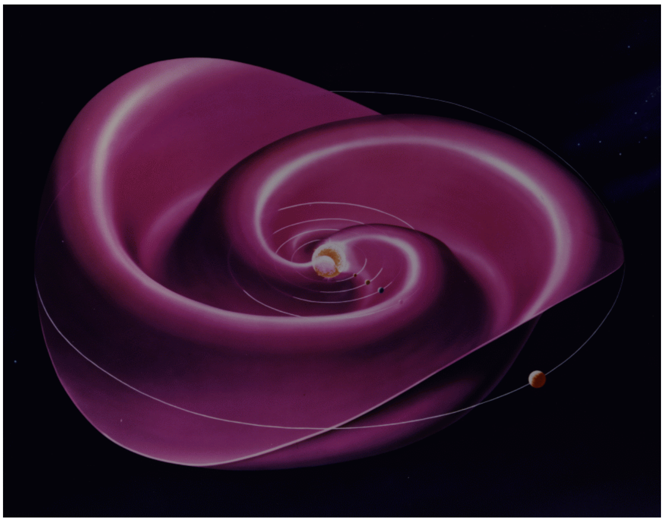

Figure 1.2: Parker spiral - Artist's impression of the variation in the location of the interplanetary current sheet. Figure taken from *NASA*

Due to the shape of the interplanetary current sheet, the Earth often switches between being above or below the current sheet and therefore the IMF at Earth frequently changes polarity. This frequent variation of the direction of the IMF near Earth coupled with the natural variability in the solar wind makes the plasma environment near Earth very dynamic, allowing for interesting interactions with the Earth's magnetosphere.

1.2 Earth's Magnetosphere

1.2.1 Magnetospheric Cavity

The concept of the Earth's magnetosphere was first conceived by *Chapman and Ferraro* (1931) with the idea that the solar wind and IMF would not mix with the Earth's magnetic field and its associated plasma environment. The two different fluids would not mix due to the plasma in both environments being considered 'frozen-in' to their associated magnetic fields, so the IMF would drape itself around the terrestrial field as shown in Figure 1.3 to form a magnetic cavity containing the Earth and its own plasma and magnetic field totally separate from the IMF and the solar wind.

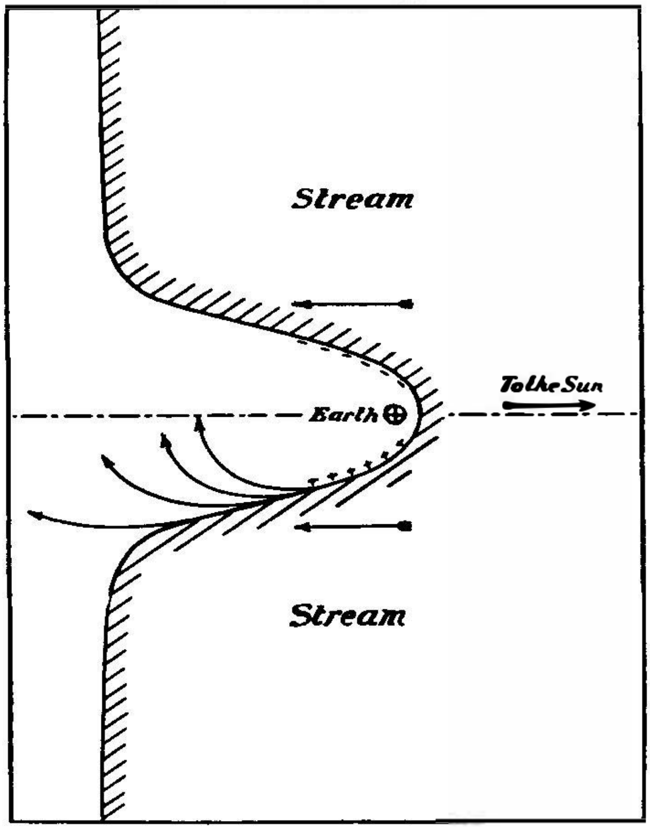

Figure 1.3: Magnetic cavity formation - A visual representation of how the solar wind would advance and surround the magnetic cavity carved out by the Earth's magnetic field, taken from *Chapman and Bartels* (1940).

The boundary where the two plasma populations meet, but do not mix, is called the magnetopause. At the magnetopause currents named the Chapman-Ferraro currents flow between the two plasmas. Figure 1.4 shows where these currents would flow in the noon-midnight meridian when the assumption is made that the IMF is zero and there is no interaction between the IMF and the terrestrial field. In this simplified case the magnetosphere contains a completely closed set of currents.

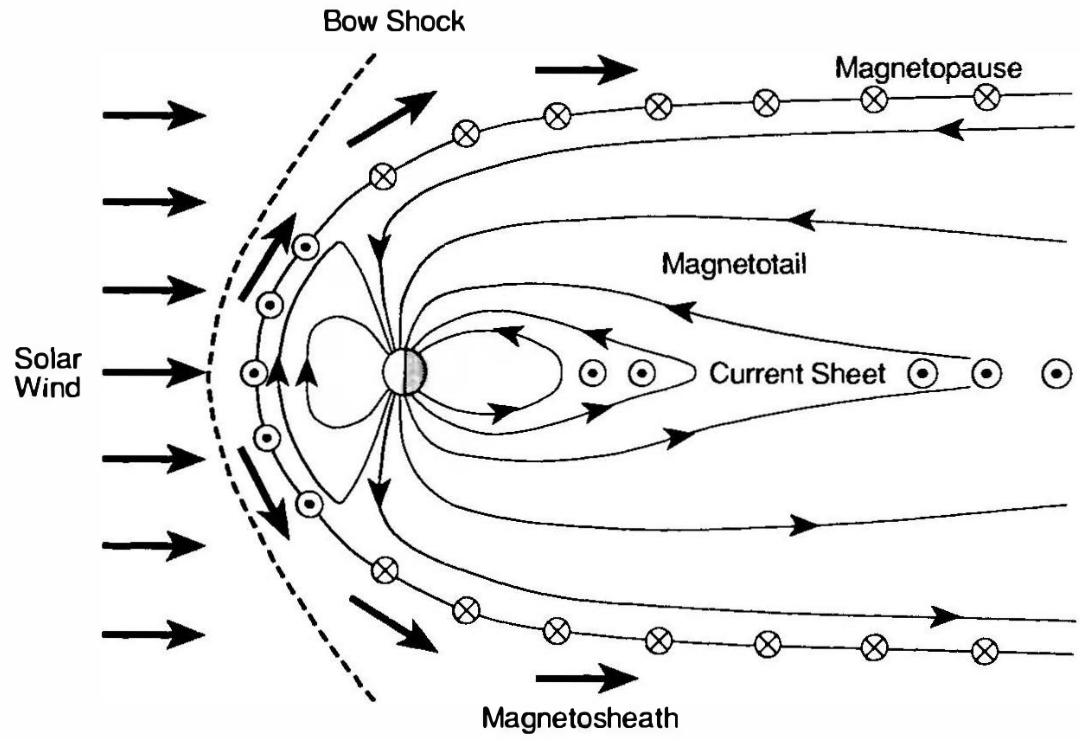

Figure 1.4: Magnetospheric current cross section - Cross section of the magnetosphere along the noon-midnight meridian, where there is no magnetic reconnection and all current systems remain completely closed within the magnetosphere, from *Kivelson and Russell* (1995).

The formation of the Chapman-Ferraro currents is explained by *Kivelson and Russell* (1995) using Figure 1.5 where the left of the diagram is the the solar wind, the centre is the magnetopause and the right is the Earth's magnetosphere. In this example, the IMF is assumed to be negligible, as is the plasma density within the magnetosphere. The incoming solar wind particles (from the left) with a velocity u cross the boundary and sense the magnetic field oriented in the z direction. When a charged particle moves in a magnetic field it gyrates, the direction of which is dependent upon the charge of the particle. As the electrons and ions sense the Earth's magnetic field, they gyrate in opposite directions within the magnetopause and return to the solar wind, resulting in a net current within the magnetopause. The motion of plasma particles within magnetic fields will be discussed in greater detail in Chapter 2.

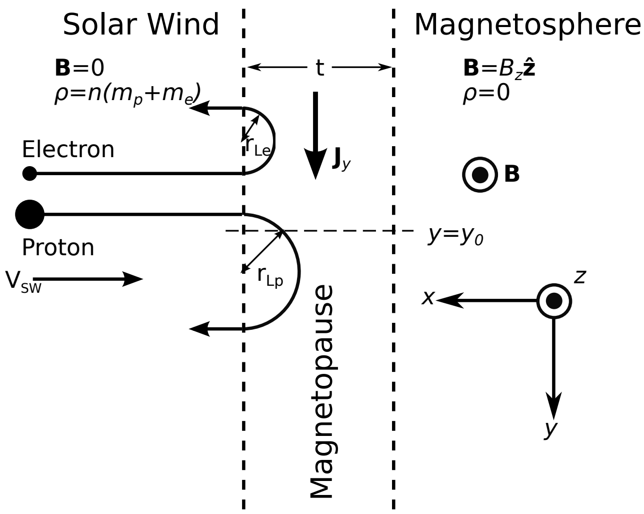

Figure 1.5: Chapman-Ferraro current - Simple illustration of the formation of the Chapman-Ferraro magnetopause current.

The magnetospheric cavity is shaped by the interaction with the solar wind. The day-side of the magnetosphere is forced towards the Earth by the plasma and magnetic pressures exerted upon the magnetopause by the solar wind, but is balanced by pressures within the magnetosphere. At Earth, due to the low plasma pressure within the magnetosphere close to the magnetopause and the insignificant magnetic pressure provided by the IMF, this pressure balance can be approximated as

$$P_{sw} = \frac{B^2}{2\mu_0}, \tag{1.1}$$

where P_{sw} is the pressure exerted by the solar wind and B is the magnetic field strength within the magnetopause. The balance of these pressures places the radial distance of the Earth's magnetopause at ~10 R_E (*Pisacane*, 2005) along the Earth-Sun line. The pressure balance for other parts of the magnetopause away from the Earth-Sun line differ in the way that the component of the force provided by the solar wind that is pushing towards the planet gets smaller, allowing the boundary to flare out. The pressure from the solar wind on the magnetosphere is reduced on the night-side allowing the magnetotail to become elongated.

As the highly supersonic solar wind approaches the Earth's magnetosphere it forms a shock wave known as the bow shock. The plasma in this region slows down to subsonic speeds in order to be able to travel around the magnetosphere and as a result becomes compressed and heated. The region of shocked plasma that surrounds the magnetopause is known as the magnetosheath.

Figure 1.6 shows the structure of the Earth's magnetosphere including the various current systems, plasma regions and fields. The currents are presented as red arrows, the magnetic field is represented by thin blue lines with arrows and the plasma populations are the shaded grey areas all of which has been inferred from spacecraft observations (*Kivelson and Russell*, 1995). It is apparent from this figure that the Earth's magnetosphere can be divided up into regions with specific characteristics.

One such region present in the magnetosphere is the plasmasphere, where relatively cold, dense plasma is held close to the Earth in the region of space occupied by the Van Allen radiation belts. This region of plasma typically extends to just a few Earth radii and contains particle densities around ~10^3 cm^{-3} *Gallagher et al.* (1988) and energies of around 1 eV (*Chang and Union*, 1986). This region ends between 3 and 5 R_E from the Earth where there is a sharp boundary called the plasmapause.

Another region of plasma is the central plasma sheet which is typically hotter and lower in density than the plasmasphere with typical densities of ~0.1-1 cm^{-3} and keV electrons (e.g., *Baumjohann et al.*, 1989; *Huang and Frank*, 1994; *Wing and Newell*,

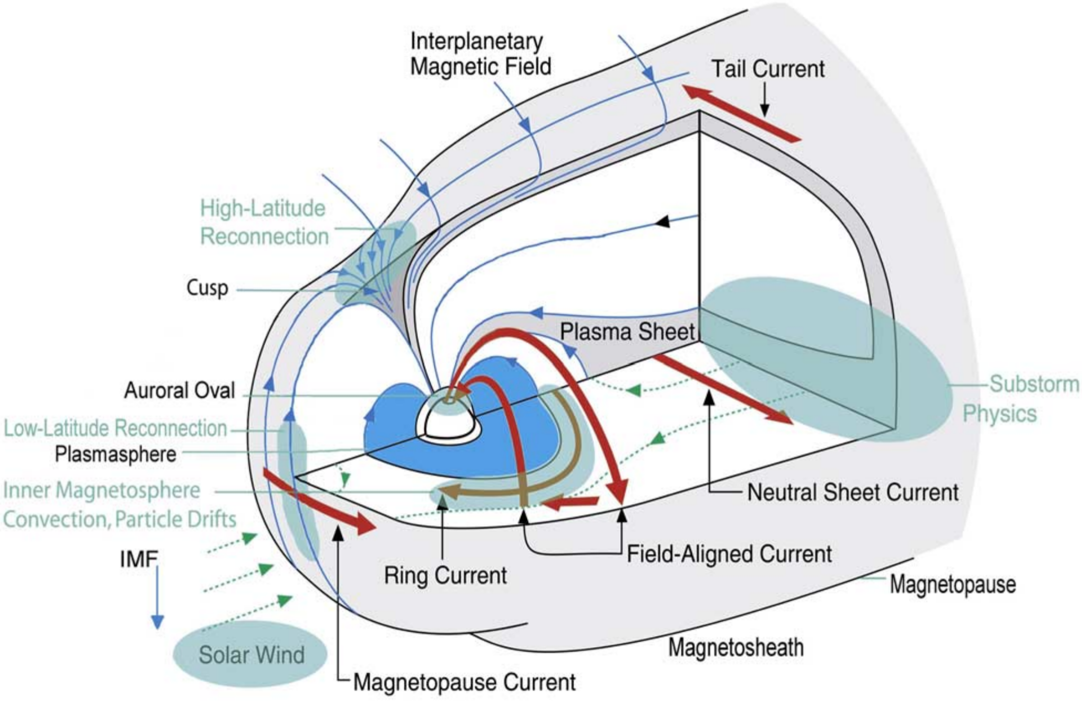

Figure 1.6: Regions of the magnetosphere - Diagram of the different regions of the Earth's magnetosphere, from *Frey* (2007)

1998). The plasma sheet typically exists on closed field lines though it may contain plasmoids.

The tail lobes of the magnetosphere contain very low densities of plasma. The plasma density in this region is typically less than 0.1 cm^{-3} (*Gosling et al.*, 1985) though the particle energies typically range from 5 - 50 keV. Magnetic field lines in the tail lobes are thought to be open to the solar wind and the composition of the ions suggests that their origin is in the ionosphere (*Kivelson and Russell*, 1995).

Separating the tail lobes from the magnetosheath is the plasma mantle. In the plasma mantle the bulk flow of the particles is tailward, parallel to the geomagnetic field at speeds of 100 - 200 km s^{-1} where the speed of the flow has been shown to correlate with the flow speeds within the magnetosheath (*Rosenbauer et al.*, 1975). The plasma that populates the plasma mantle is a mixture of magnetosheath particles which would have entered the cusp along open field lines and ionospheric particles that have flowed up field lines from the polar cap (*Banks and Holzer*, 1969; *Rosenbauer et al.*, 1975). This flow from the polar cap is known as the 'polar wind'.

1.2.2 Dungey Cycle

It is often appropriate to assume that the frozen-in-flux approximation holds up well in space plasmas, though there are some regions where this approximation breaks down. One such area where the frozen-in-flux approximation breaks down is in regions where there are anti-parallel magnetic fields present, such as the day-side magnetopause during a southward pointing IMF as postulated by *Dungey* (1961). The regions where this breakdown occurs are called neutral points and field lines are able to reconfigure themselves in order to connect the two magnetic fields from the previously separate fluids as demonstrated by Figure 1.7.

Dungey (1961) suggested that this reconnection of the IMF and the Earth's magnetic field were likely to occur at neutral points both on the day-side magnetopause and in the night-side magnetotail during a southward facing IMF. The day-side neutral point in Figure 1.8 is the point along the magnetopause where the 'closed' field line **1** intersects the IMF field line. Closed field lines are defined as field lines with both footprints in the Earth's ionosphere and open field lines have only one footprint in the ionosphere as the other is connected to the IMF. The closed field line at **1** becomes two

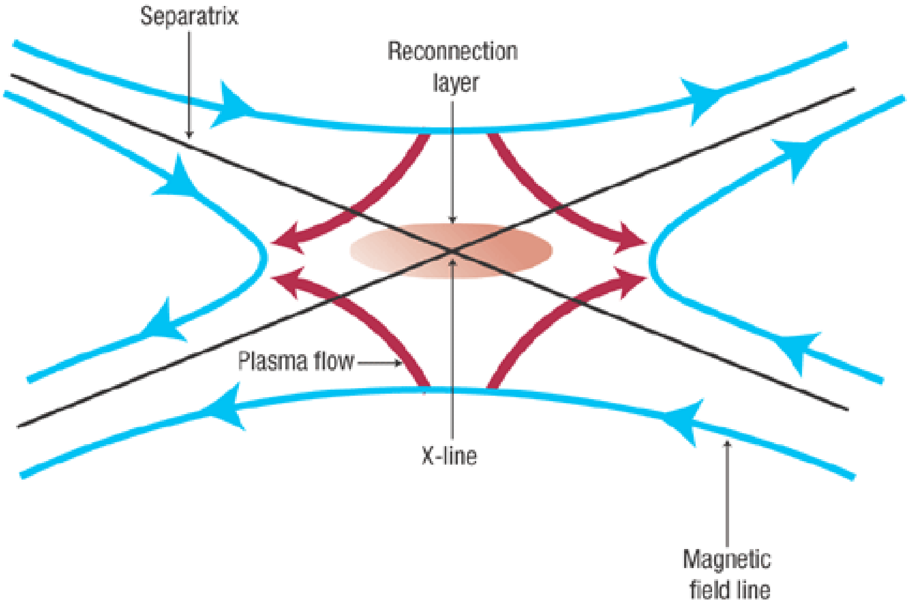

Figure 1.7: Magnetic reconnection - Demonstration of the magnetic configuration at a neutral point or X-line, taken from *Finn* (2006).

open field lines **2** and **2'** which get dragged past the Earth by the solar wind. Eventually these field lines stretch in the magnetotail (field lines **4** and **5**) until they become anti-parallel, forming another neutral point where **6** and **6'** intersect. At this point reconnection occurs, closing a field line (**7**) close to the Earth and releasing another field line away from the neutral point **7'**. The newly closed field lines dipolarise (**8**) and convect around to the day-side magnetosphere for this process to repeat.

This process of opening flux on the day-side magnetosphere and closing flux in the magnetotail is known as the Dungey Cycle. Figure 1.8 also shows that as the field lines evolve from the reconnection on the day-side to forming a neutral point in the night-side, they convect over the polar cap from noon to midnight. After reconnection in the tail the field lines then convect azimuthally back to the day-side magnetosphere forming a twin cell convection pattern. Due to the transport of flux across the polar cap, an electric field $\mathbf{E} = \mathbf{v}_{\mathbf{SW}} \times \mathbf{B}_{\mathbf{SW}}$ is sensed by the plasma in the polar cap directed from dawn to dusk (*Belmont et al.*, 2013).

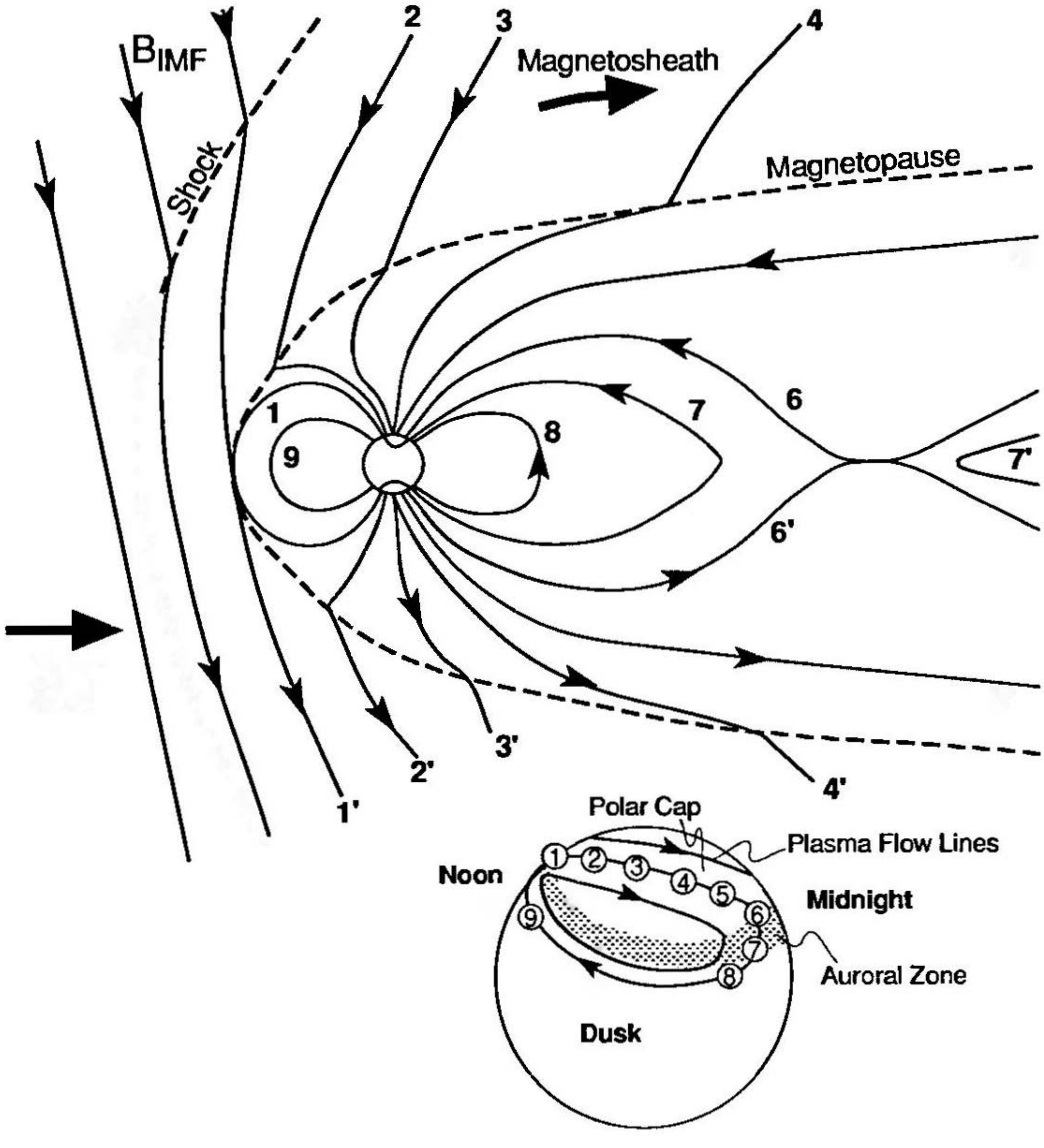

Figure 1.8: Dungey cycle - Diagram showing the evolution of magnetic field lines that make up Earth's magnetosphere as they convect around the polar cap due to the Dungey Cycle. Field lines are numbered in order from the field line which reconnects with the IMF on the day-side magnetopause (**1**) where their associated ionospheric footprints are shown in relation to the northern polar cap. (Taken from *Kivelson and Russell* (1995).

1.2.3 Substorms

The Dungey Cycle for times when there is a southward component of the IMF does not always manifest in a constant rate of magnetic reconnection on both the day-side and night-side of the magnetosphere. Often it requires there to be a large build up of open flux within the magnetotail for the reconnection to occur. The reconnection in the magnetotail is quite sudden and intense, closing large amounts of magnetic flux in a relatively short period of time. This phenomenon is known as a substorm.

The near-earth neutral-line (NENL) model (*McPherron et al.*, 1973; *Russell and McPherron*, 1973; *McPherron*, 1991; *Baker et al.*, 1996; *Baumjohann and Nakamura*, 2001) describes the different stages of a substorm in detail. The start of the substorm occurs when there is a southward component to the IMF. While there is a southward IMF, field lines are able to reconnect on the day-side magnetopause, adding open flux to the polar cap. This open flux is then transported across the polar cap and stored in the outer lobes of the magnetotail surrounding a distant neutral point (or X-line). The flow of flux from the day-side to the night-side initiates convection towards the reconnection region, but the flow is slowed by the finite conductivity of the ionosphere so flux is forced to build up within the magnetotail. The build up of flux in the tail and reduction of the day-side flux increases the flaring of the magnetosphere and thus increases the dynamic pressure on the magnetopause. The pressure on the tail of the magnetosphere causes the night-side plasma sheet to thin as shown in Figure 1.9a. This stage is known as the growth phase of the substorm and can be associated with an enlargement of the auroral oval due to the increase of flux within the polar cap.

According to the NENL model, near the end of the growth phase, the ions stop behaving adiabatically in the cross-tail current sheet due to the lack of a vertical (North-South) component in the magnetic field so magnetic reconnection can start at a new X-line. As the field lines reconnect at the new X-line, closed loops of flux form a plasmoid between the X-lines as shown by Figure 1.9b. As more field lines reconnect, the central plasma sheet thins and the reconnection rate increases rapidly. If the reconnection severs all of the field lines connected to the original distant X-line from the ionosphere then the substorm expansion occurs, otherwise the event halts and is known as a pseudo-breakup (*Baker et al.*, 1996).

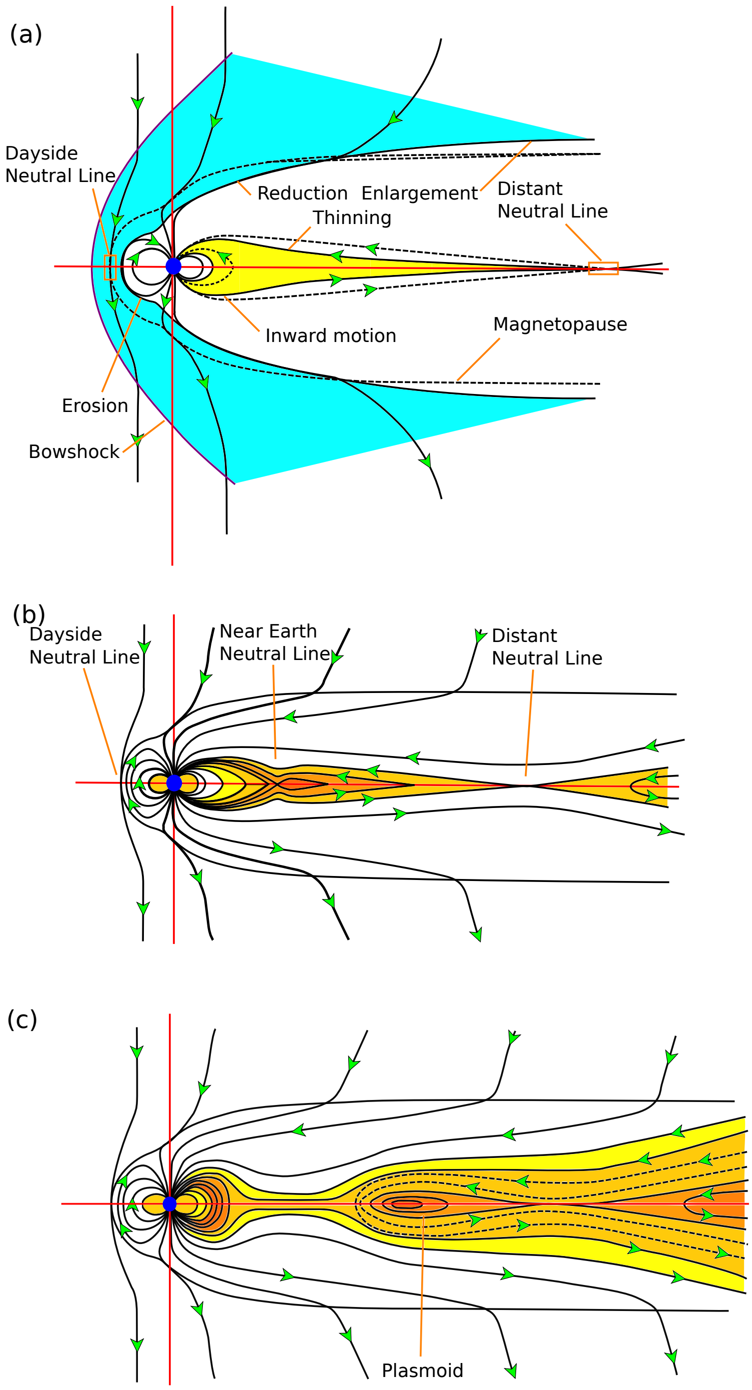

Figure 1.9: NENL substorm model - (a) Diagram illustrating the thinning of the plasma sheet due to the increase of flux being stored in the magnetotail during the growth phase of a substorm. (b) Following the thinning of the plasma sheet, a near Earth neutral line forms. (c) Magnetospheric configuration during the expansion phase of a substorm where a plasmoid formed between the two X-lines starts to accelerate tailwards. Figure based on Figures 13.21, 13.22 and 13.23 of *Kivelson and Russell* (1995)

During the Expansion phase of the substorm, the open field lines start reconnecting at the new X-line as illustrated by Figure 1.9c. The magnetic tension on the reconnected field lines that surround the plasmoid act to accelerate the plasmoid tailward. Field lines reconnected at the new X-line also act to create new closed field lines. The X-line then proceeds to move tailward and the plasma sheet starts to thicken. Eventually the X-line will reach a distant location in the tail and auroral disturbances will die off as the magnetosphere returns to its original state during the substorm's recovery phase.

The substorm has also been described in terms of the aurora produced during the event. A study by *Akasofu* (1964) described the development of the auroral substorm. Initially the aurora is calm and forms homogeneous arcs as shown in panel (a) of Figure 1.10 where the auroral arcs are presented in a polar plot projected over the north pole where noon is at the top and the concentric circles represent latitude. The auroral substorm starts off with an initial sudden brightening of the aurora caused by the injection of plasma particles into the inner magnetosphere as shown in panel (b), shortly followed by the poleward expansion of the aurora for several minutes until it reaches its highest latitude as yet more plasma is injected in panels (c) and (d). Eventually, after the expansion phase, the recovery phase will start. During this phase the aurora will move equatorward and reduce in brightness as shown in panels (e) and (f).

During a substorm, there is diversion of the tail current into the ionosphere known as the substorm current wedge (SCW). When the tail field collapses, the current flows down the magnetic field lines to close in the ionosphere forming a westward auroral electrojet as shown in Figure 1.11 (*McPherron et al.*, 1973). This current system has been shown to have a distinctive signature in mid-latitude ground magnetometer data as presented in Figure 1.12. Between the two field-aligned currents, it is expected that there would be a symmetric peak in the north-south component (H) and an anti-symmetric perturbation in the east-west component (D) with a positive peak near the westward field aligned current and a negative peak near the eastward field aligned current. The HDZ coordinate system often used to express ground magnetometer data is presented in Figure 1.13 with the geographically-oriented XYZ coordinate system. In both coordinate systems, the Z component points downward, towards the centre of the Earth. The X and Y components are oriented such that X points towards geographic

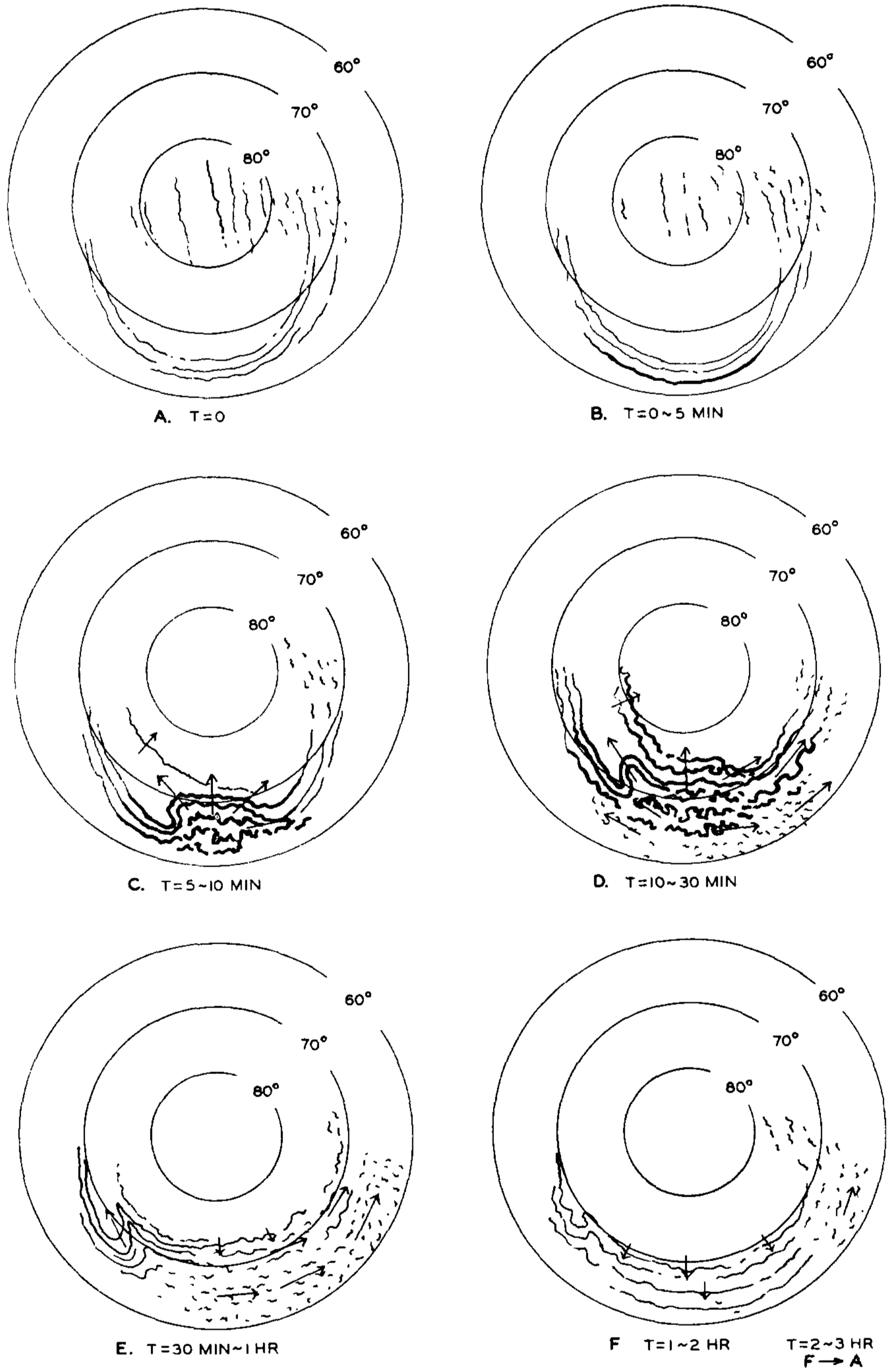

Figure 1.10: Auroral substorm - Diagram illustrating the development of the auroral substorm from onset, through the expansion phase to the recovery phase by *Akasofu* (1964). Each panel presents the aurora in a polar plot projected over the northern hemisphere where the concentric circles represent the latitude and the orientation is such that noon is at the top of the plot.

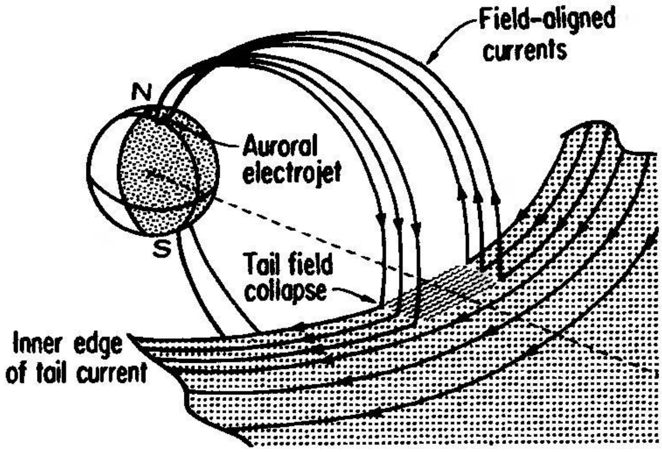

Figure 1.11: Substorm current wedge - Illustration of the formation of the substorm current wedge due to the tail field collapse, diverting the tail current along field lines and through the ionosphere. (Taken from *Clauer and McPherron* (1974).)

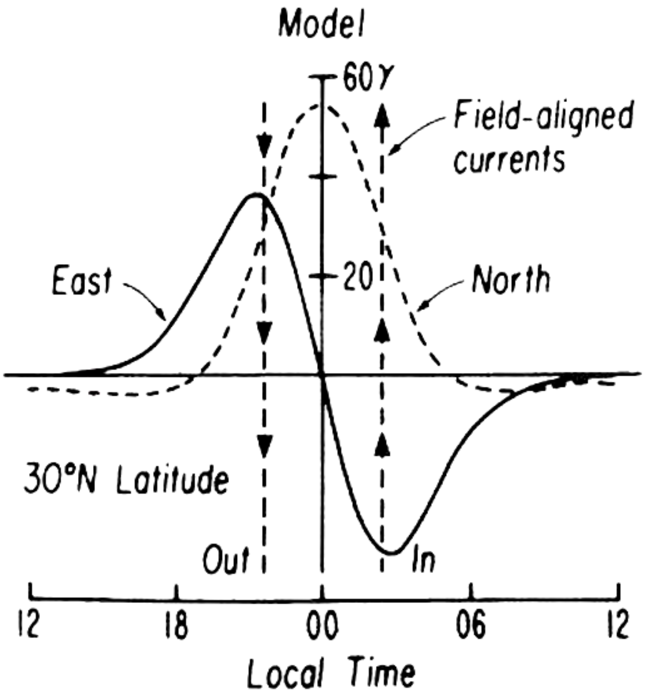

Figure 1.12: Magnetic bays - Diagram showing the 'bays' expected to exist in the North (H) and East (D) components of the Earth's magnetic field near to the substorm current wedge by *Clauer and McPherron* (1974).

north and Y points geographically east. The H and D components are obtained by rotating the X and Y components through the declination angle, θ, so that H points in the direction of the local horizontal magnetic field.

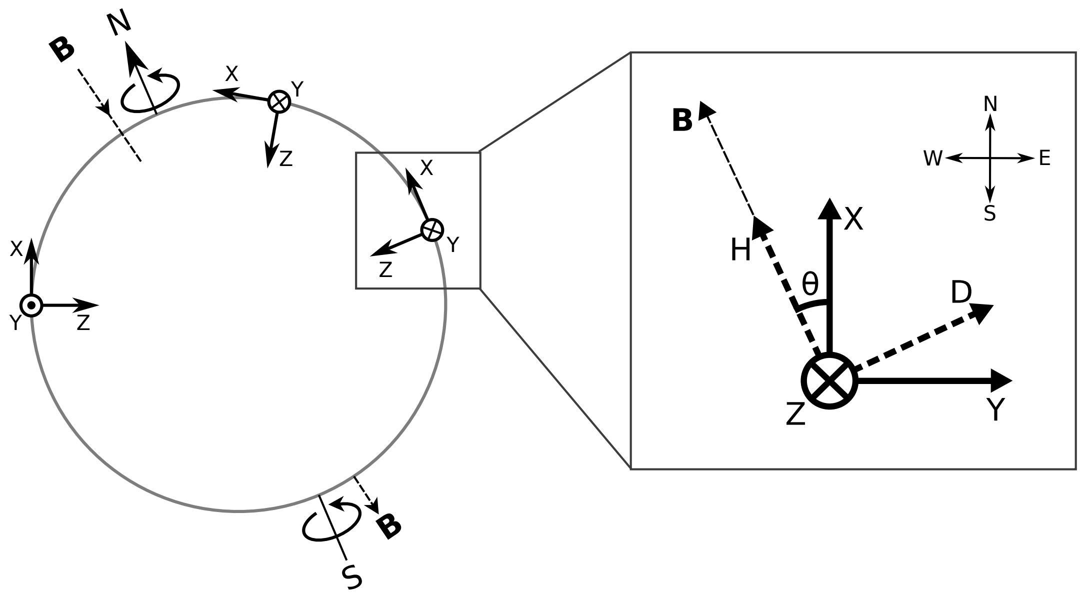

Figure 1.13: Ground magnetometer coordinate systems - The coordinate systems used by ground magnetometers are typically given in either HDZ or XYZ coordinates. In both systems, Z is orientated towards the centre of the Earth (see left of diagram). The X and Y point to geographic north and east, respectively. In the HDZ system, the X and Y components are rotated through the local declination angle, θ, such that H is in the direction of the local horizontal field.

The detection of substorms using their auroral signature will be discussed more in Chapters 4, 5 and 6. The use of ground magnetometer data and the Auroral Electrojet indices to detect and locate substorms using magnetic perturbations caused by the substorm current wedge is described in detail in Chapters 6 and 7.

1.2.4 Geomagnetic Activity Indices

1.2.4.1 Auroral Electrojet Indices

A series of indices based on data from several auroral zone ground magnetometers known as the Auroral Electrojet indices (*Davis and Sugiura*, 1966) are sensitive to substorm activity. They monitor the global electrojet activity by observing perturbations that ionospheric currents make to the H component of the magnetic field. In the event of a substorm, the AU (upper) and AL (lower) indices both depart from their typical background values where AU typically increases and AL decreases due to ionospheric currents (*Gjerloev et al.*, 2004). The AE index is the difference between AU and AL (AU-AL) and provides a measure of the overall horizontal current strength while the AO index is the average of AU and AL and provides a measure of the equivalent zonal current.

Figure 1.14 shows a typical example of a substorm signature in the AU and AL indices taken from *McPherron and Manka* (1985). The onset of the substorm in this figure (10:54 UT) is marked by an increase in the rate of the decrease of AL, further increases in the rate of AL after onset are intensifications. The AL index will continue to decrease during the expansion phase of the substorm. Once the AL index has reached its minimum value and begins to return to its normal value, this is the start of the substorm recovery phase.

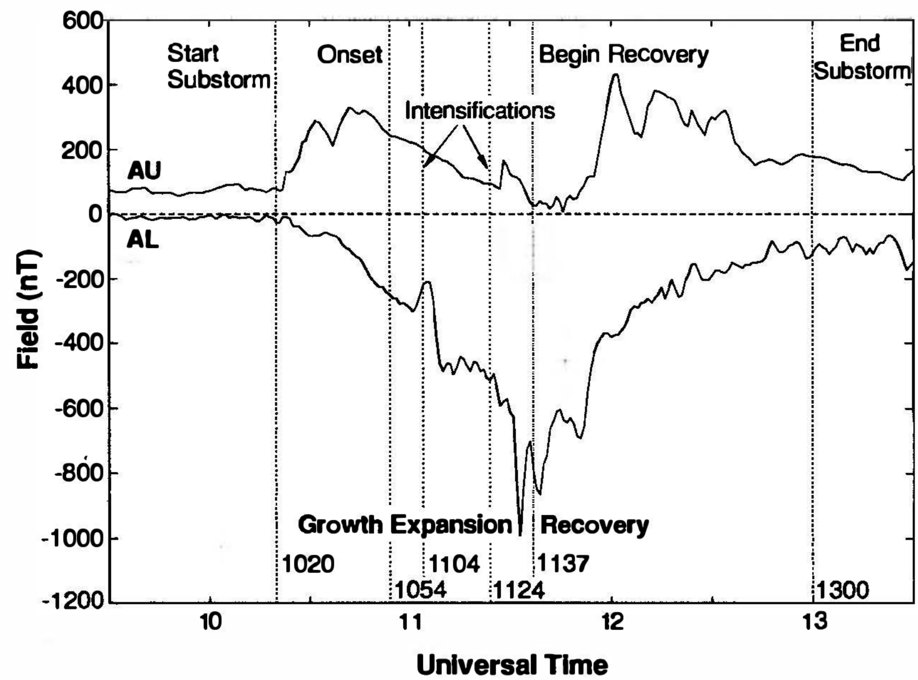

Figure 1.14: Auroral Electrojet signatures of a substorm - Stages of a substorm in terms of the AU and AL indices, taken from *McPherron and Manka* (1985).

1.2.4.2 D_{ST} Index

The D$_{st}$ (Disturbance Storm Time) index is a measure of the perturbation in the H component of the Earth's magnetic field measured by several magnetometers near the equator due to changes within the ring current. Enhancements in the Earth's ring current induce a magnetic field anti-parallel to that of the Earth causing a decrease in the horizontal field strength, H, near the Equator. Reductions in ring current intensity have the opposite effect, resulting in an increase in H near the equator. The D_{ST} index is calculated by averaging the departure of H from its baseline value for all of the magnetometer stations used (*WDC Kyoto Observatory*).

During a geomagnetic storm, the D_{ST} index can provide a measure of the storm's intensity, where a more severe storm is marked by a larger decrease in the value of D_{ST}. D_{ST} typically shows a sudden rise at the start of the storm indicating the 'sudden commencement' of the storm. This sudden rise in D_S is then immediately followed by a sharp decrease as the ring current intensifies - signifying the main phase of the storm which may last a few days. At the end of the main phase of the storm, the D_{ST} index gradually returns to quiet-time levels as the ring current reduces in intensity, thus marking the recovery phase (*Hamilton et al.*, 1988).

1.2.4.3 K_P Index

The K_p (a German acronym:'planetarische Kennziffer' or planetary index) index provides an indication of geomagnetic activity where one K_p value is produced every three hours (*Wing et al.*, 2005) from the degree of disturbance in the H and D components of the magnetic field (*GFZ Potsdam*). It is calculated using 13 ground magnetometer stations outside of the auroral zone and can have one of 28 values between 0 and 9 (0o, 0+, 1, 1o, 1+, 2-, 2o, 2+, ..., 8o, 8+, 9-, 9o) where values of $K_p = 5$ or more correspond to storm-time levels of geomagnetic activity (*National Geophysical Data Center, NOAA*).

1.3 Earth's Ionosphere

1.3.1 Structure

The Earth's ionosphere forms part of the upper atmosphere from ~60 - 600 km altitude. The ionosphere is a naturally formed, weakly ionised plasma, although it is ionised enough to affect the propagation of radio waves. In 1901 Guglielmo Marconi made use of the ionosphere's ability to alter the propagation of radio waves by transmitting a signal across the Atlantic ocean from Cornwall to Newfoundland. Arthur Kennelly and Oliver Heaviside suggested that the radio waves transmitted by Marconi were reflected by the highly conductive ionosphere. The ionosphere plays an important role in the physics of ULF waves as it is considered as one of the main sinks of wave energy.

There are three main layers to the Earth's ionosphere named D, E and F. The first of these to be discovered was the E layer which had this letter as E was used to represent the electric vector for the down-coming wave. When the next reflective layer was discovered above the E layer, the letter F was used to symbolise the electric vector of a down coming wave from this layer. It was therefore logical to name the layer later discovered below the E layer to be D, leaving A, B and C for other potential reflective layers. Figure 1.15 shows the typical electron densities of the three layers of the ionosphere as a function of height for both night and day time.

The D layer of the ionosphere exists between approximately 70 and 90 km altitude during the daytime. Ionisation of this layer is caused primarily by the absorption of X-rays and Ly-α emissions. This region is relatively dense; dense enough for both 2 and 3 body collisions to be common. Negative ions may also form in this region at night when there is little visible or UV light to break them down (*Rishbeth*, 1988).

The E layer of the ionosphere lies above the D layer at ~100 - 120 km. Photoionisation in this region is mainly due to X-rays and EUV, forming mainly NO^+ and O_2^+ ions. The atmosphere is more rarefied here so only 2 body collisions would usually occur at this altitude, so atomic ions cannot recombine as easily with electrons as molecular ions can (*Rishbeth*, 1988).

The F layer is split into two - the F1 and F2 layers. The F1 layer consists primarily of NO^+ and O_2^+ ions ionised by EUV radiation between 150 and 180 km. The F2 layer lies above the F1 layer, but this layer does not absorb much ionising radiation so it

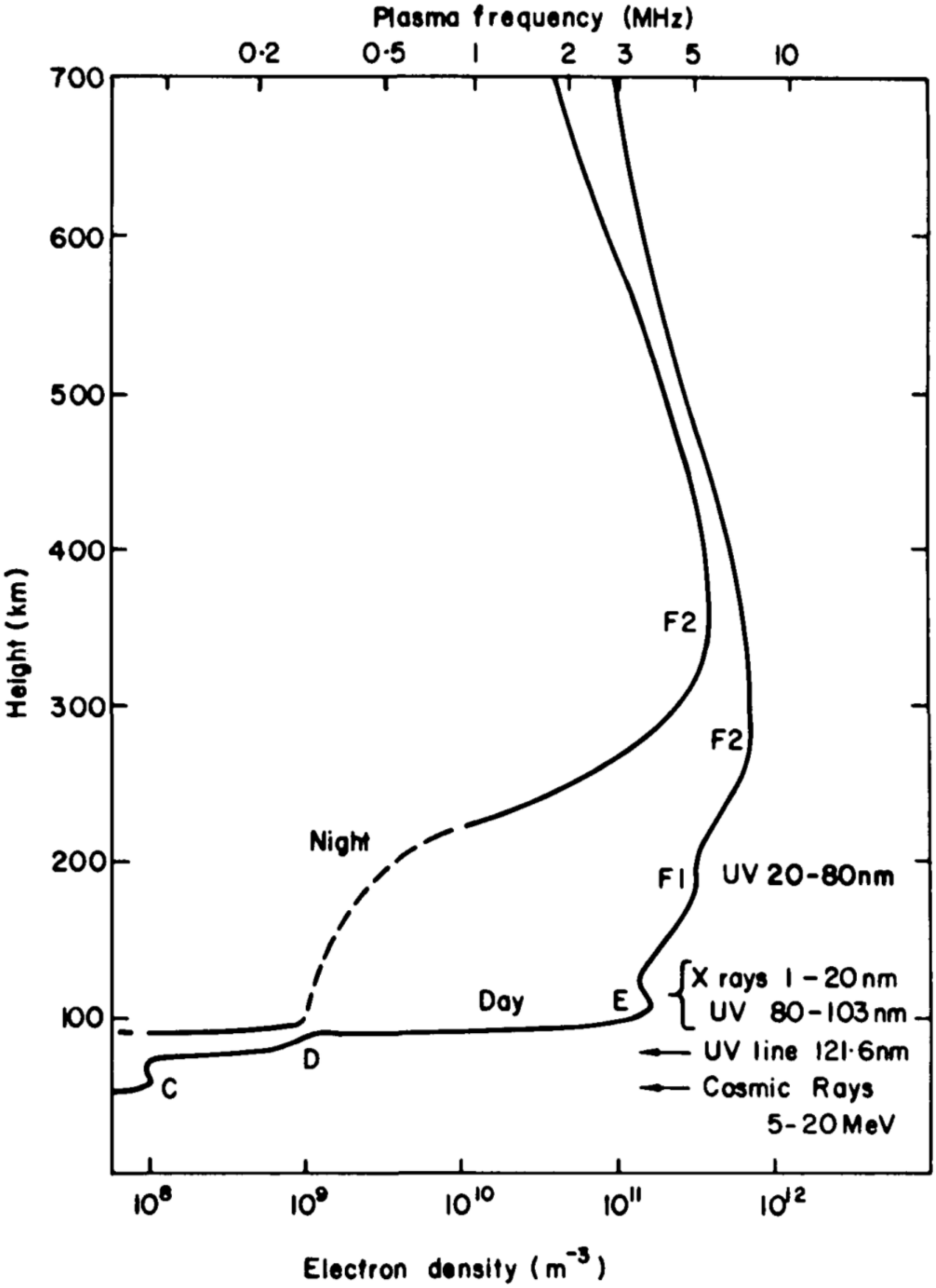

Figure 1.15: Ionospheric electron densities - Typical electron density profiles in the mid-latitude ionosphere for day and night, taken from *Rishbeth* (1988).

consists mainly of ions created by the F1 layer. The larger peak in the electron density in the F2 layer is due to the lower rate of electron loss (*Rishbeth*, 1988).

1.3.2 Ionospheric Current Systems

The ionosphere is considered a quasi-neutral plasma so there can be no divergence in **j**. Its high conductivity due to the existence of free electrons and ions quickly neutralises any electric field present by the flow of electric currents. The ionosphere has three main associated conductivities - longitudinal conductivity, σ_0; Pedersen conductivity, σ_P and Hall conductivity, σ_H.

The longitudinal conductivity is in the direction of the electric field parallel to the magnetic field ($E_{\|}$) and is primarily carried by electrons as they are more mobile. The Pedersen conductivity flows in the direction of the electric field perpendicular to the magnetic field ($E_{\perp}$) and is mainly carried by ions, peaking at around 125 km altitude. The Hall conductivity is in the direction which is normal to both the electric and magnetic fields and is carried primarily by electrons which form the main part of all of the ionospheric currents. Ohm's law for the ionospheric currents is (*Rishbeth*, 1988)

$$\mathbf{j} = \sigma_0 \mathbf{E}_{\|} + \sigma_P \mathbf{E}_{\perp} + \sigma_H (\frac{\mathbf{B} \times \mathbf{E}_{\perp}}{B}). \tag{1.2}$$

Figure 1.16 is a diagram of the current systems present within the magnetosphere. All of the currents aside from the ring current (dotted line) close within the ionosphere. Both region 1 and 2 Birkland currents are field-aligned currents, connected to the magnetopause current, and close across the polar cap as shown. Partial ring currents close in the ionosphere as auroral electrojets. The dashed line illustrates the tail current diverted due to a substorm breakup, forming the substorm current wedge, which closes within the ionosphere as a westward electrojet.

1.4 Thesis Overview

Chapter 2 of this thesis will introduce the theory behind ULF waves, beginning with the basics of space plasmas. Chapter 3 will discuss in detail some of the results from previous literature relevant to the study of ULF waves. Chapter 4 will give a description

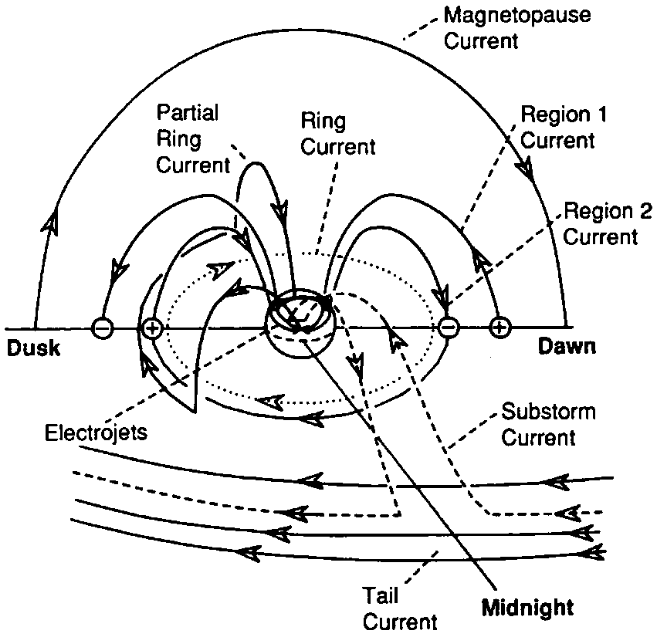

Figure 1.16: Schematic of magnetospheric current systems - Schematic showing the current systems responsible for geomagnetic activity, from *Kivelson and Russell* (1995).

of the instrumentation and some of the data analysis techniques used in this thesis. Chapter 5 explores the suggestion made by *Yeoman et al.* (2010) that the characteristics of ULF waves may be related to the proximity to the substorms that drive them with a statistical study of 83 substorm-driven waves. Chapter 6 examines the results obtained in Chapter 5 further by looking at events where more than one wave was observed at different locations relative to the location of particle injection. Chapter 7 makes use of in-situ data to observe and study the particle populations as they drive this class of ULF wave. Finally, Chapter 8 will provide a summary of this thesis and discuss potential future work in this field.

Chapter 2

Plasma Physics and Magnetohydrodynamic Wave Theory

2.1 Individual Particle Motion in an Electromagnetic Field

Plasma particles behave differently to their neutral gas counterparts in that electric and magnetic forces dominate over thermodynamic forces. The equation of motion of such a particle can be obtained by combining Newton's second law, $\mathbf{F} = m\mathbf{a}$, with the Lorentz forces, $\mathbf{F} = q(\mathbf{E} + \mathbf{v} \times \mathbf{B})$, to give Equation 2.1 where m is the mass of the particle, q is the charge, $\mathbf{E}$ is the electric field vector, $\mathbf{B}$ is the magnetic field vector and $\mathbf{v}$ is the particle's velocity vector.

$$m\frac{d\mathbf{v}}{dt} = q(\mathbf{E} + \mathbf{v} \times \mathbf{B}) \tag{2.1}$$

In this section we discuss the motion of individual charged particles in various steady electric and magnetic field configurations where $\mathbf{E}$ and $\mathbf{B}$ are assumed to vary slowly in time.

2.1.1 Motion in a Constant Magnetic Field ($E = 0$)

In this situation we assume that there is no electric field present, a constant magnetic field oriented in the $\hat{\mathbf{z}}$ direction, and the particle velocity vector, $\mathbf{v}$, can be split up in to three Cartesian components as described in 2.2.

$$\begin{aligned}
\mathbf{v} &= v_x\hat{\mathbf{x}} + v_y\hat{\mathbf{y}} + v_z\hat{\mathbf{z}} \\
\mathbf{B} &= B\hat{\mathbf{z}} \\
\mathbf{E} &= 0
\end{aligned} \tag{2.2}$$

Equation 2.1 can then be expressed in each of its Cartesian components as shown in 2.3.

$$\begin{aligned}
&\text{(a) } \frac{dv_x}{dt} = \frac{qB}{m}v_y \\
&\text{(b) } \frac{dv_y}{dt} = -\frac{qB}{m}v_x \\
&\text{(c) } \frac{dv_z}{dt} = 0
\end{aligned} \tag{2.3}$$

Equations 2.3 (a) and (b) can be combined to form Equation 2.4 - a one dimensional equation of simple harmonic motion (SHM) where Ω defines the gyrofrequency of the particle.

$$\frac{d^2v_x}{dt^2} = -\left(\frac{qB}{m}\right)^2 v_x = -\Omega^2 v_x \tag{2.4}$$

Equations 2.5 (a) and (b) are both solutions of Equation 2.4 where $v_\perp$ is the component of the particles velocity perpendicular to $\mathbf{B}$ and ϕ is the phase of the oscillation.

$$\begin{aligned}
&\text{(a) } v_x = v_\perp \cos(\Omega t + \phi) \\
&\text{(b) } v_y = \frac{1}{\Omega}\frac{dv_x}{dt} = -v_\perp \sin(\Omega t + \phi) \\
&\text{where } v_\perp = \sqrt{v_x^2 + v_y^2}
\end{aligned} \tag{2.5}$$

Integrating Equations 2.5 (a) and (b) with respect to time provides use with Equations 2.6 (a) and (b). These equations show how charged particles with a velocity component perpendicular to the magnetic field gyrate with a gyroradius of $r_g = \frac{v_\perp}{\Omega}$ and a gyroperiod $\tau = \frac{2\pi}{\Omega}$ around the field line at the position (x_0, y_0).

$$\text{(a) } x(t) = x_0 + \frac{v_\perp}{\Omega}\sin(\Omega t + \phi)$$
$$\text{(b) } y(t) = y_0 + \frac{v_\perp}{\Omega}\cos(\Omega t + \phi) \tag{2.6}$$

As Ω is a function of mass, both r_g and τ must be a function of mass too such that the gyroradius and gyrofrequency of and electron would differ to that of a proton. Also, the direction of the gyration is dependent upon q, so electrons and ions gyrate in opposite directions, forming current loops which produce a magnetic field which opposes that of the background field, $\mathbf{B}$.

Also, it can be proven using Equation 2.1 where $E = 0$ that, where there is a steady magnetic field, the speed of a particle remains constant.

$$m\frac{d\mathbf{v}}{dt} = q(\mathbf{v} \times \mathbf{B}) \tag{2.7}$$

By taking the dot product of Equation 2.7 with $\mathbf{v}$,

$$\begin{aligned} m\mathbf{v} \cdot \frac{d\mathbf{v}}{dt} &= m\frac{d}{dt}\left(\frac{1}{2}\mathbf{v} \cdot \mathbf{v}\right) \\ &= \frac{d}{dt}\left(\frac{1}{2}mv^2\right) \\ &= q\mathbf{v} \cdot (\mathbf{v} \times \mathbf{B}) \end{aligned} \tag{2.8}$$

$$\begin{aligned} \text{where } \mathbf{v} \cdot (\mathbf{v} \times \mathbf{B}) &= 0 \\ \therefore \frac{d}{dt}\left(\frac{1}{2}mv^2\right) &= 0 \end{aligned}$$

we can show that there is no change in the total kinetic energy of the particle as it gyrates through the magnetic field. Due to the constancy of the particle's kinetic energy, the speed of the particle must also remain constant such that,

$$v = \sqrt{v_\perp^2 + v_\parallel^2} = \text{constant} \tag{2.9}$$

where $v_\perp$ is the component of $\mathbf{v}$ perpendicular to $\mathbf{B}$ and $v_\parallel$ is parallel to $\mathbf{B}$.

2.1.2 Magnetic Mirroring ($E = 0$)

Figure 2.1 shows the scenario in which a steady magnetic field becomes stronger along the path of a gyrating charged particle. In this diagram, the gradient of the magnetic field and $v_{\|}$ are both oriented along the z axis where there is a component of the Lorentz force acting in the opposite direction. The component of the Lorentz force acting in the $-z$ direction must cause $v_{\|}$ to reduce as the particle penetrates into the stronger field, but as Equation 2.9 must remain true, $v_{\perp}$ must therefore increase accordingly. The increase leads to a larger component of the Lorentz force in the $-z$ direction, eventually leading to the mirroring of the particle.

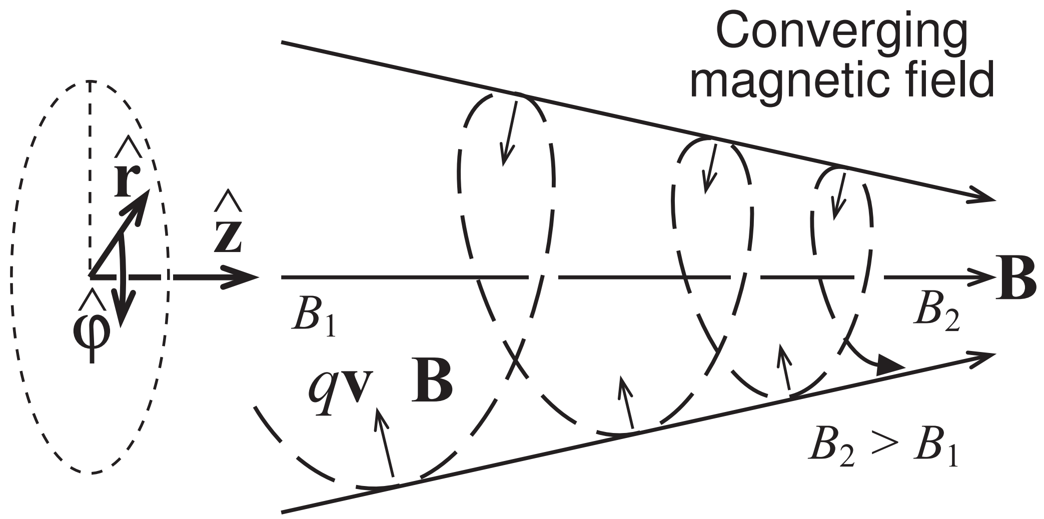

Figure 2.1: Magnetic mirroring - Diagram showing converging magnetic field lines in the $\hat{\mathbf{z}}$ direction. The path of a particle gyrating around the z-axis with a component of its velocity in the $\hat{\mathbf{z}}$ direction is presented as a dashed line, where the Lorentz force on the particle is indicated by small arrows (Figure courtesy of S.E. Milan).

The location of the mirror point of the particle can be derived using the fact that $\nabla \cdot \mathbf{B} = 0$ which can be expressed in cylindrical coordinates as

$$\frac{1}{r}\frac{\partial}{\partial r}(rB_r) + \frac{dB(z)}{dz} = 0 \tag{2.10}$$

where it is assumed that there is no twisting of $\mathbf{B}$ so $B_\phi = 0$ and that $B_z \approx B(z)$.

Equation 2.10 can then be rearranged and integrated with respect to r to find that

$$B_r = -\frac{r}{2}\frac{dB(z)}{dz}. \tag{2.11}$$

If $v_\phi = -v_\perp$ (for a positive particle) and $v_z = v_\parallel$, we can calculate the z component of the Lorentz force as

$$\begin{aligned} F_z &= -ev_\phi B_r \\ &= -\frac{ev_\perp r}{2}\frac{dB}{dz} \\ \text{where } r &= \frac{mv_\perp}{eB} \end{aligned} \tag{2.12}$$

which shows that the force is acting in the opposite direction to the gradient in $\mathbf{B}$.

Using Newton's second law we find that

$$\begin{aligned} \frac{dv_\parallel}{dt} &= \frac{F_z}{m} = -\frac{v_\perp^2}{2B}\frac{dB}{dz} \\ \Rightarrow v_\parallel dv_\parallel &= d\left(\frac{v_\parallel^2}{2}\right) = -\frac{v_\perp^2}{2}\frac{dB}{B} \\ \text{where } d(v_\parallel^2) &= d(v_\perp^2) \\ \Rightarrow \frac{d(v_\perp^2)}{v_\perp^2} &= \frac{dB}{B} \\ \text{when integrated becomes } \ln(v_\perp^2) &= \ln(B) + \text{constant} \\ \text{or } \frac{v_\perp^2}{B} &= \frac{v_{\perp 0}^2}{B_0} = \text{constant} \end{aligned} \tag{2.13}$$

where the constant is known as the first adiabatic invariant, where the mirror point, B_m, occurs when $v_\parallel = 0$ or $B_m = B_0\left(\frac{v}{v_\perp}\right)^2$.

The pitch angle of the particle's motion relative to the background magnetic field is a function of both parallel and perpendicular components of the velocity where $\alpha = \arctan\left(\frac{v_\perp}{v_\parallel}\right)$ so $v_\perp = v\sin(\alpha)$ and $v_\parallel = v\cos(\alpha)$. The first adiabatic invariant can then be expressed as,

$$\begin{aligned} \frac{v^2\sin^2\alpha}{B} &= \text{constant} \\ \text{where } v \text{ is constant so} & \\ \frac{\sin^2\alpha}{B} &= \text{constant} \end{aligned} \tag{2.14}$$

which can be used to locate the magnetic mirror point, where $\alpha = 90°$, therefore

$$B_m = \frac{B}{\sin^2 \alpha} \tag{2.15}$$

which shows that the mirror point depends only upon the pitch angle of the particle, not its mass, energy or charge.

2.1.3 The Effect of Non-Zero Electric Fields

The previous two sections discussed the motion of individual particles moving in a steady magnetic field with no electric field present, here we discuss the effect of a non-zero electric field.

The effect of $\mathbf{E}$ parallel to that of $\mathbf{B}$ is relatively straight forward. If we consider that $\mathbf{B} = B\hat{\mathbf{z}}$ and $\mathbf{E} = E_{\parallel}\hat{\mathbf{z}}$ then the equation of motion of the particle becomes

$$\frac{dv_z}{dt} = \frac{dv_{\parallel}}{dt} = \frac{q}{m}E_{\parallel} \tag{2.16}$$

as the component of the velocity perpendicular to $\mathbf{B}$ would not be affected. This would result in positive particles moving then the direction of $\mathbf{E}$ and negative particles in the opposite direction in order to reduce the electric field.

The effect of $\mathbf{E}$ perpendicular to $\mathbf{B}$ is somewhat different to the parallel case. If we consider that $\mathbf{B} = B\hat{\mathbf{z}}$ and $\mathbf{E} = E_{\perp}\hat{\mathbf{y}}$ as portrayed in Figure 2.2 then the particle initially at rest would be accelerated due to the electric field. As the particle gains velocity, the particle starts to gyrate due to the $q\mathbf{v} \times \mathbf{B}$ term of Equation 2.1. As the Lorentz force on the particle increases, the particle starts moving in the opposite direction to the acceleration provided by the electric field, the motion along y will slow and eventually reverse itself again such that the particle moves in the same direction as the acceleration due to $\mathbf{E}$, resulting in a hopping motion of the particle. The resultant flow of particles is in the $\mathbf{E} \times \mathbf{B}$ direction irrespective of charge with a drift velocity of,

$$\mathbf{V}_{\mathbf{E}\times\mathbf{B}} = \frac{\mathbf{E} \times \mathbf{B}}{B^2} \tag{2.17}$$

In a frame of reference which moves with the drift velocity, $\mathbf{V}_{\mathbf{E}\times\mathbf{B}}$, the particles would appear to be gyrating as if $E = 0$ as described in section 2.1.1. This then implies that the electric field that is felt by the particles is dependant upon what reference frame

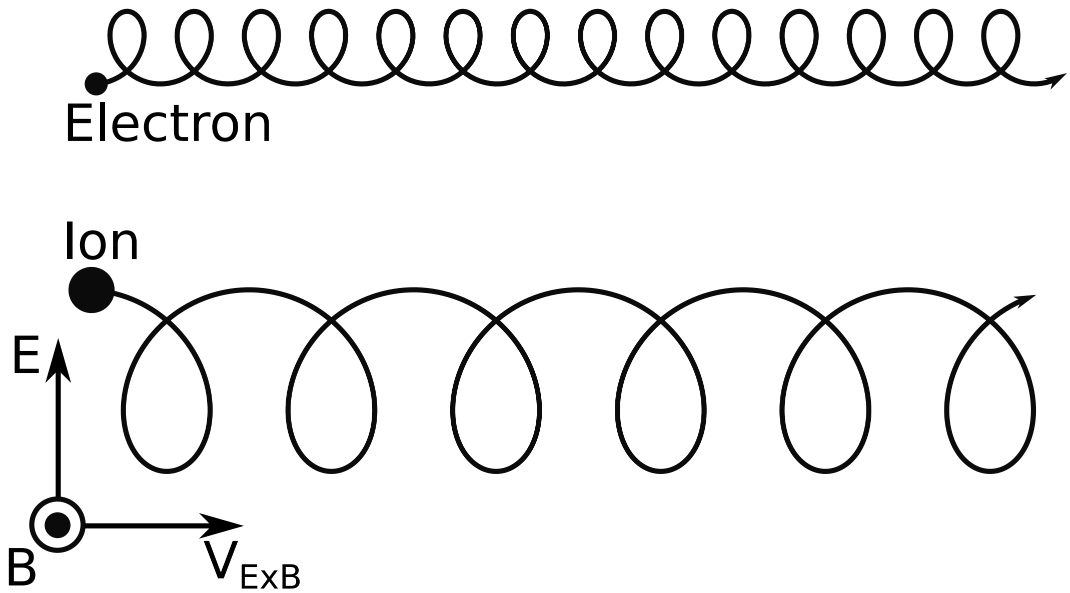

Figure 2.2: $\mathbf{E} \times \mathbf{B}$ drift - This diagram shows the $\mathbf{E} \times \mathbf{B}$ drift of both electrons and ions and the paths traced out by the particles as they gyrate.

the particles are observed in, thus where there is a plasma drift, $\mathbf{V}$ there must be an electric field,

$$\mathbf{E} = -\mathbf{V} \times \mathbf{B}. \tag{2.18}$$

2.1.4 Gradient and Curvature Drifts

In space plasmas, such as those within a planet's magnetosphere, it is often unrealistic to consider the magnetic field as constant in strength and direction. Such plasmas experience both gradients in $\mathbf{B}$ and curvature of $\mathbf{B}$. Section 2.1.2 explained the effect of a magnetic field gradient parallel to the field, this section is more concerned with the effect produced when the gradient is perpendicular to $\mathbf{B}$.

As discussed in Section 2.1.1, a particle in a uniform magnetic field with no electric field present gyrates around its guiding centre with a radius of,

$$r_g = \frac{v_\perp}{\Omega} = \frac{mv_\perp}{qB}. \tag{2.19}$$

As the gyroradius is clearly dependent upon the magnetic field strength, B, it is obvious that if a particle gyrates in a field with a gradient perpendicular to $\mathbf{B}$ that its instantaneous gyroradius must change with time. As the particle gyrates, the radius will alternate causing the particle to drift with a drift velocity of (*Bittencourt*, 2013):

$$v_g = \frac{1}{2} m v_\perp^2 \frac{\mathbf{B} \times \nabla \mathbf{B}}{q B^3} \tag{2.20}$$

where the direction of the drift is perpendicular to both the magnetic field, $\mathbf{B}$, and the gradient in the magnetic field, $\nabla \mathbf{B}$. Equation 2.20 also shows that the direction of v_g depends upon the charge of the particles, implying that a current is induced by the gradient drift of the plasma.

In a dipolar magnetic field, the gyrating particles that traverse the curved field lines experience a centrifugal acceleration. The gyroradius of the particles increases away from the curvature of the field and causes the particles to drift perpendicular to the field and the radius of curvature with a drift velocity of (*Bittencourt*, 2013),

$$v_c = -\frac{m v_\parallel^2}{R_c q B^2} \mathbf{B} \times \hat{\mathbf{n}}, \tag{2.21}$$

where R_c is the radius of the field line curvature and $\hat{\mathbf{n}}$ is the unit vector normal to the curvature. Like the gradient drift, the curvature drift is charge dependant also implying that a current will form in a plasma in a curved magnetic field.

In a dipolar, or near dipolar magnetic field such as a planetary magnetosphere, particles are subject to both gradient and curvature drifts. Both of these particle drifts occur in the same direction and, for the remainder of this thesis, will be considered together as one gradient-curvature drift.

In the Earth's magnetosphere, the gradient-curvature drifts are directed such that electrons drift around the planet eastward and positive ions drift westwards. This forms the westward flowing current known as the ring current which acts to reduce the strength of the low latitude magnetic field.

Figure 2.3 shows the combination of the gyromotion described in Section 2.1.1 with the bouncing motion explained in Section 2.1.2 alongside the gradient-curvature drift for an electron in a dipolar magnetic field. The motion of a positive ion is very similar, only with a different gyroradius/gyrofrequency and the gradient-curvature drift acts in the opposite direction.

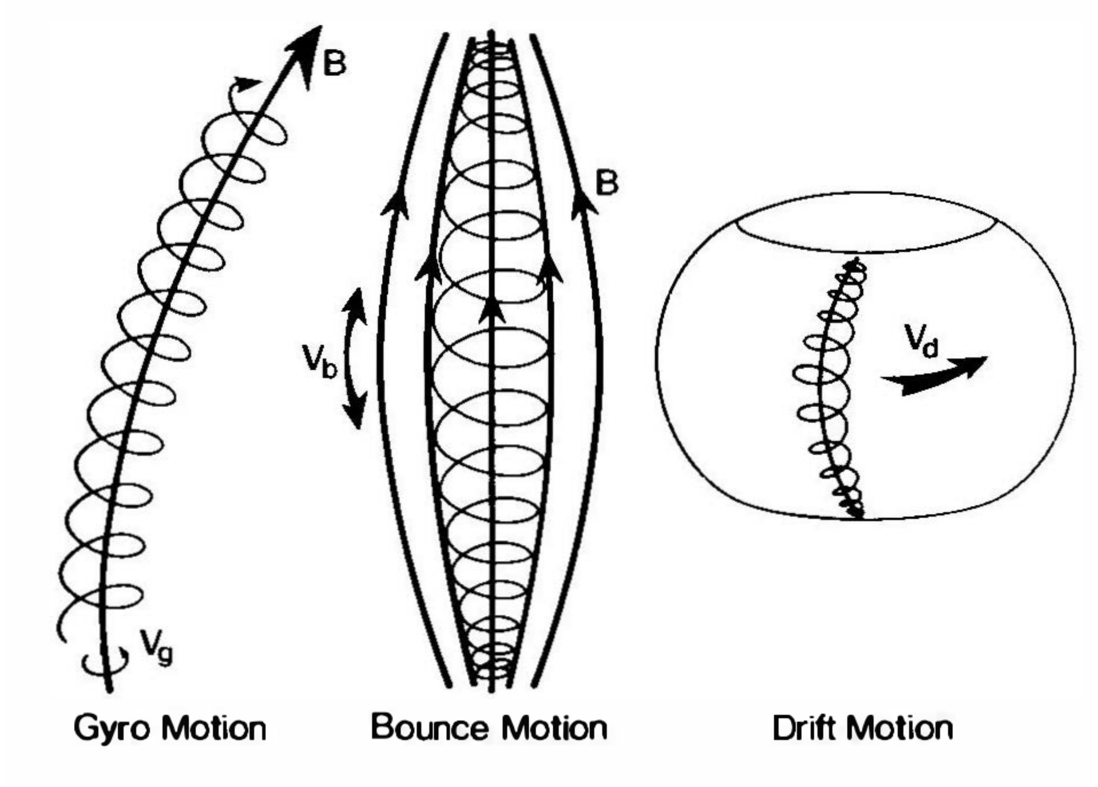

Figure 2.3: Particle motion due to magnetic morphology - An illustration of particle motion due to the morphology of the magnetic field. The left diagram shows an example of a particle gyrating along a field line to which it is frozen-in. The middle diagram shows the bounce motion of a particle trapped between two areas of increasing magnetic field strength. The diagram on the right shows the drift motion of the particle due to the gradient and curvature of a dipolar magnetic field, where the drift velocity, V_d, in this case is eastward like that of an electron within the Earth's magnetic field. Taken from *Kivelson and Russell* (1995)

2.2 Fluid Dynamics in a Plasma

2.2.1 General Equations

In order to describe a magnetised fluid it is necessary to introduce Maxwell's equations. The first of these, Equation 2.22, states that any divergence in an electric field is related to some finite charge density. The second, Equation 2.23, states that there can be no overall divergence in the magnetic field, i.e. there are no magnetic monopoles. Equation 2.24 describes the electric field that is induced in the presence of a time-varying magnetic field. Finally, Equation 2.25 is the Ampère-Maxwell relation which relates a current system, **j**, to the magnetic field. When the electric field varies slowly with time, the second term on the right hand side of Ampère-Maxwell relation (the displacement current) may be neglected, leaving only the first term (the conduction current), forming Ampère's law.

$$\text{(a)}\nabla \cdot \mathbf{E} = \frac{\rho_q}{\epsilon_0} \qquad \text{(b)} \int \mathbf{E} \cdot \mathbf{dS} = \frac{Q}{\epsilon_0} \tag{2.22}$$

$$\text{(a)}\nabla \cdot \mathbf{B} = 0 \qquad \text{(b)} \int \mathbf{B} \cdot \mathbf{dS} = 0 \tag{2.23}$$

$$\text{(a)}\nabla \times \mathbf{E} = -\frac{\partial \mathbf{B}}{\partial t} \qquad \text{(b)} \int \mathbf{E} \cdot d\mathbf{l} = -\int \frac{\partial \mathbf{B}}{\partial t} \cdot d\mathbf{S} \tag{2.24}$$

$$\text{(a)}\nabla \times \mathbf{B} = \mu_0 \mathbf{j} + \mu_0 \epsilon_0 \frac{\partial \mathbf{E}}{\partial t} \qquad \text{(b)} \int \mathbf{B} \cdot d\mathbf{l} = \mu_0 \mathbf{I} + \mu_0 \epsilon_0 \int \frac{\partial \mathbf{E}}{\partial t} \cdot d\mathbf{S} \tag{2.25}$$

Equation 2.26 describes how the plasma density, ρ, varies in a plasma where there are no sources or losses of particles. Here, the rate of change of plasma density is related to the divergence of the mass flux.

$$\frac{\partial \rho}{\partial t} + \nabla \cdot \rho \mathbf{v} = 0 \tag{2.26}$$

Momentum in the system must be conserved and can be described by Newton's second law:

$$\rho(\frac{\partial \mathbf{u}}{\partial t} + \mathbf{u} \cdot \nabla \mathbf{u}) = -\nabla p + \mathbf{j} \times \mathbf{B} \tag{2.27}$$

where the left hand side of this equation describes any change of momentum and the right hand represents the pressure and magnetic forces on the particles.

Ohm's law relates the current density, $\mathbf{j}$, to the electric and magnetic fields by

$$\mathbf{j} = \sigma(\mathbf{E} + \mathbf{u} \times \mathbf{B}), \tag{2.28}$$

where σ is the conductivity of the plasma.

2.2.2 The Frozen-in-flow Approximation

If Equation 2.28 is rearranged for $\mathbf{E}$ so,

$$\mathbf{E} = -\mathbf{u} \times \mathbf{B} + \frac{\mathbf{j}}{\sigma}. \tag{2.29}$$

Taking the curl of this equation and applying Faraday's law gives the induction equation,

$$\frac{\partial \mathbf{B}}{\partial t} = \nabla \times (\mathbf{v} \times \mathbf{B}) + \frac{\nabla^2 \mathbf{B}}{\mu_0 \sigma}, \tag{2.30}$$

where the first term is the convective term, and the second is the diffusive term. In highly conductive, almost collisionless plasmas, $\sigma \to \infty$ so the diffusive term vanishes implying that there is no plasma transport across field lines and it can therefore be considered frozen into the magnetic flux.

The ratio of the first and second terms on the right hand side of Equation 2.30 gives the magnetic Reynolds number,

$$R_m = \mu_0 \sigma u L, \tag{2.31}$$

where L is a characteristic scale length of the system begin described. For many solar phenomena, L is large so R_m also becomes large implying that changes in the field and flow of the plasma occur very slowly and the plasma remains frozen-in. R_m typically becomes small enough for the plasma to be diffusive near current sheets such as the dayside magnetopause of the Earth where there is a sharp change in the magnetic field allowing plasma to particles to diffuse from their field lines.

2.3 MHD Waves

ULF waves are magnetohydrodynamic (MHD) waves which have frequencies that are lower than the plasma frequency and the ion gyrofrequency and can be created by both mechanical and electromagnetic forces. They can also be classified by their frequency and their spectra; quasi sinusoidal waves which have a well defined spectral peak are known as continuous pulsations (Pc) while activity which has wave power over a range of frequencies are known as irregular pulsations (Pi). Table 2.1 shows the frequency bands defined for both continuous pulsations and irregular pulsations. This section will discuss the physics behind ULF waves and how they may be driven, focusing on those driven by the bump-on-tail instability.

	Pc-1	Pc-2	Pc-3	Pc-4	Pc-5	Pi-1	Pi-2
Period (s)	0.2-5	5-10	10-45	45-150	150-600	1-40	40-150
Frequency	0.2-5 Hz	0.1-0.2 Hz	22-100 mHz	7-22 mHz	2-7 mHz	0.025-1 Hz	2-25 mHz

Table 2.1: Frequency bands for Pc 1-5 and Pi 1-2 waves (*Jacobs et al.*, 1964).

Figure 2.4 shows an example of a Pc-5 pulsation (a) and a Pi-2 pulsation (b) with their associated Fourier power spectra. The Pc-5 wave presented in the top panel of Figure 2.4 (a) was detected using the Abisko ground magnetometer (part of the IMAGE magnetometer network - see Section 4.4.1.1 on page 100) between 8:00 and 10:00 UT on 29th August 2000. Red, green and blue traces correspond to the H, D and Z components of the magnetic field, where wave activity is clearly visible in all three components. The lower panel of Figure 2.4 (a) shows the Fourier power spectrum of this wave where there are distinct peaks at three different frequencies. The Pi-2 pulsation presented in Figure 2.4 (b) was detected using the Pinawa ground magnetometer (part of the CARISMA network - see Section 4.4.1.2 on page 101) on 2nd October 2013. The Fourier spectrum of this wave, shown in the bottom panel of (b), shows that there is a large range of frequencies present within the Pi-2 pulsation - in contrast to the Pc-5 class of waves, where waves are much closer to being monochromatic.

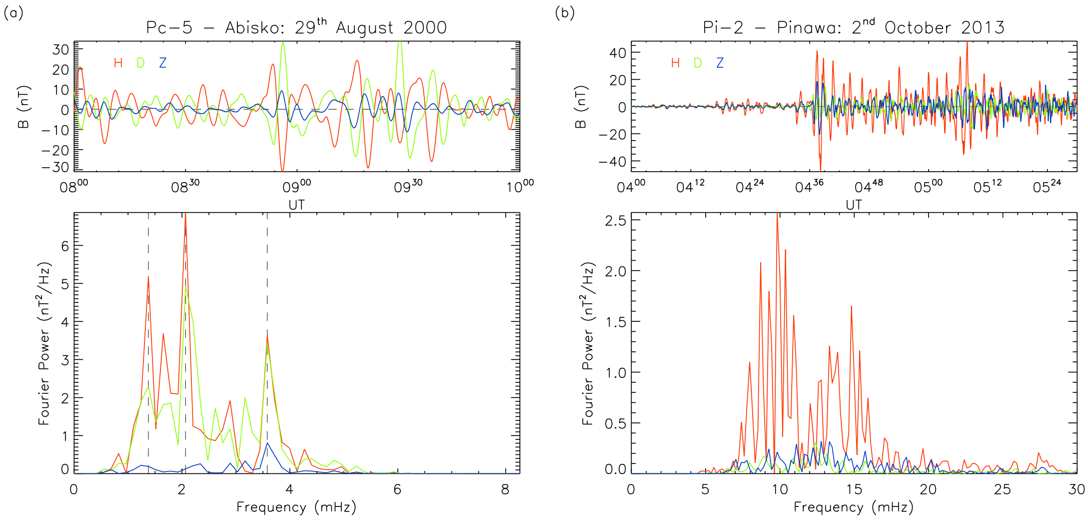

Figure 2.4: Comparison of continuous and irregular pulsations - The top panel of (a) shows the variations H, D and Z components of the magnetic field (red, green and blue, respectively), as measured by the Abisko ground magnetometer, due to the presence of a Pc-5 wave. The lower panel of (a) shows the Fourier spectrum of this wave where there are peeks at three distinct frequencies. The upper panel of (b) shows the perturbations in the magnetic field detected by the Pinawa ground magnetometer, in the same format as (a), due to the presence of Pi-2 pulsations at the onset of a substorm. The Fourier power spectrum of the wave, shown in the bottom panel, reveals a wide range of frequencies present in this class of wave.

Following *Kivelson and Russell* (1995), waves can be described using small perturbations to the background magnetic field, plasma pressure and plasma density:

$$\mathbf{B} \to \mathbf{B} + \mathbf{b} \tag{2.32}$$

$$p \to p + \delta p \tag{2.33}$$

$$\rho \to \rho + \delta \rho \tag{2.34}$$

which introduce finite but small $\mathbf{E}$, $\mathbf{j}$ and $\mathbf{u}$ where

$$\mathbf{E} = -\mathbf{u} \times \mathbf{B} \tag{2.35}$$

$$\text{and } \mathbf{j} = \frac{\nabla \times \mathbf{b}}{\mu_0}. \tag{2.36}$$

The perturbations are small enough to neglect any non-linear terms, and must satisfy the following equations,

$$\frac{\partial \delta\rho}{\partial t} + \rho \nabla \cdot \mathbf{u} = 0, \tag{2.37}$$

$$\rho \frac{\partial \mathbf{u}}{\partial t} = -\nabla \delta p + (\nabla \times \mathbf{b}) \times \frac{\mathbf{B}}{\mu_0}, \tag{2.38}$$

$$\frac{\partial \mathbf{b}}{\partial t} = \nabla \times (\mathbf{u} \times \mathbf{B}), \tag{2.39}$$

$$\nabla \cdot \mathbf{b} = 0, \tag{2.40}$$

where Equation 2.37 is the continuity equation, Equation 2.38 is the modified momentum equation, Equation 2.39 is Faraday's equation and Equation 2.40 states that there can be no divergence in the perturbation magnetic field, b. By taking the curl of Equation 2.39 and combining with Equations 2.35, 2.36 and 2.38 a wave equation can be obtained:

$$\nabla \times (\nabla \times \mathbf{E}) = -\frac{1}{v_A^2} \frac{d^2 \mathbf{E}}{dt^2} \tag{2.41}$$

$$\text{and } v_A = \sqrt{\frac{B^2}{\mu_0 \rho}} \tag{2.42}$$

where v_A is the Alfvén velocity.

2.3.1 Cold Plasma Waves

In a cold plasma, defined by $\beta \ll 1$ where β is the ratio of the plasma pressure to the magnetic pressure:

$$\beta = \frac{P}{B^2/2\mu_0}, \tag{2.43}$$

the plasma pressure is considered to be unimportant.

For a plane wave oscillating in the x-direction, the perturbed quantities mentioned above vary proportionally to

$$e^{ikx}e^{-i\omega t} = e^{i(kx-\omega t)}, \tag{2.44}$$

$$k = \frac{2\pi}{\lambda} \text{ and } \omega = 2\pi f, \tag{2.45}$$

where λ is the wavelength and f is the wave frequency. The phase speed of this wave is $v_{ph} = \frac{\omega}{k}$.

In the cold plasma limit where wave is moving along in the $\hat{\mathbf{x}}$ direction, Equations 2.37, 2.38 and 2.39 become

$$i(\omega\delta\rho - k\rho u_x) = 0, \tag{2.46}$$

$$i[\omega\rho\mathbf{u} - k(\hat{\mathbf{x}}(\mathbf{b}\cdot\mathbf{B}) - B_x\mathbf{b})/\mu_0] = 0, \tag{2.47}$$

$$i[\omega\mathbf{b} + k(B_x\mathbf{u} - u_x\mathbf{B})] = 0, \tag{2.48}$$

respectively, where $\partial/\partial t = -i\omega$ and $\partial/\partial x = -ik$ due to the exponential nature of the waves. If $\mathbf{B}$ is assumed to lie in the $x - z$ plane then $\mathbf{B} = (B\cos\theta, 0, B\sin\theta)$ where θ is the angle between $\mathbf{B}$ and $\mathbf{k}$. The variables in the above equations can be eliminated to form

$$[(\frac{w}{k})^2 - v_A^2\sin^2\theta]u_x + v_A\sin\theta\cos\theta u_z = 0 \tag{2.49}$$

$$[(\frac{w}{k})^2 - v_A^2\cos^2\theta]u_y = 0 \tag{2.50}$$

$$[(\frac{w}{k})^2 - v_A^2\cos^2\theta]u_z + v_A\sin\theta\cos\theta u_x = 0. \tag{2.51}$$

These equations can be satisfied by two dispersion relations under certain conditions,

$$(\frac{\omega}{k})^2 = v_A^2\cos^2\theta. \tag{2.52}$$

$$(\frac{\omega}{k})^2 = v_A^2. \tag{2.53}$$

In the case of a shear Alfvén wave, Equation 2.52 can satisfy the Equations 2.49, 2.50 and 2.51 for any value of u_y but only if $u_x = u_z = 0$. This means that the shear Alfvén wave travels with a phase velocity of $v_A \cos\theta$ and sets the fluid in motion perpendicular to the plane which contains the $\mathbf{k}$ and $\mathbf{B}$ vectors.

Figure 2.5a shows the direction of the perturbation vectors where B lies in the $x - z$ plane. With only small perturbations to the magnetic field, perpendicular to the background field, the magnetic field strength remains almost constant implying that there is no compression of field lines or plasma, so the shear Alfvén wave is a non-compressional wave. As there can be no compression, the perturbed field lines must remain in phase as presented in Figure 2.5c and the phase fronts of the wave travel in the direction of $\mathbf{B}$, shear Alfvén waves are therefore field-guided.

In order to satisfy the Equations 2.49, 2.50 and 2.51 with Equation 2.53, u_y must equal zero, while u_x and u_z automatically satisfy each other. In this case, the fluid is set in motion in the plane containing $\mathbf{B}$ and $\mathbf{k}$. The perturbation vectors for this wave are displayed in Figure 2.5b, where the perturbation to the magnetic field has a component parallel to $\mathbf{B}$ meaning that the magnetic field strength changes with the wave phase. If the magnetic field strength changes with the presence of the wave, the magnetic and thermal pressures must also change making this wave mode a compressional wave, known as the 'fast mode'.

Figure 2.5d shows that the fast mode wave, unlike the shear Alfvén wave, has a phase propagation oblique to $\mathbf{B}$ so the phase fronts travel in the direction of $\mathbf{k}$ rather than being field-guided. If the wave propagation vector is anything other than parallel to the background magnetic field, then the phase speed is greater for Equation 2.53 than for Equation 2.52, hence the label 'fast mode'.

The wave energy propagates in the direction of the Poynting flux vector,

$$\mathbf{S} = \frac{1}{\mu_0}\mathbf{E} \times \mathbf{b}, \tag{2.54}$$

which is shown for both the Alfvén mode and fast mode in Figures 2.5a and 2.5b. The Poynting flux vector points in the direction along $\pm\mathbf{B}$ in the case of the shear Alfvén wave, meaning that energy in information can only be transported along the field lines with this mode, but the Poynting flux vector for the compressional wave is in the direction of $\mathbf{k}$ enabling energy transfer across field lines.

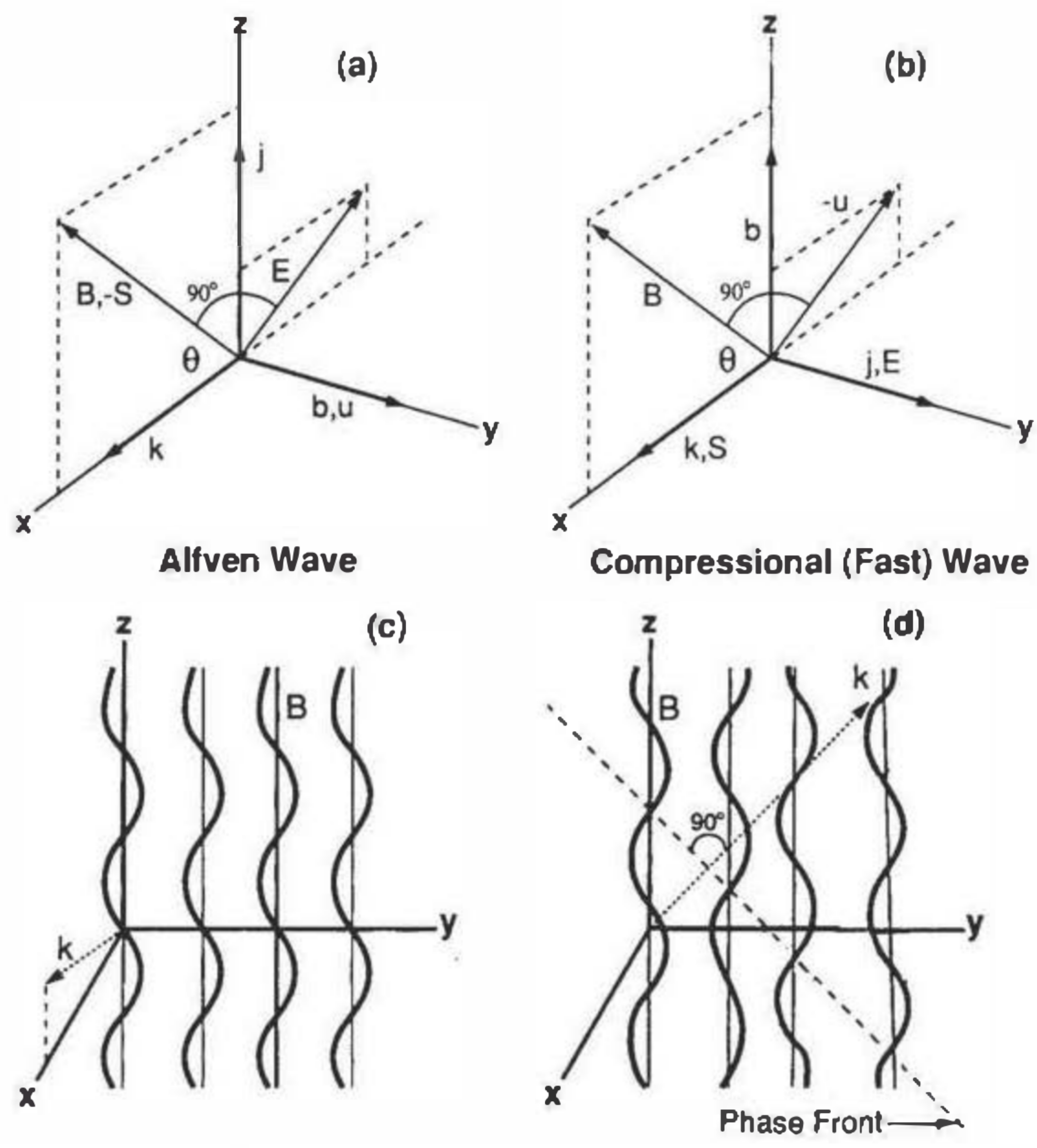

Figure 2.5: Alfvén and fast mode wave vectors - Panels (a) and (b) show the perturbation vectors created by wave activity with respect to the background magnetic field, $\mathbf{B}$, for a shear Alfvén wave and a fast-mode compressional wave. Panel (c) shows an illustration of the perturbations on the magnetic field lines in the case of an Alfvén wave where the separation of the field lines remains constant, i.e. no change of pressure. Panel (d) shows a similar diagram to (c) but for the fast mode wave, in this case field lines do not remain parallel and the phase fronts are able to travel at oblique angles to $\mathbf{B}$. Taken from *Kivelson and Russell* (1995)

2.3.2 Warm Plasma Waves

Waves that exist in warm plasmas must take into account the pressure of the plasma as it cannot be considered negligible as with cold plasmas. The dispersion relation can be derived in a similar way to that found for the cold plasma but provides a different result (*Kivelson and Russell*, 1995):

$$(\omega^2 - \cos^2\theta k^2 v_A^2)[\omega^4 - \omega^2 k^2 (c_s^2 + v_A^2) + \cos^4\theta k^4 v_A^2 c_s^2] = 0, \tag{2.55}$$

where c_s is the sound speed within the plasma. This equation has three solutions,

$$(\frac{\omega}{k})^2 = v_a^2 \cos^2\theta, \tag{2.56}$$

$$(\frac{\omega}{k})^2 = \frac{1}{2}(c_s^2 + v_A^2 \pm [(c_s^2 + v_A^2)^2 - 4c_s^2 v_A^2 \cos^2\theta]^{\frac{1}{2}}), \tag{2.57}$$

where Equation 2.56 is the same solution used for the shear Alfvén waves in a cold plasma, and Equation 2.57 is the pair of compressional solutions. The quantity in the square brackets of Equation 2.57 is positive for the fast mode and negative for the slow mode.

The fast and slow mode waves in the warm plasma are both compressional waves, or magnetoacoustic waves. They vary the magnetic and thermal pressures as they travel through a plasma. The difference between the fast mode and the slow mode is that the total pressure (magnetic and thermal) varies locally to the wave as the perturbations to the magnetic and thermal pressures are in phase (see Figure 2.6) whereas, in the slow mode, the perturbations of the two pressures are out of phase.

Figure 2.7 shows the phase velocities and group velocities for fast, slow and intermediate mode waves where the magnetic field direction is upwards in each panel, the angle with the marked magnetic field direction is the angle that $\mathbf{k}$ makes with $\mathbf{B}$ and the distance of the line from the origin represents the magnitude of the velocity. The left panels are the phase velocities and the right panels are the group velocities while the top panels represent when $v_A = 2c_s$ and the bottom panels represent the velocities when $v_A = \frac{5}{6}c_s$. The phase velocity of the fast mode wave in both top and bottom panels is largest when the direction of propagation is perpendicular to the magnetic field. The phase velocity of the slow mode is highest when the propagation direction

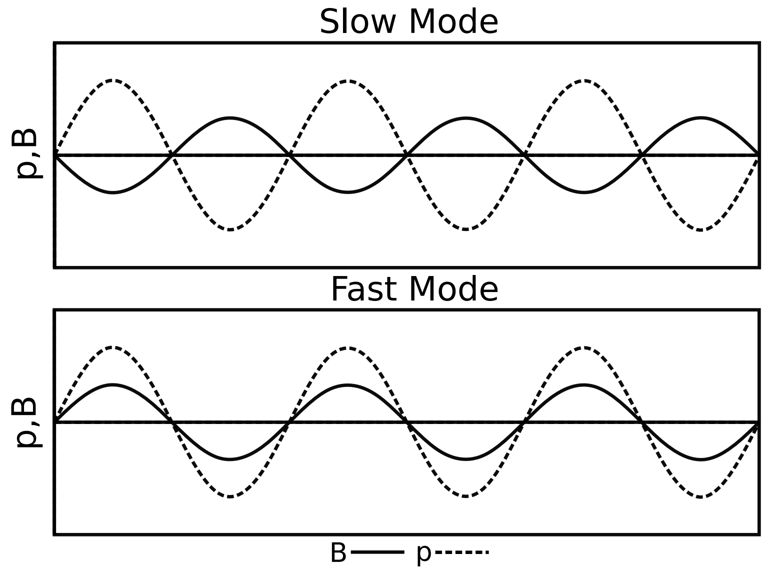

Figure 2.6: Comparison of thermal and magnetic pressures in compressional waves - A comparison of the thermal pressure, p, and the magnetic field, B, in fast and slow mode waves. In a slow mode wave, the magnetic and thermal pressure vary out of phase in order to keep the total pressure constant while the pressures vary in phase for the fast mode.

is parallel to the field and disappears when it is perpendicular to the field. In the case of both the group and phase velocities, the fast mode is the most isotropic, whereas the slow mode wave is only able to carry energy over a small range of angles to $\mathbf{B}$.

Compressional waves can be driven by changes in the total pressure of a system, or a local pressure perturbation such as that caused on the magnetosphere by the increase of solar wind pressure. The isotropic nature of fast mode waves allows them to propagate in all directions away from their source, enabling them to carry away excess pressure. The slow mode is very much field guided and travels along $\mathbf{B}$ keeping the total pressure at a constant by varying magnetic and thermal pressures out of phase. The slow mode is able to reduce pressure gradient along the magnetic field lines.

Figure 2.5a shows that there is a component of the induced current perturbation, $\mathbf{j}$ parallel to the magnetic field. Field aligned currents (FACs) created by the Alfvén wave act to reduce the bending of the magnetic field.

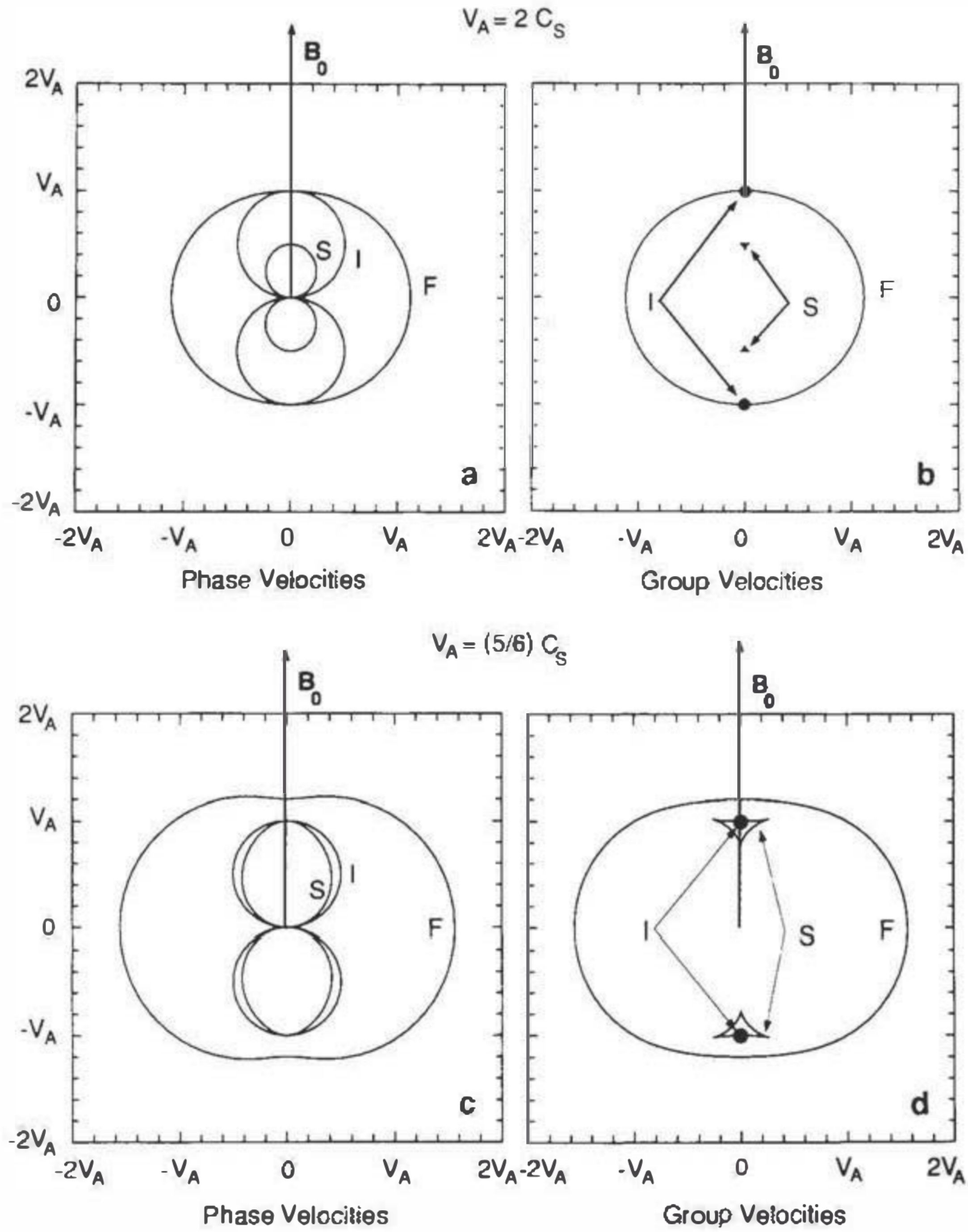

Figure 2.7: Freidrich's diagrams - Freidrich's diagrams for the phase (left panels) and group (right panels) velocities of a fast (F), intermediate (I) and slow (S) mode wave for $v_a = 2c_s$ in the top panels and $v_a = \frac{5}{6}c_s$ in the bottom panels. The diagrams are such that the direction of the background magnetic field is upwards, while the angle made with the background field is the angle which $\mathbf{k}$ makes with $\mathbf{B}$ and the distance from the origin is the phase/group velocity. Taken from *Kivelson and Russell* (1995)

2.3.3 Field Line Resonance

Southwood (1974) described the excitation of field line resonances (FLRs) using a box model magnetosphere similar to that used by *Radoski* (1971). This simplified model of the magnetosphere is presented in Figure 2.8 where the ambient magnetic field, $\mathbf{B} = B\hat{\mathbf{z}}$, points along the z axis. The magnetic field lines are straight and of a finite length as they are bound by two ionospheres. The plasma density, $\rho(x)$, and magnetic field strength, $|\mathbf{B}|$, both vary as a function of x so the Alfvén speed also varies in x.

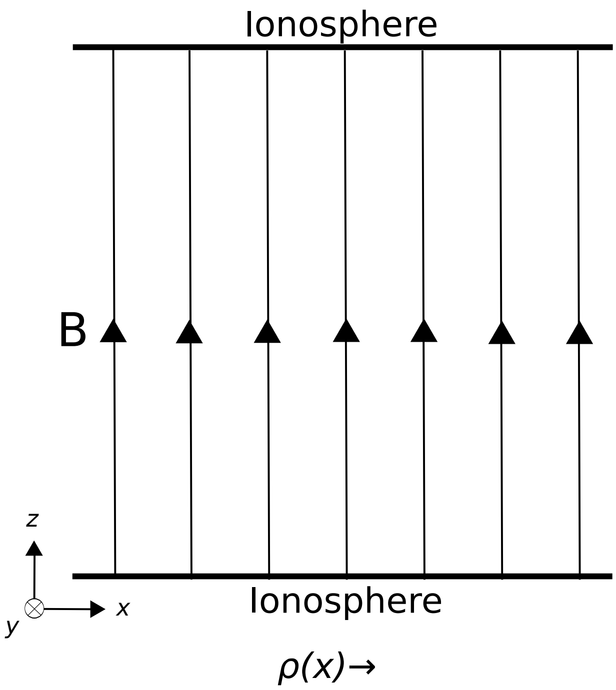

Figure 2.8: Box model magnetosphere - Box model of the magnetosphere where $\mathbf{B}$ is oriented in the z direction. The field lines are straight and bound by two ionospheres. The plasma inside the box is considered to be cold and may only support Alfvén and Fast mode waves. The plasma density, ρ, varies with x meaning that $v_A = v_A(x)$.

Equation 2.41 can be split into its two transverse components:

$$\frac{1}{v_A^2}\frac{d^2E_x}{dt^2} - \frac{d^2E_x}{dy^2} - \frac{d^2E_x}{dz^2} = -\frac{d^2E_y}{dxdy} \tag{2.58}$$

and

$$\frac{1}{v_A^2}\frac{d^2E_y}{dt^2} - \frac{d^2E_y}{dx^2} - \frac{d^2E_y}{dz^2} = -\frac{d^2E_x}{dxdy}. \tag{2.59}$$

The perturbation electric field for a transverse wave can be described by

$$\mathbf{E} = (E_x(x), E_y(x), 0)\exp\left(i[k_y y + k_z z - \omega t]\right) \tag{2.60}$$

which can be substituted into Equations 2.58 and 2.59 to give

$$(\frac{\omega^2}{v_A^2(x)} - k_y^2 - k_z^2)E_x = ik_y(\frac{dE_y}{dx}) \tag{2.61}$$

and

$$(\frac{\omega^2}{v_A^2(x)} - k_z^2)E_y = ik_y(\frac{dE_x}{dx}) - \frac{d^2E_y}{dx^2} \tag{2.62}$$

which remain coupled as long as $k_y \neq 0, \infty$. When $k_y = 0$ the equations decouple and the two modes propagate separately. Both of these equations can then be combined to become

$$\frac{d^2E_y}{dx^2} - \frac{k_y^2\frac{dK^2(x)}{dx}}{(K^2(x) - k_y^2 - k_z^2)(K^2(x) - k_z^2)}\frac{dE_y}{dx} + [K^2(x) - k_y^2 - k_z^2]Ey = 0 \tag{2.63}$$

where $K^2(x) = w^2/v_A^2(x)$.

Equation 2.63 has solutions at two locations, x_0 and x_1, where the second term on the left hand side becomes infinite:

$$K^2(x) - k_z^2 = 0 \text{ at } x = x_0 \tag{2.64}$$

$$K^2(x) - k_y^2 - k_z^2 = 0 \text{ at } x = x_1 \tag{2.65}$$

At x_0 when $k_y = 0$, the fast mode is reflected because $\frac{d^2E_y}{dx^2} = 0$. As the fast mode wave propagates away from this location, the sign of the E_y component depends on the direction which the wave is propagating along x due to K being a function of x, resulting in a phase change of π across x_0. The location at x_1 represents the reflection point for a compressional wave where it is partially reflected and partially transmitted.

After the fast mode wave crosses x_1, it decreases in amplitude until it reaches x_0. At x_0, the partially transmitted fast mode wave matches the local Alfvén mode and energy can be transferred from the fast mode allowing the field lines to resonate. Due to this local resonance, the amplitude of this wave peaks at x_0.

2.3.4 Waves in a Dipolar Field

In the Earth's magnetosphere, ULF waves stand on quasi-dipolar field lines like those in Figure 2.9a. They are bound at either end of the field line by the highly conducting ionosphere. Due to the high conductivity of the ionosphere, the electric field associated with the wave perturbation and the wave displacement itself must vanish and the ULF pulsation can be reflected to the other ionosphere.

Figure 2.9b shows the box model of the magnetosphere where the field lines are bound together between the northern and southern ionospheres. Figure 2.9c shows what a shear Alfvén wave would look like when projected from the dipolar field onto the box model, where all of the field lines remain equally spaced from each other, introducing no compressional components. Figure 2.9d shows what a compressional wave would look like in the box model, demonstrating where there are increases and decreases in plasma density.

Due to the boundary condition that the wave must vanish in the ionosphere, the waves that stand on these field lines must be quantised. The only wavelengths that can stand on a field line of length l are $\lambda_{\|} = 2l/n$, where n is an integer meaning that only discrete wavelengths and frequencies may exist. The propagation vector along the field line for an Alfvén wave is $k_{\|} = k\cos\theta = 2\pi/\lambda_{\|}$ and the angular frequency of the wave is $\omega = v_A k_{\|}$. Using this information with Equation 2.42 , the eigenfrequencies allowed to stand on a field line can be expressed by

$$f = \frac{nv_A}{2l} = \frac{nB}{2l\sqrt{\mu_0\rho}}, \tag{2.66}$$

meaning that the frequency is controlled by the length of the field line. This equation also allows the estimation of ρ using observed wave frequencies.

Figure 2.10 shows the displacement of a field line connected at either end to the Earth's ionosphere due to an odd mode/fundamental (a) and an even mode/second harmonic (b) wave. In the odd mode, the electric field created by the wave is smallest near

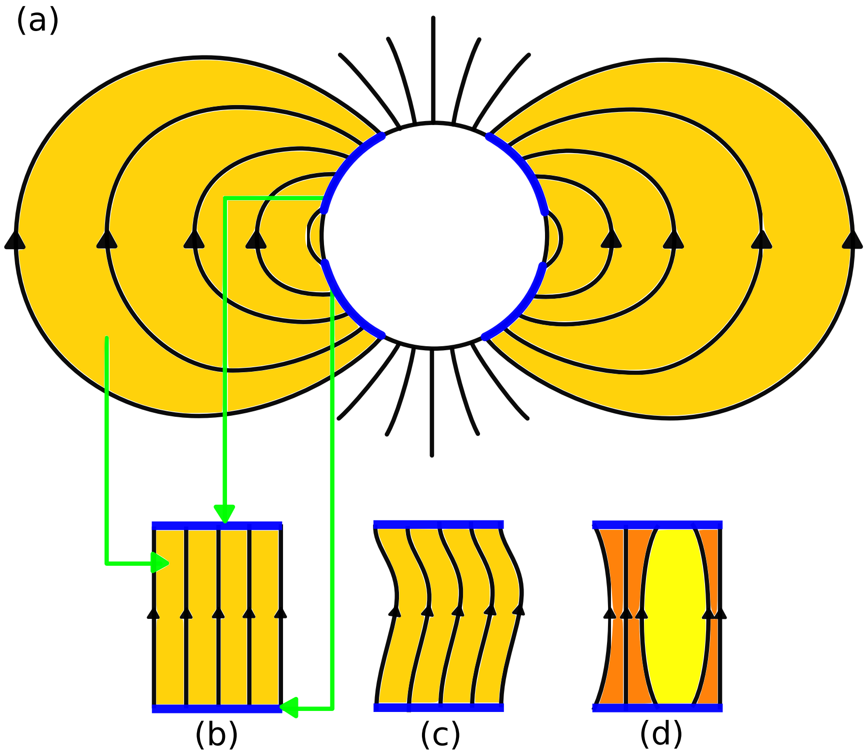

Figure 2.9: Dipolar magnetosphere - An illustration of how the box model magnetosphere (b) relates to the dipolar magnetic field (a) where the field lines are bound by the northern and southern ionospheres. Panel (c) shows the magnetic perturbations that would be present in a shear Alfvén wave where there the field lines remain a constant distance from each other, causing no compression of the plasma. Panel (d) shows the fast mode wave where the field lines become more compressed in the same regions that the plasma density increases (dark shading) and the field lines move apart where the plasma becomes more sparse (light regions). Based on Figure 11.4 of *Kivelson and Russell* (1995)

the ionosphere and largest near the equator. The opposite is true of the displacement magnetic field, $\mathbf{b}$, where it is smallest at the equator where the field line is pointing in the same direction, but largest near the ionosphere due to the tilt in the field line. In the even mode, there is a full wavelength along the field line, the electric field has opposite polarity in each hemisphere and the maxima in $\mathbf{b}$ are both in the ionosphere and at the equator.

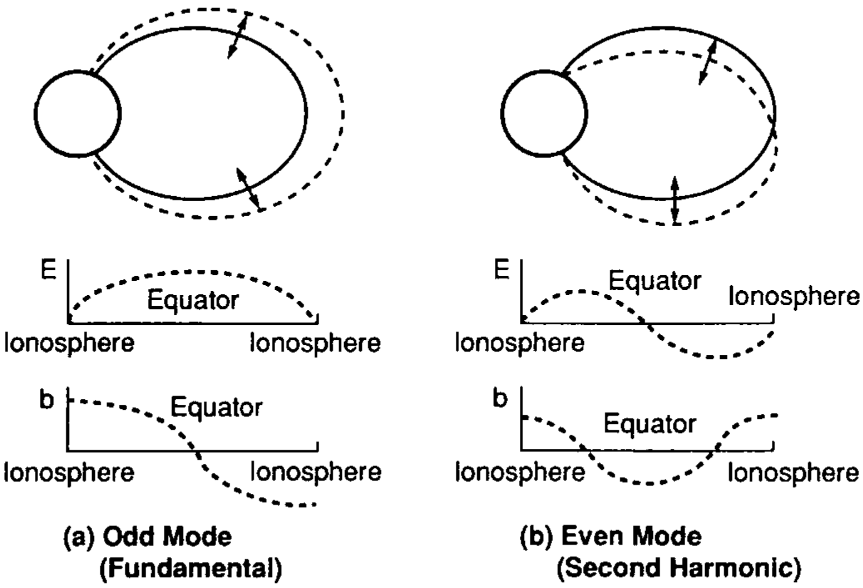

Figure 2.10: Electric and magnetic perturbations in magnetospheric waves - The perturbations of the magnetic field and the wave electric field for both fundamental (a) and second harmonic (b) ULF waves. The top diagram shows the displacement of the magnetic field lines due to these waves and the lower part shows the magnitudes of the electric field, $\mathbf{E}$, and the perturbation magnetic field, $\mathbf{b}$, along the field line between the northern and southern ionospheres. From *Hughes* (1983)

In a dipolar field, a wave variation takes the form $e^{i(m\phi-\omega t)}$ where m, an integer, is the azimuthal wave number. The azimuthal wave number of an event is an indicator of the azimuthal scale size of the wave, where $m \propto \frac{1}{\lambda_\theta}$ where λ_θ is the azimuthal wavelength. *Dungey* (1963) used three equations,

$$(\omega^2\mu_0\rho - \frac{1}{r}(\mathbf{B}\cdot\nabla)r^2(\mathbf{B}\cdot\nabla))(\frac{u_\phi}{r}) = \omega m(\frac{\mathbf{B}\cdot\mathbf{b}}{r}), \tag{2.67}$$

$$(\omega^2\mu_0\rho - rB^2(\mathbf{B}\cdot\nabla)\frac{1}{r^2B^2}(\mathbf{B}\cdot\nabla))(rE_\phi) = i\omega B^2(\mathbf{B}\times\nabla)_\phi(\frac{\mathbf{B}\cdot\mathbf{b}}{B^2}), \tag{2.68}$$

$$i\omega\mathbf{B}\cdot\mathbf{b} = \frac{1}{r}(\mathbf{B}\times\nabla)_\phi(rE_\phi) - imB^2\frac{u_\phi}{r}, \tag{2.69}$$

to describe a wave in a dipolar field using a cylindrical polar co-ordinate system (r, ϕ, z) assuming that $\mathbf{B}_\phi = 0$. In equations 2.67 and 2.68, the left hand side represents a one-dimensional wave equation with the derivative along the directions of the ambient magnetic field, $\mathbf{B}\cdot\nabla$, as the only spatial operator. These equations are coupled by the right-hand side of the equations which depend on the compressional term, $\mathbf{B}\cdot\mathbf{b}$. Equation 2.69 completes the set of equations by relating $\mathbf{B}\cdot\mathbf{b}$, E_ϕ and u_ϕ.

It was shown by Dungey that the right hand side of Equation 2.67 disappears when $m = 0$. The left hand side then describes the mode in which the electric field variation is purely radial and the magnetic and velocity perturbations are in the azimuthal direction. This mode is the toroidal mode, the magnetic perturbations are contained within an L-shell which becomes decoupled and oscillates independently of any other L-shell. This type of wave exists without any compressional component so it must be an Alfvén wave.

Another solution is found when $m \to \infty$. In this case $\mathbf{B}\cdot\mathbf{b} \to 0$ in order for the right hand side of Equation 2.67 to remain finite so the right hand side of Equation 2.68 becomes 0. Now Equation 2.68 describes a wave in which the electric field oscillates purely in the azimuthal direction and the magnetic perturbation and velocity lie within a meridional plane. This mode is the poloidal mode and due to the radial perturbation of the magnetic field, this type of wave is capable of altering both magnetic and plasma pressures implying that it is a compressional wave.

Usually ULF waves in the magnetosphere are observed to have $m \neq 0, \infty$ and do not satisfy either of the solutions mentioned above and must have a combination of both toroidal and poloidal components. For a monochromatic wave, the coupling of the Alfvén and compressional modes is strongest where the compressional mode matches the local Alfvén mode. The scale size of the observed wave can be related to the source of the waves energy. Events with $m \to 0$ are large scale events and can be either poloidal or toroidal events often driven by sources external to the magnetosphere. Events with large azimuthal wave numbers are smaller scale size events and can often be associated with the wave-particle interactions of recently injected plasma populations injected into the magnetosphere by substorms.

2.3.5 Instabilities

ULF waves can be driven by any process that alters the equilibrium of the plasmas where plasma conditions which lead to non-linear growth of waves are known as instabilities. One such method of inducing waves to the Earth's magnetosphere is from the shear flow across the magnetopause boundary by the solar wind creating a Kelvin-Helmholtz instability causing surface waves (e.g. *Agapitov et al.* (2009)) as described above. These perturbations send compressional waves into the magnetosphere and couple with the shear Alfvén waves through field line resonance. Another external source is a displacement of the magnetopause from a solar wind shock can also send fast mode compressional waves into the magnetosphere.

Waves also have the ability to grow when the velocity space distribution of plasma departs from an equilibrium state. Unstable velocity distributions can develop in the ring current from the injection of energetic particles during storms and substorms. These instabilities are usually unable to transfer their free energy to the surrounding plasma directly due to the infrequency of collisions and require other means to return to equilibrium (*Hughes*, 1983). One such way of spreading the free energy around is through wave-particle interactions. The particle distribution functions responsible for driving ULF waves will be discussed in Section 2.3.6.

In order for there to be transfer of energy between waves and particles, they must be resonant with each other. For a particle to be in resonance with a ULF wave, it should have a velocity that matches the phase velocity of the wave. When this is the case, the particle doesn't sense any variations due to the wave as the wave would have been Doppler shifted to zero frequency. Any energy transfer to or from the particle will be matched exactly by energy loss or gain from the wave.

Resonance can occur when the drift bounce resonance condition (*Southwood et al.*, 1969)

$$\omega - m\omega_d = N\omega_b \tag{2.70}$$

is satisfied, where ω is the wave angular frequency, m is the azimuthal wave number, ω_d is the angular drift frequency of the particles, ω_b is the bounce frequency of the particles and N is an integer, usually equal to 0 or ± 1. When $N = \pm 1$, the particles are in drift-bounce resonance with a second harmonic (even mode) ULF wave as they bounce between the hemispheres. If $N = 0$, the particles are in drift resonance with the fundamental (odd mode) ULF wave where Equation 2.70 becomes

$$\omega - m\omega_d = 0 \tag{2.71}$$

so the angular drift frequency of the particles must be able to match the azimuthal propagation of the wave:

$$\omega_d = \frac{2\pi f}{m}. \tag{2.72}$$

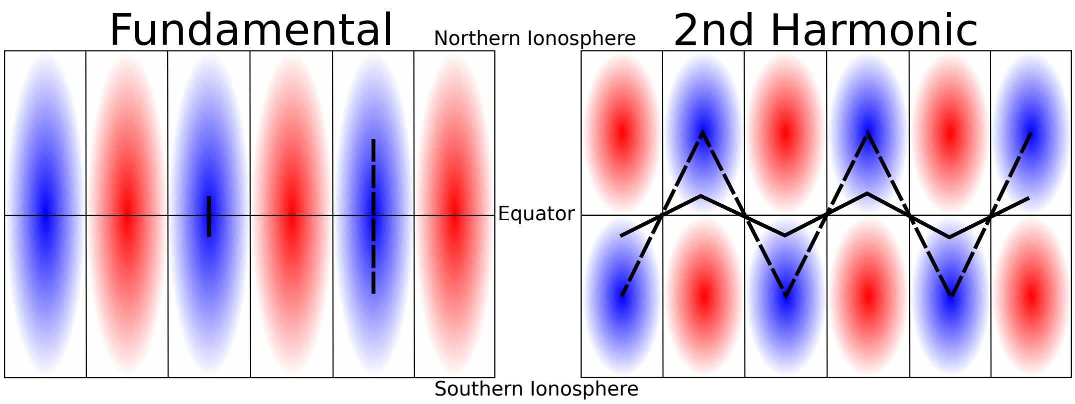

Figure 2.11: Drift and drift-bounce resonance - An illustration of the resonant particle drift and bounce paths in the frame of reference of a fundamental wave (left) and a second harmonic wave (right). The wave electric field is represented by red and blue shading where the magnitude of this field is represented by the intensity of the colour. The particle drift paths are shown for a large equatorial pitch angle particle (solid line) and a small equatorial pitch angle (dashed line) where the particle with the smaller pitch angle is able to bounce further along the field line. The particle drift paths for the fundamental wave are such that the particle remains still in the frame of reference of the wave and senses a constant electric field. In the case of the 2nd harmonic, the particles must undergo a full bounce motion in the time it takes to drift one wavelength with respect to the wave in order to remain in the same sense of the electric field. Diagram adapted from similar diagrams by *Southwood and Kivelson* (1982); *Hughes* (1983).

Figure 2.11 is a graphical representation of both drift-resonance (left) and drift-bounce resonance (right) based upon various other representations (e.g., *Southwood and Kivelson*, 1982; *Hughes*, 1983). Both panels are in the frame of reference of the ULF wave phase velocity so the wave is stationary, where west is to the left and east is to the right. The wave is bound by the northern and southern ionospheres at the top and bottom of each panel. The colours represent the opposing directions of the wave electric field, where the intensity of the colour represents the magnitude of $\mathbf{E}$.

In the left panel of Figure 2.11, the electric field perturbations are representative of the fundamental mode wave as shown in Figure 2.10a where $\mathbf{E}$ is strongest near the equator and weakest in the ionosphere. For particles to be resonant with this wave, Equation 2.71 must be true ($N = 0$). The two vertical lines represent the bounce motion of two resonant particles in the frame of the wave, where the solid line represents a particle with a large equatorial pitch angle and the dashed line represents a particle with a smaller equatorial pitch angle. In this case the particles remain in the same location relative to the wave and therefore remain within the same local electric field depression.

In the right panel of Figure 2.11, the electric field perturbations are in opposite directions in each hemisphere for the second harmonic like that in Figure 2.10b where there is a minimum at the equator as well as at the ionospheres. Equation 2.70 must be satisfied for particles to be in resonance with this wave. A solid and a dashed line represent the paths of two resonant particles where the solid line represents a particle with a large equatorial pitch angle and the dashed line represents that of a particle with a small pitch angle. In both cases, for the particles to remain in an electric field pointing in the same direction as the bounce between hemispheres, they must drift one full wavelength azimuthally in each full bounce.

Previous work by *Chisham* (1996) was able to quantify the angular drift frequency of these resonant particles using parameters based on the location of the particle within the magnetosphere and geomagnetic activity,

$$\omega_d = -\frac{6WL(0.35 + 0.15\sin\alpha)}{B_s R_E^2} + \frac{90(1 - 0.159K_p + 0.0093K_p^2)^{-3}L^3\sin\phi}{B_s R_E^2}. \quad (2.73)$$

In this equation, W is the energy of the particle, L is the L-shell, α is the equatorial pitch angle, K_p is the geomagnetic activity index, B_s is the surface magnetic field strength, R_E is the radius of the Earth and ϕ is the magnetic local time of the particle. The first term on the right hand side of this equation represents the gradient-curvature drift that is exhibited by a particle of energy W in the magnetosphere. The second term on the right hand side is the term that quantifies the approximate $\mathbf{E} \times \mathbf{B}$ drift of the particle based upon the strength of the geomagnetic activity.

In the case of the drift-resonant particle ($N = 0$) it is trivial to calculate the particle energy expected to drive a wave with known parameters m and f at a known location. The energy of the particle is obtained by equating Equation 2.73 to Equation 2.72 and rearranging for W. The solution for a drift bounce particle is not as trivial because the angular bounce frequency must also be considered,

$$\omega_b = \frac{\pi\sqrt{W}}{\sqrt{2m_p} L R_E (1.3 - 0.56 \sin\alpha)}, \tag{2.74}$$

where m_p is the mass of the particle and α is the equatorial pitch angle. When $N = 1$ this equation can be substituted into Equation 2.70 alongside Equation 2.73 to form a quadratic equation of the form

$$0 = aW + b\sqrt{W} + c, \tag{2.75}$$

$$\text{where } a = -\frac{6L(0.35 + 0.15\sin\alpha)m}{B_s R_E^2}, \tag{2.76}$$

$$b = \frac{-\pi}{\sqrt{2m_p} L R_E (1.3 - 0.56 \sin\alpha)}, \tag{2.77}$$

$$c = \frac{90(1 - 0.159K_p + 0.0093K_p^2)^{-3} l^3 \sin\phi m}{B_s R_E^2} - 2\pi f, \tag{2.78}$$

and the solutions to this are given by:

$$\sqrt{W} = \frac{-b \pm \sqrt{b^2 - 4ac}}{2a}. \tag{2.79}$$

2.3.6 Particle Distribution Functions

A wave driven by a velocity space instability can be explained further by studying the particle distribution function. Such a wave could be described using a modified angular frequency such that $\omega = \omega_r + i\gamma$. This would alter Equation 2.44 such that

$e^{i\omega t} = e^{i\omega_r t} e^{-\gamma t}$ where γ greater than 0 would indicate damping of the wave and γ less than zero would indicate wave growth. This section will provide a derivation of growth and damping of ULF waves due to the shape of the particle distribution function using a method described in a personal communication with S.W.H. Cowley.

The particle distribution function (PDF) of an unperturbed system is $f_0(\mathbf{r}', \mathbf{v}', t)$ where $\mathbf{r}'$ and $\mathbf{v}'$ are the three dimensional position and velocity vectors respectively. In the presence of the wave fields $\mathbf{E}(\mathbf{r}, t)$ and $\mathbf{B}(\mathbf{r}, t)$, a particle would be displaced from $(\mathbf{r}', \mathbf{v}', t)$ to $(\mathbf{r}, \mathbf{v}, t)$ where $\delta\mathbf{r} = \mathbf{r} - \mathbf{r}'$ and $\delta\mathbf{v} = \mathbf{v} - \mathbf{v}'$.

As the forces that are exerted upon the particles are differentiable conservative forces, Liouville's theorem states that f is conserved so

$$f(\mathbf{r}, \mathbf{v}, t) = f_0(\mathbf{r}', \mathbf{v}', t) = f_0(\mathbf{r} - \delta\mathbf{r}, \mathbf{v} - \delta\mathbf{v}, t), \tag{2.80}$$

which, using the linear approximation of Taylor's theorem, becomes

$$f(\mathbf{r}, \mathbf{v}, t) = f_0(\mathbf{r}, \mathbf{v}, t) - \delta\mathbf{r} \cdot \nabla f_0 - \delta\mathbf{v} \cdot \nabla_v f_0, \tag{2.81}$$

$$f_1(\mathbf{r}, \mathbf{v}, t) = -\delta\mathbf{r} \cdot \nabla f_0 - \delta\mathbf{v} \cdot \nabla_v f_0, \tag{2.82}$$

where $\nabla_v = (\frac{\partial}{\partial v_x}, \frac{\partial}{\partial v_y}, \frac{\partial}{\partial v_z})$ and f_1 is the perturbation to the PDF. The equation can be simplified further if the unperturbed system is considered to be spatially uniform and steady to become

$$f_1(\mathbf{r}, \mathbf{v}, t) = -\delta\mathbf{v} \cdot \nabla_v f_0. \tag{2.83}$$

If $\mathbf{r}'(t)$ is the trajectory arriving at $\mathbf{r}, \mathbf{v}$ at time t then $\mathbf{v}'(t') = \frac{d\mathbf{r}'}{dt}$. $\delta\mathbf{v}$ is calculated by integrating the effect of the wave force, $q(\mathbf{E} + \mathbf{v} \times \mathbf{B})$ along the unperturbed trajectory:

$$m\frac{d}{dt}(\delta\mathbf{v}) = F_1 = q(\mathbf{E} + \mathbf{v} \times \mathbf{B}) \tag{2.84}$$

$$\Rightarrow \delta\mathbf{v}(\mathbf{r}, \mathbf{v}, t) = \frac{q}{m}\int_{-\infty}^{t} (\mathbf{E}(\mathbf{r}'(t'), t') + \mathbf{v}'(t') \times \mathbf{B}(\mathbf{r}'(t'), t'))dt', \tag{2.85}$$

where m is the particle mass.

This can be simplified by considering the linear kinetic theory of plasma oscillations, in this case the above equation becomes

$$\delta \mathbf{v}(z, v_z, t) = \frac{-q_e}{m_e} \int_{-\infty}^{t} E_z(z', t')\hat{\mathbf{z}} dt'. \tag{2.86}$$

Since the trajectory that arrives at $\mathbf{z}$ at time t with velocity v_z can be expressed by $z'(t') = z + v_z(t' - t)$, the wave electric field can be expressed as

$$E_z(z', t') = E_0 e^{i(\omega t' - kz')} = E_0 e^{ik(v_z - z)} e^{i(\omega - kv_z)t'}, \tag{2.87}$$

so

$$\delta \mathbf{v}(z, v_z, t) = \frac{iq_e E_z z, t}{m_e(\omega - kv_z)}, \tag{2.88}$$

which can be substituted into Equation 2.83 to show that the perturbation to the PDF becomes

$$f_1(z, v_z, t) = -\delta v_z \frac{\partial f_0}{\partial v_z} = -\frac{iq_e}{m_e} \frac{\frac{\partial f_0}{\partial v_z}}{(\omega - kv_z)} E_z(z, t). \tag{2.89}$$

Using the fact that the perturbed number density is $n_1(z, t) = \int f_1 d^3 v$ and using Gauss' law (Equation 2.22), the dispersion equation can be found,

$$1 + \frac{\omega_e^2}{kn_0} \int \frac{\partial f_0/\partial v_z}{(\omega - kv_z)} d^3\mathbf{v} = 0 \tag{2.90}$$

$$\text{where } \omega_e^2 = \frac{n_o q_e^2}{\epsilon_0 m_e} \tag{2.91}$$

where the integrals over velocity space can be analysed for v_x and v_y to provide us with the Landau dispersion relation simply by defining a 1-D 'longitudinal PDF':

$$g_0(v_z) = \int_{-\infty}^{\infty} dv_x \int_{-\infty}^{\infty} dv_y f_0(v_x, v_y, v_z), \tag{2.92}$$

$$\Rightarrow 1 + \frac{w_e^2}{kn_0} \int_{-\infty}^{\infty} \frac{\partial g_0/\partial v_z}{(\omega - kv_z)} dv_z = 0 \tag{2.93}$$

By substituting $\omega = \omega_r + i\gamma$ into Equation 2.93 and analysing the real and imaginary parts of the integral, it is possible to find an equation for γ at the point where $v_z = \omega_r/k$,

$$\gamma \simeq -\frac{\pi \omega_r^3}{2k_2 n_o} \left.\frac{\partial v_z}{\partial g_0}\right|_{\frac{\omega_r}{k}} . \tag{2.94}$$

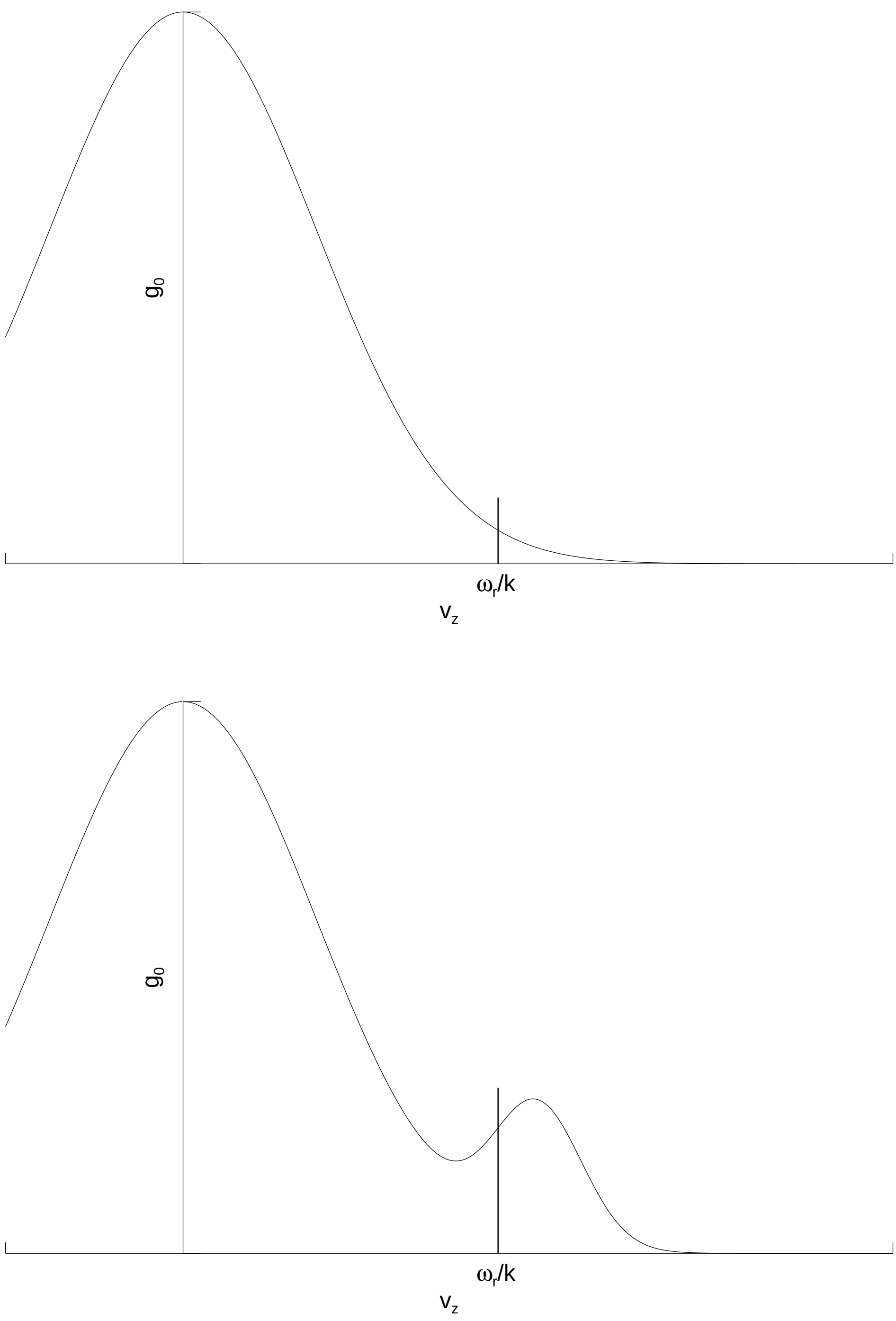

Figure 2.12: Bump-on-tail distribution - Two particle distribution functions are presented where the top panel shows a PDF with no free energy at the velocity equal to the phase velocity of the wave (ω_r/k) and the bottom panel shows a bump-on-tail distribution with free energy at ω_r/k to allow for wave growth.

This is represented graphically in Figure 2.12 where two particle distribution functions are plotted against the particle velocity, v_z. In both panels, the phase speed of the wave (ω_r/k) is marked along the x-axis. In panel (a) the gradient of the PDF analysed at the phase speed, $\frac{\partial v_z}{\partial g_0}\Big|_{\omega_r/k}$, is negative meaning that γ is positive and that there can only be wave damping at this speed. Panel (b) shows the PDF for a 'bump-on-tail' distribution, where $\frac{\partial v_z}{\partial g_0}\Big|_{\omega_r/k}$ is positive, so γ must be negative. A negative γ, as discussed above, indicates that there is free energy in the distribution at this phase velocity and wave growth can occur.

The energy exchange from the particle distribution to the wave is most significant when there is a significant number of particles in the population with nearly the correct energy to be in phase with the wave. The slope of the particle distribution function controls whether there can be wave damping or growth, where a negative gradient will cause 'Landau damping' and a positive gradient allows for wave growth. The positive gradient around the phase speed of the wave indicates that there are more particles with a velocity slightly higher than the wave phase speed itself, so some of that energy can be taken from the particles and added to the wave to put them in phase. The particle energy and velocity are directly related to each other by $W = \frac{1}{2}mv^2$, so a positive gradient in PDF in velocity space is equivalent to a positive gradient in energy space.

In order for there to be wave growth within a plasma due to an energy contribution from the plasma particles themselves, then the particle distribution function, f, must increase with particle energy, W (*Mann and Chisham*, 2000):

$$\frac{\mathrm{d}f}{\mathrm{d}W} = \frac{\partial f}{\partial W} + \frac{\mathrm{d}L}{\mathrm{d}W}\frac{\partial f}{\partial L} > 0 \tag{2.95}$$

where W is a measurable quantity. The term $\frac{\partial f}{\partial W}$ becomes positive when there is a bump-on-tail distribution as discussed above. The term $\frac{\mathrm{d}L}{\mathrm{d}W}\frac{\partial f}{\partial L}$ relates to the spatial variations in the particle distribution function which are also able to supply energy for wave growth. The direction of the spatial gradient required for there to be energy available depends upon the charge of the particles, q, as *Southwood and Hughes* (1983):

$$\frac{\mathrm{d}W}{\mathrm{d}L} = \frac{q\omega}{m} B_{eq} L R_E^2. \tag{2.96}$$

This implies that wave growth can occur when there is an inward density gradient ($\frac{\partial f}{\partial L} < 0$) of positive ions drifting westwards - driving westward propagating waves.

When the ions closer to the Earth move outwards, they lose energy, which gets transferred to the wave (*McPherron*, 2005). Wave growth is also able to occur in the situation where there is an inward density gradient ($\frac{\partial f}{\partial L} < 0$) of electrons drifting eastwards - driving eastward propagating waves.

2.3.7 Energy Dissipation

Energy dissipation from the waves can occur through Landau damping as discussed above, where there is a particle distribution function with a negative gradient at the energy which particles are in phase with the wave, the wave energy is transferred to the particles.

Another possibility is the damping from the ionosphere. Figure 2.5a shows that there is a component of the perturbation current, $\mathbf{j}$, existent within a shear Alfvén wave driving field aligned currents. These field aligned currents close in the ionosphere as Pedersen currents. As there are currents flowing in the ionosphere due to the wave fields, there must be joule dissipation providing the main sink of energy for ULF waves (*Hughes*, 1983; *Allan and Poulter*, 1992).

2.4 Summary

This chapter has introduced some of the basic principles of space plasma physics and some theory behind MHD waves. The mechanisms by which ULF waves are formed within the Earth's magnetosphere have been mentioned where small-scale pulsations driven by the bump-on-tail instability was the primary focus. This mechanism of wave-particle interactions driving ULF waves will remain as the primary focus as the source of energy for the wave events that will be discussed in the following chapters. The next chapter will outline some of the previous publications of observations and results obtained on ULF waves.

Chapter 3

Review of Previous Studies of ULF Waves

3.1 Introduction

The previous chapters of this thesis have described some of the background theory relevant to the study of ULF waves. Chapter 1 introduced the solar-terrestrial system and some of the interactions that occur within that system focusing on the substorm cycle. Chapter 2 introduced a general background to space plasmas and proceeded to describe the physics behind ULF waves and their generation mechanisms. The generation mechanism that is the primary focus of this thesis involves wave particle interactions. This chapter aims to discuss some of the literature relevant to waves driven by particle instabilities such as studies based on storm-time, quiet-time or substorm related ULF waves.

Magnetospheric Ultra Low Frequency (ULF) waves can be classified into two types depending on whether their polarization is predominantly toroidal or poloidal (e.g., *Klimushkin et al.*, 2012). Toroidal waves are those in which the magnetic field oscillates azimuthally and are characterized by low azimuthal wave numbers (m), or equivalently a large azimuthal scale size. Poloidal waves oscillate in the meridional/radial direction with high m numbers (a smaller azimuthal scale size). In either case these waves represent standing Alfvén waves between two conjugate points in the Earth's ionosphere.

Low-m (toroidal) waves are thought to have their energy source external to the magnetosphere. An example is *Agapitov et al.* (2009) where a ULF pulsation coincided with a compressional wave on the magnetopause. The compressional wave appeared to be generated by the Kelvin-Helmholtz instability (e.g., *Mazur and Chuiko*, 2011) or to have penetrated into the magnetosphere from the solar wind (e.g., *Nedie et al.*, 2012), and in-turn generated the ULF wave observed inside the magnetosphere through field line resonance.

High-m (poloidal) events are believed to have a different generation mechanism to the low-m events, where the energy source is thought to be from energetic particle populations within the magnetosphere. The energetic particle populations responsible for high-m waves enter the inner magnetosphere from the magnetotail, subsequently gradient-curvature drifting around the planet as part of the global ring current.

3.1.1 Field Line Resonance

Section 2.3.3 describes some of the theory behind the driving of field line resonances using a simple box model magnetosphere. Figure 3.1 taken from *Allan and Poulter* (1992) shows how field line resonances are driven in the Earth's magnetosphere. As a Kelvin-Helmholtz instability on the magnetopause drives fast-mode compressional waves, such as those observed by *Agapitov et al.* (2009), evanescent waves are transmitted into the magnetosphere with decreasing amplitude towards the Earth. Eventually the compressional wave encounters an L-shell which can resonate with the fast-mode wave, driving a toroidal Alfvén wave.

At the location of the field line resonance, the amplitude of the wave should peak. Also across the resonant region, the wave should undergo a phase change of π as the sign of the wave electric field should be opposite on either side of the resonance region.

Such characteristics expected of field line resonances (FLRs) have been observed by *Walker et al.* (1979). Figure 3.2 shows an example taken from *Walker et al.* (1979), where several field line resonances were observed using the STARE (Scandinavian Twin Auroral Radar Experiment, (*Greenwald et al.*, 1978)) auroral radar. The top panel shows the observed amplitude of a wave as a function of latitude and the bottom panel shows the corresponding phase of the wave against latitude. As was predicted by theory, there was an amplitude peak at the resonant latitude, where the half power

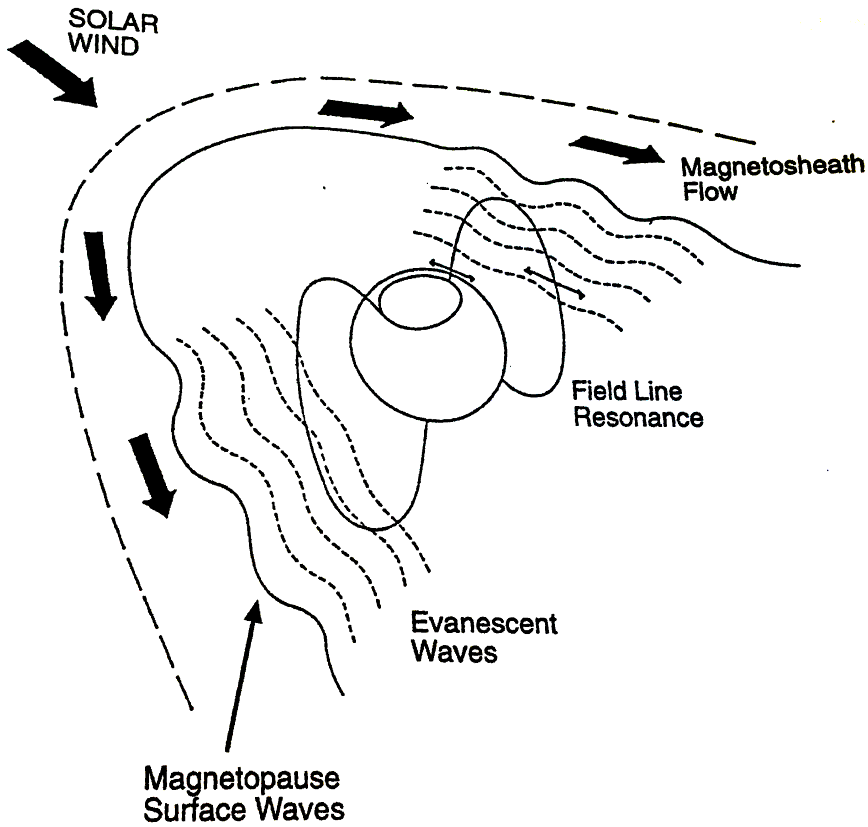

Figure 3.1: Magnetopause surface waves - This figure, taken from *Allan and Poulter* (1992) demonstrated the excitation of field line resonances by compressional waves driven by Kelvin-Helmholtz waves on the magnetopause.

width of the wave is approximately 1° in latitude. Also predicted by the FLR theory is the observed phase change of π which occurs over the same region of latitudes as the amplitude peak.

3.1.2 Observed Wave Polarisation

Agapitov and Cheremnykh (2011) suggested that the polarisation of a ULF wave was related to the direction which the wave-driving disturbing force acts upon the magnetic surface. It was suggested that a disturbing force acting along the magnetic surface would excite toroidal Alfvén waves such as those thought to be driven by the Kelvin-Helmholtz instability on the dawn and dusk flanks of the Earth's magnetosphere. It was

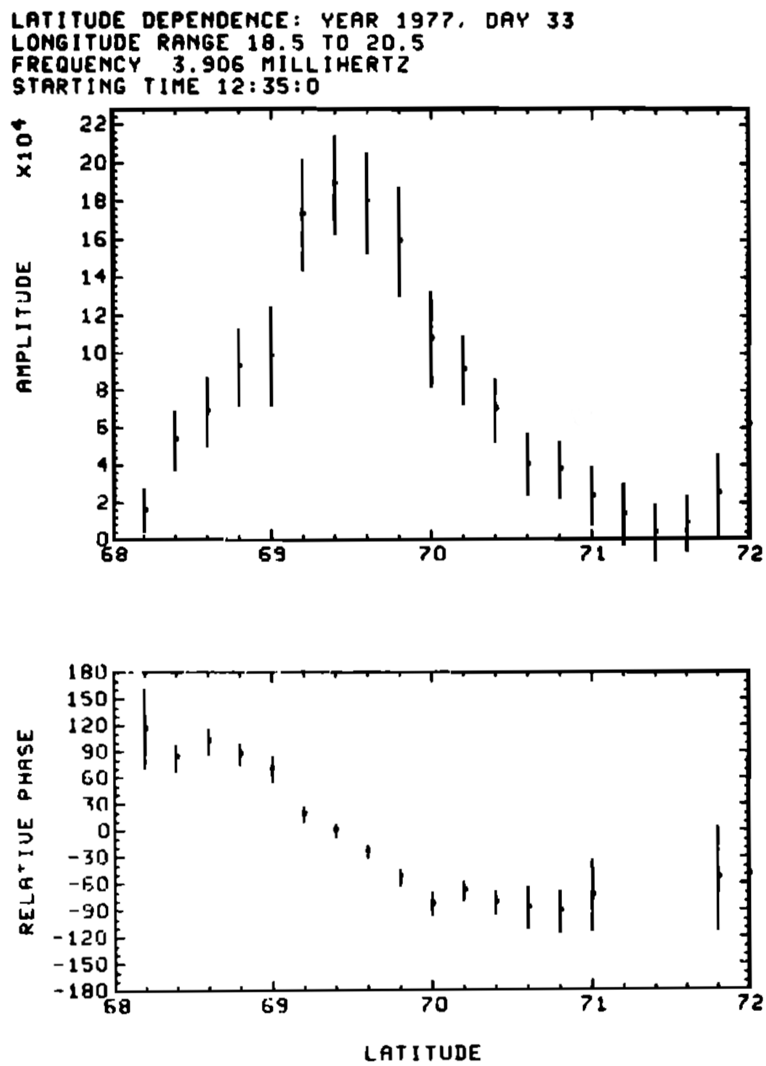

Figure 3.2: Field line resonance amplitude and phase - This figure, taken from *Walker et al.* (1979), shows the amplitude and phase of a field line resonance as a function of latitude. The wave peaks in amplitude over a fairly small range of latitude and there is a phase shift of π as predicted by field line resonance theory over this small latitude range.

also suggested that if the disturbing force were to act in a direction perpendicular to the magnetic field, for example solar wind disturbances on the dayside magnetopause, poloidal Alfvén waves would be excited.

Figure 3.3 shows examples of observations of both toroidal and poloidal ULF waves in space taken from *Agapitov and Cheremnykh* (2011). The panel on the left shows the three components of the magnetic field as measured by the Equator-S spacecraft, where x points to the east, perpendicular the the meridional plane, z is along the field line and y lies within the meridional plane. The strongest pulsations are observed in the z direction and correspond to a poloidally orientated wave. The variations in the magnetic and dynamic pressure of the plasma are included in the bottom panel, where the two pressures vary out of phase from each other as for a slow wave in Figure 2.6. The panel on the right shows the data from the AMPTE/CCE spacecraft given in the same coordinate system as before. In this case, the wave primarily oscillates in the x direction, perpendicular to the magnetic plane, with no periodic variations in the pressure plot below. This wave is an example of a toroidally polarised Alfvén wave.

Figure 3.4 shows the polarisations of a number of ULF waves against their MLT observed during 1986 by the AMPTE/CCE spacecraft. The polarisation parameter is a ratio of the poloidal and toroidal amplitudes measured in the magnetometer data where the size of the circle is a ratio of the longitudinal component of the magnetic disturbance to the transverse component of magnetic disturbance. Toroidal mode waves in the diagram exist mainly along the flanks and the ratio of longitudinal disturbance to transverse disturbance is very low. Waves with a circular polarisation of ~1 have the largest longitudinal components of field disturbance and are likely to be identified as slow-mode waves. Poloidal mode waves are spread over a larger range of MLT to the toroidal and circular modes and are able to propagate with smaller disturbances to the longitudinal magnetic field than circular modes.

As can be seen by Figure 3.4, ULF waves can be categorised by their polarisation but they are always a mixture of toroidal and poloidal polarisations. A purely toroidal wave would have an m number equal to 0 while for a purely poloidal wave $m = \infty$. In reality, waves observed in the Earth's magnetosphere have a finite azimuthal wave number and a finite scale size due to the mixture of polarisations. This also means that all waves have some compressional component present. The fact that no wave is purely

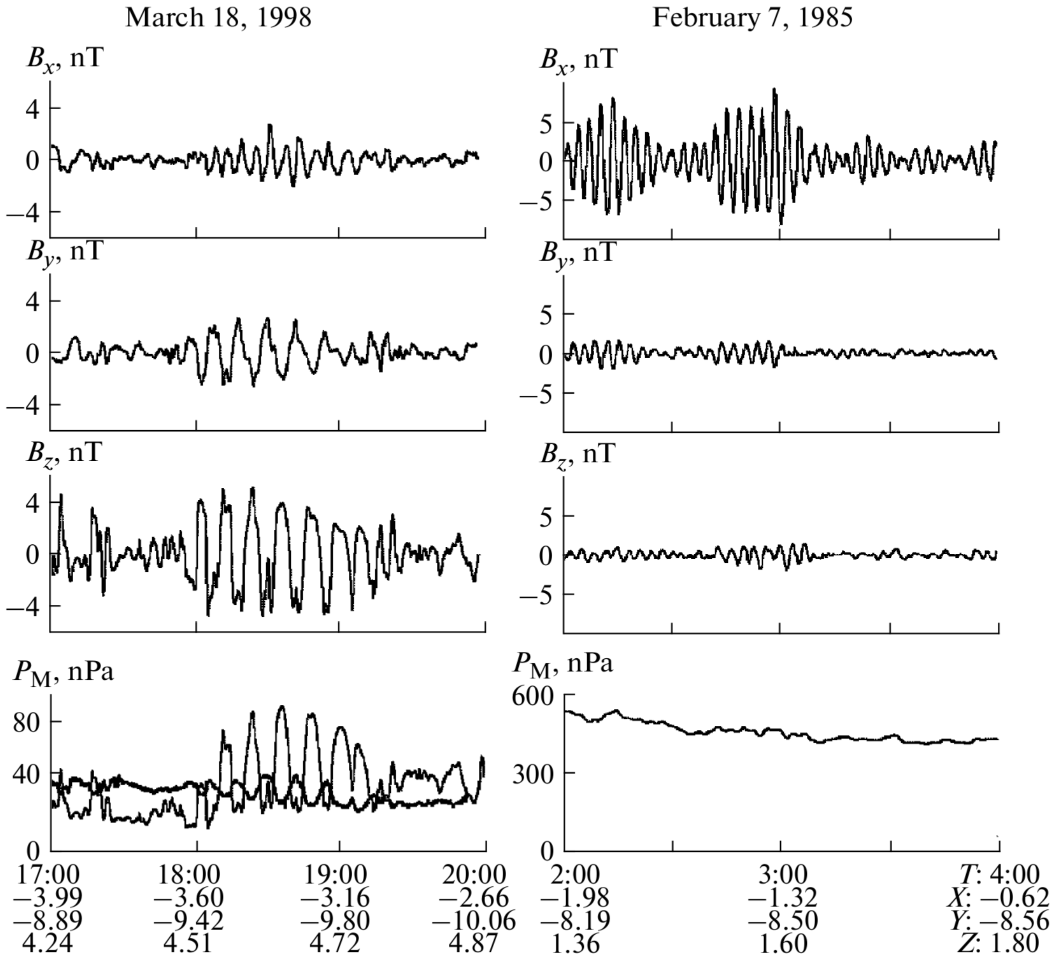

Figure 3.3: Wave polarisations observed in space - Magnetometer data for a poloidally polarised wave observed using the Equator-S spacecraft (left) and a toroidally polarised wave observed by the AMPTE/CCE spacecraft (right) taken from *Agapitov and Cheremnykh* (2011). In both cases the x component is the azimuthal component, y is directed y lies within the meridional plane and z is directed along the field line. The fourth plot shows the magnetic and plasma pressure variation due to the wave.

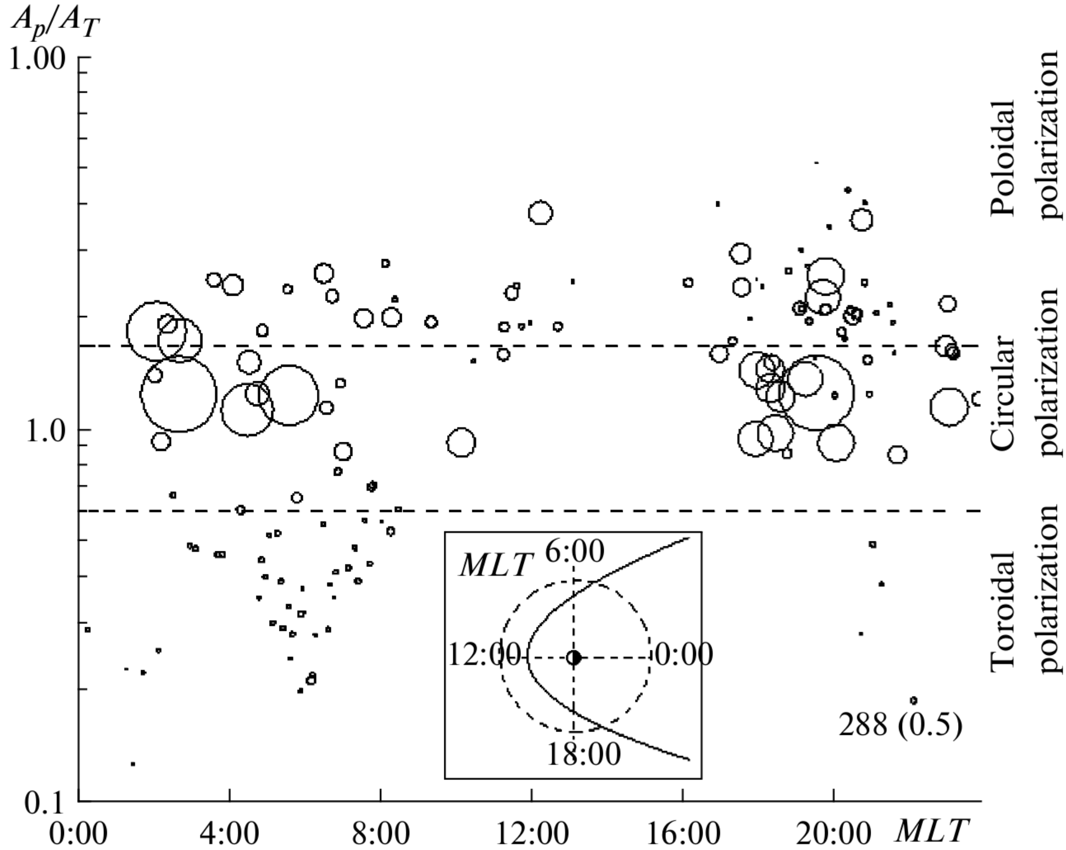

Figure 3.4: Wave polarisations in magnetic local time - The distribution of wave events studied by *Agapitov and Cheremnykh* (2011) where the polarisation of the wave is plotted against the location in MLT. The size of the circle is related to the ratio of the longitudinal and transverse magnetic disturbances.

poloidal or toroidal means that ULF waves have to be classified by their predominant polarisation.

For the remainder of this chapter, the focus will be on studies of high-m ULF waves. High-m ULF waves are observed at various locations in the magnetosphere and have different phase characteristics both depending upon the particle instabilities that drive them. Particle instabilities are often related to storms and substorm injection but also occur during geomagnetically quiet periods.

3.2 Westward Propagating Particle-Driven Waves

Storm-time ULF waves have been observed using ground based instrumentation such as magnetometer networks (e.g., *Allan et al.*, 1983a) and radars like STARE (Scandinavian Twin Auroral Radar Experiment, (*Greenwald et al.*, 1978)) (e.g., *Allan et al.*, 1982) and space based instrumentation such as geostationary satellites used by *Hughes et al.* (1979).

3.2.1 Storm Time Spacecraft Observations

Takahashi et al. (1985) noted the observation of eight compressional ULF waves at geostationary orbit on the dayside of the magnetosphere using magnetometer data from the GOES 2 and 3 satellites and particle data from the LANL 1977-007 and 1979-053 satellites. The waves mostly occurred during the recover phase of a geomagnetic storm and all had westward phase propagation. The azimuthal wave numbers observed in this study were very typical of particle driven waves where $m \approx -40$ to -120 and the associated propagation speeds were of the order of $4 - 14$ km s^{-1}.

Figure 3.5 shows an example of the data obtained during one of these eight waves. The top panel shows the electron count rate, next panel shows the proton count rate for various energy channels, third panel shows the tilt angle and the final three show the radial (B_R), azimuthal (B_A) and parallel (B_P) components of the magnetic field. The tilt angle is the angle by which the local field line is tilted compared to the ambient field. In this diagram, oscillations of ~500 s are clearly present in both radial and parallel components of the magnetic field, as expected for a poloidally polarised wave. Variations in the electron and proton count rates are also present with the same period

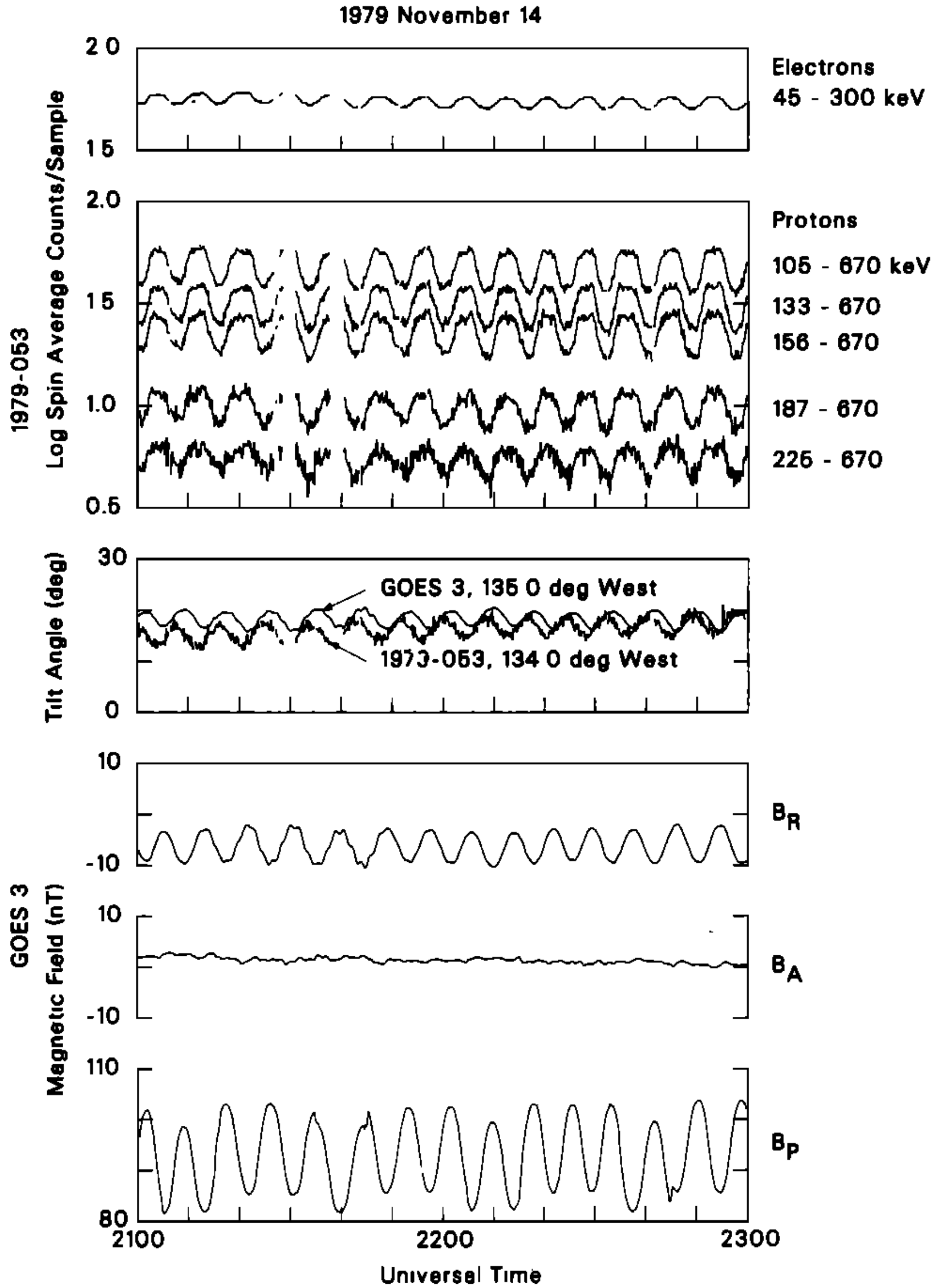

Figure 3.5: Magnetic and plasma variations observed in space - Variations in electron counts (top panel) and proton counts (second panel) observed by the 1979-053 spacecraft, field line tilt angle (third panel) and the radial, azimuthal and parallel (fourth, fifth and sixth panels) components of the magnetic field as measured by GOES 3. This figure was taken from *Takahashi et al.* (1985).

as the magnetic perturbations and are 180° out of phase with the tilt angle of the field. It was suggested this class of waves in the dayside magnetosphere were driven by a drift-mirror instability from the ring current.

Woch et al. (1990) also investigated a number of compressional ULF waves similar to those observed by *Takahashi et al.* (1985). This study focused on locating pulsations in both particle and magnetometer data. The population of waves were split up into two types: 42 diamagnetic waves and 34 non-diamagnetic waves. Diamagnetic waves are those in which the plasma on the field lines acts to reduce the strength of the magnetic field perturbation associated with the wave activity. For the diamagnetic events, modulation onset in the magnetometer data was accompanied by or immediately preceded by an enhancement in ion densities and a decrease in the overall magnetic field strength. Non-diamagnetic events were those in which the onset of the wave was not connected to any enhancement of the ion intensity of any decrease in the strength of the magnetic field.

Figure 3.6, taken from *Woch et al.* (1990), shows the distribution of both diamagnetic and non-diamagnetic events in magnetic local time, where noon is to the left and dawn is to the top. Diamagnetic wave occurrence occurs mainly in post-noon and dusk sectors, peaking a little before dusk. The diamagnetic events were shown to occur during times when the AE index is enhanced and increasing during the onset of the events where 70% of these waves were associated with substorm activity. Unlike the diamagnetic events, non-diamagnetic events occurred during storm recovery phase when AE is low or decreasing and there is still an enhanced ring current. The distribution of these waves shown in Figure 3.6 occur throughout most of the dayside magnetosphere, peaking around noon.

A statistical study of Pc 3-5 pulsations (see Table 2.1) was undertaken using the AMPTE/CCE spacecraft by *Anderson et al.* (1990). This study included the observation of harmonic toroidal resonances, fundamental toroidal resonances, radially polarised waves and storm time Pc 5 waves. Figures 3.7 and 3.8 show the rate of occurrences for the storm time Pc 5 waves and the radially polarised waves as a function of both magnetic local time and L-shells between 5 and 9. The peaks in the storm time distribution at both dawn and dusk suggest that these waves are connected to substorm injections. The radially polarised waves were observed 10% of the time everywhere

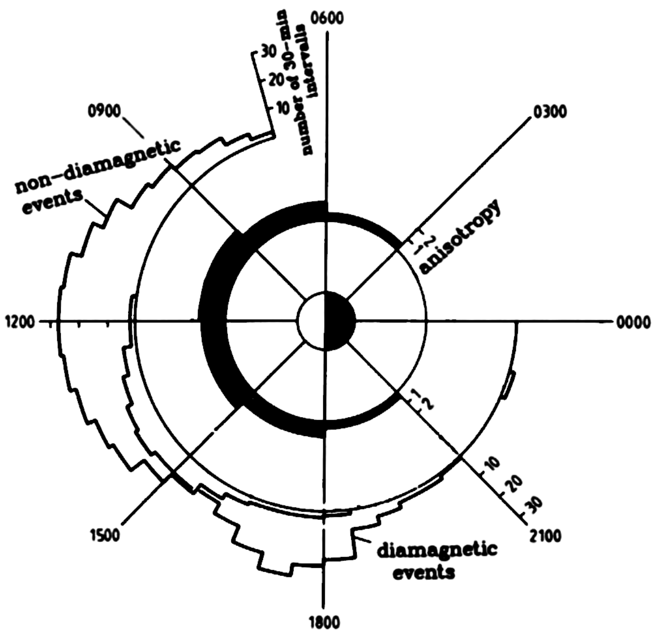

Figure 3.6: Diamagnetic and non-diamagnetic wave events - Distribution of diamagnetic and non-diamagnetic events in magnetic local time where noon is to the left and dawn to the top, from *Woch et al.* (1990).

except within 04:00 MLT and 11:00 MLT and were associated with wave-particle interactions but not with recent injections. These radial waves were postulated to be driven by spatial inhomogeneities related to the evolution of injected particles.

The case study by *Hughes et al.* (1979) observed a poloidal Pc 4 pulsation using three geostationary satellites between 21:00 and 24:00 local time. This pulsation had a large compressional magnetic component which was in anti-phase with pressure fluctuations within the ring current plasma - indicating the presence of a field-guided slow mode wave. This wave was a second harmonic field line resonance with a short azimuthal wavelength, $m \sim 100$. The group velocity of 30 km s^{-1} and phase velocity of 50 km s^{-1} are of a similar order to the speed of ring current protons. The suggested source of energy for this wave was drift-bounce resonance with westward drifting protons.

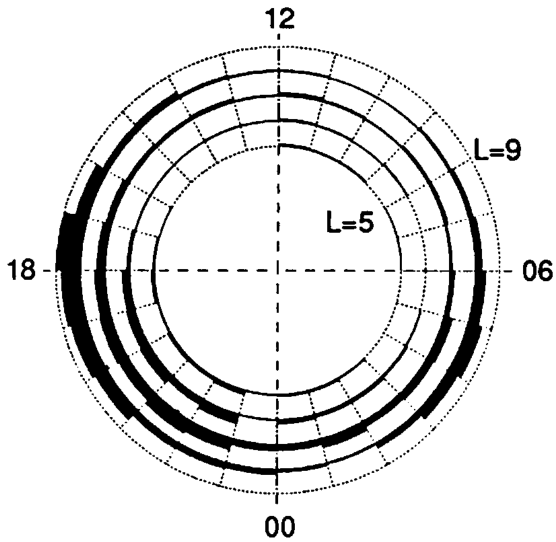

Figure 3.7: Storm-time Pc 5 wave distribution - Distribution of storm time Pc 5 waves studied by *Anderson et al.* (1990) in both magnetic local time and L-shells from 5 to 9.

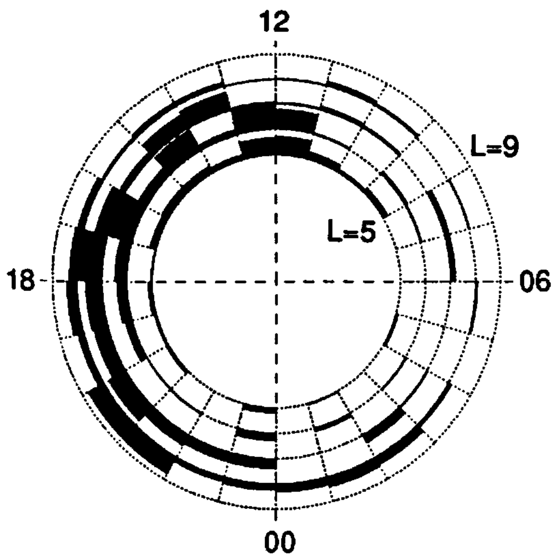

Figure 3.8: Radially polarised wave distribution - Distribution of radially polarised waves studied by *Anderson et al.* (1990) in both magnetic local time and L-shells from 5 to 9.

A recent study by *Claudepierre et al.* (2013) made use of Van Allen Probe data in order to study the electron flux modulations that occurred shortly after the arrival of an interplanetary shock at the Earth's magnetosphere. Just prior to the onset of the shock, substorm activity had been detected in the AE indices. Magnetic field variations occurred simultaneously with the modulation of electron fluxes in the 50 - 100 keV range with periods of ~3 min. The amplitudes of the electron flux oscillations peaked at around ~57 - 80 keV and were in phase over all pitch angles. The particle flux modulations combined with the magnetic field measurements were consistent with a fundamental drift resonance interaction with resonant electrons with energies close to 60 keV. The estimated energy and wave periods were used to estimate the azimuthal wave number of ~44.

3.2.2 Storm Time Ground-Based Observations

Allan et al. (1983a) used STARE (Scandinavian Twin Auroral Radar Experiment, (*Greenwald et al.*, 1978)) alongside ground magnetometers to study high-m Pc 5 waves. The azimuthal wave numbers observed in this study ranged from 32 to 48, typical of particle driven waves. *Allan et al.* (1983b) also made use of STARE to observe a number of high-m ULF waves. When mapped to the equatorial plane, the azimuthal phase velocity resembled that of gradient-curvature drifting protons. Figure 3.9 shows the phase velocity for four different waves with m ranging from 18 to 80 as a function of L-shell, compared to the velocity of 22 and 38 keV protons.

A more recent study by *Yeoman et al.* (2000) used the DOPE (DOppler Pulsation Experiment, (*Wright et al.*, 1997)) HF sounder for the study of ULF waves with high azimuthal wave numbers. *Yeoman et al.* (2000) found a number of ULF waves which correlated with ground magnetometer data and some which could not be correlated with magnetometer data. Figure 3.10a shows the occurrence of the correlated waves as a function of both UT and MLT. This distribution is spread over a large range of magnetic local times and is centred upon noon. Figure 3.10b shows the distribution of uncorrelated waves in the same format as that used in panel (a). This distribution shows a large peak in the wave occurrence around 10:00 MLT and a smaller peak around 18:00 MLT. The afternoon waves in this case were associated with storm time Pc 5 pulsations.

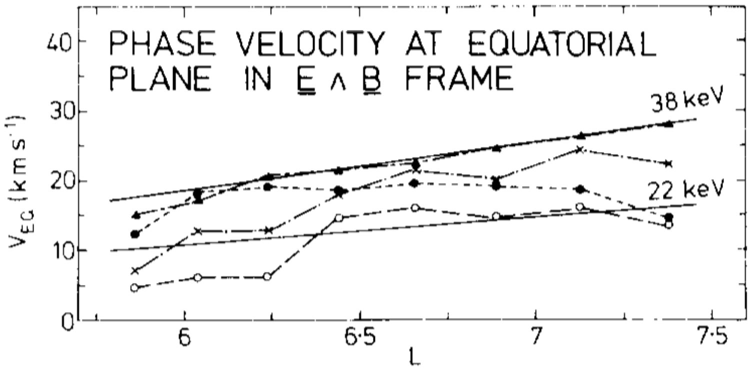

Figure 3.9: STARE phase velocities - This figure, taken from *Allan et al.* (1983b) compares the azimuthal phase velocities of four ULF waves observed using STARE as a function of L-shell with that of drifting protons with energies of 22 to 38 keV.

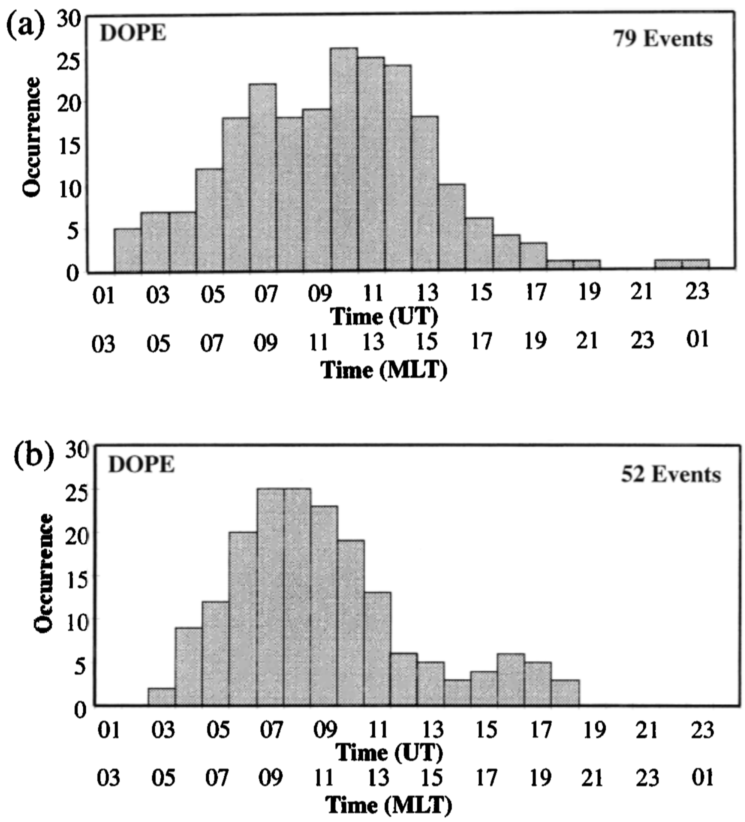

Figure 3.10: DOPE wave occurrences in local time - Occurrences of waves observed by *Yeoman et al.* (2000) which are correlated with magnetometer data (a) and uncorrelated with magnetometer data (b) as a function of magnetic local time.

Long period, irregular pulsations (Pi 3) were observed by *Pilipenko et al.* (2001a) during a storm on 15^{th} May 1997. The intensifications in the magnetic activity were accompanied by intense ULF pulsations in the 0.5 - 6.0 mHz range. The broadband ULF waves occurred primarily in two locations, one in the morning sector, one near dusk. The waves observed near morning were likely to be due to injected electrons and intensifications in the nearby westward electrojet and those observed near dusk were driven by injected protons and were related to the partial ring current.

Pilipenko et al. (2001b) observed variations in Pc 5 wave power in the morning sector was likely to be related to the location and intensity of the auroral electrojet. ULF waves can be related to energetic electron injection, where precipitation of electrons can increase the ionospheric conductivity and therefore increase enhance the auroral electrojet intensity. This effect was shown to be strongest for the westward electrojet but is also present for the eastward electrojet.

A case study by *Zolotukhina et al.* (2008) studied the waves observed by two satellites, one either side of the onset of a substorm. A schematic of this is shown in Figure 3.11 where GOES 10 detected a westward propagating wave to the west of the onset and GOES 8 detected a wave propagating eastwards to the east of the substorm onset. The westward propagating waves were driven by westward propagating ions with an estimated energy of 60 keV and the eastward drifting wave was driven by eastward drifting electrons, where the presence of particle clouds were confirmed by the LANL satellites. The wave activity during the event was shown to transform from mixed to poloidal and back to mixed polarisation as suggested by *Mager and Klimushkin* (2008); *Mager et al.* (2009).

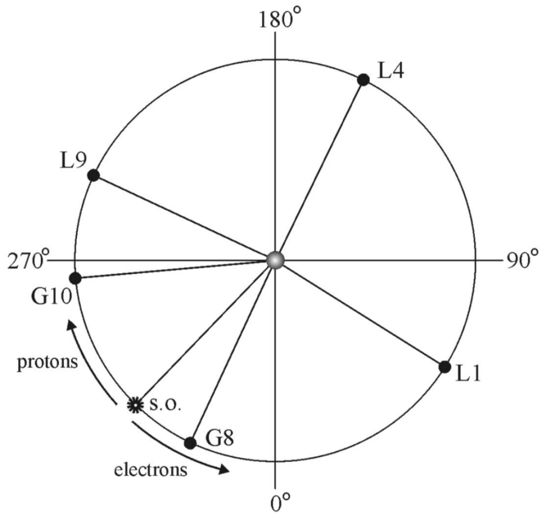

Figure 3.11: Particle drift paths in MLT following substorm onset - Positions of the GOES 8 (G8) and GOES 10 (G10) in magnetic local time, where the location of the substorm onset is marked in between the two spacecraft. From *Zolotukhina et al.* (2008).

3.2.3 Quiet Time Spacecraft Observations

Takahashi et al. (1990) observed a transverse Pc 5 wave event during a quiet period following a few days of geomagnetic disturbance. The wave was observed using AMPTE/CCE at 13:00 MLT with an azimuthal wave number of ~-110. This wave was poloidally polarised with a peak to peak amplitude of ~15 nT. Oscillations in the particle fluxes were maximised in the field aligned direction and approached 0 at 90° pitch-angle. The wave was determined to be an antisymmetric, 2nd harmonic standing wave thought to be associated with drift-bounce resonant particles which may have been related to substorm injected particles, but not recently injected particles.

Dayside observations of quite time ULF waves were studied further by *Engebretson et al.* (1992) using AMPTE/CCE, GOES 5 and GOES 6. The 21 waves in this study had predominantly radial polarisations and occurred between 9:00 and 19:00 MLT. The wave activity often started approximately 1 hour following a sharp drop in the AE index. Wave activity onsets occurred simultaneously over a large longitudinal extent with various frequencies present suggesting that the instability responsible also spanned a large longitudinal extent but the frequencies driven were determined by local Alfvén resonances and local variations in plasma density. The particle responsible for driving the waves were thought to be of the order 100 keV in energy, where the instability itself may be caused by the refilling of the plasmasphere.

A case study by *Dai et al.* (2013) used Van Allen Probe data to identify wave activity in the dawn-noon sector at $L \approx 5$. Particle flux data was used alongside magnetic and electric field data in a similar manner to *Claudepierre et al.* (2013). Figure 3.12 shows the radial and azimuthal components of the electric field (top panel), radial, azimuthal and parallel magnetic field components (middle panel) and the differential proton flux over a range of energy channels (bottom panel) during this event. The electric and magnetic field data show a mostly poloidally polarised wave. Particle fluxes vary with the same period as the fluctuations in the field data, though phase and amplitude varies with the energy channels. *Dai et al.* (2013) concluded that the particles most responsible for the driving of this wave were in the 88 keV band as they were most in phase with the azimuthal field oscillations. The wave energy was determined to originate from an instability caused by an inward gradient of energetic ions within the ring current driving the drift-resonance interaction.

3.2.4 Quiet Time Ground-based Observations

The peak in uncorrelated waves observed by *Yeoman et al.* (2000) around dusk often occurred in conditions that were slightly quieter than average. These waves were expected to have compressional, radially polarised signatures and were thought to have a source in gradient-drifting protons. It was determined that the energy of the source particles was likely to be in the range of 10 - 40 keV and were likely to be bounce-resonant.

During geomagnetically quiet periods giant pulsations (Pg) may occur. Giant pulsations are a special class of Pc 4 wave with long wave packet durations which are highly sinusoidal in nature. One such example of a giant pulsation is that observed by *Chisham et al.* (1992) using SABRE (Sweden And Britain auroral Radar Experiment, (*Nielson et al.*, 1983)) and various ground magnetometers in Scandinavia, Iceland and the Faroe Islands. The wave had an azimuthal wave number, $m \sim -20$ and it was concluded that the wave was most likely to be a 2nd harmonic wave. This event occurred following a day of very little activity and was associated with drift-bounce resonant

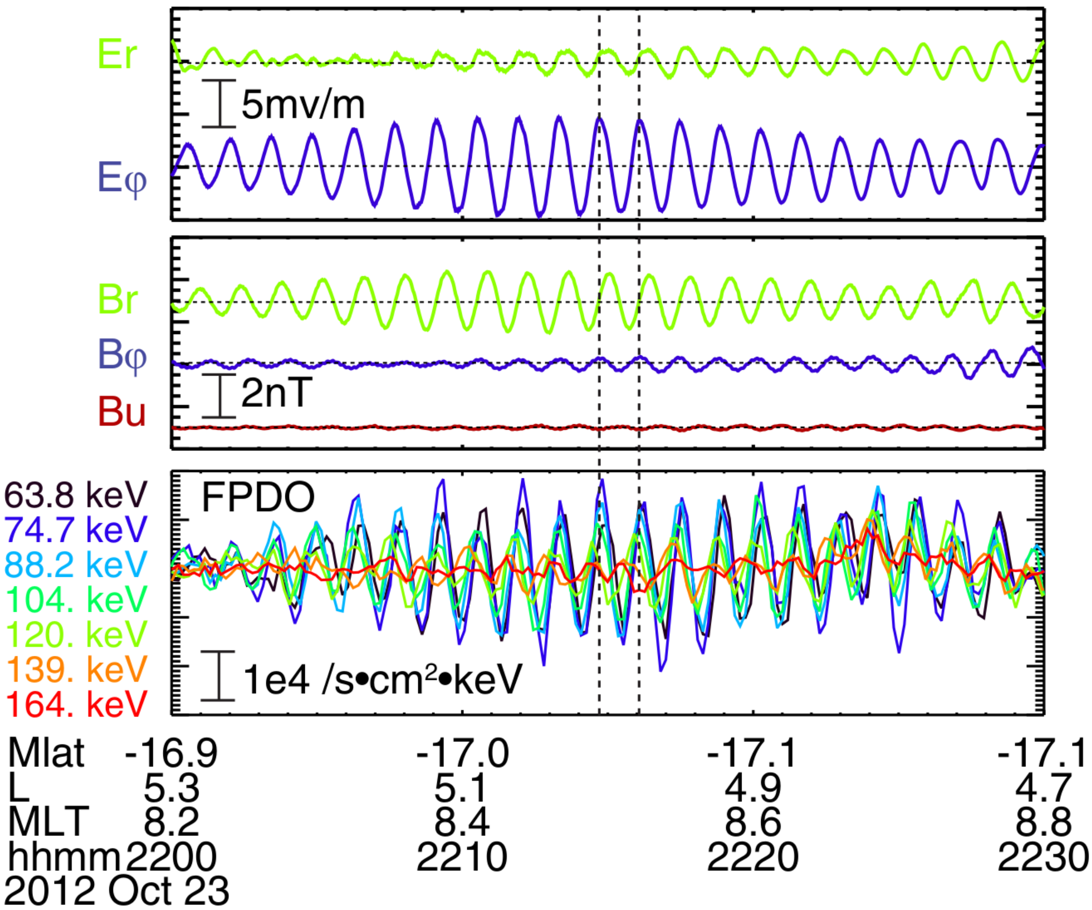

Figure 3.12: Electric field, magnetic field and proton flux variations - Van Allen Probe measurements of the electric and magnetic field variations (top and middle panels) alongside the proton flux variations (bottom panel). The radial, azimuthal and parallel components of the fields are in green, purple and red respectively. Differential proton fluxes are presented from 63.8 to 164 keV, where the 88.2 keV channel is in phase with the azimuthal wave components. From *Dai et al.* (2013).

protons with an energy of 10-20 keV, likely to be associated with previous substorm activity.

Another example similar to *Chisham et al.* (1992) is *Wright et al.* (2001) where a giant pulsation with an azimuthal wave number of -30 was observed in the morning sector using the IMAGE magnetometer network and DOPE HF sounder. A 'bump-on-tail distribution' (like that shown in Figure 2.12) was observed by the POLAR spacecraft prior to wave generation where the positive gradient indicative of free energy existed between $\sim 6 - 24$ keV. For an even mode wave, particle energies of ~7 keV satisfy the drift-bounce resonance condition and agree with the POLAR data. The source of the instability that drove this wave was suggested to be substorm injection, where a subsequent lack of geomagnetic activity allowed the injected protons to drift to the morning sector to drive the wave.

Giant pulsations are rare and only occur during geomagnetically quiet conditions. *Chisham* (1996) provided an explanation as to why this is the case. Giant pulsations are often driven by westward drifting protons in the energy range of $\sim 5 - 30$ keV. Particles with energies as low as this will experience small gradient-curvature drifts which may be overcome by the $\mathbf{E} \times \mathbf{B}$ drift due to the magnetospheric convection electric field. When the $\mathbf{E} \times \mathbf{B}$ drift is significant it can cause particles to depart from closed drift paths, allowing them to drift outwards towards the magnetopause.

Figure 3.13, from *Chisham* (1996), shows the paths of particles of four different energies (10 keV, 20 keV, 30 keV and 50 keV) around the magnetosphere injected between 5 and 10 R_E when $K_P = 2$. In this case, most of the 50 keV particles and a few 30 keV particles on low L-shells make the journey around the Earth without drifting into the magnetopause but all of the 10 keV and 20 keV protons are lost. Figure 3.14, also from *Chisham* (1996), shows the drift paths of the particles when $K_P = 0$. In this case the majority of the particles with an energy greater than 20 keV drift to the morning sector without being lost to the magnetopause where they are able to drive a giant pulsation. *Chisham* (1996) showed that the particle populations responsible for driving giant pulsations were only able to do so during very low magnetic activity.

A statistical examination of 27 high-m waves by *Baddeley et al.* (2005a) determined that most of the free energy carried by the ion distribution functions (IDFs) was within the range of 5 - 40 keV. The large azimuthal wave numbers observed in this study (20 - 287) implied that these waves were all radially polarised. It was suggested

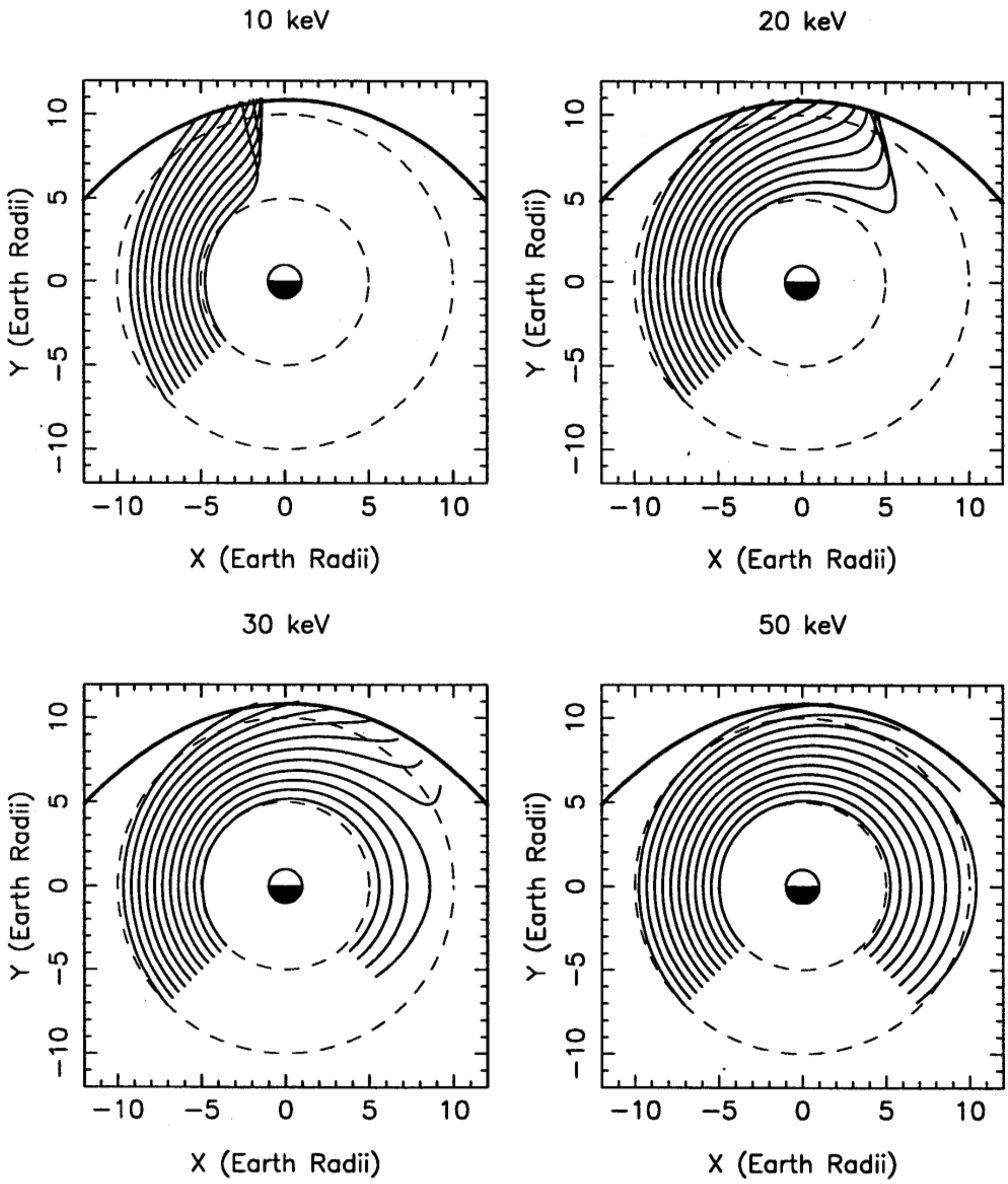

Figure 3.13: Proton drift paths ($K_p = 2$) - Simulated paths of 10 keV (top left), 20 keV (top right), 30 keV (bottom left) and 50 keV (bottom right) starting in the premidnight sector and drifting west when $K_P = 2$. Particles with lower energies and on higher L-shells are more susceptible to drifting into the magnetopause. From *Chisham* (1996).

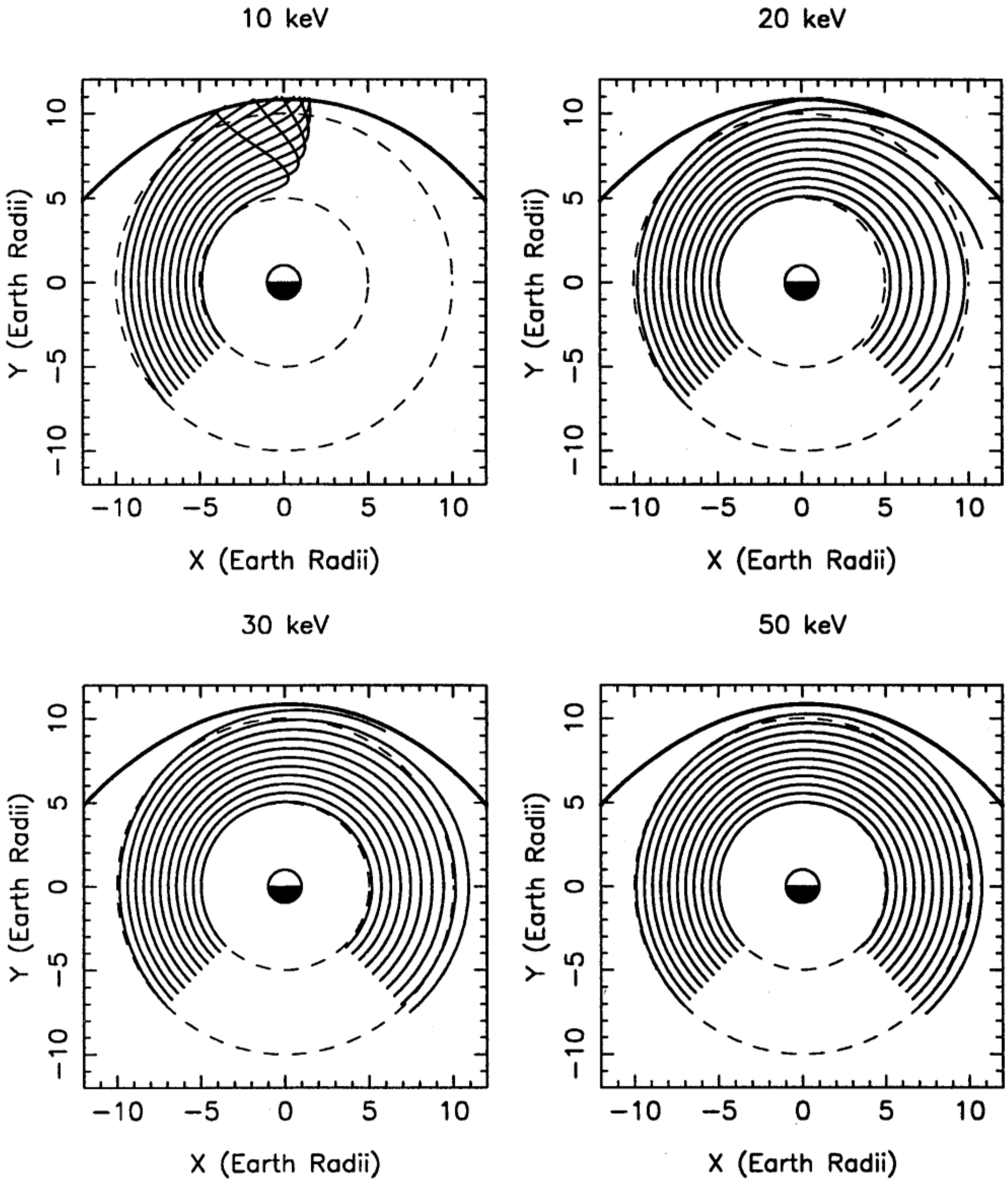

Figure 3.14: Proton drift paths ($K_p = 0$) - Simulated paths of 10 keV (top left), 20 keV (top right), 30 keV (bottom left) and 50 keV (bottom right) starting in the premidnight sector and drifting west when $K_P = 0$. Particles with lower energies are less susceptible to drifting into the magnetopause then when $K_P = 2$ as in Figure 3.13. From *Chisham* (1996).

that waves with moderately large wave numbers ($|m| < 60$) were most likely to be driven by a drift-bounce resonance mechanism, while higher m waves could be driven by either drift or drift-bounce resonance. The IDFs responsible for driving such waves were studied in detail by *Baddeley et al.* (2005b), where DOPE HF observations of ULF waves and particle data from the POLAR spacecraft was used to determine the IDFs in the presence of ULF waves statistically have more free energy than those not in the presence of a ULF wave. Six events were found where the particle data existed during the ULF waves. The IDFs in these events each showed that there was free energy between 2 and 12 keV between 9:00 and 16:00 MLT. It was also shown that for a typical high-m wave, there is $\sim 10^{10}$ J of free energy available in the IDF and that $\sim 10^{11}$ J for giant pulsations.

3.3 Eastward Phase Propagation

Eastward propagating ULF waves are less frequently discussed in the past literature due to there being less observations of such events. Unlike many of the westward propagating waves associated with drifting ion instabilities, eastward propagating events are usually associated with electrons. The dawn waves observed by *Pilipenko et al.* (2001b) exhibited eastward phase propagation and were associated with an energy source in energetic electrons related to a nearby westward electrojet.

Dayside ULF wave observations have been made using Cluster, a group of four identical spacecraft flying in a tetrahedral formation. *Eriksson et al.* (2006) observed a spatially localised, monochromatic wave in magnetic and electric field data. The wave exhibited eastward phase propagation with an azimuthal wave number of ~130. The wave also had a stable frequency over a latitude range of ~1 R_E where particle instabilities were again determined to be the source.

Other, more recent studies such as *Zolotukhina et al.* (2008) and *Yeoman et al.* (2010) also observed ULF waves with eastward phase propagation. Both events were observed nearby to a substorm onset and were also attributed to eastward drifting electrons.

3.4 Latitudinal Phase Propagation

Field line resonances typically exhibit a phase reversal of π at the resonant latitude *Walker et al.* (1978, 1979), where the propagation of the phase appears to be poleward. Often particle driven waves such as those observed by *Grant et al.* (1992); *Yeoman et al.* (1992); *Yeoman and Wright* (2001) exhibit equatorward phase propagation.

Grant et al. (1992) observed a number of poloidal ULF waves which exhibited equatorward phase propagations. The characteristics of these waves were similar to the storm time Pc 5 waves, with azimuthal wave numbers ranging from -26 to -60 and periods which remain constant over a range of latitudes. Most of these events occurred when $K_P = 3$ to 4 and show some similarities to the diamagnetic events observed by *Woch et al.* (1990).

Another study by *Yeoman et al.* (1992) observed equatorward propagating waves with a rapid westward phase propagation. An example of one of these equatorward events is shown in Figure 3.15 where the backscatter intensity as measured by SABRE is plotted both as a function of time and magnetic latitude where the phase fronts can be seen to propagate south with time. The waves are consistent with a source in wave-particle interactions with particle energies of 35-70 keV. On average, the phase changes observed were greater than the 180° expected for a field line resonance.

A SuperDARN study by *Fenrich et al.* (1995) observed a population of westward propagating, high-m waves around noon and dusk. The high-m waves of this study all exhibited equatorward propagation similar to *Yeoman et al.* (1992) and *Grant et al.* (1992). The frequencies of these waves were found to be related to the L shell which they existed on, where f decreased with L. The field line resonances were also quantised, most of which had discrete frequencies of 1.3, 1.9 and 2.5 mHz as shown in Figure 3.16.

Yeoman et al. (2008) observed an equatorward propagating wave with a high azimuthal wave number ($m \sim -60$) at 14:00 MLT in backscatter artificially induced by SPEAR (Space Plasma Exploration by Active Radar, *Wright et al.* (2000); *Robinson et al.* (2006)). This small scale wave was observed at a higher L-shell than previous wave observations, with a lower energy of ~10 keV. When compared with the other, similar waves it appeared that the energy of the particles decreased with the increase in L-shell (values shown in Table 3.1). *Yeoman et al.* (2008) suggested that lower energy

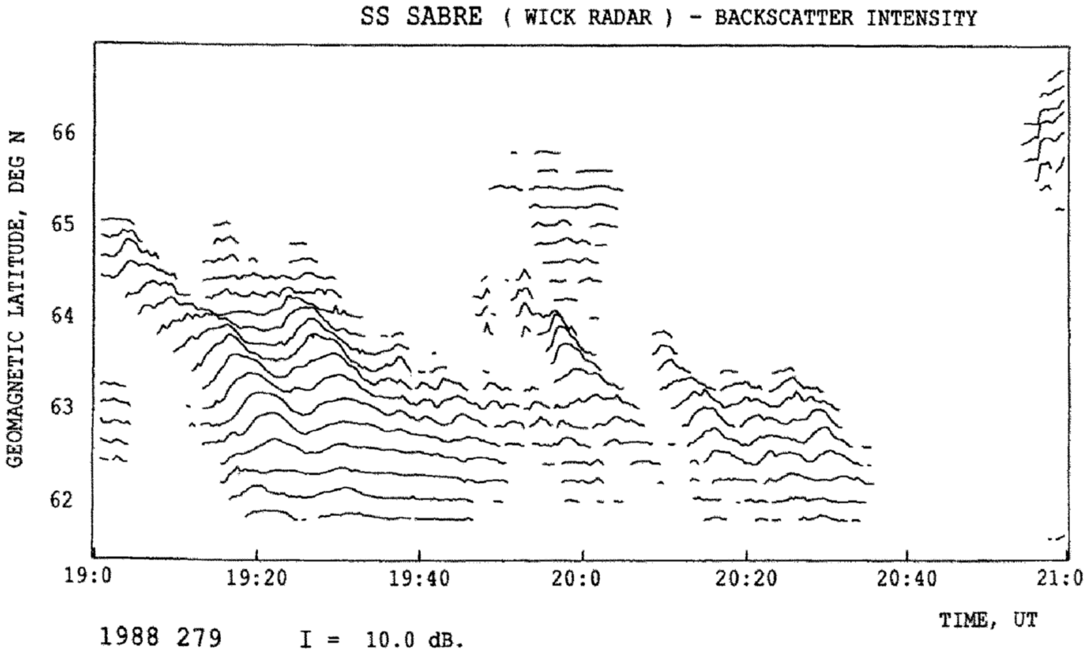

Figure 3.15: Equatorward propagating phase - An example of a wave which exhibits equatorward propagating phase as observed by *Yeoman et al.* (1992) using SABRE. Lines represent the backscatter intensity as a function of magnetic latitude and universal time.

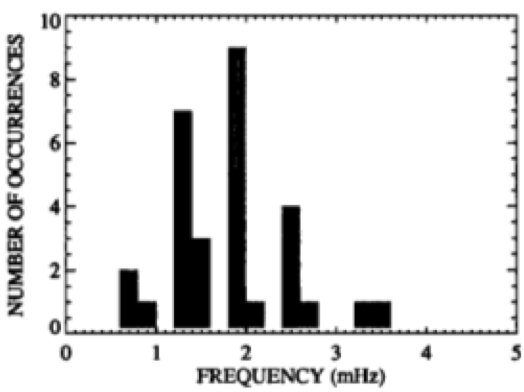

Figure 3.16: Discrete ULF wave frequencies - Occurrences of ULF waves at discrete frequencies by *Fenrich et al.* (1995).

particles exist on higher latitude field lines and require higher m numbers in order to satisfy the drift resonance condition.

Study	m	t(s)	L-shell	Implied Particle Energy (keV)
Yeoman et al.(2010)	+13	580	7.5-15	33
Yeoman et al.(2008)	-60	300	15	10
Grant et al.(1992)	~-50	~300	7.5	20
Yeoman and Wright (2001)	-35	260	6.4	50
Yeoman et al.(1992)	~-20	~400	5	60

Table 3.1: Results from various studies of ULF waves driven by bounce-resonant particles used as a comparison of m and particle energy with L-shell, taken from *Yeoman et al.* (2010).

One explanation for why particle driven waves exhibit equatorward phase propagation is provided by *Mager et al.* (2009). A cloud of particles is injected into the magnetosphere at some azimuthal location, where the particles proceed to drift azimuthally away from the point of injection with some angular drift frequency, ω_d. If ω_d increases with L-shell, then the cloud of particles is stretched into a spiral where lower latitude particles move ahead of higher latitude particles. As the phase of the wave must match the angular drift frequency of the particles, the lower latitude phase propagates ahead of the higher latitude phase.

3.5 Substorm Related ULF Waves

A number of the waves in the above research are thought to be linked to a source in drifting particle populations that may have been injected into the magnetosphere by substorm activity. Substorms provide a way of generating a bump-on-tail distribution that can supply the energy for ULF wave growth. A theory was developed in *Mager and Klimushkin* (2007, 2008) where it was supposed that the poloidal ULF waves were generated by the non-steady azimuthal current associated with the azimuthally drifting substorm-injected cloud of charged particles.

One aspect of the theory developed by *Mager and Klimushkin* (2007, 2008) is that the wave starts with a mixed polarisation which, as the wave and the particles propagate away from the injection point, becomes poloidal. After this stage, the wave then progresses to become toroidal. When wave-particle interactions and a finitely conducting ionosphere are taken into account, the wave is attenuated before it can become toroidal.

An important case study involving substorm-driven ULF waves is that by *Yeoman et al.* (2010). Figure 3.17 shows the fields of view of the Hankasalmi (a) and Þykkvibær (b) SuperDARN radars used to observe this ULF wave and the IMAGE FUV data (c,d,e) at several points during the substorm. The substorm in this event started off slightly to the east of the Hankasalmi radar field of view then rapidly expanded westward to cover the field of view. During the expansion if this substorm, immediately following the onset, an equatorward propagating wave was observed by Hankasalmi as seen in Figure 3.18. The wave observed by *Yeoman et al.* (2010) was shown to exhibit eastward phase propagation with an intermediate-m number of 13 and was associated with a cloud of eastward drifting electrons with an estimated energy of ~25-70 keV. The azimuthal wave number of this wave appeared unusually low and the particle energy appeared to be unusually high for the latitude of the wave when compared to the results in Table 3.1, where it was suggested by *Yeoman et al.* (2008) that the particle energy decreased and m increased with L-shell. Because this wave did not fit with previous results, it was suggested that the properties of the wave such as the m number were related to the proximity of the wave observation to the substorm.

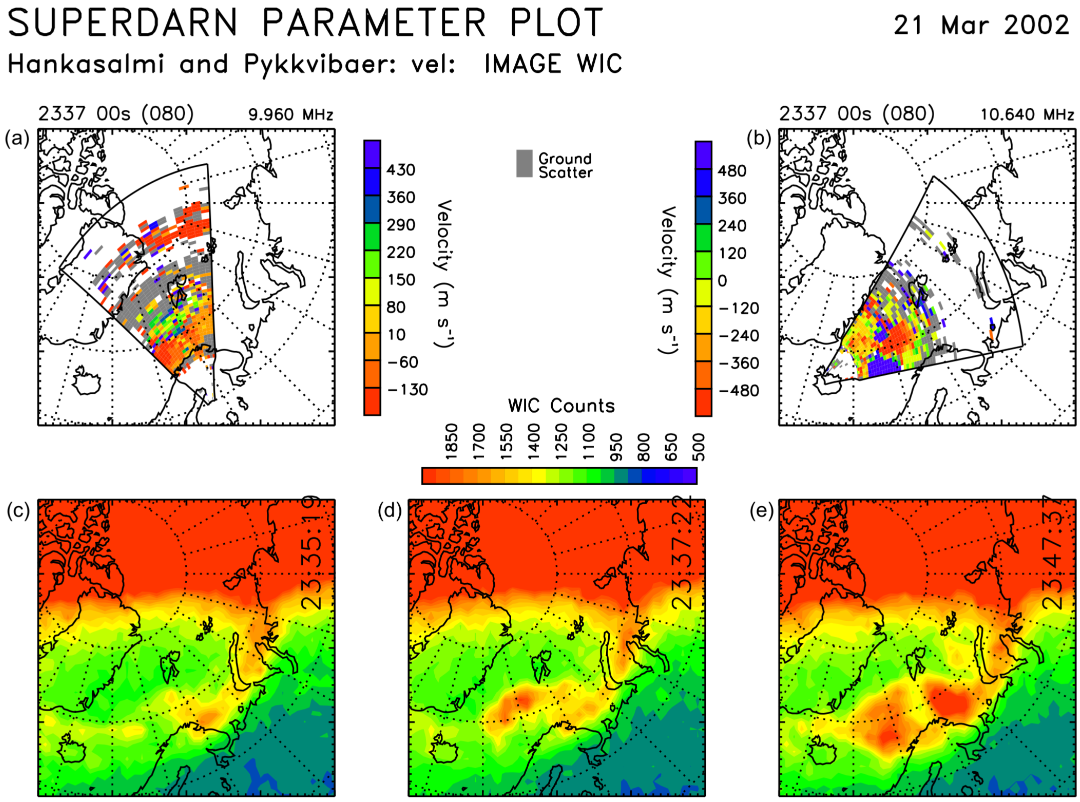

Figure 3.17: Substorm expansion over Hankasalmi and Þykkvibær radar fields-of-view - Fields-of-view of the Hankasalmi (a) and Þykkvibær (b) SuperDARN radars projected over the northern hemisphere, positioned such as noon is at the top. Panels (c), (d) and (e) show the auroral FUV data as measured by IMAGE at three times during the a substorm nearby to the radars. From *Yeoman et al.* (2010).

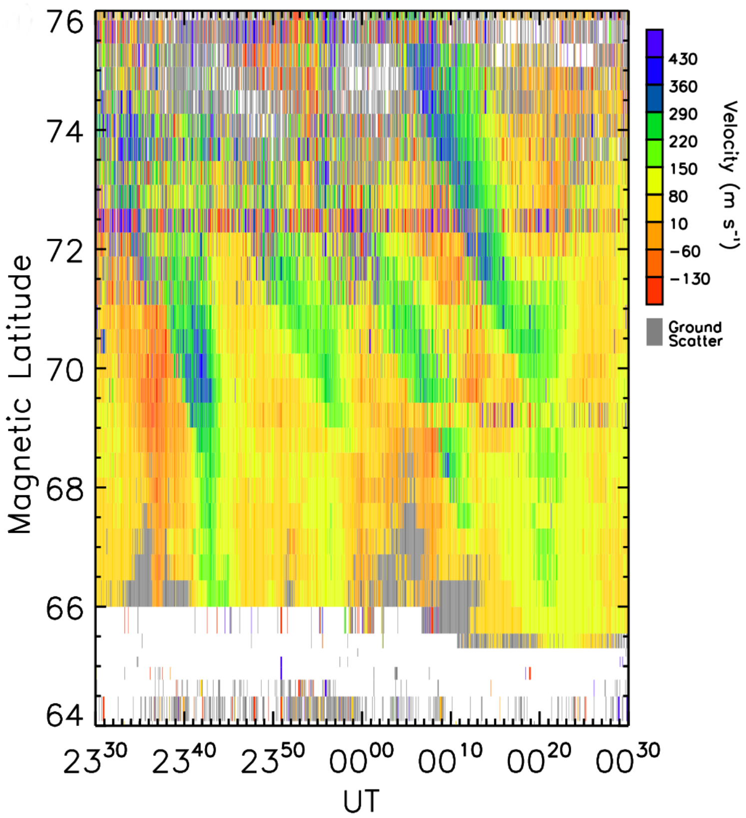

Figure 3.18: Equatorward propagating wave observed using SuperDARN - Equatorward phase propagating ULF wave as observed by the Hankasalmi radar in *Yeoman et al.* (2010). The wave is plotted against magnetic latitude and universal time and the colour represents the line of sight velocity where red is away from the radar and blue towards.

3.6 Summary

This chapter has discussed some of the previous observations of ULF waves driven by wave-particle interactions, including storm-time waves, quiet-time waves and substorm driven waves. The aim of this thesis is to study in more detail the characteristics of ULF waves driven by substorm injected energetic particles. Chapter 5 begins the study of this class of waves by investigating the suggestion made by *Yeoman et al.* (2010) that the proximity to the substorm plays a role in defining the wave characteristics. This study is then extended by Chapter 6 with the study of multiple waves driven by individual substorms. Finally, Chapter 7 investigates the particle distribution functions involved in driving this class of waves.

Chapter 4

Instrumentation

4.1 Introduction

A wide variety of instruments can be useful in the study of ULF wave activity, as shown by the previous work reviewed in Chapter 3. Studies have made use of both in-situ measurements and ground based measurements in order to learn about the different wave modes which exist in the magnetosphere and to study the processes which drive them. Spacecraft based studies have often required the use of multiple spacecraft in order to disambiguate the spatial and temporal variations measured. The sole use of spacecraft observations can provide constraints on what can be learned about ULF waves as events can be highly localised in both space and/or time. A spacecraft may speed through resonant L-shells too quickly to get a good picture of the ULF waves that exist on them, or they may just be in the wrong part of their orbit to see anything at all. However, spacecraft are ideal for the study of the particle populations responsible for the driving of ULF waves as they do sometimes pass directly through them.

Ground based instrumentation such as HF radars and ground magnetometers can be used to observe the effects of ULF waves in the ionosphere and on the ground. Ground magnetometers have the advantage that they can be placed anywhere that there is land for them to rest on meaning that magnetometer networks have spread to cover large parts of the Earth's solid surface. Their global coverage makes them idea for the study of large events such as substorms. The limitation with studying ULF waves using ground magnetometers is that the spatial resolution is relatively low, thus limiting what information can be obtained about small-scale waves. HF radars such as SuperDARN

(Super Dual Auroral Radar Network, (*Greenwald et al.*, 1995; *Chisham et al.*, 2007)) with a typical range resolution of 45 km are far more suited to the study of small-scale ULF waves.

This chapter is intended to discuss the instrumentation used for the studies undertaken in this thesis alongside the explanation of some key data analysis techniques used. The SuperDARN radars were the main tool for the study of the ULF waves themselves. For the study of earlier events it was possible to make use of the FUV (Far Ultraviolet Imager, (*Burch*, 2000; *Mende et al.*, 2000a,b)) auroral imager on board the IMAGE (Imager for Magnetopause-to-Aurora Global Exploration, (*Burch*, 2000)) spacecraft in order to locate substorms using their auroral signature. For later events where IMAGE FUV data was not available it was necessary to make use of ground magnetometers from CARISMA (Canadian Array for Real time InvestigationS of Magnetic Activity (*Mann et al.*, 2008)) fluxgate ground magnetometer network, formerly the CANOPUS (Canadian Auroral Network for the OPEN Program Unified Study (*Mann et al.*, 2008)), IMAGE (International Monitor for Auroral Geomagnetic Effects, (*Lühr*, 1994)), INTERMAGNET (International Real-time Magnetic Observatory Network, (*INTERMAGNET*, a)) and SuperMAG to locate the perturbations caused by the substorm current wedge. Finally, the particle data from the HOPE (Helium, Oxygen, Proton and Electron Mass Spectrometer, (*Funsten et al.*, 2013)) and MagEIS (Magnetic Electron Ion Spectrometer,(*Blake et al.*, 2013)) instruments on board the Van Allen Probes (formerly Radiation Belt Storm Probes (RBSP), (*Mauk et al.*, 2013)) were used in order to study the particles responsible for driving ULF waves.

4.2 SuperDARN

SuperDARN is a global array of 32 coherent ionospheric HF radars, 21 in the northern hemisphere and 11 in the southern hemisphere. This array is presented in Figure 4.1 where the northern fields-of-view are presented in the left panel and the southern fields-of-view are presented in the right panel. The radar fields-of-view have been shaded such that the polar cap radars are in green, the high-latitude (main array) are in blue and the mid latitude radars are in orange.

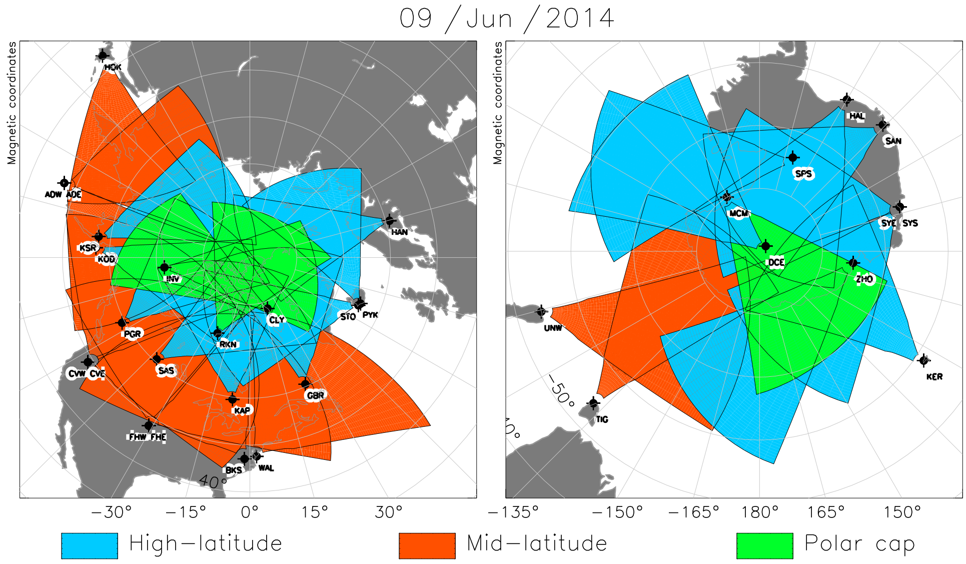

Figure 4.1: SuperDARN fields-of-view - The fields of view of the SuperDARN array in the northern (left) and southern (right) hemispheres. Created using the Radar Field-of-View Tool created by Virginia Tech (*VT-SuperDARN*)

4.2.1 Radar Operation

Each radar consists of 16 log-periodic antennas which are able to both transmit and receive signals (*Greenwald et al.*, 1995). The transmitted signals are often steered by time delay phasing which typically allows for 16 beam directions separated by 3.24° (See Figure 4.2), though some radars may be steered in up to 24 beam directions. Four more antennae exist behind the main antennas, these are only able to receive signals and are phased with the main array to allow for the determination of the elevation angle of the backscattered signal. When combined with a range, a virtual height of the backscatter can then be deduced.

Coherent radars are sensitive to Bragg scattering from electron density irregularities (*Greenwald et al.*, 1995). Ionospheric irregularities are field aligned so, in order for there to be backscatter, the transmitted signal must reach orthogonality in order to return to the radar. Due to the operational frequency of 8 to 20 MHz, signals transmitted by SuperDARN radars are able to achieve orthogonality by means of ionospheric refraction in both the E and F regions of the ionosphere.

Figure 4.3 from *Milan et al.* (1997) shows an illustration of the possible modes

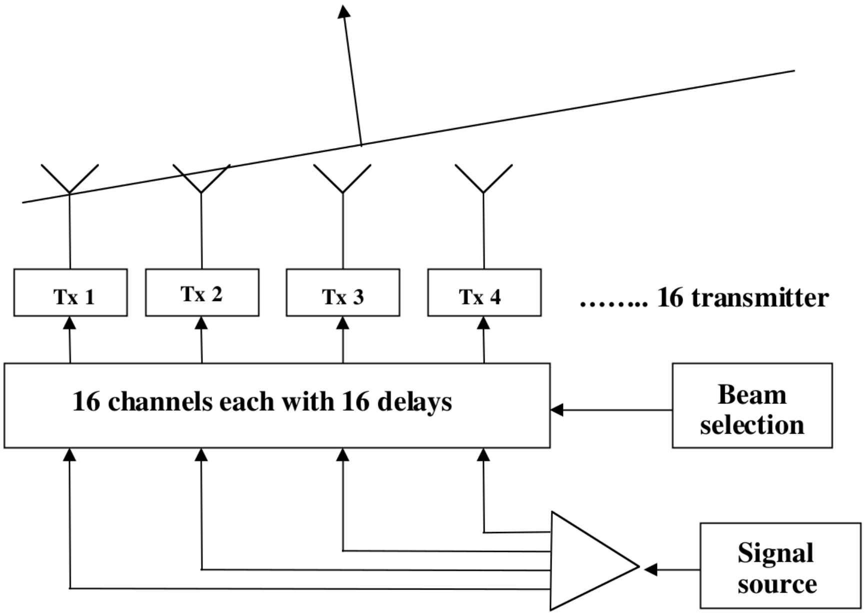

Figure 4.2: SuperDARN beam forming - Schematic of beam steering using time-delay phasing. Figure courtesy of E. C. Thomas.

of propagation and where backscatter is likely to occur. This figure shows that orthogonality can be reached in both E and F regions at a 1/2 hop, but also there is the possibility of backscatter from the ground and for ionospheric backscatter at greater distances than a single hop.

The radars sample the returned signals along each beam and using the time lag of the returned signal can determine the approximate range. There are typically 75 range gates used for each beam on each radar though some incorporate up to 110 range gates. The size of these range gates varies depending on the length of the transmitted pulses, usually 300 μs would be used and would allow for range gates 45 km in size or a 100 μs pulse would allow for 15 km range gates. The receiver bandwidth is then set to the appropriate frequency in order to receive the backscattered pulses.

Usually a 7-pulse sequence is used to discriminate between received pulses from different distances. These received signals are processed using autocorrelation functions (ACF). The ACFs can be fitted and provide values for the backscatter power, mean Doppler velocity and the spectral width of the Doppler velocity.

One of the main functions of SuperDARN is measuring ionospheric convection.

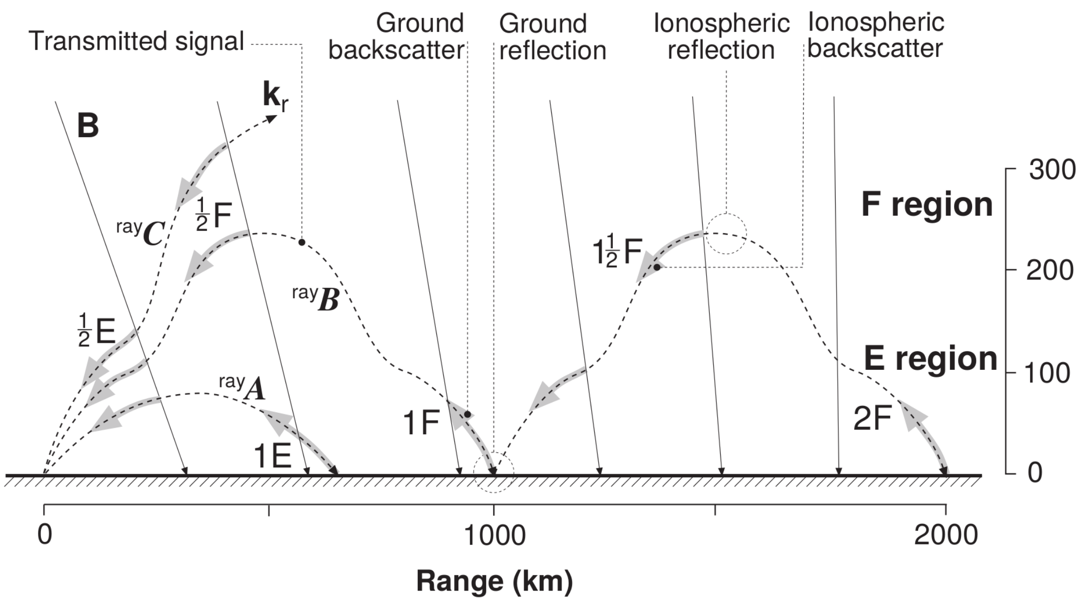

Figure 4.3: Ionospheric propagation - Possible propagation modes of transmitted radar pulses and potential reflection points (*Milan et al.*, 1997).

The radars only provide a line of sight Doppler velocity for each beam and range gate combination, but with more than one line of sight velocity measurement from two different positions it is possible to calculate a two dimensional velocity vector. The overlapping of SuperDARN fields of view allow for these velocity vectors to be calculated.

4.2.2 Time-Series Analysis of ULF Waves

Another science topic that SuperDARN is useful for is the study of ULF waves. On a typical scan mode, the data collected by the radars would typically have a 1 minute time resolution, where ULF wave periods are often longer than this, allowing them to be observed as periodic variations in the Doppler velocity measured. Some scan modes also allow higher resolution scanning of a single beam interlaced within the scanning of the entire field view, enabling the detection of higher frequency waves along a single direction.

The analysis of ULF waves in this thesis involves the use of Fourier analysis in order to determine the frequencies and phases of each time-series. In order to do this the data must be preprocessed first. The first step in preparing the data for analysis is by removing any data gaps or irregularities within the time series by interpolating the data over a uniform time array.

Due to the fact that the time series of a ULF wave measured by SuperDARN is always finite, a window function must be applied to the data to taper the ends of the time series in order to reduce spectral leakage. The window function used here is a split cosine bell function, in mathematical form,

$$w(t) = \begin{cases} \frac{1}{2}(1 - cos\frac{\pi}{a}t), & t \leq a \\ 1, & a \leq t \leq (T-a) \\ \frac{1}{2}(1 - cos\frac{\pi}{a}(1-t)), & (T-a) \leq t \leq T \end{cases}$$

where a is a fixed fraction of the total length of the time series T. We set a to be 10% of T such that the middle 80% of the time series remained untouched.

The time series can then be processed using a Fast Fourier Transform (FFT) to provide the power and phase spectra of the wave. The frequency of the wave is determined as the frequency at which the Fourier power is at its highest in the power spectrum, for each frequency there is a Fourier phase value provided.

As each of the beam/range gate cells provides its own time series, a string of these cells can be used to work out the phase propagation in a given direction. Using a string of range cells along a constant magnetic longitude allows us to compare Fourier phases as a function of magnetic latitude, from which it is possible to determine whether the wave is propagating poleward or equatorward. When a chain of range cells is used along a constant latitude, it is be possible to determine whether a wave is propagating east or west, and thus calculate an azimuthal wave number. The azimuthal wave number is defined as the number of degrees of phase change per degree of magnetic longitude, or the inverse of the azimuthal scale size of the wave.

4.3 IMAGE FUV

The IMAGE (Imager for Magnetopause-to-Aurora Global Exploration, (*Mende et al.*, 2000a,b)) spacecraft was launched on 25th March 2000 into an elliptical polar orbit (90° inclination) with an apogee altitude of $7R_E$ and a perigee altitude of of 1000 km. The line of apsides was inclined at 40°, which would precess over the north pole during the first two years of the spacecraft's lifetime and return to 40° once again as shown in Figure 4.4, taken from *Burch* (2000).

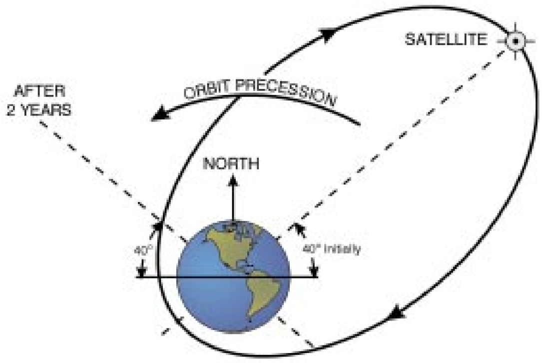

Figure 4.4: IMAGE orbit - Orbital configuration for the IMAGE spacecraft with an initial inclination of the line of apsides of 40° which will precess over the north pole, taken from *Burch* (2000).

The IMAGE spacecraft was designed to be able to help determine what the dominant mechanisms were for injecting plasma into the magnetosphere on substorm and magnetic storm time scales, what the directly driven responses of the magnetosphere were to solar wind changes, and finally to find out where magnetospheric plasmas were energised, transported and lost during storms and substorms (*Burch*, 2000).

In order to realise these objectives, the IMAGE spacecraft hosted an array of experiments. These experiments included the Radio Plasma Imager (RPI), Low-Energy Neutral Atom Imager (LENA), Medium-Energy Neutral Atom Imager (HENA), Far Ultraviolet Imager (FUV) and Extreme Ultraviolet Imager (EUV).

Of these experiments, this thesis makes use of just the FUV experiment. This contained three separate imagers: the Spectrographic Imager (SI), the Wideband Imaging Camera (WIC) and the Geocoronal Imager (GEO).

4.3.1 Wideband Imaging Camera

The Wideband Imaging Camera was aimed at imaging the total intensity of the aurora in regions most representative of the auroral source but least affected by dayglow. The imager is sensitive a broad band of UV aurora with a pass-band of 140-190 nm (*Mende et al.*, 2000b). The main auroral emissions in this range of wavelengths are provided by N_2 Lyman-Birge-Hopfield (LBH) system (127.3 to 255.5 nm) and spectral lines associated with NI (141.2 nm, 149.3 nm and 174.4 nm) (*Galand and Lummerzheim*, 2004).

The camera had to have a resolution high enough such that it would be able to see features of the order of 100 km in size at apogee. The camera had a resolution of 256 x 256 pixels with a 17°x17° field of view (*Mende et al.*, 2000b), which meant that each pixel corresponded to about 52 km x 52 km at apogee and about 1.2 km x 1.2 km at perigee. The time resolution of the images produced by the spacecraft were limited to two minutes at this was the spin period of the IMAGE spacecraft.

4.3.2 Dayglow Removal

Images produced by WIC are often contaminated by dayglow, which can obfuscate auroral features. This effect is most apparent when IMAGE is observing the summer hemisphere as more of the auroral oval would be in direct sunlight, which can be problematic when attempting to study auroral substorms. Here, a similar method of dayglow removal to that outlined by *Laundal* (2010); *Reistad* (2012) has been used.

Figure 4.5 shows how the field of view of two different pixels on the imager would project down to the atmosphere of the Earth. The area of this projection is clearly a function of the satellite zenith angle for the observed area, θ_{DZA}, and is actually proportional to $\frac{1}{cos\theta_{DZA}}$. This means that when a pixel is observing an area at a larger angle, a larger area of atmosphere emitting dayglow is observed.

As the dayglow is primarily caused by solar radiation incident on the atmosphere, we must consider the component of the projected area which is perpendicular to the incident radiation. This area is approximately proportional to $cos\theta_{SZA}$ where θ_{SZA} is the solar zenith angle for the area observed by the pixel.

When these two rules are combined, a simple expression for the background intensity, I_{bg}, can be found,

$$I_{bg} = I_0 \frac{cos\theta_{SZA}}{cos\theta_{DZA}}, \tag{4.1}$$

where I_{bg} should vary linearly with the ratio of $\frac{cos\theta_{SZA}}{cos\theta_{DZA}}$.

This linear relationship was found to be incorrect for WIC images, as shown by Figure 4.6a where the intensity for each pixel excluding pixels observing the auroral

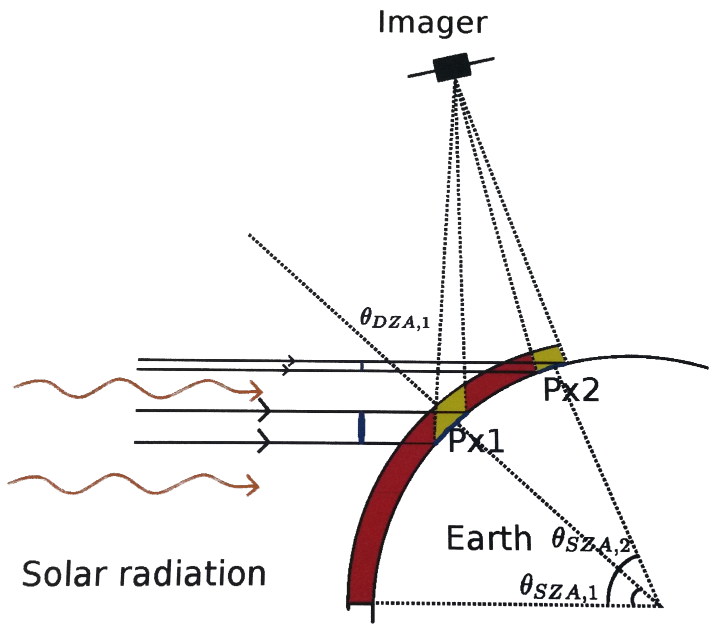

Figure 4.5: IMAGE pixel field-of-view - Figure taken from *Reistad* (2012) shows how the fields-of-view of two pixels with different spacecraft zenith angles are projected onto the atmosphere at locations with different solar zenith angles.

zone, from each image during 12 May 2000 is plotted against $\frac{cos\theta_{SZA}}{cos\theta_{DZA}}$. In this plot, for $\frac{cos\theta_{SZA}}{cos\theta_{DZA}} < 0$ the intensity remains almost constant, but for $\frac{cos\theta_{SZA}}{cos\theta_{DZA}} > 0$ the intensity varies non-linearly. For this reason *Reistad* (2012) used a high order polynomial to fit the data, where the fitted lines are shown in red.

Figure 4.6b shows an example image taken at 20:27:38 on this day before the removal of any dayglow. For each pixel in this image, the intensity of the dayglow can be calculated using the fitting described above to produce Figure 4.6c. Figure 4.6d shows the result of subtracting the predicted dayglow in panel c from the original image in panel b. Figure 4.6d can be smoothed to produce the image presented in Figure 4.6e. When the dayglow is removed for this particular image, features on the day-side of the auroral oval have become more obvious and are surrounded by a similar background level to that which surrounds the night-side features.

This thesis employed a similar technique of dayglow removal by using θ_{DZA} and θ_{SZA} calculated for each pixel to estimate the background dayglow values. Unlike *Reistad* (2012) the resultant images were not smoothed.

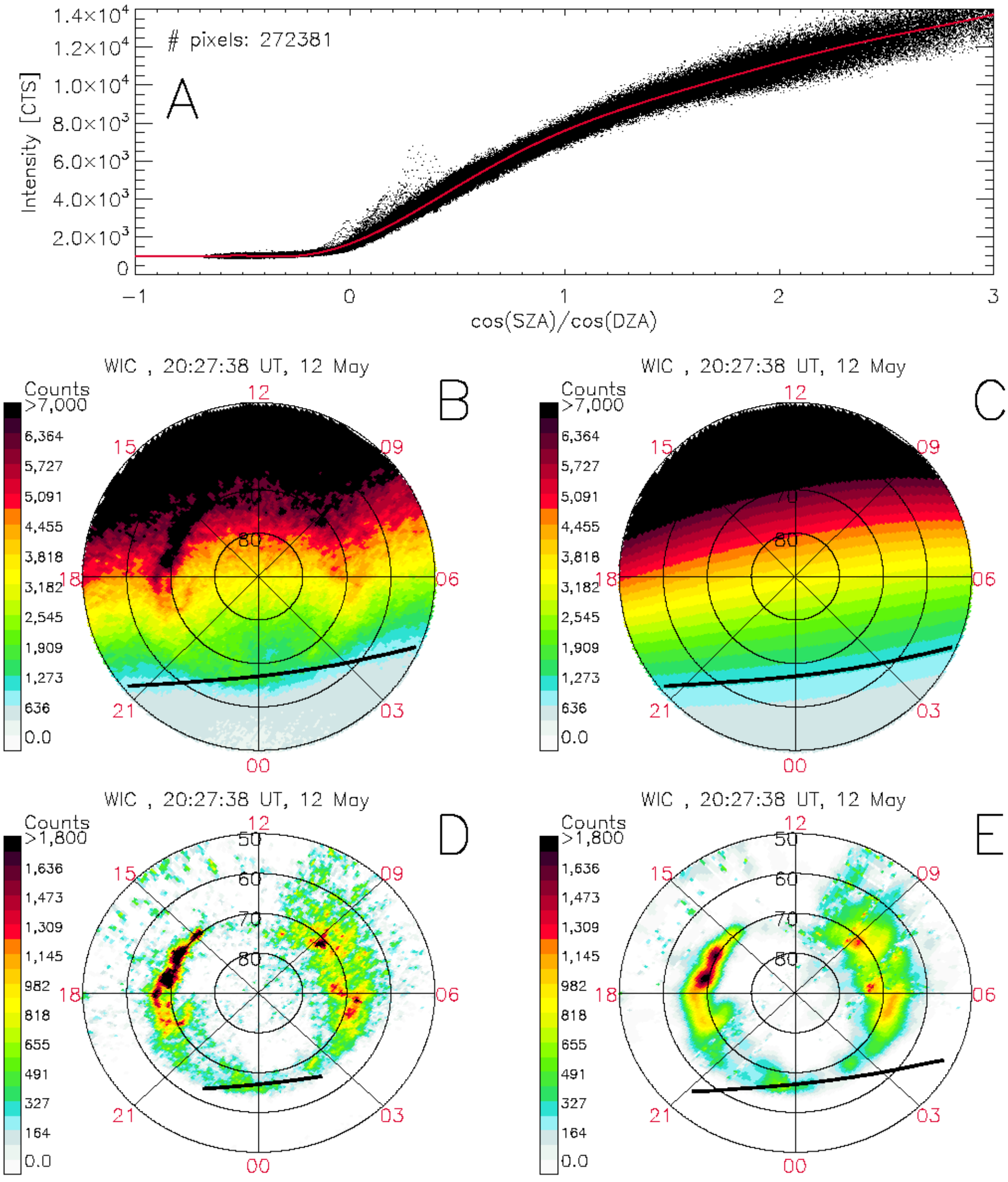

Figure 4.6: Dayglow removal - Panel A shows the intensity of non-auroral pixels from images taken on 12 May 2000 by IMAGE WIC plotted against the value of $\frac{cos\theta_{SZA}}{cos\theta_{DZA}}$ with functional fit represented by the red line. Panel B shows an example of an auroral image at 20:27:38 UT before the removal of the dayglow. Panel C shows the value of $\frac{cos\theta_{SZA}}{cos\theta_{DZA}}$ for each pixel calculated from the fitted line in A. D shows the result of subtracting C from B where auroral features can now be seen where they would have been originally hidden by dayglow. E shows the same image as in D after applying a filter to smooth the image. Figure taken from *Reistad* (2012)

4.3.3 Substorm Observations

The Wideband Imaging Camera aboard the IMAGE spacecraft is an ideal tool for the observation of auroral substorms in the northern hemisphere. Due to the nature of the orbit, the spacecraft spends a large amount of with most of the northern hemisphere in view of the spacecraft often allowing entire substorms to be observed uninterrupted by large data gaps. The time resolution of 2 minutes is also ideal for the observation of the substorms UV aurora as this is a fairly short time interval compared to the time scales associated with the substorm phases.

Frey et al. (2004) compiled a list of substorms observed using the WIC and SI instruments originally containing 2437 substorm onsets, but later updated to 4193. Chapters 5 and 6 make use of the list provided by *Frey et al.* (2004) alongside WIC to observe substorms from the time of onset until they reach the end of their expansion phase. Some of the substorms observed in Chapter 5 did not appear on this list but were found by manual inspection of WIC data and were analysed in the same manner.

When determining the latitudinal and longitudinal limits of the substorm's UV aurora, a threshold based on the highest number of counts observed during the substorm was used to determine approximately where the UV aurora returned to background levels. This threshold was 5% of the peak counts during each substorm. Images where the background was sufficiently noisy for this threshold to be ineffective due to poor dayglow removal or due to other problems were avoided during the analysis of the substorms.

4.4 Ground Magnetometers

Due to the limited lifetime of the IMAGE spacecraft, it was necessary to use ground magnetometers to look for the magnetic signature of the substorm current wedge (SCW) beyond 2005. In order to use ground magnetometers to determine the location of the substorms it was necessary to make use of the data provided by various different sources and in some cases convert the data from geographic to geomagnetic coordinates and to remove the baseline field.

4.4.1 Magnetometer Stations

4.4.1.1 IMAGE

The IMAGE magnetometer network covers northern Europe, primarily Scandinavia and Svalbard. The data provided by IMAGE is typically sampled at 10 second resolution and is given in geographic coordinates. Figure 4.7 shows the locations of the stations currently providing data (*IMAGE*).

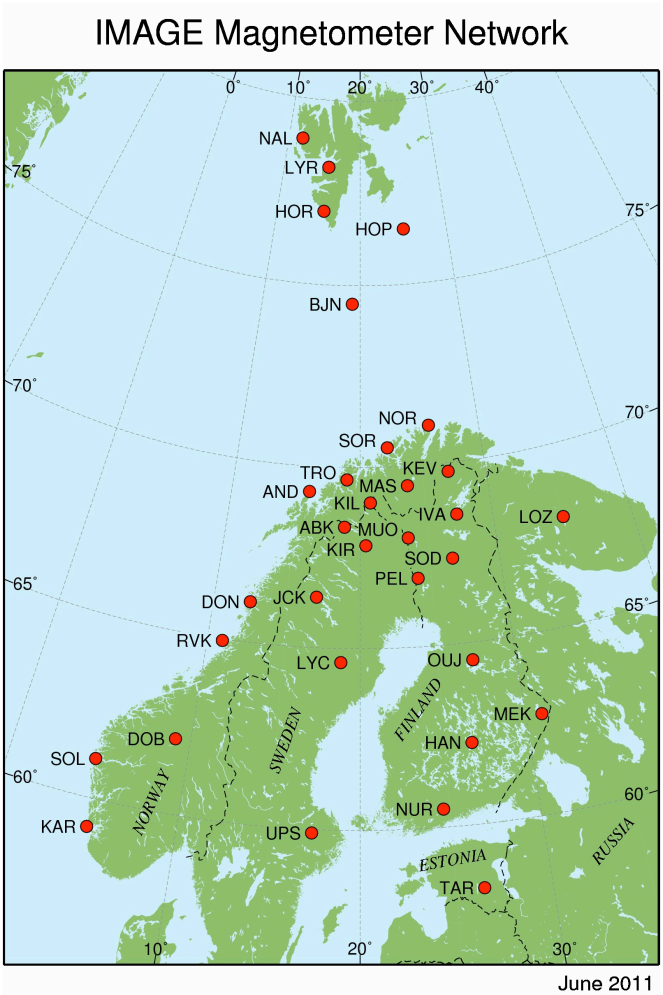

Figure 4.7: IMAGE magnetometer network - Map of IMAGE magnetometer stations in Europe in geographic coordinates, taken from *IMAGE*

4.4.1.2 CARISMA/CANOPUS

CARISMA, formerly named CANOPUS, is an array of magnetometers spanning Canada and some of the northern USA. Figure 4.8 shows the locations of the magnetometers that make up the array, including fluxgate magnetometers (FGM) and induction coil magnetometers (ICM) (*Mann et al.*, 2008). For the purposes of this thesis we make use of the fluxgate magnetometer data which provides data in geographic coordinates at a 1 s time resolution.

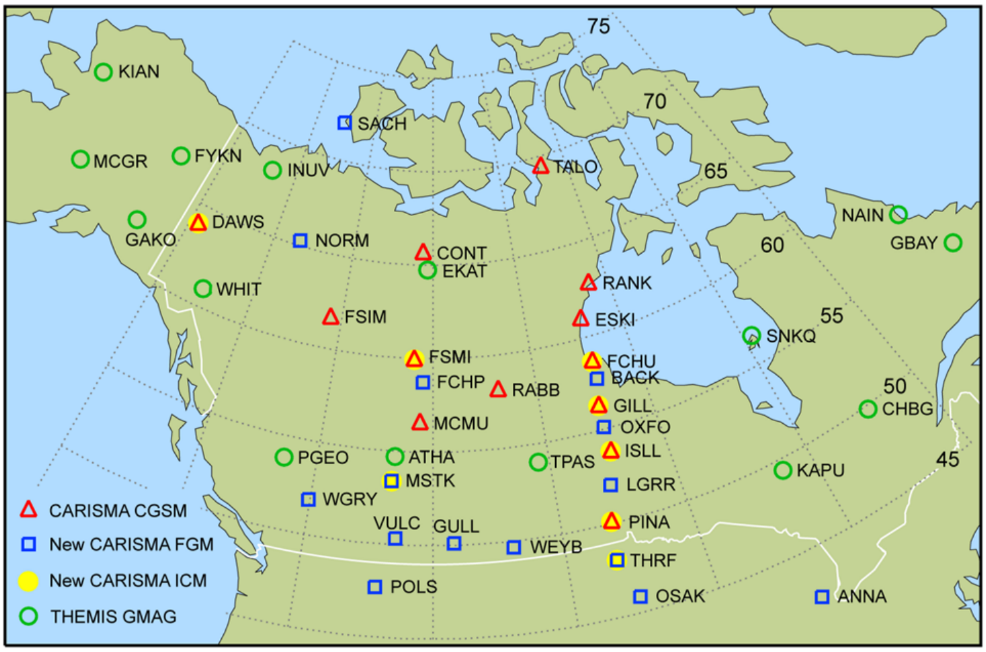

Figure 4.8: CARISMA magnetometer network - Map of CARISMA magnetometer locations in North America in geographic coordinates, taken from *Mann et al.* (2008)

4.4.1.3 INTERMAGNET

INTERMAGNET provides data from magnetic observatories worldwide from many participating countries and institutions. The stations which INTERMAGNET provides the data for are shown in Figure 4.9 (*INTERMAGNET*, b) and includes a few of the magnetometers that make up the IMAGE network . Data provided by INTERMAGNET are usually in 1 minute time resolution, where the coordinate system varies from magnetometer to magnetometer and must be converted to geomagnetic where necessary.

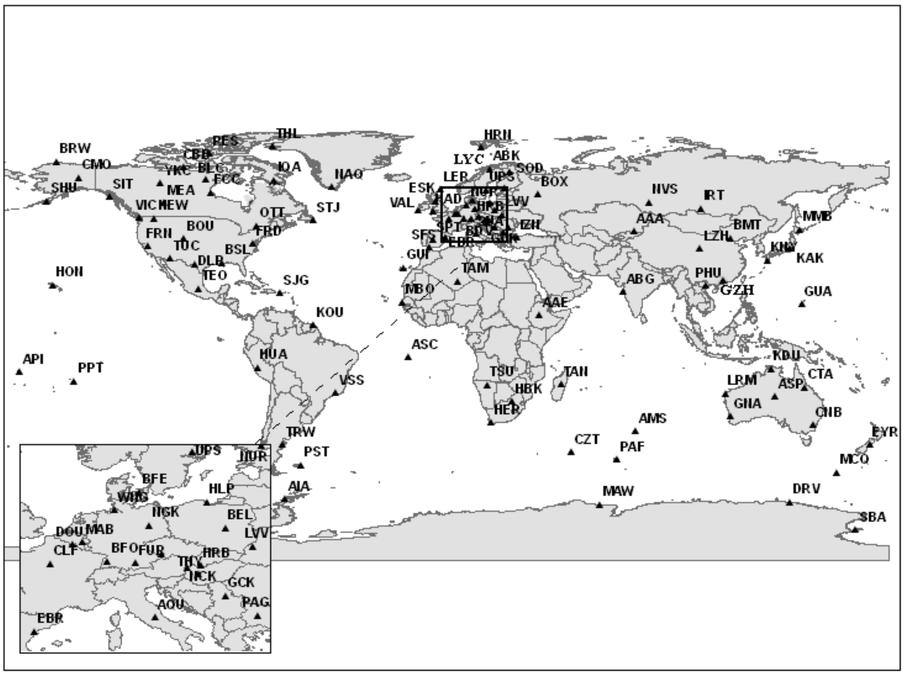

Figure 4.9: INTERMAGNET magnetometer map - Map of magnetometer stations associated with INTERMAGNET in geographic coordinates, taken from *INTERMAGNET* (b)

4.4.1.4 SuperMAG

SuperMAG is a collaboration of organizations and national agencies worldwide to provide the data from more than 300 ground magnetometers. The stations that SuperMAG provides data for are shown in Figure 4.10 (*Gjerloev*, 2012), some of which are also provided by IMAGE, INTERMAGNET and CARISMA. The data provided by SuperMAG has a one minute time resolution and is processed such that the data is in geomagnetic coordinates and already has the baseline removed.

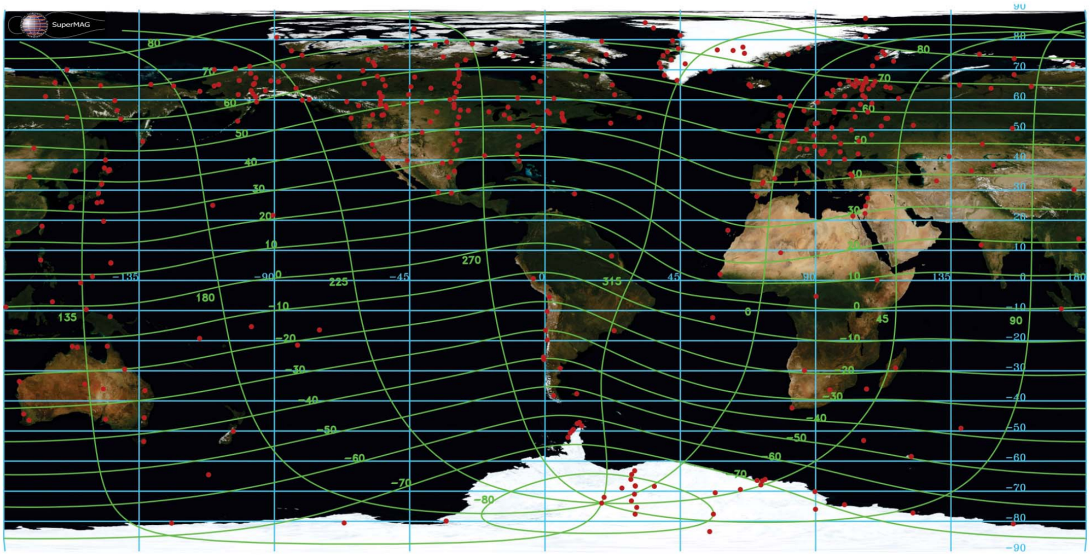

Figure 4.10: SuperMAG magnetometer map - Locations of magnetometer stations used by SuperMAG, taken from *Gjerloev* (2012).

4.4.2 Baseline Removal

To be able to see the magnetic signatures caused by the substorm current wedge (SCW) it is necessary to remove the baseline field from the magnetometer data to leave only those perturbations due to ionospheric currents. The method for baseline removal used here is the same as that which is used to produce the SuperMAG dataset as described in detail by *Gjerloev* (2012).

The first stage of this process is to orientate the data such that it is in geomagnetic coordinates. Due to the fact that the Earth's magnetic dipole moves with time, it is necessary to find the declination of the magnetic field as a function of time for each magnetometer. This is done be using a 17 day sliding window to determine typical values for the X (geographic north) and Y (geographic east) components, from which the declination as a function of time is

$$\theta(t) = tan^{-1}\frac{B_Y}{B_X}, \tag{4.2}$$

where the 17 day window is a compromise between avoiding the removal of short time scale events such as the build-up and decay of the ring current while retaining seasonal variations.

The typical values for each day are calculated by least-squares fitting a Gaussian to the data. The typical value is defined as the mode of the distribution unless the magnitude of the fitted Gaussian is larger than the average of the mode and its two surrounding values. The X and Y components of the field are then rotated through the angle θ to become H (geomagnetic north) and D (geomagnetic east) respectively (see Figure 1.13 on page 18). Once the data has been rotated appropriately from XYZ coordinates to HDZ coordinates, where Z in both coordinate systems points to the centre of the planet, the D component would be typically around zero.

The next stage is to determine and remove diurnal variations in the data. To do this, variations on time scales longer than one day must be removed initially by defining typical values for each day. These typical values are subsequently removed from the data.

The data from each day is then combined and binned into 30 minute sections of the day, providing 48 bins in a 24 h period. The diurnal trend is then interpolated back to a one minute time resolution from these 48 bins and can be subtracted from from the data.

The final step is to remove any yearly trend in the data. A 17 day sliding window is used to find the typical values again, which is then smoothed and subtracted from the data. This data is then ready for being used to locate the SCW. The method of locating the SCW is discussed in detail in section 6.4.

4.5 Van Allen Probes

The Van Allen Probes, previously called Radiation Belt Storm Probes (RBSP), were launched in August 2013 to study the Van Allen radiation belts. The pair of spacecraft were launched into very similar, low inclination orbits. The orbits have a similar but not completely identical apogee of ~5.8 R_E and a perigee of ~1.1 R_E where the slight difference in the orbits causes one spacecraft to lap the other every 2.5 months (*Mauk et al.*, 2013).

The main objective of the Van Allen Probes was to study the creation, evolution and depletion of populations of high energy charged particles within the radiation belts. To do this, the probes are both equipped with identical suites of instruments able to study electrons, ions, ion compositions, electric fields, magnetic fields and waves in both of these fields. The list of instrument suites included on the probes is as follows: ECT (Energetic Particle Composition and Thermal Plasma, *Funsten et al.* (2013); *Blake et al.* (2013); *Baker et al.* (2013)), EMFISIS (Electric and Magnetic Field Instrument Suite and Integrated Science, *Kletzing et al.* (2013)), EFW (Electric Field and Waves instrument, *Wygant et al.* (2013)), RBSPICE (Radiation Belt Storm Probes Ion Composition Experiment, *Mitchell et al.* (2013)) and RPS (Relativistic Proton Spectrometer, *Mazur et al.* (2013)).

The Van Allen Probes are useful for the study of recently injected energetic particle populations originating from substorms due to the configuration of the orbit. Due to the large range of L-shells traversed by the probes, it would be possible to intercept and detect clouds of energetic particles injected during substorms as they drift around the planet driving ULF waves.

In order to detect these particles we use the ECT suite of instruments. Of the instruments included in this suite, we make use of HOPE and MagEIS as they cover the appropriate energy range of the particles we expect to see, where the energy of the particles detected using REPT (Relativistic Electron-Proton Telescope, (*Baker et al.*, 2013)) lies far beyond this energy range.

4.5.1 HOPE

HOPE is a mass spectrometer designed to measure the plasmasphere, plasma sheet and lower energy ring current (*Funsten et al.*, 2013). It is able to detect proton, helium ion, oxygen ion and electron fluxes between the energy of 1 eV and 50 keV using 36 log-spaced bins.

HOPE uses the spin of the spacecraft to be able to get a full 4π sr distribution of particle fluxes. This allows the ability to produce both spin averaged and pitch angle distributions of the particle fluxes.

4.5.2 MagEIS

The MagEIS instrument consists of four electron spectrometers and one proton telescope (*Blake et al.*, 2013). Of the four electron spectrometers there is one low energy (20-240 keV), two medium energy (80-1200 keV) and one high energy (800-4800 keV).

The proton telescope is contained within the high energy unit and is able to measure energies from 50 keV - 1 MeV. The proton telescope is unable to determine the composition of the ions that it detects, though protons would be expected to dominate.

In a similar way to the HOPE instrument, MagEIS uses the spin of the spacecraft in order to get a three-dimensional particle distribution of the electrons. This allows for the creation of pitch angle distributions for the electron data.

4.5.3 Particle Distribution Functions

The differential particle fluxes measured by HOPE and MagEIS can be combined together and converted into a particle distribution function (PDF). A PDF allows us to see at what energy levels there is free energy available to drive ULF waves and what energies Landau damping would occur, as discussed in Section 2.3.6.

The PDF can be derived from the differential particle flux measurements provided by HOPE and MagEIS using the method described by *Baddeley* (2003). To do this we must consider that a detector would be observing a volume of velocity space d^3v which is centred on some velocity $\mathbf{v}$. The detectors have many pass-bands, where each passband, E to $E + dE$, corresponds to a range of particle speeds v to $v + dv$. If the detector looks into some solid angle $d\Omega$ then the volume in velocity space becomes,

$$d^3v = v^2 d\Omega dv, \tag{4.3}$$

and since $dE = mvdv$,

$$d^3v = (\frac{v}{m})d\Omega dE. \tag{4.4}$$

The number density that the detector would see is $f(\mathbf{v})d^3v$ which corresponds to a flux of $vf(\mathbf{v})d^3v$. Given that the detector has an area dA, over the integration time dt the total number of particles that pass into the detector can be expressed by

$$dN = vf(\mathbf{v})d^3v dAdt, \tag{4.5}$$

which, when combined with Equation 4.4, becomes

$$dN = (\frac{v^2}{m})f(\mathbf{v})dAdtd\Omega dE. \tag{4.6}$$

The differential particle flux, $\frac{dn}{dE}$, is defined as

$$\frac{dn}{dE} = \frac{dN}{dAdtd\Omega dE} = (\frac{v^2}{m})f(\mathbf{v}) = (\frac{2E}{m^2})f(\mathbf{v}), \tag{4.7}$$

which can be rearranged for $f(\mathbf{v})$ to give

$$f(\mathbf{v}) = (\frac{m^2}{2E})\frac{dn}{dE}. \tag{4.8}$$

As the differential particle flux provided by the instruments is given in units cm^{-2} s^{-1} sr^{-1} keV^{-1}, the units must be converted appropriately in order to use Equation 4.8 correctly. The gradients in the resultant PDF show at what energies, and therefore wave phase speeds, wave growth (positive gradient) and wave damping (negative gradient) will occur.

Chapter 5

Spatio-temporal Characteristics of Substorm-Driven ULF Waves

5.1 Introduction

Previous studies such as *Chisham et al.* (1992); *Wright et al.* (2001); *Zolotukhina et al.* (2008) have provided evidence that high-m ULF waves are driven by energetic particles when pulsations have been observed at the same time as the occurrence of clouds of energetic particles injected during substorm expansion. *Mager and Klimushkin* (2007, 2008) developed a theory of this process where it was supposed that poloidal ULF waves are generated by the non-steady azimuthal current associated with the azimuthally drifting substorm-injected cloud of charge particles. This mechanism can be responsible for the equatorward component of the poloidal wave's phase velocity revealed with the radars (*Mager et al.*, 2009). Even earlier, *Pilipenko et al.* (2001a) interpreted a moderately high-m Pi3 event as a result of generation by a transverse fluctuating current developed during a large storm.

The particles could also drive wave modes through a bump-on-tail instability via drift or drift-bounce resonance wave-particle interactions at the eigenfrequency of the field line on which they are drifting (*Baddeley et al.*, 2005a,b; *Mager and Klimushkin*, 2005). The instability and the non-steady current mechanism of *Pilipenko et al.* (2001a) and *Mager and Klimushkin* (2007, 2008) can work simultaneously: the moving source or fluctuating current can provide an oscillation seed which will be further amplified by means of the instability.

As driving particles, 10-100 keV protons are usually suggested, which can explain the westward phase propagation observed with radars (e.g., *Chisham et al.*, 1992; *Fenrich et al.*, 1995; *Yeoman et al.*, 2008). More recently, a case study by *Yeoman et al.* (2010) observed an equatorward propagating wave with a period of 580 s that appeared immediately after the expansion of a substorm. This particular event was the only one of the five events considered in *Yeoman et al.* (2008) and *Yeoman et al.* (2010) to exhibit a wave with eastward phase propagation. The eastward phase propagation of this wave, where $m = 13$, suggested an energy source in the form of an eastward drifting cloud of energetic electrons, rather than protons, with energies of 25-70 keV at L shells of 7.5-15. The triggering of solar wind-driven Pc5 ULF waves by the injection of electrons into the magnetosphere was also suggested by *Belakhovsky and Pilipenko* (2010). The period of this wave is somewhat longer than in earlier observations, and it was suggested in *Yeoman et al.* (2010) that this was due to the wave occurring near midnight shortly after substorm onset, in agreement with the theory developed by *Mager and Klimushkin* (2007, 2008). The field lines at that time and location would have been stretched, leading to lower eigenfrequencies. The azimuthal wave number was unusually low compared to the previous results, while the energy of the inferred driving particles (~33 keV at the central L shell) was higher than that expected for the latitude of the wave. *Yeoman et al.* (2010) suggested that the proximity of the observed wave to the substorm onset was a strong controlling factor for the particle energy and the azimuthal wave number m.

Here, a statistical study of ULF events with a similar generation mechanism to that of the studies mentioned above is presented, in order to elucidate the dependence of the waves on their temporal and spatial separation from the particle injection region and test the inferences made in *Yeoman et al.* (2010).

5.2 Instrumentation

Data from the five SuperDARN (Super Dual Auroral Radar Network, (*Greenwald et al.*, 1995; *Chisham et al.*, 2007)) radars located at Hankasalmi in Finland, Kapuskasing, Saskatoon and Goose Bay in Canada and Kodiak in Alaska were used to study the waves. Each radar uses 16 beams with a 3.24° separation while each beam typically has 75 range gates separated by 45 km where the first gate starts at 180 km from the radar. During the events studied a variety of radar scans were in use on the radars giving a data cadence for individual beams which ranged from 3 to 120 seconds. The fields of view of each of the radars are shown in Figure 5.1 where the meridional beams are highlighted in each case. The northward beams for Hankasalmi (beam 6), Kapuskasing (beam 11), Saskatoon (beam 3), Goose Bay (beam 4) and Kodiak (beam 3) were used to determine the latitudinal phase propagation of the waves, while two or three beams from either side of these were used to analyse the longitudinal phase propagation.

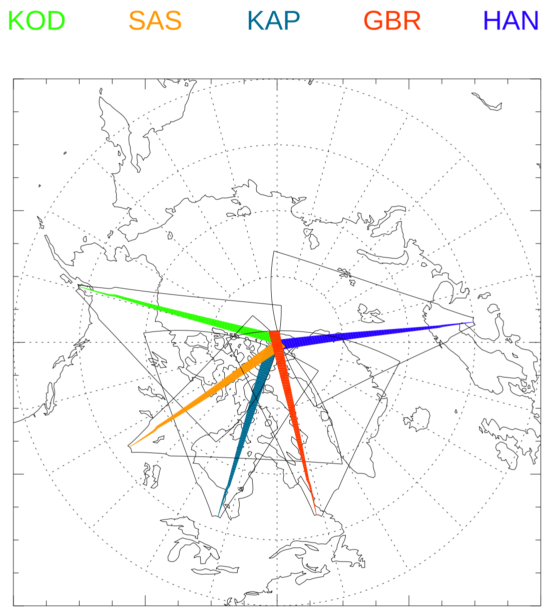

Figure 5.1: Radar fields-of-view - The fields-of-view of the SuperDARN Kodiak (KOD), Saskatoon (SAS), Kapuskasing (KAP), Goose Bay (GBR) and Hankasalmi (HAN) radars used in this study. The meridional beams for each radar are highlighted in colour.

Many of the events studied are associated with substorm expansions initially taken from a list of substorms identified by *Frey et al.* (2004) which used the FUV (Far Ultraviolet Imager) instrument onboard the IMAGE (Imager for Magnetopause-to-Aurora Global Exploration, (*Mende et al.*, 2000a,b)) spacecraft to identify the time and location of substorms. The list used was an updated version of their original list which contains the time and location of 4193 substorm events between May 2000 and December 2005.

As an example, Figure 5.2 shows the FUV data for the onset and expansion phase of one of the events on the list above, where *Frey et al.* (2004) identified a substorm at ~1904 UT on 14th December 2001. Each of the images are oriented such that noon is at the top of each panel and dawn is to the right, where the centre of the panel corresponds to the north magnetic pole and the concentric circles around the pole represent 10° magnetic latitude increments. The initial auroral brightening of this substorm (panel (a)) appeared slightly to the east of the field-of-view of the Hankasalmi radar in Finland at 1850 UT, a little earlier than the onset time originally identified by *Frey et al.* (2004) (the outline of the full field-of-view and beam 6 are both shown in each panel. The green line of constant longitude present in each panel will be discussed later). Subsequent to the initial onset, the substorm can be seen to expand both eastwards and westwards for around 20 minutes in Figure 5.2, panels (a)–(f).

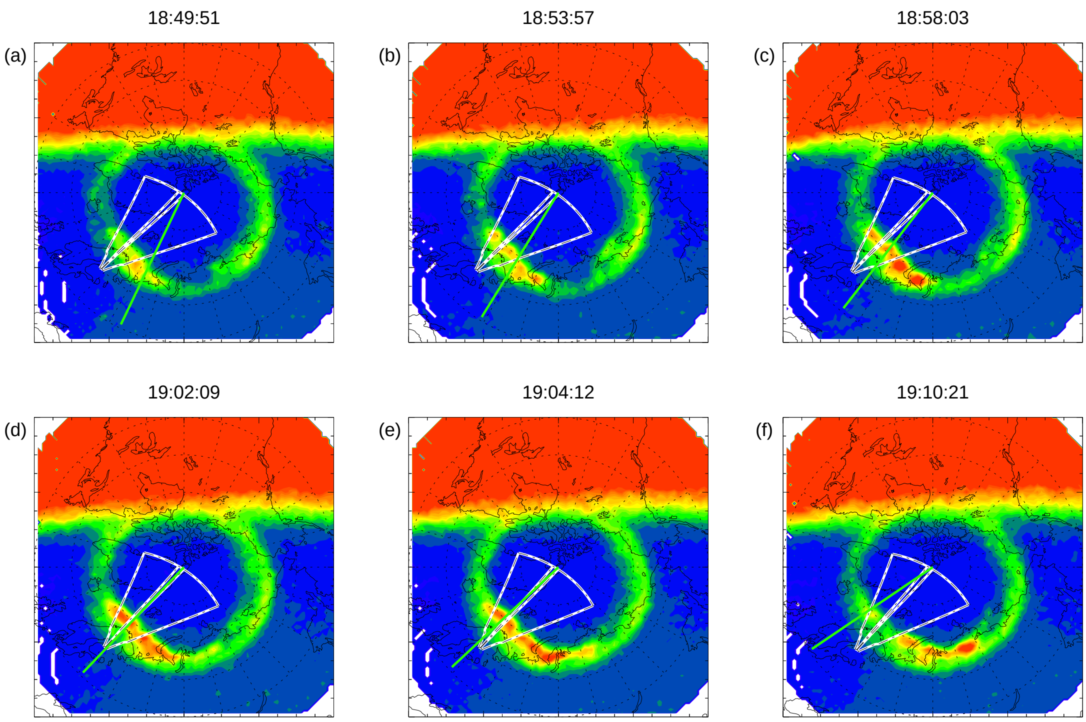

Figure 5.2: IMAGE WIC data - December 14th 2001 - An example of IMAGE WIC data used to locate a substorm onset on Friday December 14th 2001 at 1850 UT, as identified by *Frey et al.* (2004). The top of each panel corresponds to noon while dawn is to the right.

5.3 Data

The substorm events from the list above were selected such that they occurred within ~±50° magnetic longitude of each of the radars used to characterize the wave activity. The number of events was further reduced by the requirement to perform reliable Fourier analysis on the wave as, in a number of the unused events, the time resolution of the data were too low to provide accurate values for wave frequency and phase. Finally the list of events was reduced to the ones where the substorm onset and expansion could be identified with confidence in the IMAGE FUV data, eliminating the cases where there had been multiple substorms and consequently associating an individual wave event with an individual substorm was not possible. This resulted in a final number of 83 events occurring between June 2000 and September 2005, the onsets of 40 of which were identified by *Frey et al.* (2004). The remaining 43 events have been associated with other substorm onsets seen using the FUV instrument, but which did not appear in the list made by *Frey et al.* (2004).

For each of the events studied, Fourier analysis was used to find the latitudinal and longitudinal phase propagation of the waves. The wave periods were determined using the dominant peaks in the Fourier power spectrum produced for each range gate and beam used. In each of the events studied, the dominant frequency found using Fourier analysis was typically the same everywhere where the wave was observed within the radar's field-of-view. To find the latitudinal phase propagation, the Fourier phases at the dominant frequencies of the waves were obtained from the data in several range gates along the northward pointing beams. Whilst the use of single-radar data for the analysis of each individual event precludes a full polarization analysis, the fact that the waves are observed using meridional beams suggests that they have a strong poloidal component, in common with previous observations of similar waves (e.g., *Allan et al.*, 1983b; *Yeoman et al.*, 2008). The longitudinal phase propagation of the waves was found in a similar manner to that of the latitudinal phase. However, rather than several range gates on a single beam, multiple beams either side of (and including) the northward pointing beams were used with range gates at an approximately constant latitude.

5.4 Example Event

Figure 5.3 shows a ULF wave event detected in the line of sight velocity as measured by the Hankasalmi radar corresponding to the expansion phase of the substorm event identified by *Frey et al.* (2004) and illustrated in Figure 5.2. The velocity is colour coded such that red corresponds to ionospheric flow away from the radar and blue represents flow towards the radar. Panel (a) shows the meridional view of the wave from range gates 19 to 23 within beam 6, while (b) shows the longitudinal view of the wave using beams 3 to 12 along an approximately constant L-shell of about 7. The wave appears shortly after the onset of the substorm, a little after 1900 UT, suggesting that the wave is associated with particles injected during the substorm. The top panel in Figure 5.3 shows the data from beam 6 where it is clear that the wave exhibits equatorward phase propagation, while the bottom panel shows a westward phase propagation. Panel (b) also shows that there is a bulk flow in the ionosphere away from the substorm, in the westward direction. Multiple harmonics can be seen in the data though Fourier analysis reveals a dominant period of ~1500 s. Figure 5.4 shows the Fourier power and phase variation at the dominant frequency of 0.67 mHz in both latitude and longitude. It can be seen that the wave has an effective azimuthal wave number, m, of ~-10 (positive m represents eastward propagation) and a latitudinal phase gradient, l, of ~-41° (positive l represents poleward propagation) where values for m and l are the gradients calculated using linear least squares fit to the phase values as displayed by the dashed lines in Figure 5.4.

The wave period, τ, and its azimuthal wave number can be used to calculate the waves azimuthal phase propagation frequency, ω,

$$\omega = \frac{2\pi}{\tau m}, \tag{5.1}$$

which, for the wave in Figure 5.3 gives ω~-4.3×10^{-4} rads s^{-1}, where a negative ω corresponds to a westward propagation. If the higher harmonics of the wave visible in Figure 5.3 are considered, we find that the angular drift frequency of these harmonics is almost identical to that of the dominant frequency.

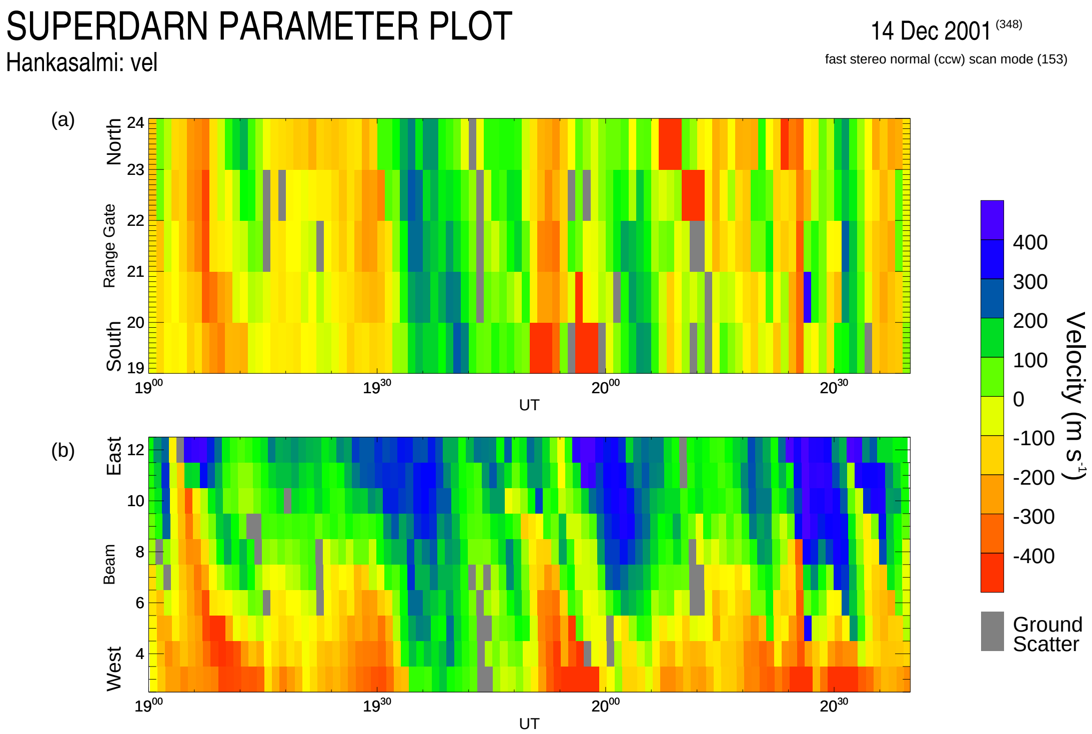

Figure 5.3: Hankasalmi wave observation - December 14th 2001 - Hankasalmi radar data corresponding to the substorm shown in Figure 5.2, where the top panel presents the latitudinal profile of the wave (from beam 6) and the bottom panel shows the longitudinal profile (beams 3-12 at L ~7). The wave has a dominant period of ~1500 s.

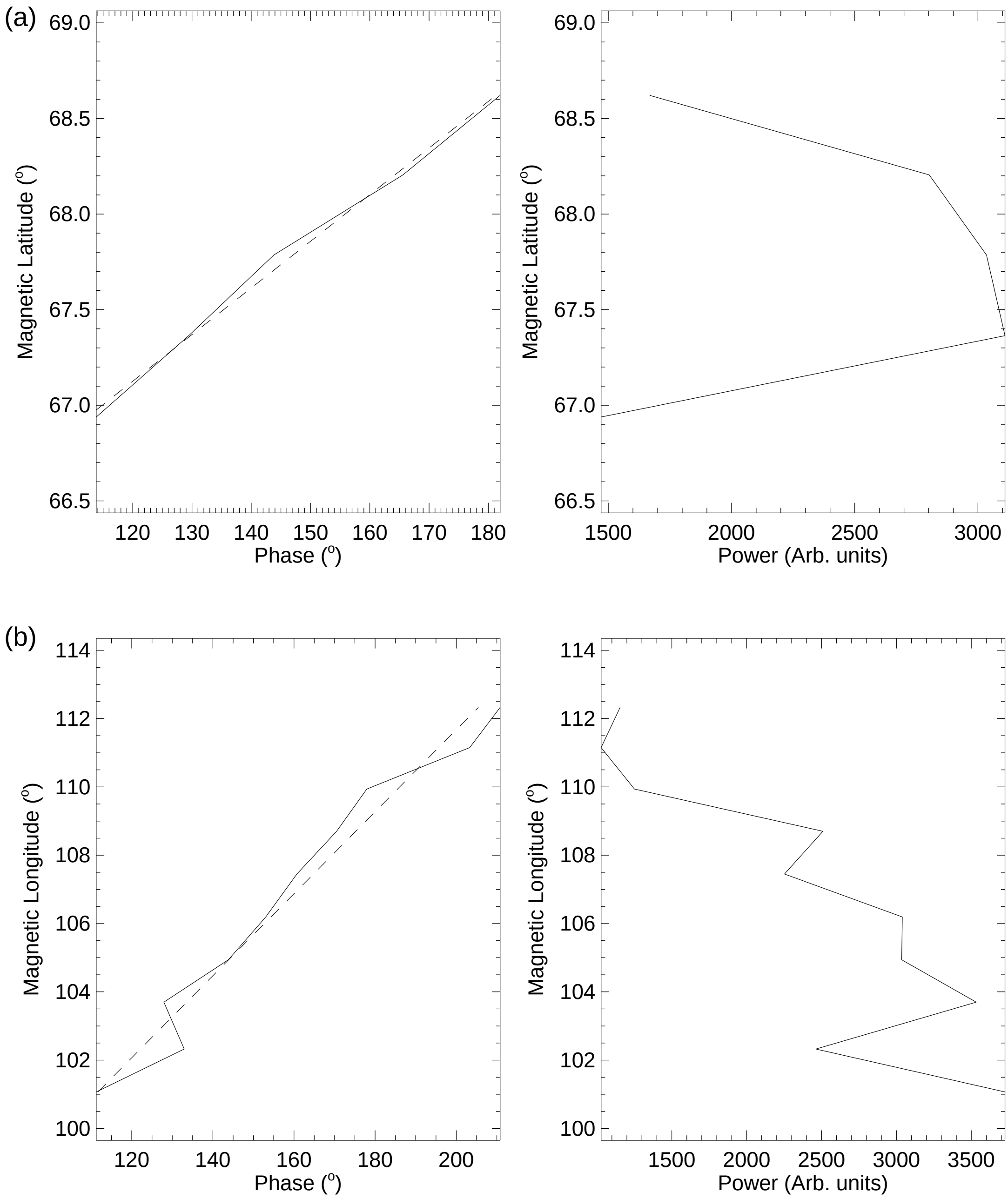

Figure 5.4: Fourier phase and power profiles - Fourier power and phase profiles for the wave event presented in Figure 5.3. (a) Latitude profile. (b) Longitude profile. The dashed line is a linear fit to the phase gradients.

5.5 Statistical Study

All of the 83 events identified have been analysed in the same manner as the example in the previous section. This has revealed that there is a relationship between the azimuthal wave number and the azimuthal separation of the substorm onset regions and the wave observations.

Panel (a) of Figure 5.5 shows the m-numbers for each of the events plotted against the azimuthal separation of the corresponding wave observations and substorm onsets, where the error bars represent the approximate longitudinal extent of the substorm UV auroras at the time of onset. The events which appeared on the list of substorms identified by *Frey et al.* (2004) are coloured green, while the remainder are coloured red. Panel (b) shows the data from panel (a) placed into 15° magnetic longitude bins, where the error bars are the standard errors associated with each bin. Figure 5.5 reveals that m increases in magnitude with the azimuthal separation, where m is generally positive when the wave is observed to the east of a substorm, and negative to the west, though it may be noted that there is some overlap in the two populations.

Figure 5.6 shows the latitudinal phase gradient, l in a similar format to Figure 5.5 where wave events that appeared poleward of the substorm onset position are on the right side of the origin, and wave events which appeared equatorward of the substorm onset position are shown to the left of the origin. The majority of the waves observed exhibit equatorward phase propagation which is characterized by a negative value of l as defined in Section 3.1, though there are a small number of poleward events observed. In common with previous observations of particle-driven poloidal waves (*Yeoman et al.*, 1992; *Fenrich et al.*, 1995; *Yeoman et al.*, 2010), the 180° phase change characteristic of toroidal field line resonances is not observed. There appears to be a weak correlation between the latitudinal separation of the wave observations and the substorm onsets and l, where the farther equatorward the wave is with respect to the substorm, the more negative l becomes. There is some suggestion that poleward propagating waves became more increasingly likely to be observed $\gtrsim 4°$ poleward of the substorm onset position. However, the majority of waves in all regions have equatorward phase propagation. It may be noted that there is a large amount of scatter in the data, this is likely due to the uncertainties involved in estimating the latitudes of the waves. The waves studied tend to extend over a range of a few degrees of magnetic

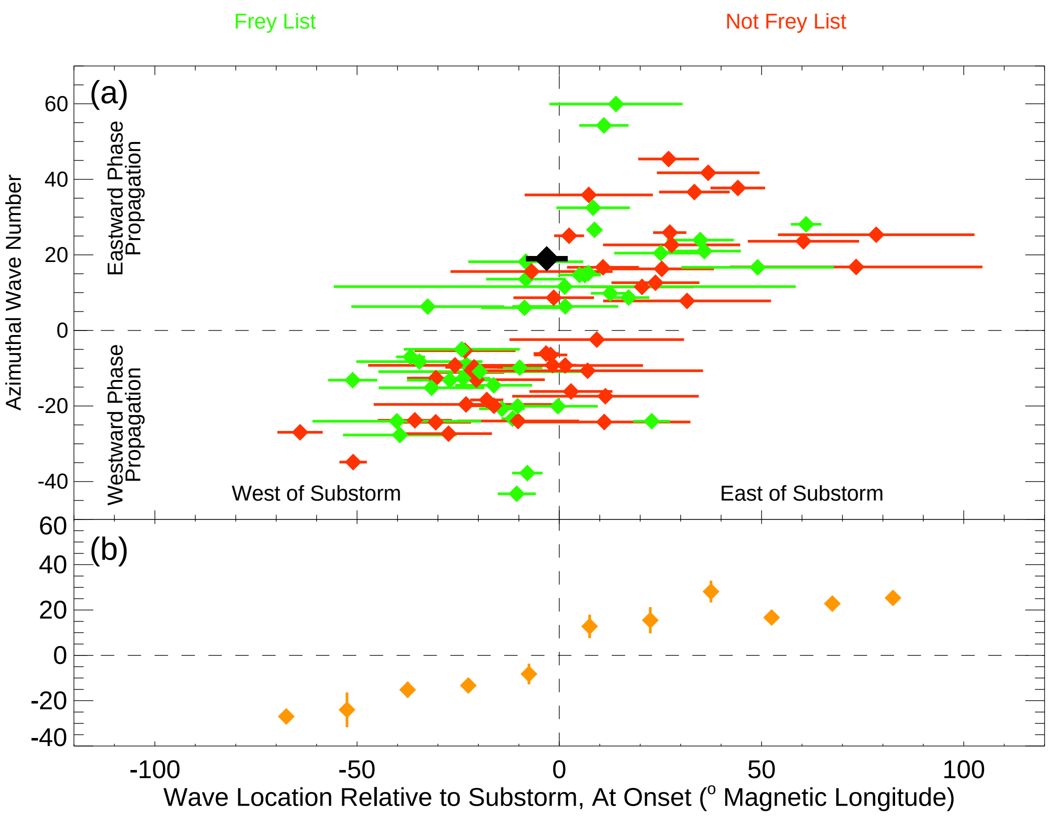

Figure 5.5: Azimuthal wave numbers - In panel (a) azimuthal wave numbers of each of the waves are plotted against the magnetic longitude separation of the waves with the substorm onset positions. Panel (b) shows the same data as in (a) but now placed into 15° magnetic longitude bins. The black diamond represents the *Yeoman et al.* (2010) event.

latitude and the latitudes used here are estimated as the middle of the range covered by the wave.

Also, in Figures 5.5 and 5.6, the event studied by *Yeoman et al.* (2010) is shown with a larger black symbol, where the azimuthal wave number was determined to be ~19 and the latitudinal phase gradient was ~-62. The latitudinal phase propagation of this wave event seen in Figure 5.6 shows a larger than average equatorward phase propagation although is fairly typical of the ensemble of wave events investigated here. The initial brightening of the substorm UV aurora for this case study appeared ~3° to the east of the observed wave. This data point does not fit in with the majority of the waves with positive m numbers as the wave, in this case, was observed slightly west of

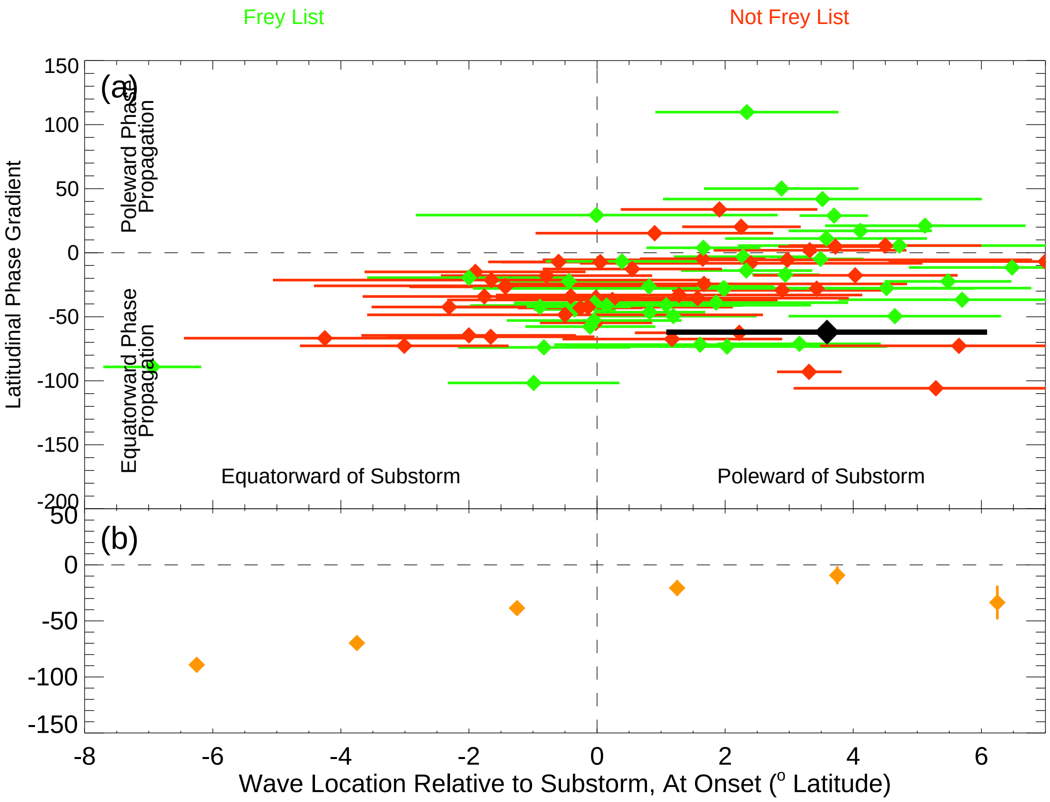

Figure 5.6: Latitudinal phase gradients - In panel (a) magnetic latitudinal phase gradient for each of the waves are plotted against the magnetic latitude separation of the waves from the substorm onset positions. Panel (b) shows the same data as in (a) but now placed into 2.5° latitude bins. The black diamond represents the *Yeoman et al.* (2010) event.

the substorm onset location. This wave event will be discussed further in section 5.6.1.

The periods of the waves studied are shown in the form of a histogram in Figure 5.7. They range from 200 to 3500 seconds, where the majority of the population exists within the range of 200 to 2000 seconds. The wave studied in *Yeoman et al.* (2010) had a period of ~600s which is typical for the distribution shown in Figure 5.7. It may also be noted that the most common range of wave periods observed in Figure 5.7 is 700-800 s which corresponds to one of the discrete field line resonance frequencies proposed by *Samson et al.* (1992). This long period was interpreted in *Yeoman et al.* (2010) as implying that the wave existed on stretched field lines in the night side of the magnetosphere. The long periods found from this statistical study could suggest a similar interpretation. An alternative interpretation can also be suggested. It is well known that the frequencies of poloidal waves are strongly controlled by the plasma pressure and ring current values in the plasmasphere where variations in the plasma density can alter the Alfvén speed (see Equation 2.42). In the magnetosphere with a strong ring current, the poloidal eigenfrequencies can be significantly lower than the toroidal eigenfrequencies (e.g., *Klimushkin et al.*, 2012).

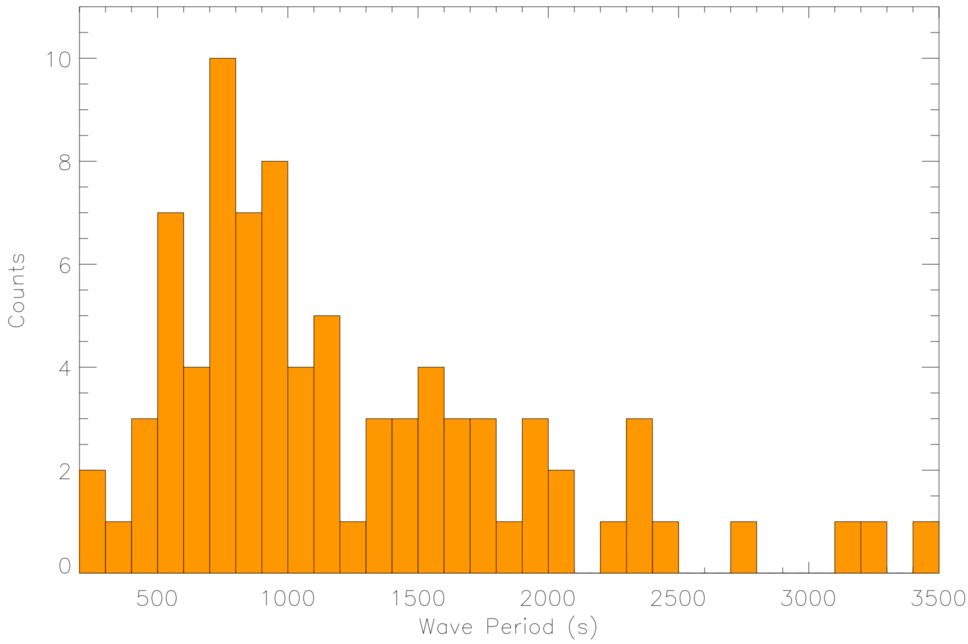

Figure 5.7: Wave periods - Histogram displaying the periods of the waves studied placed into 100s bins.

5.6 Discussion

The results from Figures 5.5 and 5.6 show that the phase propagation of the observed wave is dependent on the waves' position relative to where the substorm UV aurora occurs. This is most obvious in the case of the azimuthal wave number, where the phase fronts propagate azimuthally away from the substorm onset location, while the phase speed decreases in magnitude with increasing separation. The dependence of phase propagation on the separation of the substorm and the wave observation is somewhat similar when considering l, although poleward propagating waves are less commonly observed. In this case, the phase propagation becomes more strongly equatorward if the wave is observed farther equatorward of the substorm, but whilst there is some evidence of increased numbers of poleward propagating events poleward of the substorm, the average propagation remains equatorward. The low proportion of poleward propagating waves to equatorward propagating waves may be explained by the nature of the magnetic field lines in the vicinity of the wave. If equatorward propagating waves appear on closed field lines equatorward of the substorm, it may be expected that poleward propagating waves would exist on field lines poleward of the substorm, however at some latitude poleward of the substorm, these field lines would be connected directly to the IMF rather than being closed within the magnetosphere. These open field lines would not be excited by field line resonance in the same way as those which are closed, possibly explaining the low number of poleward propagating waves.

5.6.1 Substorm Evolution

The existence of small numbers of westward propagating waves east of the substorm and eastward propagating waves west of the substorm in Figure 5.5, along with the ~4 ° separation between the substorm latitude and the latitude where the majority of poleward propagating events are seen in could possibly be explained by the motion of the substorm events after the substorm expansion phase onset. Typically, after the initial brightening of the aurora during the onset of a substorm, the substorm would expand poleward while expanding azimuthally in both directions with the dominant azimuthal expansion being westward (*Akasofu*, 1964). The azimuthal expansion of the substorm may be predominantly to the east or west of the original onset position as observed by *Carbary et al.* (2000) and *Liou and Rouhoniemi* (2006). The statistical study undertaken by *Carbary et al.* (2000) revealed that 90% of the substorms in their study exhibited a poleward expansion, more then 60% expanded predominantly in the westward direction and ~35% expanded eastwards. The expansion of the substorm aurora will follow the evolution of the energetic particle injections as the substorm expansion proceeds. It is probable that the observed waves are most likely to be driven by the particles injected at the peak of the expansion phase when the auroras are at their most intense.

Figure 5.8 shows a comparison of m and the azimuthal separation of the observed waves and substorm UV auroras at the onset position, (a), and the position at the point where the substorm has expanded to its most intense auroral activity, (b) where the orange points are those which correspond to eastward expanding substorms, and green correspond to westward expansion. Red and blue squares in panels (a) and (b) show the orange and green data points (respectively) placed into 15° bins. While the use of the substorm position at the end of the expansion phase instead of the onset position alters the results slightly, there appears to be little change in the overall trend. The comparison of m with the azimuthal separation of the observed waves and the substorms at the peak of their expansion phases does, however, result in a smaller amount of overlap in the positive and negative m-number populations. For the event studied by *Yeoman et al.* (2010), again shown with a larger black symbol, the westward expansion of the substorm aurora moved the centre of the substorm responsible for driving the wave ~14° westward across to the opposite side of the radar's field-of-view. This expansion shifts the relative longitudinal location of the wave and substorm, such that the location of the substorm west of the wave observation and eastward azimuthal phase propagation of the wave become consistent, as was noted in *Yeoman et al.* (2010).

If we consider the poleward expansion of the substorms, the l values in Figure 5.6 can be replotted against the latitudinal separation of the waves with the expanded substorms. This is shown in panels (c) and (d) of Figure 5.8 where panel (c) uses the substorm onset position (as in Figure 5.6) and panel (d) uses the position at the peak intensity of the substorm UV aurora. Green data points in both plots are the l values for each event plotted against latitudinal separation of the substorms and the observed waves, while red squares show the same data after being placed into 2.5° bins. Panels (c) and (d) of Figure 5.8 shows that, while the data points are still very scattered as in Figure 5.6, the general trend suggested by Figure 5.6 is still apparent, but with a general poleward shift in the position of the data points.

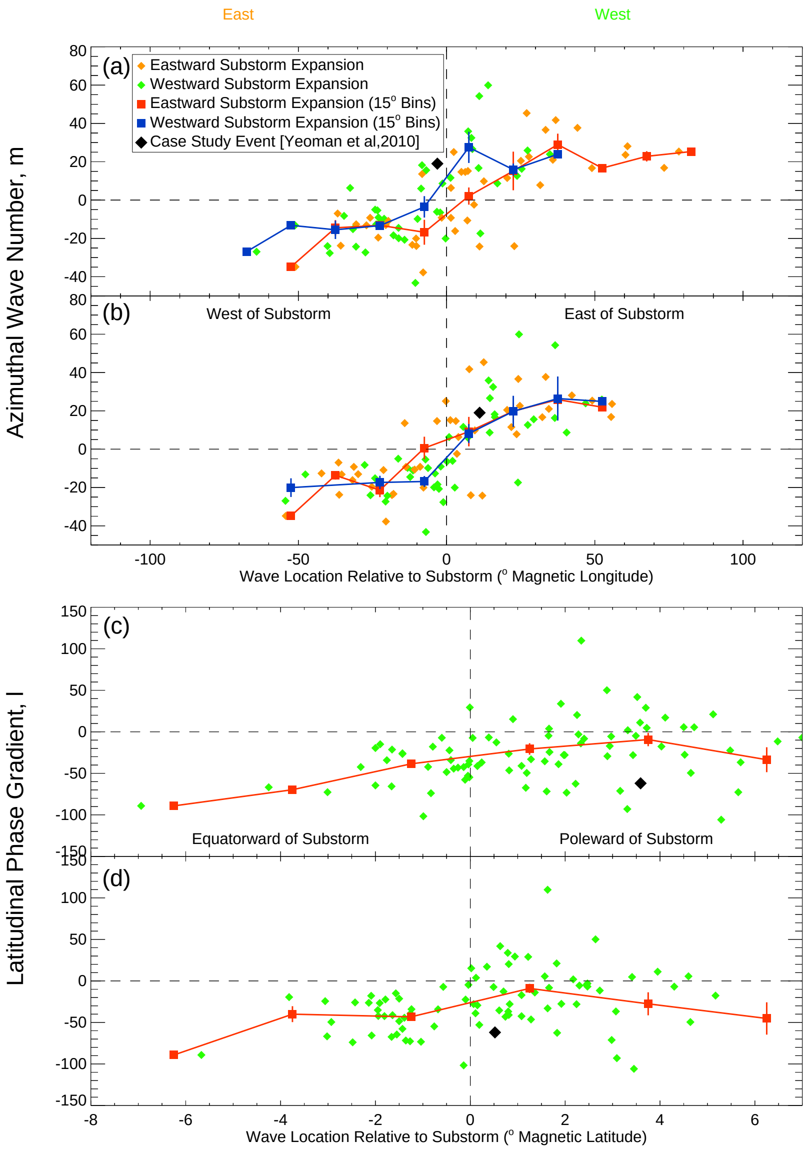

Figure 5.8: Comparison before and after expansion - (a) Azimuthal wave numbers of each of the waves plotted as a function of distance from the substorm in a similar manner to Figure 5.5 using substorm onset position for comparison with (b) which shows m relative to the wave location when the substorms have expanded to their largest size. Green data points represent events in which the substorms have expanded in the westward direction while orange data points represent eastward expansion. Panels (a) and (b) also show the eastward expanding (red) and westward expanding (blue) events placed into 15° bins shown by square symbols. Panels (c) and (d) show latitudinal phase gradient, l, against latitudinal separation of the substorm UV aurora and the observed wave in green at the substorm onset time (c) and after expansion (d). Red square points in (c) and (d) represent the green data points when placed into 2.5° bins. The black diamond represents the *Yeoman et al.* (2010) event in all panels.

5.6.2 Notes on the Generation Mechanism

The results presented in this chapter show that substorm-injected particles can effectively generate the ULF waves. The westward drifting protons generate the wave west of the substorm onset, and eastward drifting electrons generate the wave east of the onset as illustrated in Figure 5.9. For this situation, a theory of wave generation by non-stationary currents associated with the moving source can be more relevant (*Mager and Klimushkin*, 2007, 2008). As a driving mechanism, the drift-bounce Alfvénic instability has usually been suggested for the particle-driven waves. This instability develops when particles of angular frequency ω exchange energy with waves under the drift-bounce resonance condition, Equation 2.70 (page 51; *Southwood et al.*, 1969), where ω_d is the angular drift frequency, ω_b is the angular bounce frequency, and N is the bounce harmonic number. Usually, an instability due to a non-monotonic particle distribution function is invoked (*Hughes et al.*, 1979; *Baddeley et al.*, 2005a,b), although instabilities due to sharp spatial gradients of the distribution function (*Takahashi et al.*, 1990) and temperature anisotropy (*Pokhotelov et al.*, 1985; *Klimushkin and Mager*, 2012) can also be significant.

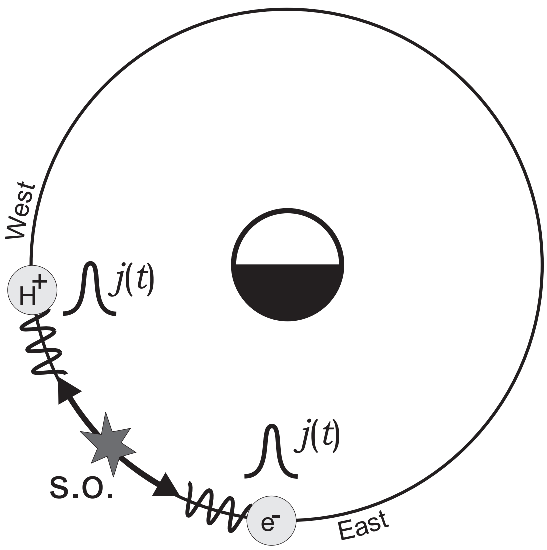

Figure 5.9: Particle populations drift east and west of substorm onset - Schematic illustration of the interpretation of the event considered in the chapter: clouds of protons H^+ and electrons e^- generate waves west and east of the substorm onset. Also shown are the non-steady currents $j(t)$.

The theory of drift-bounce instability has been developed for the case of a stationary and axisymmetric distribution function of driving particles. Clearly this is not the case for the present work, where the driving particles are supposed to appear in the magnetosphere during the substorm injection and form a moving cloud limited in the azimuthal coordinate. At a given location of the azimuthal coordinate, the wave is generated when the cloud reaches this point. The event observed by *Yeoman et al.* (2010) was interpreted in terms of the theory of *Mager and Klimushkin* (2007, 2008). The event observed by *Yeoman et al.* (2010) was interpreted in terms of that theory. To date, this theory has been elaborated for the case when the field aligned structure of the cloud of injected particles is settled much faster than the characteristic Alfvénic time, which assumes the inequality $\omega \ll \omega_b$ to hold. In this case, the wave frequency must satisfy the condition

$$\omega - m\omega_d = 0, \tag{2.71}$$

which can be formally obtained from Equation (2.70) for the case of drift resonance ($N = 0$).The L-dependent arrival of drifting injected particles at observational meridian can explain the apparent equatorward phase propagation of pulsations observed with radars (*Mager et al.*, 2009). For each event studied here, the dominant frequency was typically the same everywhere within the radar's field-of-view. Thus it appears that only a narrow range of particle energies within the particle injection are contributing to the wave growth for each individual event.

It is interesting to find analogies of the substorm generated waves reported in this chapter among the high- and intermediate-m waves reported in earlier publications. *Zolotukhina et al.* (2008) reported Pc5 waves with strong poloidal component observed after a substorm onset with satellites located east and west of the substorm onset location. It was suggested that the satellites detected the waves generated by substorm injected clouds of charged particles drifting in the magnetosphere in opposite azimuthal directions: a satellite located east (west) of the onset detected the wave generated by an electron (proton) cloud. This interpretation was confirmed by the energetic particle data recorded by LANL satellites. In the course of the event, the wave polarization changed as expected from the theory (*Mager and Klimushkin*, 2008).

Using ground data, *Pilipenko et al.* (2001a,c) studied Pi3 pulsations which appeared during the main phase of an intense magnetic storm. They found two regions of ULF activity, one observed in the early morning hours, the other near dusk. The first one was interpreted as being related to an energetic electron injection, whereas the second was due to the injection of ring current protons. Fluctuating current developed during a storm was suggested as a generation mechanism (*Pilipenko et al.*, 2001a). This interpretation is in accordance with the moving source theory of *Mager and Klimushkin* (2007, 2008): in both cases the waves are supposed to be driven by a non-steady current, which constitutes a source term in the wave equations.

It cannot be excluded that Pi3 waves observed on the ground, like those described in (*Pilipenko et al.*, 2001a,c), represent a part of the Pc5 wave spectrum with moderate m numbers. At least, *Vaivads et al.* (2001) found a correspondence between Pc5 waves observed in space and a Ps6 wave observed on the ground (note that Ps6 waves represent a subclass within the Pi3 band). The waves reported in the present study also might be categorized as Pi3 pulsations, similar to those published in *Pilipenko et al.* (2001a,c), although no radar features of those Pi3 pulsations have been reported in those publications.

An interesting feature of the present study is the possibility that relatively low-m waves can be generated by energetic particles in the same way as high-m pulsations. This is in apparent contradiction with the common and well established opinion that low-m shear Alfvén waves are generated by the fast modes propagated into the magnetosphere from the magnetopause, where they are generated by processes external to the magnetosphere. However, it has been noted that by virtue of the field line non-uniformity of the magnetosphere shear Alfvén and fast modes have a rather different spatial structure and their coupling can be rather weak (*Leonovich*, 2001). Also, some other observational confirmations that Pc5 waves with $m \sim 1$ can be generated by particle injections were found earlier in *Saka et al.* (1992, 1996). Another apparent contradiction with the common view of low-m waves is the strong poloidal component of the observed pulsations, even of those with $m \sim 1$. It is usually supposed that low-m Alfvén modes are always toroidal. However, this can be true only in the case of an external monochromatic driver, while the modes reported here are generated by an impulsive process. Newly generated low-m shear Alfvén waves can have the poloidal or mixed polarization, and only in the course of their evolution due to phase mixing does their polarization become toroidal (*Radoski*, 1974).

5.6.3 Driving Particles

Independently of which of the two driving mechanisms mentioned in the previous subsection (instability or moving source) is invoked for the pulsations observed in this study, the similarity of the wave characteristics for eastward and westward propagating waves in Figure 5.5 suggests that the drift resonance condition in Equation (2.71) is appropriate for both eastward and westward propagating waves. In this case, the angular drift frequency ω_d can be calculated from the equation

$$\omega_d = \frac{\omega}{m}. \tag{5.2}$$

When this is the case, a westward propagating wave such as that in Figure 5.3 would require a population of westward drifting ions to be the source of the wave's energy and, as in *Yeoman et al.* (2010), an eastward propagating wave would be associated with eastward drifting electrons.

The result of invoking the drift resonance condition for all of the waves observed, such that, by combining their frequency and m-number, they can be related to the azimuthal angular drift frequency of the particles that drive, them is shown in Figure 5.10. Here where ω_d is expressed in terms of the azimuthal separation of the wave and the expanded substorms. From this, it becomes apparent that two distinct populations of waves exist where one is driven by eastward drifting particles, and the other by westward drifting particles. The direction of the particle drift in a dipolar magnetic field is dependent on the particles charge which implies that the eastward and westward propagating waves would be associated with clouds of eastward drifting electrons and westward drifting ions respectively. There is also a notable trend in the magnitude of the particle drift speeds where particles that have drifted farther from their initial injection point (i.e. are driving waves at larger longitudinal separations from substorm onset) tend to be drifting considerably more slowly than those nearer the substorm. An explanation for the reduction in ω_d with larger azimuthal separations is suggested later in this section. This reduction in $|\omega_d|$ is obvious in the case of both electrons and ions, and fits with the apparent increase in $|m|$ that is suggested by equation 5.2 and was observed in Figure 5.5.

This analysis can then be taken further to estimate the energy of the drifting particles by using Equation 2.73, where W is the particle energy, L is the L-shell, B_s is the

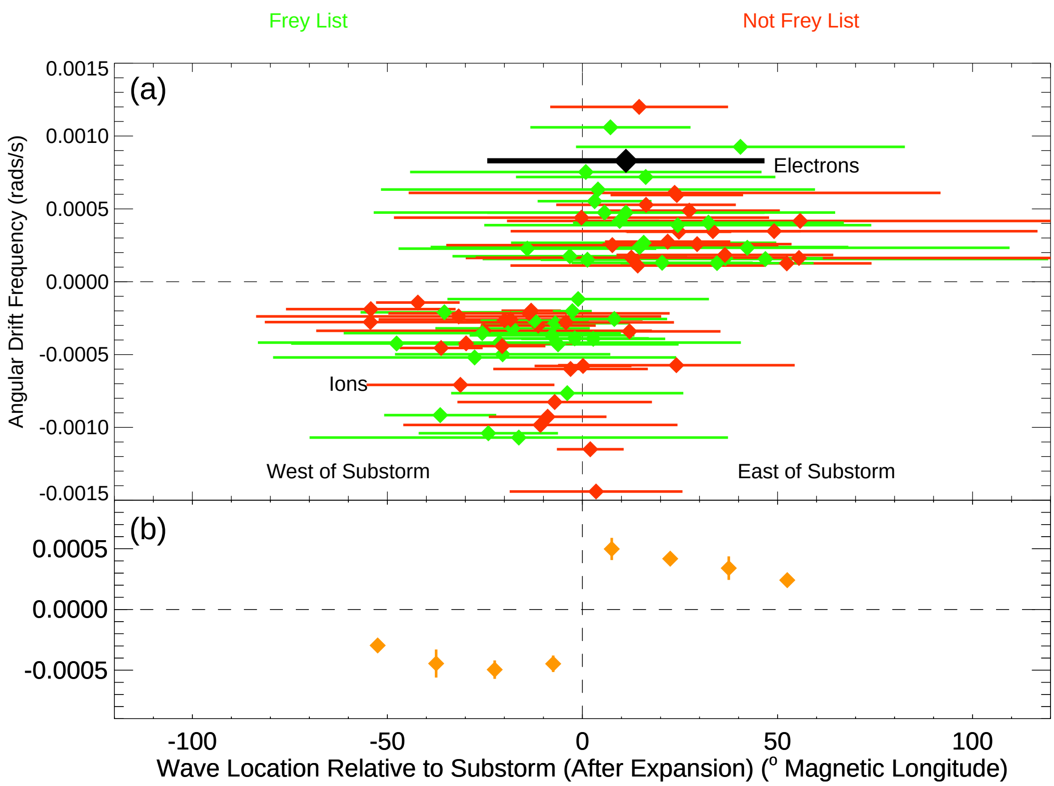

Figure 5.10: Angular drift frequencies - Panel (a) shows angular drift frequencies calculated from the periods and azimuthal wave numbers for each of the waves, where positive values are defined to be eastward and negative westward. (b) shows the same data as in (a) which has been placed into 15° magnetic longitude bins. The black diamond represents the *Yeoman et al.* (2010) event.

equatorial magnetic field strength, α is the equatorial pitch angle, K_p is the planetary magnetic activity index, R_E is the Earth's radius and ϕ is the azimuthal position of the particle from local midnight (*Yeoman and Wright*, 2001). For the case study presented in Section 3.1 where $\omega_d = -4.3 \times 10^{-4}$ rad s $^{-1}$, this implies an energy range of ~24 to 29 keV over the latitudinal extent of the wave in Figure 5.3 ($L \sim 6.5 - 7.5$) or ~26.7 keV at the central L shell ($L \sim 7$) where large pitch angles (α ~90°) are used.

Figure 5.11 shows the estimated particle energies for each of the 83 events calculated using equation 2.73 in the same format as Figure 5.10. There is a significant drop in the particle energy, W, for the events which occurred with a larger azimuthal separation compared to those nearest to the substorms. This reduction in W with azimuthal separation fits with the reduction in $|\omega_d|$ as would be expected from equation 2.73. In Figures 5.10 and 5.11, the event studied by *Yeoman et al.* (2010), shown with a larger black symbol, can be seen to be fairly typical of the ensemble of wave events investigated here.

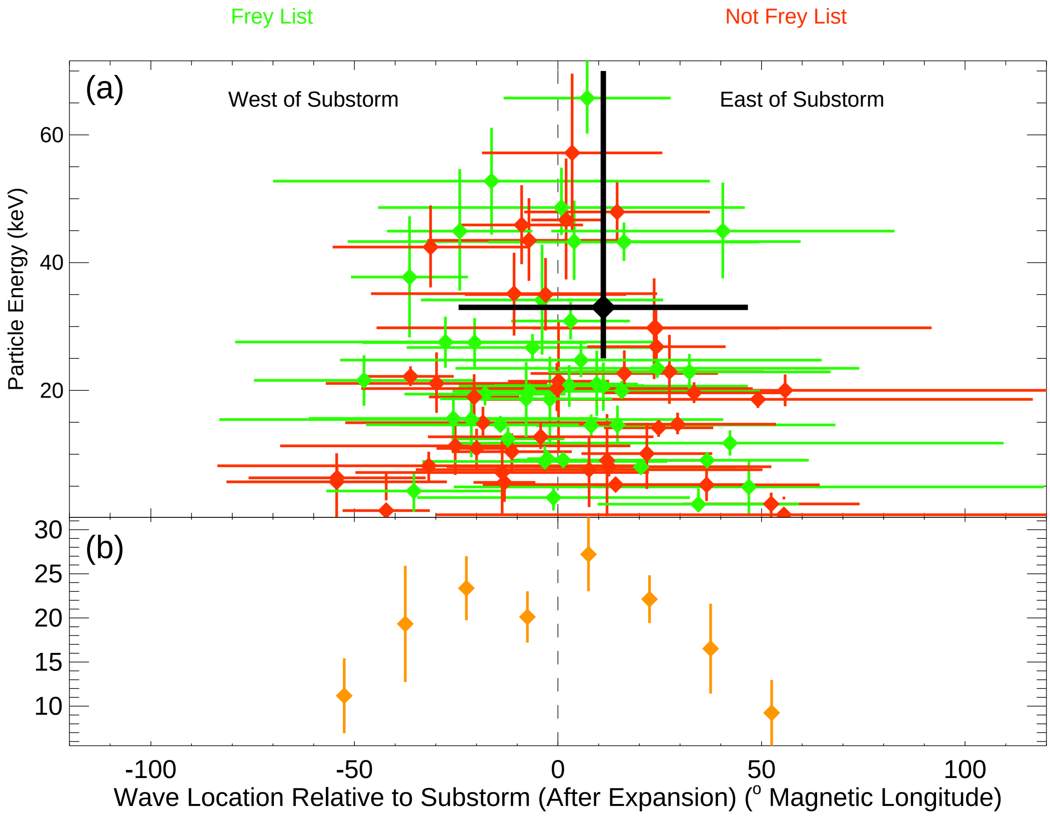

Figure 5.11: Estimated particle energies - (a) Calculated particle energies for each of the events plotted against the azimuthal separation between waves and their associated substorm positions. (b) shows the same data as in (a) which has been placed into 15° magnetic longitude bins. The black diamond represents the *Yeoman et al.* (2010) event.

Yeoman et al. (2008) suggested that the particle energy may be related to the L-shell of the wave observation with the results in Table 3.1. Figure 5.12 shows the particle energies calculated for the 83 ULF waves in this study against the L-shell of the wave observation. The black line in the plot shows the average of every 10 points in order of energy. It appears that the lower energy events (0 - 20 keV) show some trend of decreasing in energy with an increase in L, though it is not the case for events over 20 keV. The large spread in the events, especially over 20 keV, is likely due to the various different parameters involved in calculating the energy. As is seen in Equation 2.73, the energy is likely to decrease with an increase in L-shell, but parameters such as K_p, m and ϕ could potentially have a large enough impact to obscure any trend with L by creating scatter in the results.

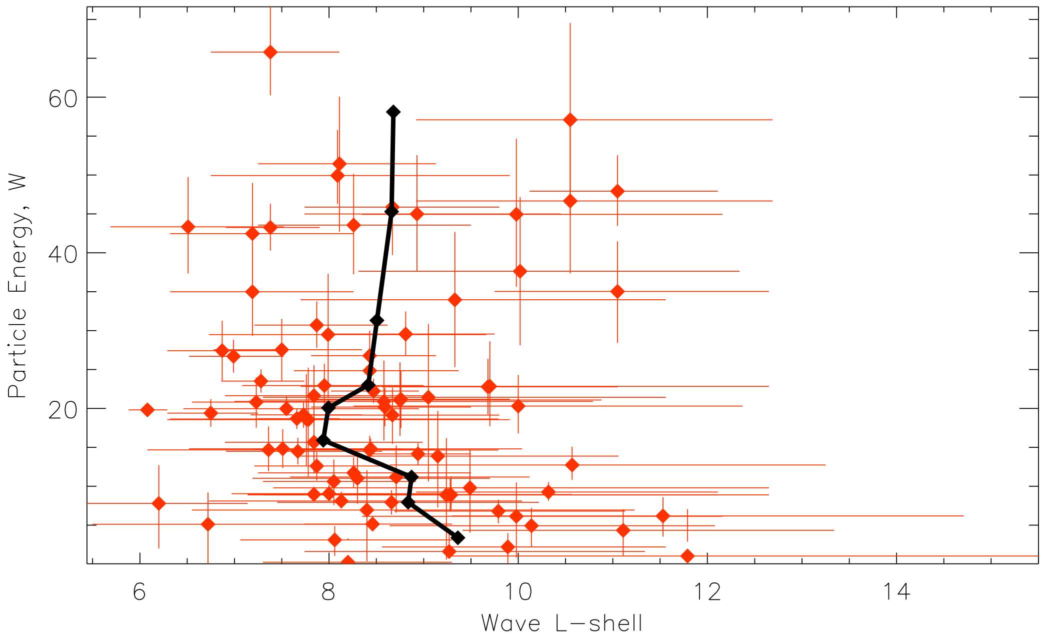

Figure 5.12: L-shell comparison - Estimated particle energies for the events in this study plotted against the L-shell of the wave observation. The black line represents the average values for every 10 data points in order of energy.

A possible explanation for the trends defined by Figures 5.10 and 5.11 would be that higher energy particles injected into the inner magnetosphere during a substorm have less time to drive waves as they gradient-curvature drift around the planet before they are lost by some process, perhaps escape through the duskside magnetopause (*Takahashi and Iyemori*, 1989). This would leave the particles with lowest energies (and thus the lowest angular drift frequencies) to drift farther from where they were injected, thus allowing them to drive higher-m waves as suggested by *Yeoman et al.* (2010).

The angular drift frequency calculated for the particles responsible for driving the wave in Figure 5.3 can be used to back-track the azimuthal location of the particles prior to the formation of the wave within the radars field-of-view. Figure 5.2 shows the result of this back-tracking of the driving particles where the estimated MLT is displayed as a green meridional line of constant MLT in each panel. The particles, calculated above to have an energy of ~26.7 keV are injected at ~22.3 MLT in Figure 5.2 (a). They then drift westwards and their subsequent locations are shown in panels (b)–(f), passing through the radar field-of-view between 1858 and 1910 UT. When displayed in this manner it appears that the initial driving particles are those near the eastern-most edge of the substorm expansion, which drift farther westward towards the radar field-of-view as the substorm expands. Subsequent to the start of the wave, particles continue to be injected to the east of the radar, where they can also drift westwards and continue to drive the wave after the initial particles have passed completely over the radar field-of-view.

As illustrated in Figure 5.2, a time lag is expected to be present between the time of particle injection during the substorm and the time of arrival of the recently injected particles after they drift across the radar field-of-view to drive the observed waves. This time lag would be expected to be a function of ω_d (and therefore particle energy) and also the azimuthal separation of the substorm and the observed wave, as particles with lower angular drift frequencies and larger distances to travel would be expected to take longer to reach the radar location than those with high values of ω_d and smaller azimuthal separations. The time lag expected from the calculated ω_d combined with the azimuthal separation of the wave observation and the substorm location (when the UV aurora of the substorm is at its most intense) is displayed in Figure 5.13 and is plotted against the observed time lag. The orange data points represent those values calculated from positive values of ω_d and the green are from negative ω_d. The data has also been placed in bins (shown in blue in Figure 5.13) to show the overall trend, these bins each contain 10 data points except for the final data point, which contains only the remaining 3. The calculated time lag increases in magnitude with the observed time lag as expected. However, there are a number of values with negative expected time lags. These arise from the overlapping portion of data points in Figures 5.5 and

5.10 where it is likely that the estimated position of the centre of the substorm is not exactly where the driving particles originate from. There are also a number of events where the observed time lag is small but their predicted time lags are too large. This may be attributed to uncertainties in the estimated particle energies or uncertainty in the relative locations when wave observations are made close to the substorm onset.

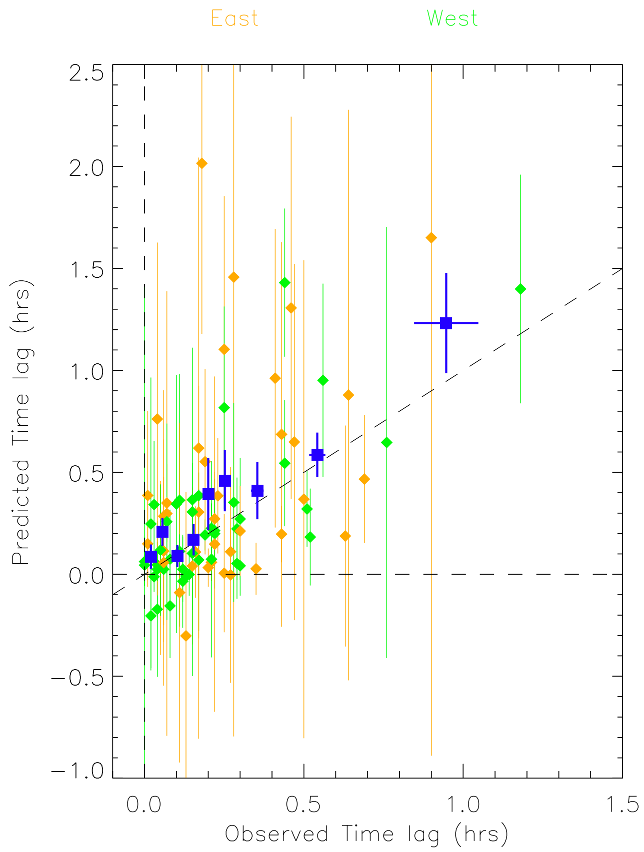

Figure 5.13: Time lags - Time lag expected between particle injection and wave observation calculated from ω_d and the azimuthal separation of the substorm (at the time the UV aurora for the substorm reaches its most intense) and the observed wave, plotted against the observed time lag. Yellow points are those obtained from positive values of ω_d and green are negative. Blue data points represent the same data placed into bins, the first 8 of which contain 10 data points each and the last containing the remaining 3.

5.7 Summary

Using multiple SuperDARN radars (Hankasalmi, Saskatoon, Goose Bay, and Kapuskasing), 83 poloidal ULF wave events with m numbers from 2 to 60 were identified. These are interpreted as waves generated by particles injected during the substorm onsets identified partly by *Frey et al.* (2004) and partly by ourselves from the IMAGE FUV data. The eastward and westward phase propagations of these events have been associated with eastward drifting electron and westward drifting ion populations respectively. The angular particle drift velocities were determined with the drift resonance condition (Equation 5.2) as well as from the time lag between the wave events and the substorm onset, using the azimuthal separation of the wave observations and the onsets. Both estimates are in a good agreement, which confirms the suggestion that the observed waves were generated by the substorm-injected azimuthally drifting ion/electron particle clouds.

Previously, only a few such cases have been reported (*Chisham et al.*, 1992; *Wright et al.*, 2001; *Zolotukhina et al.*, 2008). Another novel feature is the large number of electron-related poloidal wave events. Such events are rare in published literature (*Eriksson et al.*, 2006; *Zolotukhina et al.*, 2008; *Yeoman et al.*, 2010; *Belakhovsky and Pilipenko*, 2010). Further more, it should be underlined that some of the observed waves had relatively low m numbers, which hints that some of the low-m Alfvén waves reported in the earlier literature could be generated by internal magnetospheric processes, possibly by energetic particles, rather than by the resonant interaction with the fast modes propagating from the magnetopause, as is usually supposed.

These observations can be interpreted in two ways: first, in terms of wave-particle drift resonances invoking kinetic instability theories (*Southwood et al.*, 1969), and second, in terms of the moving source theory (*Mager and Klimushkin*, 2007, 2008). The previous observation of a poloidal wave with eastward phase motion by *Yeoman et al.* (2010) suggested the second option, as did several other case studies (*Zolotukhina et al.*, 2008; *Yeoman et al.*, 2012). We can suppose that these two mechanisms can work simultaneously, that is, the moving source of substorm-injected particles can provide an oscillation seed which will be further amplified by means of the instability. However, the theory of such combined driving mechanism has not been developed to date.

The magnitude of the azimuthal wave number tends to increase when the waves are observed at larger azimuthal separations from the substorms. This, in-turn, corresponds to lower angular drift frequencies as shown in Figure 5.10, which is then reflected in lower particle energies in Figure 5.11. This reduction in particle energy farther from the substorm implies that, as these particle populations gradient-curvature drift away from the point at which they were injected, the higher energy particles are lost relatively quickly, leaving behind particles with lower energies to drive higher-m waves.

The latitudinal phase propagation (l) behaviour is less clear. While there is a large amount of scatter in the data, with a large bias towards the observation of equatorward propagating waves, Figure 5.6 and panels (c) and (d) of Figure 5.8 hint that l may be somewhat dependent on the latitudinal separation of the observed wave and the substorm. This possible trend appears to be similar in nature to that of m where the phase direction points away from the expansion of the substorms, however it is only apparent with equatorward propagating waves exhibiting a larger magnitude of l when they are observed farther equatorward from the substorm and is most certainly not conclusive with the data at hand. The only explanation of the equatorward phase motion developed to date is provided by the moving source theory of *Mager and Klimushkin* (2008); *Mager et al.* (2009). The moving source consists of an injection of energetic particles on a range of L-shells where the particles on the outermost field lines gradient-curvature drift around the planet faster than the particles on inner L-shells - stretching the injected cloud of particles into a spiral. This leads to the particles driving waves on field lines which map down to higher latitudes in the ionosphere first, then exciting waves at successively lower latitudes - thus forming the apparent equatorward phase propagation observed in Figures 3.18 and 5.3.

It is clear that the phase propagation characteristics of the observed waves is heavily dependent on the azimuthal separation of the substorm and the wave itself, as suggested by *Yeoman et al.* (2010), where it appears that phase fronts propagate in a direction pointing away from where the particles are injected and the time lag between substorm onset and wave observation is also a function of this separation and m. In the case of m and l it appears that it may be more appropriate to consider the position of the substorm once it has reached the peak of its expansion phase, where there is the highest flux of injected particles.

Chapter 6

Multi-Radar Observations of Substorm-Driven ULF Waves.

6.1 Introduction

In the previous chapter, we discussed the effect of proximity of the wave observations to the substorm on the observed waves. It was shown that the sign of the azimuthal wave number, m, is affected such that positive-m waves typically occur in waves observed to the east of the location of the substorm and negative-m waves occur to the west of the substorm. There was also evidence to suggest that the magnitude of m varied with the distance between the location at which particles are injected and the location where the wave is observed. This was such that high-m waves often occur farther from the substorm and relatively low-m waves appear much closer to the epicentre of the substorm.

This dependence was also evident with the calculated angular drift frequencies, ω_d, associated with the waves. The sign of ω_d behaves in the same way as that of m, but unlike m, the magnitude of ω_d generally decreases with the azimuthal separation between the substorm and the wave. This decrease in ω_d was reflected in the particle energies associated with the wave-driving process, derived using Equation 2.73, where it was apparent that higher particle energies were calculated for events which were closer to the substorm.

Each of the events presented in the previous chapter consisted of a single wave observation associated with each substorm. As such there is no clear indication as to whether these trends would be reflected by each individual event. In this chapter we address this issue by studying three events where data from multiple SuperDARN radars were available to diagnose the wave events at different azimuthal separations during three different substorms to ascertain whether $|m|$ increases in magnitude with distance and whether highest energy particles appear closest to the substorms in individual events and to establish whether, in a single substorm, a range of particle energies can drive waves with a range of phase characteristics to the east and west of the substorm.

6.2 Instrumentation

To study each these three events we used data from various SuperDARN (Super Dual Auroral Radar Network, (*Greenwald et al.*, 1995; *Chisham et al.*, 2007)) radars located in North America and Iceland. For event 1 we observed ULF waves using the Kapuskasing (kap), Saskatoon (sas) and Kodiak (kod) radars as described in section 6.3.1. In event 2 we used Prince George (pgr) and Kodiak (kod) as presented in section 6.3.2. Finally, in event 3 we used Þykkvibær (pyk), Stokkseyri (sto), Saskatoon (sas) and Prince George (pgr), as presented in section 6.5.

Events 1 and 2 are associated with substorm expansions taken from a list of substorms originally identified by *Frey et al.* (2004) using the FUV (Far Ultraviolet Imager) instrument onboard the IMAGE (See Section 4.3; *Mende et al.*, 2000a,b) spacecraft. The list used was an updated version of their original list which contains the time and location of 4193 substorm events between May 2000 and December 2005. Here we use the IMAGE FUV data to track the location of the substorms as they expanded after onset as discussed in sections 6.3.1 and 6.3.2.

In event 3 the substorm was identified by means of the CARISMA/CANOPUS fluxgate magnetometer network (See Section 4.4.1.2; *Mann et al.*, 2008). The substorm itself was identified within a list of substorm Pi1 and Pi2 onsets detected using the Pinawa (PINA) flux gate magnetometer in Manitoba (*Mann et al.*, 2008).

Additional ground based magnetometers from CARISMA/CANOPUS, IMAGE (*Lühr*, 1994), SuperMAG and INTERMAGNET (See section 4.4) were used in each of the three events to locate the ionospheric footprint of the Substorm Current Wedge

(SCW, (*McPherron et al.*, 1973)) associated with the substorms, where the baseline was removed from each of the datasets as outlined in Section 4.4.2.

We compared the SCW of 27 substorms with the IMAGE FUV data, to ensure that using magnetometers to infer the substorm location did not introduce any systematic offset in the substorm location identification, as in event 3 the magnetometer data alone were used to identify the substorm location (as shown in Section 6.4 on page 145), as this event did not occur during the lifetime of the IMAGE spacecraft.

6.3 Data

Substorms to be analysed were selected from the above list such that their onset location occurred within ~50° magnetic longitude of the field of view of any of the SuperDARN radars that were operational at the time of the substorm. Data from nearby radars were surveyed in order to find events in which ULF pulsations occurred following the onset of each substorm. The list of substorms was then reduced to only include those where waves, for which it was possible to perform reliable Fourier analysis upon, could be observed at multiple locations by different radars. Finally, each event where there were multiple substorms and those in which it was not possible to confidently locate the substorm onset and expansion using IMAGE FUV were eliminated to reduce the ambiguity in the location of particle injection. Two events remained where there were multiple wave observations at a range of longitudinal separations relative to their associated substorms.

In order to track the size and location of the substorm in both events, the background and dayglow of the auroral images provided by IMAGE FUV was removed, as discussed in Section 4.3.2. Then the approximate longitudinal and latitudinal limits for each image of the auroral substorm were defined by a threshold where the auroral intensity drops below ~5 % of its most intense value for the entire expansion phase. The 5 % threshold was found to be reliable enough to allow the removal of most background auroral features without the removal of the initial brightening of the UV aurora at the time of substorm onset.

Fourier analysis was used to determine the dominant frequency for each of the ULF waves observed, which was typically the same everywhere that the wave could be seen within an individual radar's field-of-view. The azimuthal phase propagation for each wave was derived from the Fourier phase values at the dominant frequency of the wave, taken from several range gate and beam combinations covering a range of magnetic longitudes, while remaining approximately constant in magnetic latitude. The azimuthal wave number was then calculated as the gradient of Fourier phase as a function of magnetic longitude.

6.3.1 Substorm Event 1, November 24th 2000

6.3.1.1 Substorm Observations

The substorm UV aurora measured by the IMAGE FUV instrument are presented in Figure 6.1 in magnetic latitude - magnetic local time coordinates, where noon is at the top of each panel, magnetic latitude is represented by concentric circles in 10° increments and MLT is displayed in 1 hour increments. Substorm onset occurred at ~04:21 UT on 24^{th} November 2000 over Canada with the UV aurora expanding and strengthening over the next ~40 minutes. The ground instrumentation used to investigate the wave activity generated by the substorm is also shown in Figure 6.1 in which the approximate location of the substorm at the time of onset given by *Frey et al.* (2004) is represented by a black box just west of local midnight. The latitudinal and longitudinal limits of the box are defined by where the number of WIC counts reaches ~5% of the peak counts observed during the substorm. This figure shows that the fields of view of the three radars used are all west of the substorm, where results in Chapter 5 would suggest that each of these waves should have a westward phase propagation.

6.3.1.2 Wave Observations

Figure 6.2a shows the line of sight velocity as measured by the Kapuskasing radar between 04:20 – 05:00 UT as a function of magnetic longitude, where red represents flow velocities moving away from the radar and blue towards. Oscillations in the measured velocity, with a period of ~700 seconds (a frequency of 1.4 mHz), became apparent in the radar data shortly after the onset of the substorm (04:21 UT) at around 04:23 UT, as would be expected due to the very close proximity of the radar to the substorm as seen in Figure 6.1. The repeating black lines in Figure 6.2a are derived from the Fourier analysis of the wave and represent the wave 'crests' as calculated

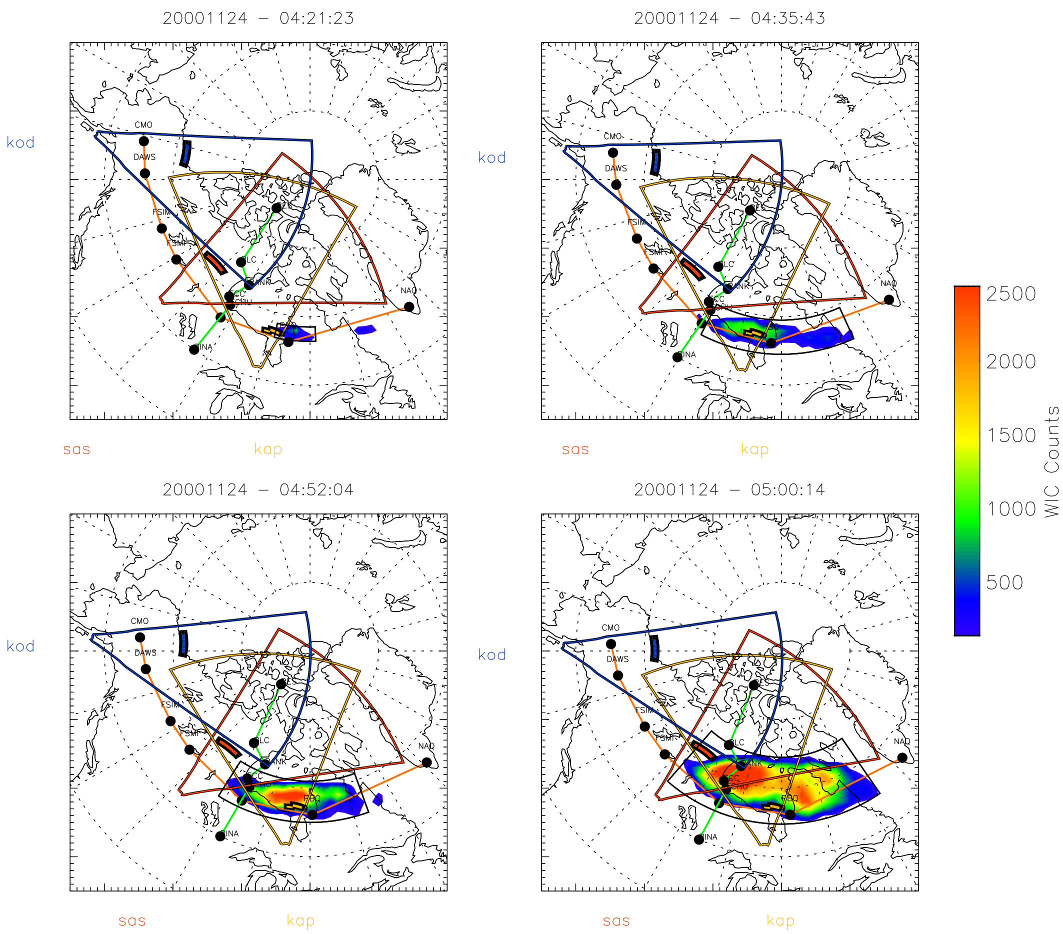

Figure 6.1: IMAGE data - 24th November 2000 - IMAGE FUV data during the substorm expansion phase shortly after onset on 24th November 2000 at 04:21 UT. Data is shown for the northern hemisphere and is oriented such that noon is at the top of each panel and dawn to the right where concentric circles represent magnetic latitude in 10° intervals and magnetic local time is displayed in 1 hour intervals. IMAGE auroral data is shown for where the intensity is greater than 5% of the maximum intensity during the entire substorm event where green corresponds with low intensity aurora and red is the most intense. The figure includes the locations of the radar fields of view of Kodiak, Alaska (kod, blue); Saskatoon, Canada (sas, red); and Kapuskasing, Canada (kap, yellow) along with the two chains of magnetometers used. The radar beams and range gates used to characterise the waves are highlighted in each field of view in the colour of the radar which they correspond to. The black box present just before local midnight shows the approximate latitudinal and longitudinal extent of the substorm UV aurora. The time stamp for each image is displayed above each panel. The green and orange lines connecting magnetometers will be discussed in section 6.4.

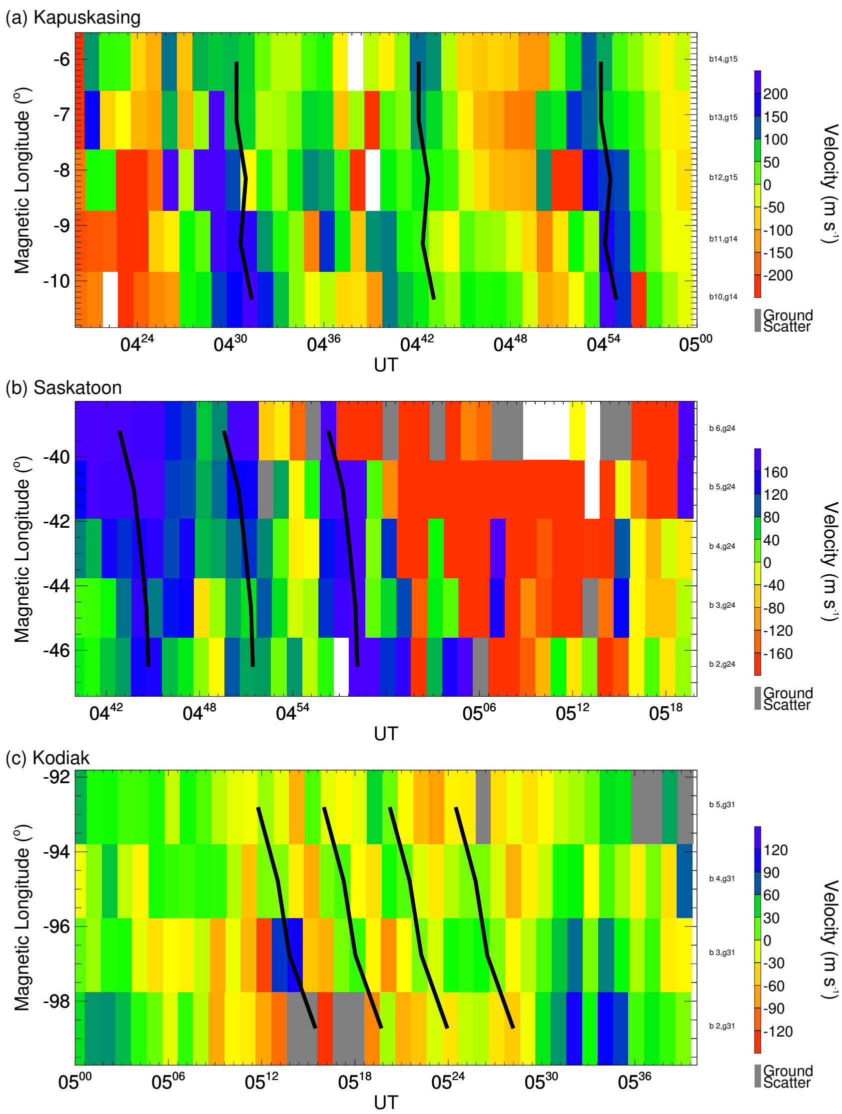

Figure 6.2: ULF waves - 24th November 2000 - Colour coded radar measurements of the line-of-sight velocity as observed by (a) Kapuskasing, from 04:20 – 05:00 UT; (b) Saskatoon, from 04:40 – 05:20 UT; and Kodiak, from 05:00 – 05:40 UT on 24th November 2000 in universal time - magnetic longitude coordinates, following the substorm onset at 04:21 UT depicted in Figure 6.1, where blue corresponds to flow towards the radar and red away from the radar. Panels (a), (b) and (c) show oscillations in the velocity which each exhibit westward phase propagation at 1.47, 2.50 and 3.51 mHz respectively where black lines indicate the wave crests as determined from the Fourier phase of the wave at their corresponding frequencies.

from the Fourier phase at the dominant frequency of the wave. The azimuthal wave number, m, of this wave calculated from the Fourier phase is -6 which corresponds with a westward phase propagation, as expected.

Figure 6.2b presents data from the Saskatoon radar in the same format as Figure 6.2a, but now for a slightly later time interval of 04:40 – 05:20 UT. Wave activity is detected in the Saskatoon radar data between 04:40 and 05:00 UT, starting approximately 20 minutes after the onset of the substorm at 04:21 UT. In this case Fourier analysis of the wave revealed a period that was somewhat lower than that previously observed at Kapuskasing at ~400 s (a frequency of 2.5 mHz). This wave exhibited westward phase propagation, as at Kapuskasing, but the azimuthal phase propagation at Saskatoon was more rapid, with a derived azimuthal wave number, m, being slightly larger at ~-15.

Figure 6.2c shows data from the Kodiak radar in the same format as 6.2a and 6.2b, with an even later time interval of 05:00 – 05:40 UT. Wave activity was present from ~05:12 UT where Fourier analysis revealed a lower wave period than both the waves observed using Saskatoon and Kapuskasing at ~285 seconds (a frequency of 3.5 mHz). With an azimuthal wave number of $m = -44$, this wave exhibited a more rapid westward phase propagation than those at Kapuskasing and Saskatoon.

The azimuthal phase propagation frequency, ω_w, of these waves is given by,

$$\omega_w = \frac{2\pi}{\tau m} = \frac{\omega}{m}, \tag{6.1}$$

where ω is the wave's angular frequency, τ is the wave period and m is the azimuthal wave number discussed above. The angular frequency of the wave can be related to the angular drift frequency, ω_d, and bounce frequency, ω_b, of the driving particles, assuming a drift-bounce resonance is the wave source, by using Equation 2.70 (defined in Chapter 2; *Southwood et al.*, 1969), where N is the bounce harmonic number. In the situation where the driving particles are drift-resonant ($N = 0$), Equation 2.70 becomes Equation 2.71, which, when combined with Equation 6.1, can be used to show that the azimuthal phase propagation of the wave, ω_w, is equivalent the the angular drift frequency of the driving particles, ω_d.

The energy of the particles can also be estimated using Equation 2.73 defined in Chapter 2, where W is the particle energy, L is the L-shell, B_s is the equatorial magnetic field strength, α is the equatorial pitch angle, K_p is the planetary magnetic activity index, R_E is the Earth's radius and ϕ is the azimuthal position of the particle anticlockwise from local midnight (*Yeoman and Wright*, 2001).

Following the analysis of Chapter 5, and assuming a drift-resonance condition as the wave source, the angular drift frequencies and inferred particle energies corresponding to the three waves portrayed in Figure 6.2 are presented in Table 6.1 on page 155. In each case, ω_d is negative, corresponding to westward drifting ions as the energy source. In a similar manner to the results presented in Chapter 5, the magnitude of ω_d is higher nearer to the epicentre of the substorm where the lowest m number was observed by the Kapuskasing radar, and is lower farther from the substorm where the m number is at its highest. Also similar to Chapter 5, the particle energies appear to be highest closest to the substorm and get progressively lower as they drive the waves observed at larger azimuthal separations from where they were initially injected by the substorm.

6.3.2 Substorm Event 2, September 6th 2001

6.3.2.1 Substorm Observations

Figure 6.3 shows the IMAGE FUV data in the same format as in Figure 6.1 where the onset of the substorm occurs over western Canada then proceeds to spread rapidly eastwards and westwards. The onset of the substorm occurred at ~06:25 UT on 6^{th} September 2001 and continued to expand for ~50 minutes. In a similar manner to Figure 6.1, the ground instrumentation used to observe the wave activity during this event is shown in Figure 6.3 in which a black box centred around ~22:00 MLT represents the approximate location of the substorm at the time of onset, the dimensions of which are defined by where the WIC counts reach the threshold of 5% of the peak number of counts during the substorm. During this event waves were observed in the Prince George and Kodiak radars, where Figure 6.3 shows that both fields of view are to the west of the substorm onset, similar to the previously mentioned event.

6.3.2.2 Wave Observations

Data from the Prince George radar is presented in Figure 6.4a between 06:10 and 07:10 UT in the same format as that in Figure 6.2. Oscillations became visible immediately

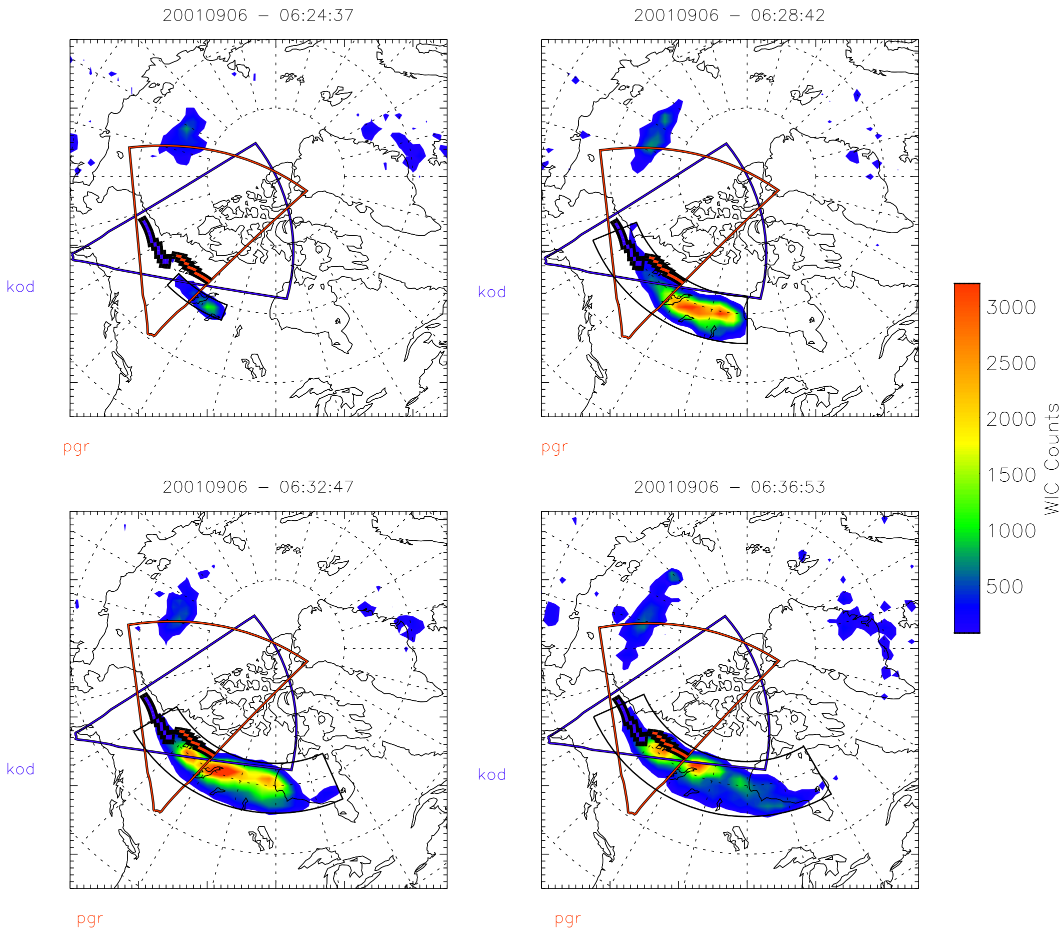

Figure 6.3: IMAGE data - 6th September 2001 - IMAGE FUV data during the substorm expansion phase shortly after onset at 06:21 UT on 6th September 2001, where coordinate system is as described for Figure 6.1. Also included are the projections of the fields of view of Kodiak, Alaska (kod, purple) and Prince George, Canada (pgr, red).

after the onset of the substorm at ~06:25 UT with a period of 1440 seconds (a frequency of 0.69 mHz). The azimuthal wave number derived from the Fourier phase of the wave was ~-11, corresponding to westward propagating phase, away from the epicentre of the substorm.

Figure 6.4b shows the line of sight velocity as measured by the Kodiak radar between 06:40 and 07:40 UT in the same format as Figure 6.2. At approximately 06:48 UT, oscillations in the velocity were observed with similar characteristics to those observed using the Prince George radar. The wave period found using Fourier analysis was similar to that observed by Prince George at ~1350 s (a frequency of 0.74 mHz). Also similar to Prince George, the wave exhibited westward phase propagation away from the epicentre of the substorm, but with a higher m of -24.

As with event 1, the angular drift frequencies and driving particle energies have been estimated using Equations 6.1 and 2.73 and are shown in Table 6.1 on page 155. The m numbers of the waves in this event became higher farther west of the location of the substorm. Angular drift frequency and particles energies also behave in a similar way to those shown in event 1 where the higher energy particles and higher angular drift frequencies are observed closest to the substorm.

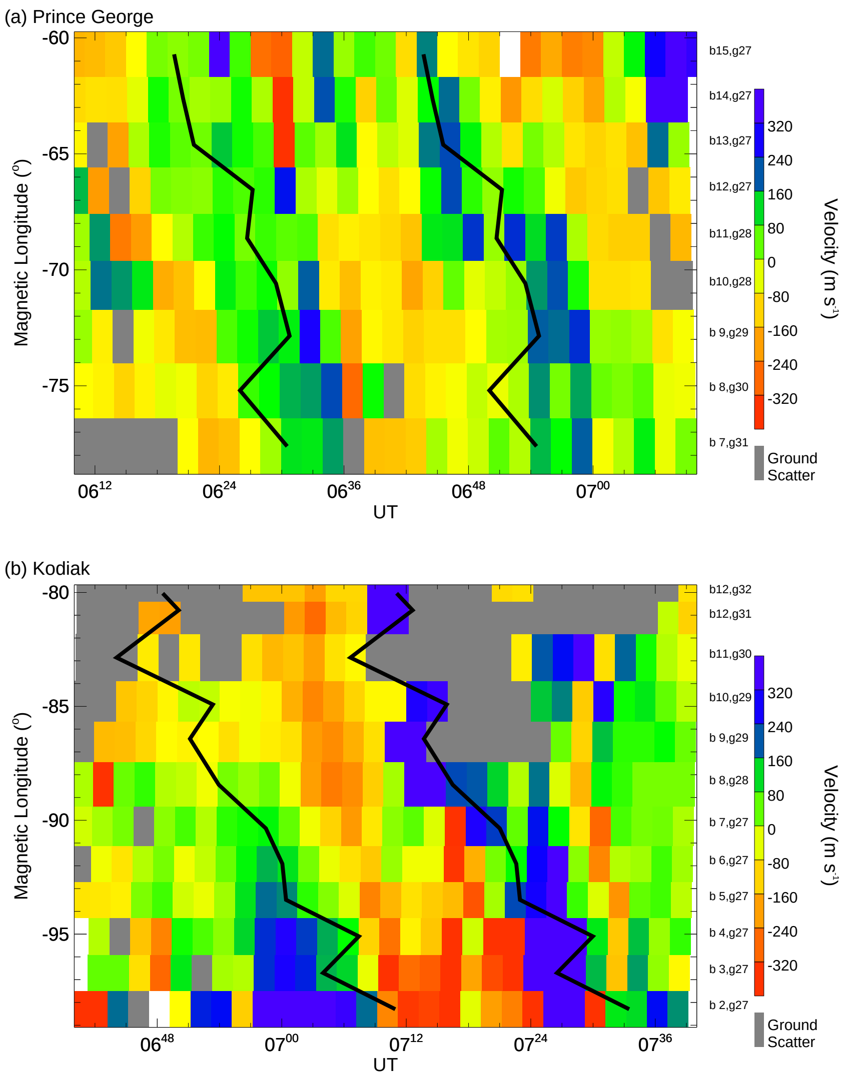

Figure 6.4: ULF waves - 6^{th} September 2001 - Line of sight velocity as measured by the Prince George radar between 06:10 and 07:10 UT, (a), and the Kodiak radar between 06:40 and 07:40 UT, (b), on 6^{th} September 2001 in the same format as described in Figure 6.2. Oscillations in the line of site velocity are observed shortly after substorm onset in (a) with a frequency of 0.69 mHz and ~20 minutes after the substorm onset in (b) with a frequency of 0.74 mHz, where both exhibit westward phase propagation.

6.4 Locating Substorms Using Ground Magnetometers

Chapter 5 presented the study of 83 ULF waves, each driven by an individual substorm. About half of these events were taken from the list of 4193 substorms published by *Frey et al.* (2004), thus showing that the chance of observing a wave and confidently associating it with a substorm is reasonably low. It follows then that the chance of finding an event where there was more than one wave observation is significantly lower. Sections 6.3.1 and 6.3.2 presented the only two of these events from the 4193 substorms detected using IMAGE FUV in which we could associate multiple ULF waves with a single substorm. In order to find more similar events it was necessary to look beyond the lifetime of the IMAGE spacecraft. As a substitute for auroral images, we chose to use magnetometers in order to detect the location of a substorm already detected using the Pinawa (PINA) magnetometer by bandpass filtering the data in order to see Pi1 and Pi2 waves appear as the substorm current wedge formed (*Mann et al.*, 2008).

To find the location of the substorm current wedge, we used the bays (large, sustained aberrations of the magnetic field from its baseline value) in the D and Z components of the magnetic field. In order to determine the approximate azimuthal location of the substorm, we used the perturbations in D. These occur in locations as defined by *McPherron et al.* (1973) and *Clauer and McPherron* (1974), where we expect a large negative bay around the eastward (downward) field aligned current and a large positive bay around the westward (upward) field aligned current. Z was used to determine the latitude of the westward electrojet between the two upward and downward field aligned currents, where a negative bay would be seen south of the current and a positive bay north of the current (*Wu et al.*, 1991).

An example of this technique applied to the substorm presented in Event 1 is presented in Figure 6.5. Figure 6.5a shows the perturbations in the Z component of the magnetic field as a function of magnetic latitude (left axis) and UT (bottom axis) during the interval of 04:00 – 06:00 UT on 24^{th} November 2000 using the magnetometer chain highlighted in green in Figure 6.1 for event 1. The time series data from each of the magnetometer stations were low-pass filtered with a cut off period of 1000s in order to remove most ULF waves from the data, then data was linearly interpolated across the gaps between each magnetometer station to a 1° resolution in latitude. The vertical dashed line at 04:21 UT represents the onset of the substorm as determined

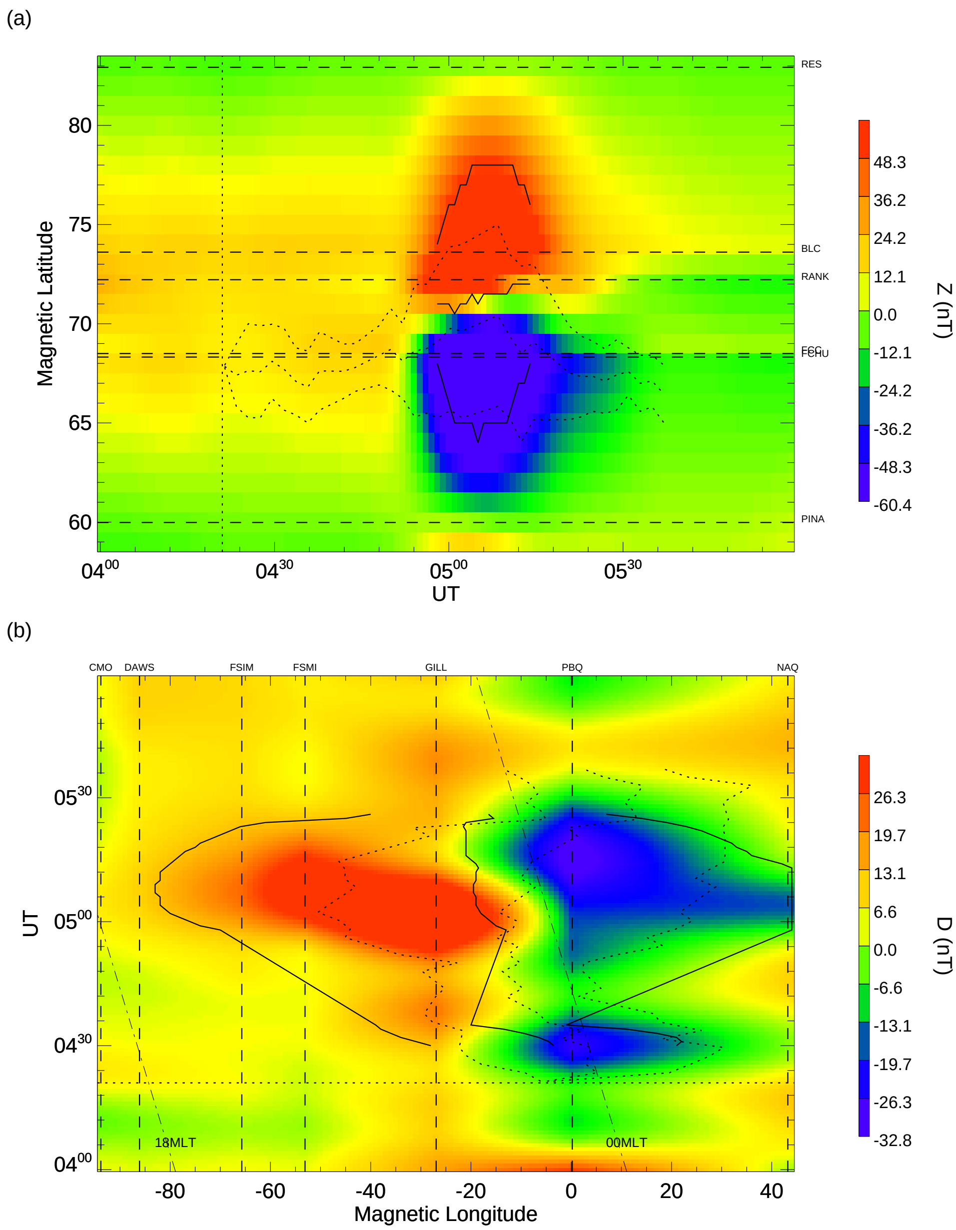

Figure 6.5: Magnetic bays - 24th November 2000 - Magnetic perturbations during the substorm of November 24th 2000.(a) Perturbations in Z as a function of UT (bottom axis) and magnetic latitude (left axis). (b) Perturbations in D as a function of UT (left axis) and magnetic longitude (bottom axis). In both panels, dashed lines parallel to UT axis represent the magnetic coordinate of each magnetometer station, and the dashed line at constant UT represents the onset of the substorm. Dotted lines in both panels represent latitudinal and longitudinal extents and midpoints of the UV aurora in (a) and (b) respectively. Solid lines surrounding the bays in both plots represent where the perturbations in B due to the substorm current wedge return close to the background field.

by *Frey et al.* (2004) and the three dotted lines represent the approximate latitudinal extent, and midpoint, of the aurora as observed by IMAGE in Figure 6.1 where the extent of the substorm's UV aurora is defined by where the number of WIC counts drop below 5% of the peak value for the entire substorm. As suggested by *Wu et al.* (1991), a positive bay (indicated by red) in Z is observed to the north of the SCW and a negative bay (indicated by blue) to the south. Three solid lines represent the northern and southern edges of the substorm and the midpoint of these two lines as determined using the ground magnetometers. The perturbations caused by the SCW do not appear until around 4:50 UT as the substorm had not yet spread far enough west for the current wedge to be in the vicinity of the latitudinal chain of magnetometers. It is apparent that for this event, the latitude of the UV aurora and the bays in Z caused by the SCW are fairly consistent with each other for the short amount of time which the bays are observable using this latitudinal chain.

Figure 6.5b shows the perturbations in the D component of the magnetic field as a function of both longitude (bottom axis) and UT (left axis) for event 1 using the magnetometer chain highlighted in orange in Figure 6.1. Here the horizontal dashed line at 04:21 UT represents the substorm onset, while the dotted lines show the longitudinal extent and midpoint of the substorm estimated using the IMAGE FUV data presented in Figure 6.1. Positive and negative bays in D are observed near to the upward and downward field aligned currents respectively where the solid black lines surrounding the bays show where we would have predicted the longitudinal extent and midpoint of the substorm based on the magnetometer data alone. The midpoints measured appear to remain within the $\pm 20°$ uncertainty mentioned above for the duration of the substorm.

In order to demonstrate that the use of magnetometer data produces a substorm location and extent consistent with our previous use of the IMAGE FUV data, we used IMAGE data from 27 substorms and compared this to bays observed in the ground magnetometer data. The edges of the bays observed in the magnetometer data were defined by where the magnetic field value dropped below a certain threshold value. This threshold value was different for both the positive and negative bays in both the latitudinal and longitudinal cases and was based upon the magnitude of the largest perturbation within that bay. The threshold values were chosen such that they minimised the difference between the edges of the substorm as defined by IMAGE observations and the outer edges of the magnetometer bays.

The threshold percentages that gave the closest fit to the northern and southern edges of the substorms for the bays in Z were both found to be at ~50% of the peak bay magnitude. When these were used and compared to the UV aurora, the errors were found to be within about $\pm 2.5°$ (1 standard deviation) magnetic latitude. The thresholds for the bays in D used to determine the azimuthal location of the substorm current wedge were slightly different, where 20% was used for the positive (westward) bay and 25% was used for the negative (eastward) bay. The errors associated with the eastward limit of the substorm were found to be $\pm 38°$ magnetic longitude and $\pm 29°$ for the westward edge.

The azimuthal separation between the waves and the substorm observations as used in Chapter 5 are measured from the centre of the wave to the centre of the substorm so the most relevant comparison between the substorms detected using magnetometers and those using IMAGE is that of the midpoint between the bays compared to the midpoint of the UV aurora. Figure 6.6 shows the differences in longitude and latitude of all of the times during the 27 events at which WIC images could be compared with the bays in the magnetometer data (this gives a total of 409 comparison points). Panels (a) and (c) show the western and eastern edge comparisons, where there is a large spread in values. The midpoints of the eastern and western edges of the magnetometer bays are compared to the midpoints of the UV aurora in panel (b) where the spread in values is much narrower. The peak in the graph is at $0°$ longitude difference and 67% of all of these values are contained within $\pm 20°$ of 0, which means that there is little overall difference between the midpoints in longitude calculated using either method.

Similarly, panels (d), (e) and (f) show the latitudinal differences between the southern edge, central point and northern edge of each measurement using IMAGE and magnetometers during the substorms. The difference between the northern and southern edges as measured using ground magnetometers and IMAGE are much smaller than the longitudinal differences. Panel (e) shows that there is no overall difference in latitude between the midpoint measured using both methods and that there is an error of about $\pm 2°$.

For Event 3, we used these magnetic perturbations to locate the substorm current wedge. Figure 6.7a shows the bays in Z in the same format as that used for Figure

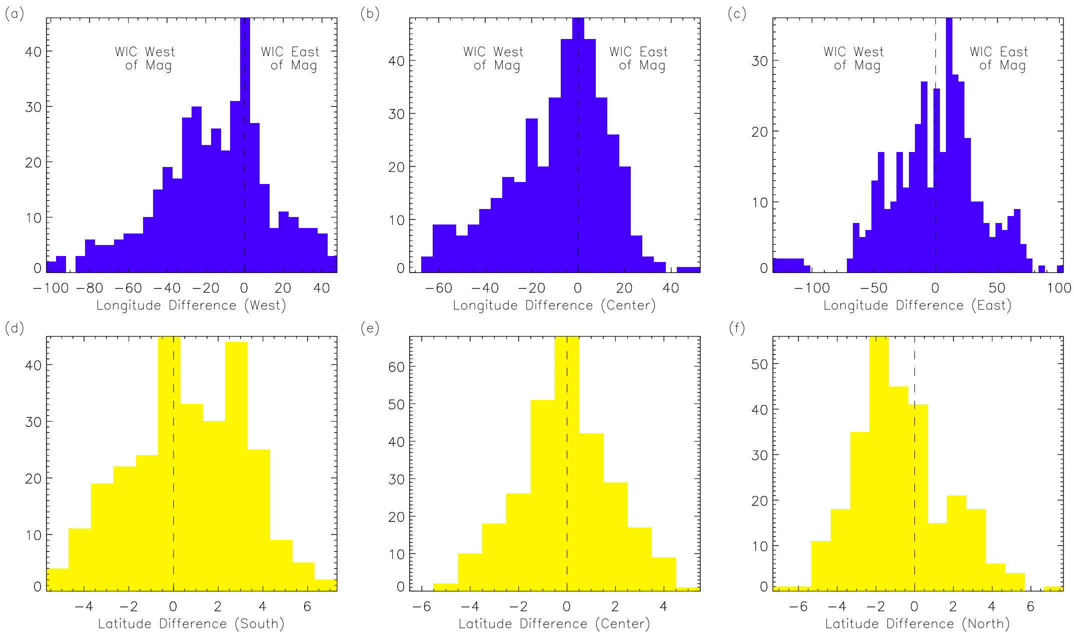

Figure 6.6: Comparisons of auroral and magnetic substorms - Histograms showing the differences in magnetic longitude and magnetic latitude between measurements made using IMAGE data and magnetometer data. Panels (a), (b) and (c) show the differences in longitude of the western edge, central point and eastern edge respectively for each comparison between the two data sets. Panels (d), (e) and (f) show the comparisons of the magnetic latitudes of the southern edge, central point and northern edge of each point.

6.5a, using the magnetometer chain shown in green in Figure 6.8. Due to the large threshold values, smaller bays such as the negative bay between 4:00 UT and 4:40 UT at around 60° magnetic latitude are not always detected by this algorithm as shown by the solid white lines. In order to detect the lower magnitude bays, the time series was split into three sections: 3:00 to 4:06 UT, 4:06 to 4:30 and 4:30 to 5:00. The latitudinal extent and central location calculated using this method is presented for each of the three time periods by three black lines. In this case, the low amplitude negative bay in the second time period is detected correctly. The centre of the current wedge was observed to vary between ~65° – ~72° magnetic latitude.

The H component data from the magnetometers used to create Figure 6.7a are presented in Figure 6.9 between 3 and 7 UT where the first data point in each panel is set to zero. A large drop of more than 300 nT in H occurs after the approximate

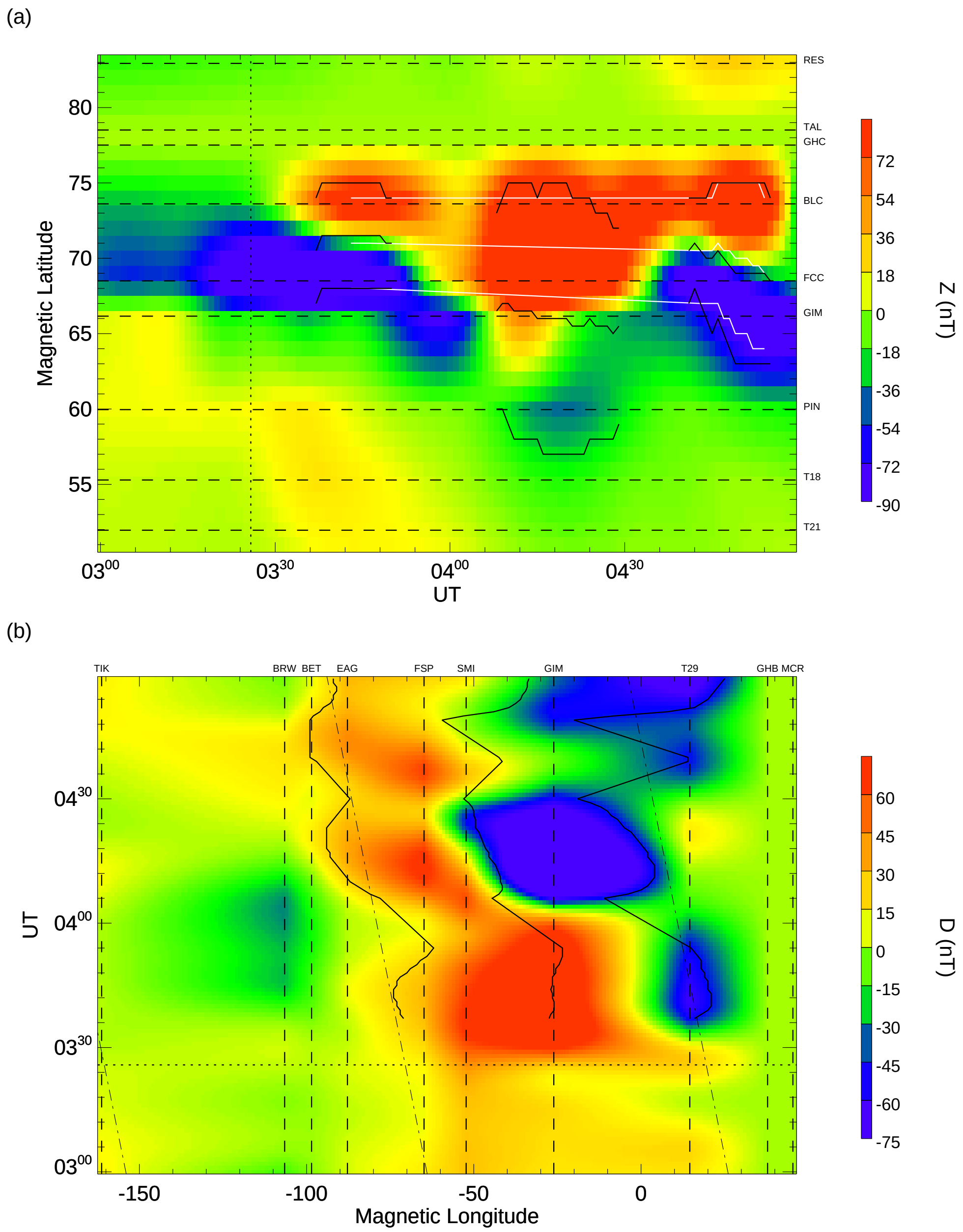

Figure 6.7: Magnetic bays - 8th September 2008 - Perturbation of the magnetic field during the substorm of 8th September 2008 at 03:26 UT in the same format as that of Figure 6.5. White lines show the latitudinal extent and central latitude calculated using the bays on Z for the entire time series. Black lines show the latitudinal extent of the substorm when the time series is split into three sections in order to detect the middle, less prominent negative bay.

onset time at ~3:26 UT in three of the magnetometers. This large drop in the local H component is associated with the westward electrojet forming part of the substorm current wedge overhead.

Figure 6.7b shows the longitudinal extent of the bays associated with the current wedge, using the chain of magnetometers again shown in orange in Figure 6.8. The algorithm that estimates the edges of these bays placed the substorm over a reasonably large range of magnetic longitudes (~-92° – ~25°) at its largest point. The bays observed here are very variable, much like those in Figure 6.7a and were determined using the technique described above.

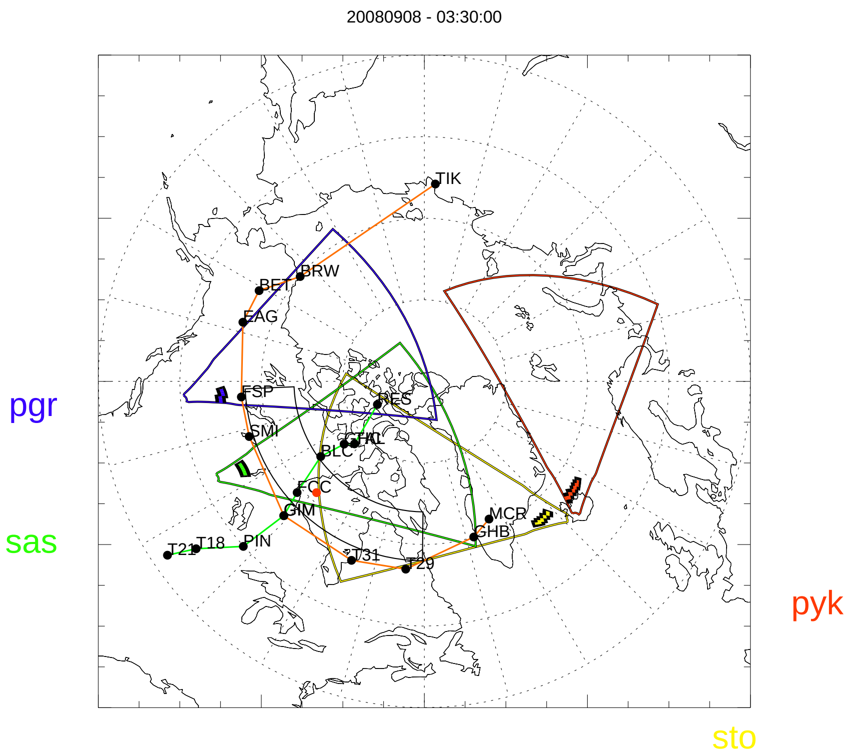

Figure 6.8: Radar field of view - 8th September 2008 - A magnetic latitude - magnetic local time projection of the fields of view of Prince George (pgr) and Saskatoon (sas) radars, both in Canada; Stokkseyri (sto) and Þykkvibær (pyk), both in Iceland with the two chains of magnetometers used in a similar format to Figure 6.1. The black box present between 18 and 24 MLT shows the approximate latitudinal and longitudinal extent of the bays in D caused by the substorm current wedge at the time of onset from Figure 6.7 where the centre is marked with a red circle.

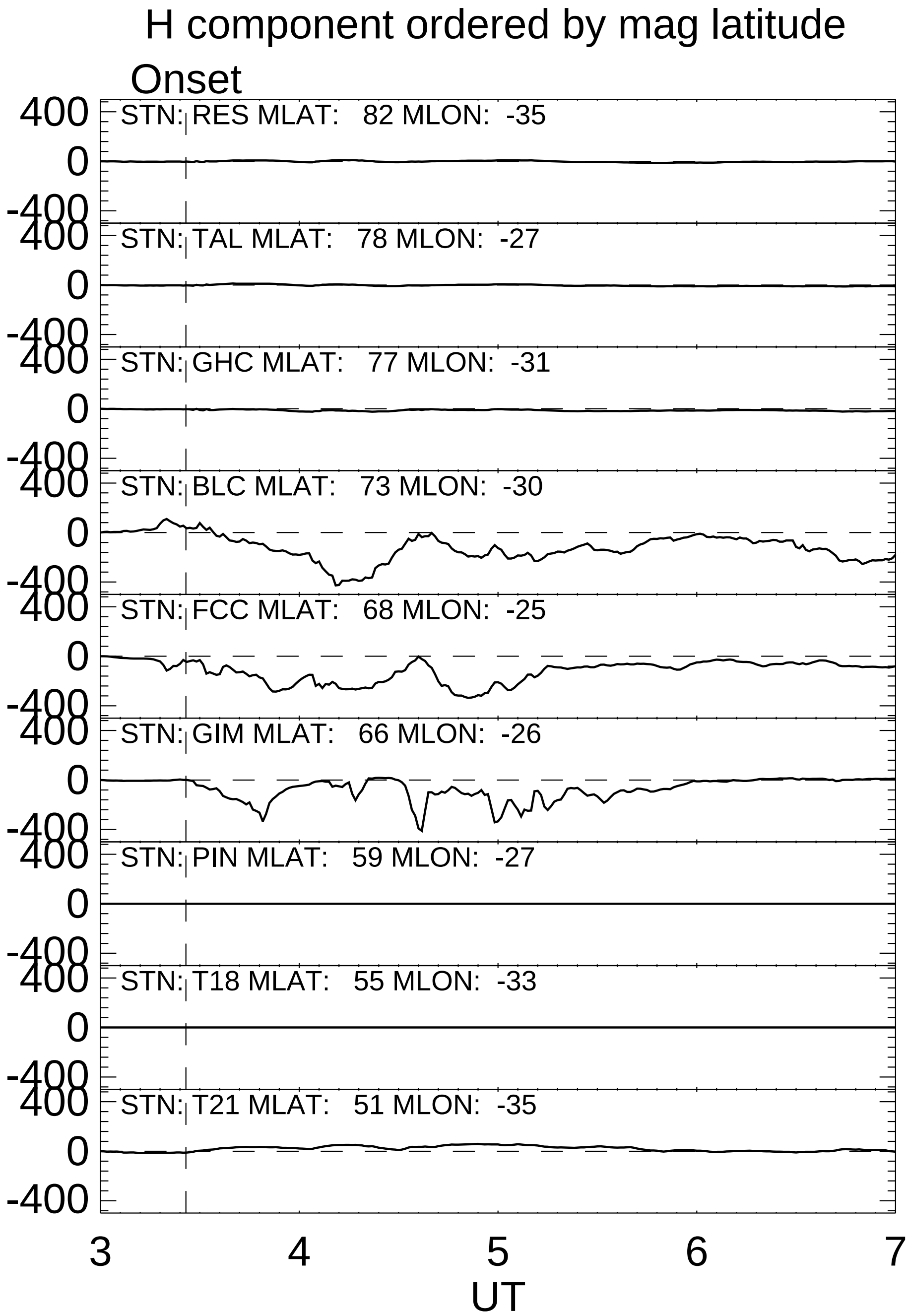

Figure 6.9: H **component - 8th September 2008** - H component measured by each of the magnetometers used to create Figure 6.7a. Substorm onset is marked on the plot at ~3:26 UT, where a drop of over 300 nT is observed by three magnetometers.

6.5 Substorm Event 3, September 8th 2008

6.5.1 Substorm Observations

This substorm, as identified from the magnetic field bays in Figure 6.7, was detected to start at around 03:30 UT where the current wedge occupied a large azimuthal extent between dusk and midnight. Figure 6.8 shows the ground instrumentation used for event 3, along with the large spatial extent of the bays in Z and D as defined in 6.4 represented by the large black box centred around local midnight, within which the substorm current wedge would have existed. The centre of the substorm is marked with a red circle. This figure shows that two of the four radars were located to the west of the centre of the substorm, and the others to the east.

6.5.2 Wave Observations

Data taken from east of the substorm using the Þykkvibær radar is presented in Figure 6.10a from 04:00 – 04:30 UT in the same format as that of Figure 6.2. Pulsations were observed from ~04:00 UT where Fourier analysis of the wave revealed a period of 500 s (a frequency of 2 mHz). This wave exhibited a rapid phase propagation with an azimuthal wave number of $m = 79$.

Slightly to the west of the Þykkvibær radar, data from the Stokkseyri radar between 03:54 and 04:24 is displayed in the Figure 6.10b where the format is the same as used in Figure 6.2. Although the data quality from Stokkseyri is not high during this period, there is evidence of the onset of an eastward propagating wave at ~04:00 UT. This wave was found to have a period of 480 s (a frequency of 2.1 mHz), only slightly shorter than that observed by the Þykkvibær radar, but the azimuthal wave number for this wave was found to be much lower at $m = 43$.

Data from the Saskatoon radar is displayed in Figure 6.10c within the time range of 04:06 – 04:36 using the same format as Figure 6.2. At approximately 04:09 UT the onset of a wave was observed by the radar where Fourier analysis revealed that the wave had a period of ~410s (a frequency of 2.4 mHz). This wave exhibited westward phase propagation with an azimuthal wave number of $m = -29$.

Figure 6.10d shows data from the Prince George radar between 04:15 and 04:45 UT in the same format as 6.2 where oscillations became apparent at ~04:18. The period

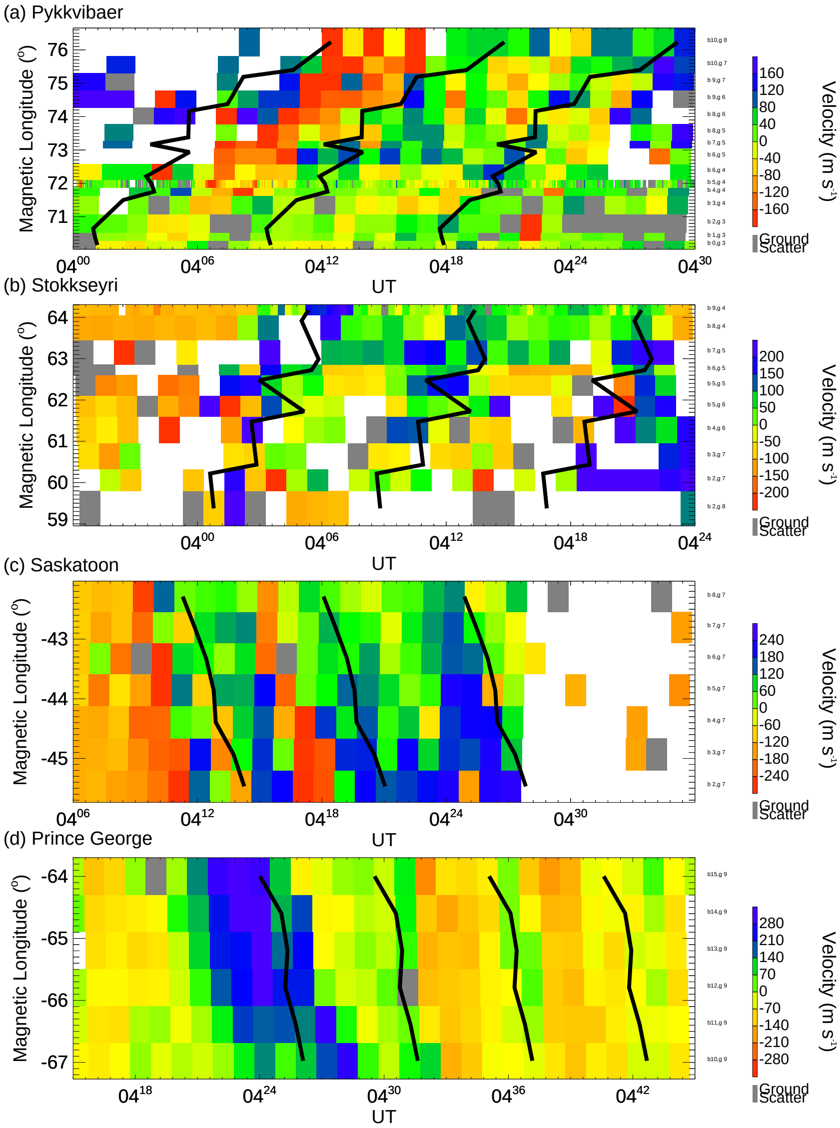

Figure 6.10: ULF waves - 8th September 2008 - Line of sight velocity as measured by(a) the Þykkvibær radar between 04:00 – 04:30 UT, (b) the Stokkseyri radar between 03:54 – 04:24, (c) the Saskatoon radar between 04:06 and 04:36 UT and (d) the Prince George radar between 04:15 and 04:45 UT on 8th September 2008. In (a) and (b) westward propagating waves were observed with frequencies of 3.0 and 2.5 mHz respectively. In (c) and (d) oscillations in the line of sight velocity exhibited eastward phase propagation with frequencies of 2.1 and 2.0 mHz.

of this wave was found to by slightly shorter than that which was observed using the Saskatoon radar at 330 s (a frequency of 3 mHz). The wave was found to have an azimuthal wave number of $m = -41$ indicating a westward phase propagation similar to that observed using Saskatoon however with a smaller azimuthal scale size.

The waves observed to the west of the substorm using the Saskatoon and Prince George radars both exhibited negative m numbers such that the direction of phase propagation was away from the location of the substorm. This event is also the only of the three in which eastward propagating waves with positive m numbers were observed to the east of the substorm. As with the results from Chapter 5, the m numbers observed during this event were lowest for those waves closest to the substorm and highest for those farthest away. The angular drift frequencies and inferred particle energies for all four waves are displayed in Table 6.1 on page 155. It is apparent that, for both eastward and westward propagating waves during this event, the driving particles behave in similar ways such that those with the largest angular drift frequencies and highest energies exist closest to the substorm location.

6.6 Discussion

	Radar	Wave Period (s)	m	ω_d (rad s^{-1})	W (keV)	λ (°)
Event 1	Kapuskasing	700	-6	-1.4×10^{-3}	82 – 95	-3 ±7
	Saskatoon	400	-15	-1.0×10^{-3}	35 – 55	-33 ±7
	Kodiak	285	-44	-0.5×10^{-3}	20 – 23	-79 ±7
Event 2	Prince George	1440	-11	-0.4×10^{-3}	9 – 20	-12 ±11
	Kodiak	1350	-24	-0.2×10^{-3}	2 – 7	-26 ±11
Event 3	Prince George	330	-41	-0.46×10^{-3}	29 – 39	-38 ±44
	Saskatoon	410	-29	-0.53×10^{-3}	33 – 41	-16 ±44
	Stokkseyri	480	43	0.30×10^{-3}	14 – 17	89 ±44
	Þykkvibær	500	79	0.16×10^{-3}	4 – 7	101 ±44

Table 6.1: Attributes of the waves and the particles that drive them during all three events where m is the azimuthal wave number, ω_d is the angular drift frequency, W is the inferred particle energy and λ is the longitudinal separation of the wave observation from the substorm onset and the error is half the width of the substorm in longitude.

In all three of the events presented, we observe waves at multiple locations following the onset of a substorm. Each of the waves display a unique set of characteristics, such as period and wave number and these have been summarised in Table 6.1. The wave characteristics are clearly affected by their proximity to the substorm. Only one of these events (event 3) includes waves that are propagating eastward, however all of the events include two or more westward propagating waves. Using the interpretation of Chapter 5 we would interpret the westward-propagating waves as being driven by westward-drifting protons and the eastward-propagating waves as being driven by eastward-drifting electrons.

Chapter 5 determined that in general for observations of single substorm-driven waves, the phase propagation, angular drift frequency and particle energy depends on the proximity of the wave to the substorm. However, this study was not able to determine whether an individual substorm event would generate multiple waves, and if so what the characteristics of these waves would be. The three events presented here give a clearer depiction of this situation.

In event 1 we observed three waves occurring at various azimuthal separations from the epicentre of a substorm. The closest of the three waves to the substorm, observed by the Kapuskasing radar, exhibits a very low m number of ~-6 which corresponds to a driving particle energy of 82 – 95 keV. The waves observed farther to the west of the substorm by the Saskatoon and Kodiak radars exhibited progressively higher m numbers of -15 and -44 respectively and lower inferred particle energies of 35 – 55 and 20 – 23 keV.

Figure 6.11 shows the azimuthal wave number (a), angular drift frequency calculated from Equation 6.1 (b) and inferred particle energies calculated from Equation 2.73 (c) for each wave during this event (left axis) as a function of magnetic longitude. Also in each panel of Figure 6.11, pairs of vertical dashed lines indicate the minimum (short dashes) and maximum (long dashes) approximate azimuthal extent of the substorm's UV aurora as observed by IMAGE. Figure 6.11a shows that the azimuthal wave number, m, became more negative with the azimuthal separation of each wave observation with the substorm as seen in the previous chapter. In a similar manner to the waves that were analysed in chapter 4, we assume that each of the waves is driven by drift-resonant particles. Figure 6.11b shows that the largest angular drift frequencies for this event existed closest to the location of the substorm UV aurora and reduced as

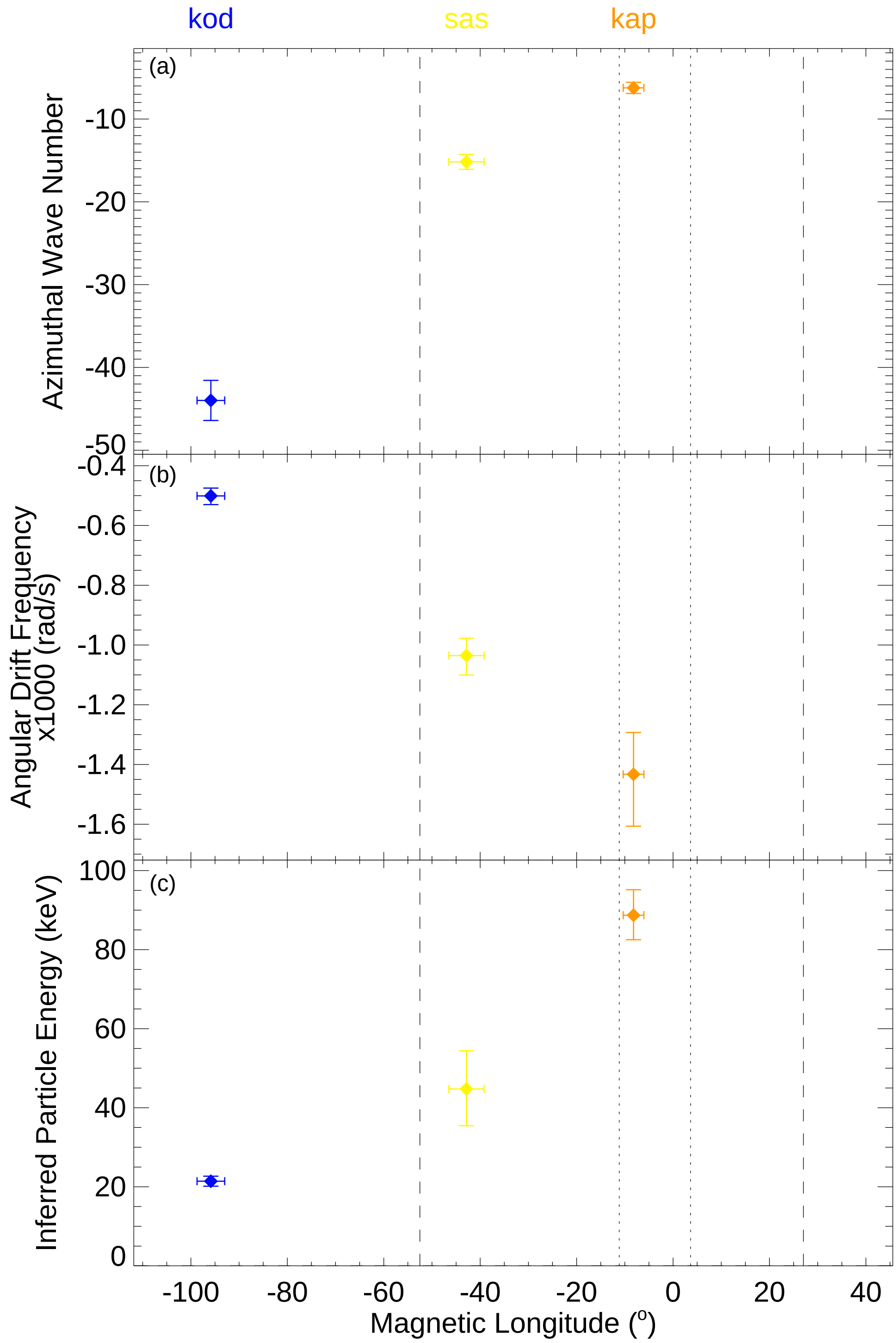

Figure 6.11: Parameters plotted in longitude - 24th November 2000 - Azimuthal wave numbers (a), angular drift frequencies (b) and particle energies (c) calculated from each of the waves in event 1 (left axis) as a function of magnetic longitude (bottom axis). Vertical dashed line indicate the location of the substorm UV aurora at its minimum (short dashes) and maximum (long dashes) longitudinal extent.

separation increased. Similarly, the inferred particle energies presented in Figure 6.11c were also the highest for wave observations closest to the location of the substorm.

In event 2, two waves were observed to the west of the substorm onset with m numbers of -11 at Prince George and - 24 at Kodiak. Figure 6.12 shows the azimuthal wave number (a), angular drift frequency (b) and the inferred particle energies (c) for the waves observed during event 2 in the same format as those presented in Figure 6.11. In a similar manner to those waves observed during event 1, the magnitude of the azimuthal wave numbers was higher in the wave observed farthest from the substorm as presented in Figure 6.12a. Angular drift frequency and particles energies displayed in Figures 6.12b and 6.12c also behave in a similar way to those shown in event 1 where the higher energy particles and higher angular drift frequencies are observed closest to the substorm. Event 2 differs from the other two events in that each of the waves observed here exhibit much larger wave periods than those in the other two events. They are not abnormal when compared to the distribution of wave periods presented in Chapter 5 (Figure 5.7), and indeed the characteristics of all of the waves studied here fit within the main bulk of that distribution. The other unusual thing about the waves in event 2 were that the angular drift frequencies and inferred particle energies were much lower than the other two events considering the proximity of the waves to the substorm. These relatively low particle energies of 9 – 20 keV (Prince George) and 2 – 7 keV (Kodiak) could be the due to the occurrence of such low frequency waves or visa versa.

Events 1 and 2 demonstrate that an individual substorm can inject particles with a wide variety of energies, and that within these energy ranges subsections of the particle distribution can drive distinct wave events at locations where the drift resonance condition is satisfied. The characteristics of these waves is consistent with the observations of individual events presented in Chapter 5.

Event 3 differs from the other two events mainly due to the existence of wave observations to the east of the substorm, but also due to the larger uncertainty in the substorm's location. The waves observed to the west of the substorm by the Prince George and Saskatoon radars both exhibit westward phase propagation, where the most distant of the two waves has the more rapid phase propagation, an m number of -41, and the closest of the two exhibited an m of -29. The particle energies calculated using the properties of these two waves were 33 – 41 keV and 29 – 39 keV in order of

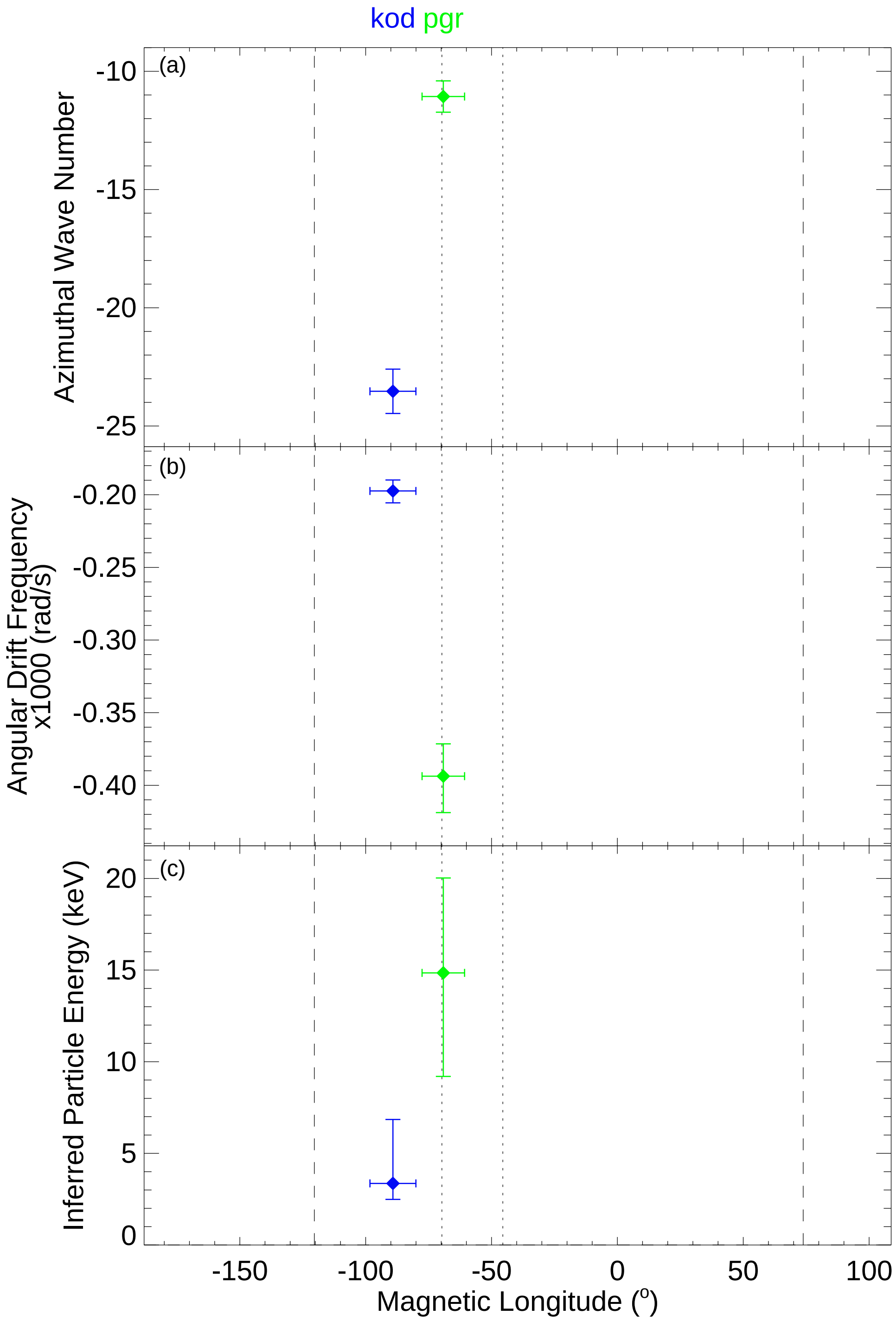

Figure 6.12: Parameters plotted in longitude - 6th September 2001 - Azimuthal wave numbers (a), angular drift frequencies (b) and particle energies (c) calculated from each of the waves in event 2 (left axis) as a function of magnetic longitude (bottom axis). Vertical dashed line indicate the location of the substorm UV aurora at its minimum (short dashes) and maximum (long dashes) longitudinal extent.

increasing distance from the centre of the substorm. Figure 6.13, presented in the same format as both Figures 6.11 and 6.12, shows that this behaviour is very similar to the behaviour observed in events 1 and 2 where the lowest m numbers and highest inferred particle energies were seen at smaller azimuthal separations with the substorm. The two waves observed by the Stokkseyri and Þykkvibær radars both possessed positive m numbers of 68 and 79 respectively, which we would interpret as corresponding to eastward drifting electrons as the source, as opposed to westward drifting ions. Both the azimuthal wave numbers and the particle energies associated with these two waves behave in much the same way as with the ion driven waves, where the highest energy of 14 – 17 keV was predicted for the wave closest to the substorm and 4 – 7 keV for the most distant.

Figure 6.14 shows a comparison of the three events investigated here with the results presented in Chapter 5, where (a) shows the m numbers, (b) shows ω_d and (c) shows W, all of which are plotted against the wave location relative to the substorm at its most expanded state. In each panel, the grey points are the results from Chapter 5, red points correspond to event 1, blue points are from event 2 and orange points are from event 3. The error bars in this plot are representative of the azimuthal extent of the substorm while it is at its most expanded state, the substorm in Event 2 had the largest expansion out of the three. In all of the events we do see that, whether the driving particles are westward drifting ions or eastward drifting electrons, the trends for m, ω_d and W all appear to be consistent with those observed in Chapter 5. The range of inferred particles energies observed in each event would suggest that, during a substorm, the particle populations injected into the inner magnetosphere contain a wide range of energies, resulting in the range of ω_d and m that is observed. When comparing the results from these three events to each other, it also becomes apparent that the range of particle energies varies from substorm to substorm, for example – those predicted in event 1 appear to be consistently higher than those of the other two events across the range of magnetic longitudes where the waves are observed.

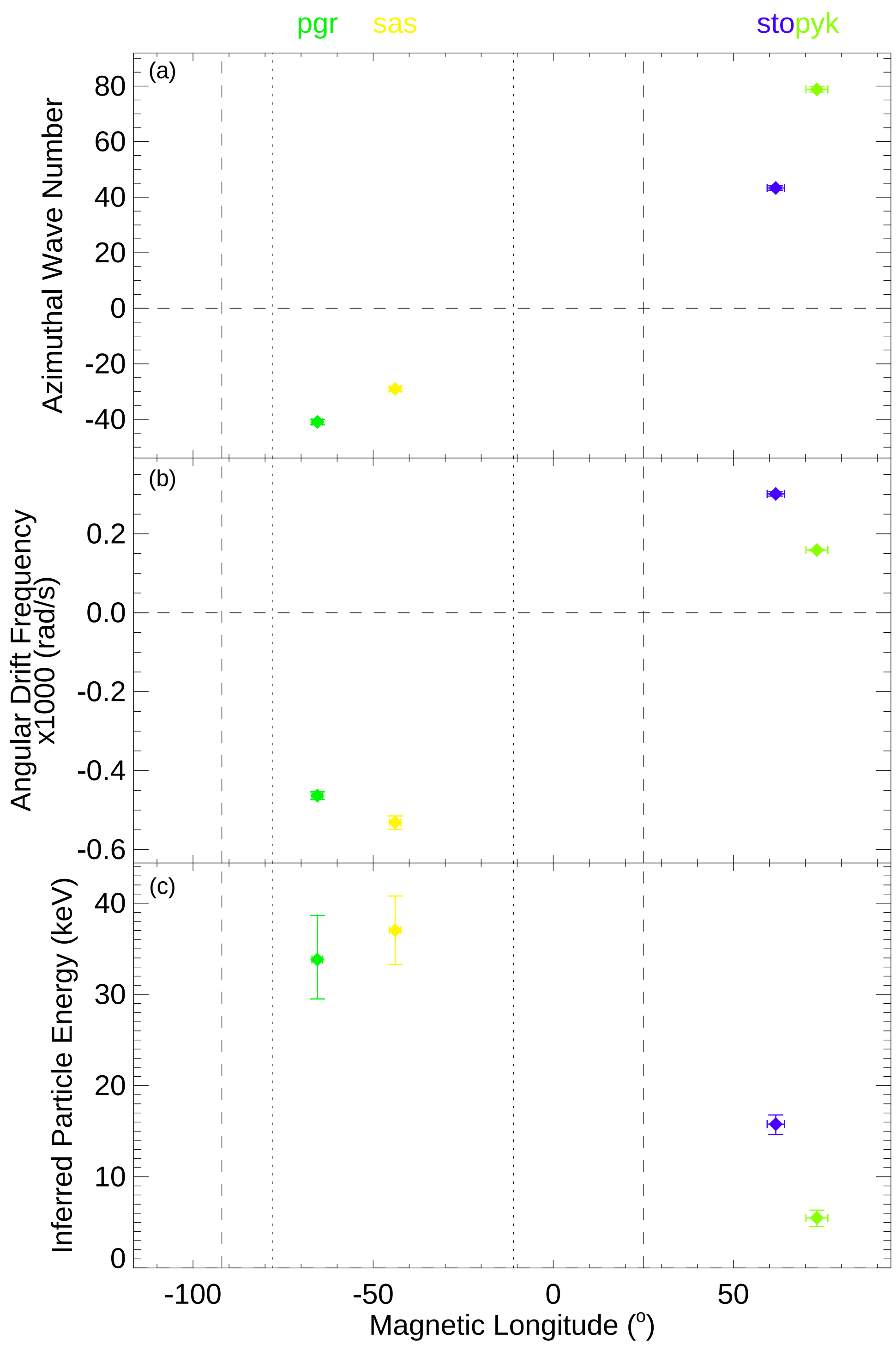

Figure 6.13: Parameters plotted in longitude - 8th September 2008 - Azimuthal wave numbers (a), angular drift frequencies (b) and particle energies (c) calculated from each of the waves in event 3 (left axis) as a function of magnetic longitude (bottom axis). Vertical dashed line indicate the location of the substorm at its minimum (short dashes) and maximum (long dashes) longitudinal extent.

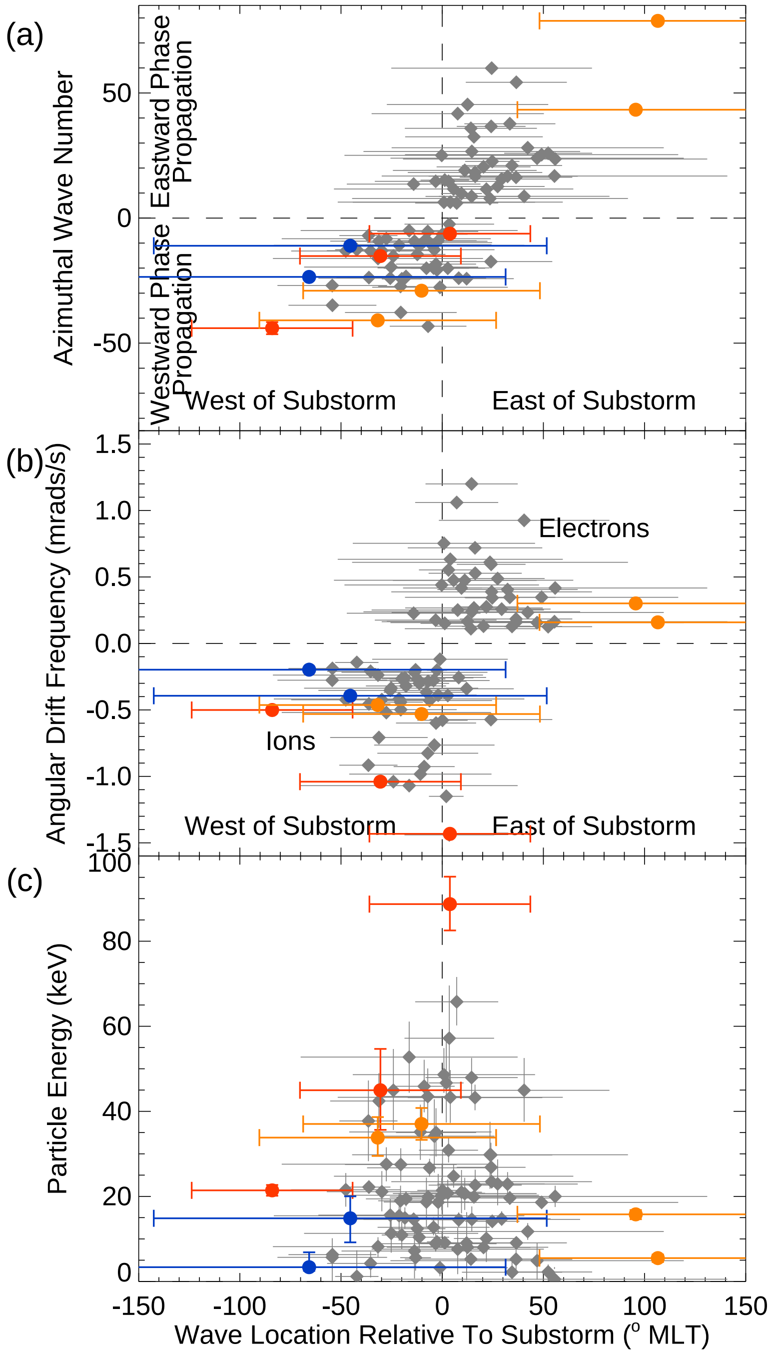

Figure 6.14: Comparison to previous results - Comparison of the results of events 1-3 with results from Chapter 5, the previous results are displayed in grey, results from event 1 are in red, those from event 2 are blue and event 3 is in orange. (a) shows the comparison of azimuthal wave numbers, (b) shows the comparison of the angular drift frequencies and (c) shows the comparison of the inferred particle energies.

6.7 Summary

Using the data from various SuperDARN radars alongside IMAGE FUV and ground magnetometers, we identified three substorm events associated with which are multiple observations of ULF waves. This enabled an examination of how these wave events evolve as the substorm-injected particles gradient-curvature drift away from the injection source. In two events we see multiple westward drifting, ion-driven waves, and in one event we observe both eastward and westward propagating waves to the east and west of the substorm.

In order to determine the location of the substorm in event 3, it was necessary to make use of ground magnetometer data in order to use the substorm current wedge location as a proxy for the auroral emission which would have been observed by IMAGE. This method of substorm location was refined with the comparison of magnetometer and auroral data collected during 27 substorms which had occurred within the lifetime of the IMAGE spacecraft. The midpoint of the substorm as defined using both auroral data and magnetometer bays appeared to be reasonably well correlated with an uncertainty of ~20°. While this uncertainty was not small, it was small enough, when compared to the azimuthal extent of the substorms themselves (typically 50 - 200°), to allow us to define an approximate location of substorms which occurred beyond the lifetime of the IMAGE mission.

We observe a very similar picture in each individual event to what has been previously observed in the statistical study of events where only one ULF wave was observed per substorm. It is therefore evident that during a substorm, a range of particle energies exist within the population of injected particles, and that the highest energy particles tend to drive waves much closer to the epicentre of the substorm while lower energy particles drive those waves at larger azimuthal separations from the substorm.

Chapter 7

Van Allen Probe Observations of Particle Distributions During Substorm-Driven ULF Waves

7.1 Introduction

Chapters 5 and 6 made use of a number of SuperDARN radars in order to characterise ULF waves driven by substorm-injected particle populations. They have both shown that the proximity of the wave to the substorm plays a key part in determining the properties of the waves, in particular the azimuthal wave numbers and angular drift frequencies. Typically, waves observed closer to the epicentre of the substorm have smaller m numbers than those observed farther out, where the angular drift frequencies have the inverse relationship with the proximity to the substorm.

Also it has been shown that the type of particles responsible for driving this class of waves depends upon whether the waves were observed to the east or the west of the point of particle injection. Waves observed to the east of the substorm have been linked to a source of energy in an eastward drifting population of electrons and waves observed to the west are attributed to a source in westward drifting ions.

It was possible to provide an estimate of the energy of the particle populations responsible for driving these ULF waves. Equation 2.73 (See page 53; *Chisham*, 1996; *Yeoman and Wright*, 2001) allows the prediction of the particle energy when provided with certain parameters. The pitch angle parameter has been assumed to be close to 90°

throughout this thesis so far, as the particles injected into the night-side magnetosphere by substorms are assumed to have large equatorial pitch angle. This is because smaller pitch angle particles are likely to be lost into the atmosphere as they drift azimuthally, though it is possible that there could be a more appropriate value for the equatorial pitch angle to use when making these energy estimates. Also, there has been no direct measurement of the particle energy in the two previous chapters so the energies calculated have been purely theoretical.

There is some uncertainty in the estimates of the particle energies predicted by Chapters 5 and 6 due to the assumption that $\alpha = 90°$ and the lack of direct observations of the particle distribution functions. This chapter aims to provide a assessment of the accuracy of these particle energies by discussing a case study event where these particle populations were directly observed as they drifted from the substorm onset longitude towards the observed ULF wave events.

7.2 Instrumentation and Event Selection

In order to be able to take measurements of the particle populations as they drive ULF waves, the spacecraft must exist on the right field line at the right time. As the ULF waves will be observed using the SuperDARN radars as they had in Chapters 5 and 6, these field lines must have an ionospheric footprint within or near the field of view of a radar. To establish this, the ionospheric footprints of both of the Van Allen Probes were traced to the ionosphere of the northern hemisphere where the majority of the radars exist, using the Tsyganenko 96 (T96) field model. The T96 model is parametrised using values for the solar wind dynamic pressure (P_{dyn}), D_{ST} and IMF B_y and B_z. Due to the low L-shells which the Van Allen Probes pass through, it was more likely for the footprints to coincide with the StormDARN radar fields of view (fields of view in orange in Figure 4.1) than the main SuperDARN array.

Figure 7.1 shows the result of the field line trace for a single day, 14th November 2012, where the ionospheric footprints are plotted on a top-down projection of the northern hemisphere with a 5 minute time resolution. Magnetic latitude is represented in 10° increments by the concentric circles, where magnetic longitude is represented in 15° increments by the radial lines. The footprints for probes A and B are green and blue respectively when they trace down to a location within a radar field of view, and

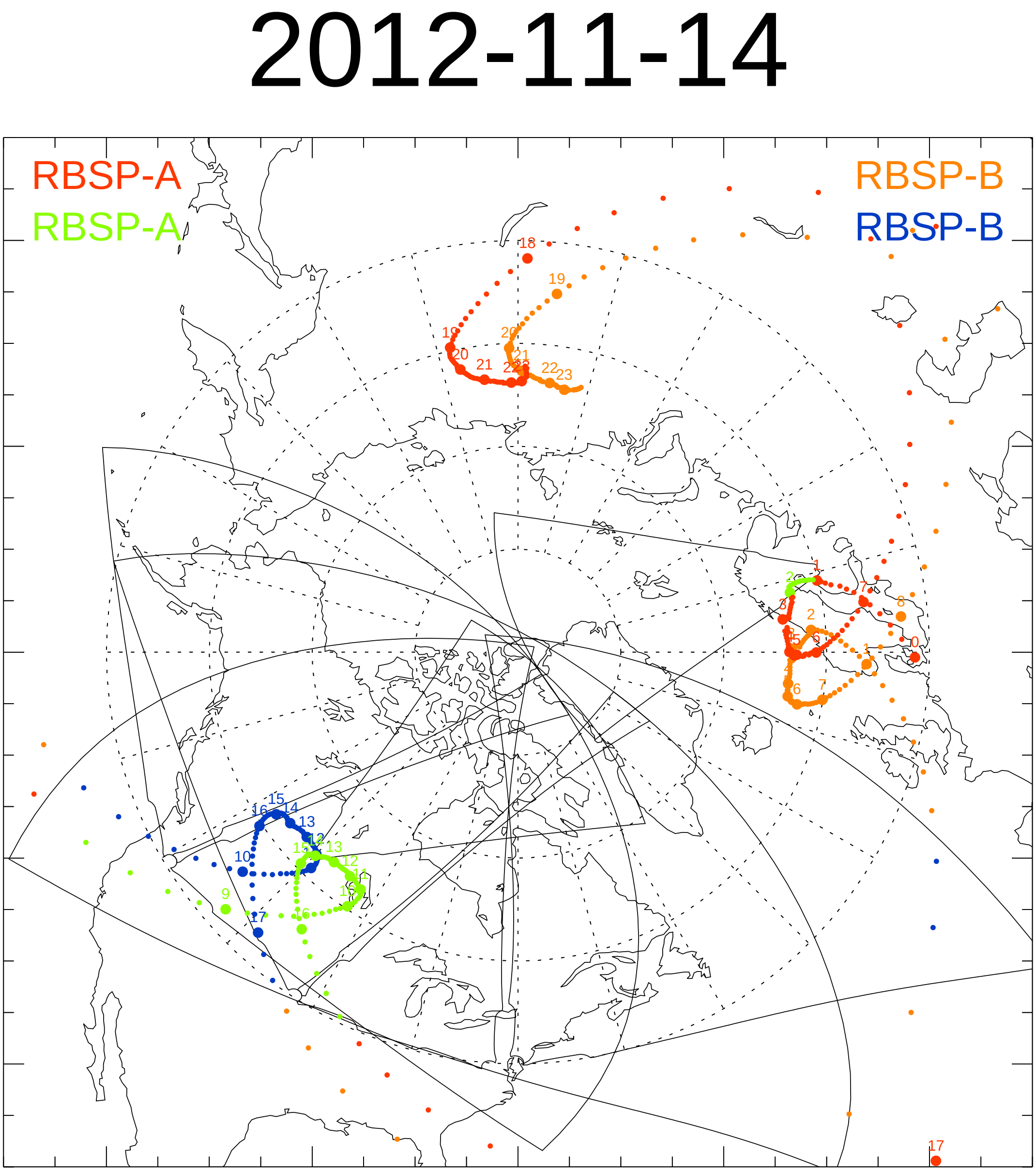

Figure 7.1: Radar conjunctions - Projection of the T96 field line trace for both Van Allen Probes over the northern hemisphere for one day at a 5 minute time resolution. In green and blue are the times when there is a conjunction with at least one radar field of view and probe A and B respectively. Only fields of view that had a conjunction during this day are shown.

are red and orange when they are outside the radar field of view. Figure 7.1 shows that there are a number of conjunctions with SuperDARN in the northern hemisphere during a single day, where one individual conjunction is defined as one pass of the spacecraft footprint in and out of a radar's field-of-view. In total, there were over 1000 of these conjunctions from November 2012 to July 2013.

This number however was greatly reduced by the requirement that a ULF wave must be observed by the radar during the conjunction and must be within a few degrees of magnetic latitude of the conjunction. The requirement for the wave to exist at a similar latitude to the footprint of at least one of the probes is due to the latitudinal dependency of the particle energy required to drive the waves: particles that exist at different latitudes to the ULF wave may not be representative of the actual driving particles.

The final step in event reduction was to use ground magnetometers to determine whether there were any nearby substorms with the aid of auroral electrojet indices and using the method described in Chapter 6 to determine the location of the substorms if they existed. This reduced the number of events of potential interest to just four.

This chapter will discuss one of these four events in which both spacecraft were in the right place at the right time to observe the particles responsible for driving waves observed in two SuperDARN radars on 14^{th} November 2012. The particle observations were made using the HOPE and MagEIS instruments described in Section 4.5.

7.3 Data

7.3.1 Wave Analysis

Figure 7.2 shows the fields of view of both the CVE (yellow) and CVW (red) radars, where the beam/range gate cells used for the observation of the waves along a constant latitude are highlighted in the appropriate colour for each radar. The map is orientated such that is shows the MLT of the radars at the time of the start of the waves (10:00 UT). Also included in the plot are the latitudinal and longitudinal magnetometer chains used to locate the substorm current wedge in purple and red respectively. The ionospheric footprints of probe A (red) and probe B (orange) are plotted as a function of time over the field of view of the CVE radar. The black box represents the maximum

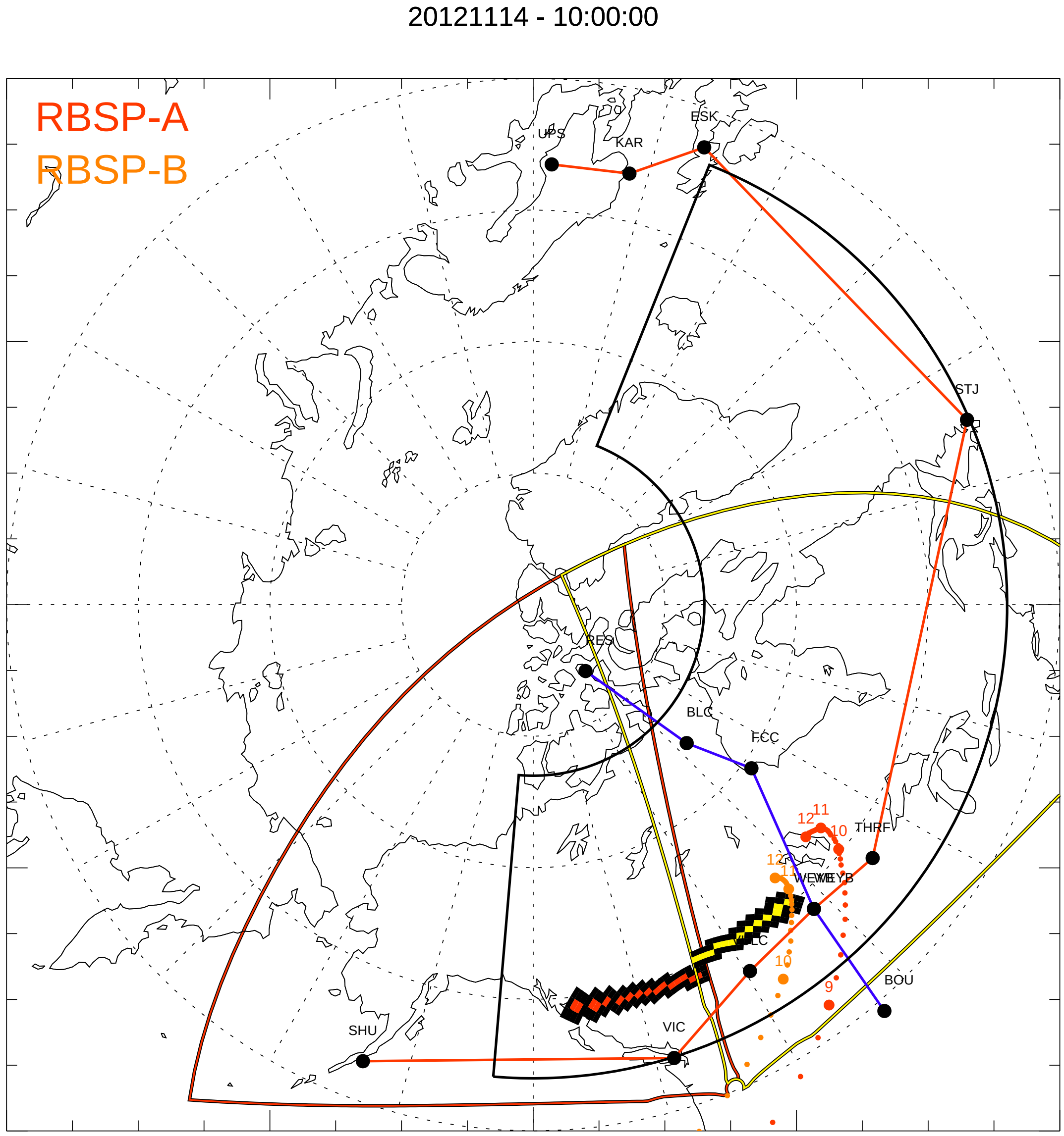

Figure 7.2: Radar fields-of-view - Projection of the fields of view of the CVE (yellow) and CVW (red) radars over the north pole in magnetic latitude and MLT coordinates where noon is at the top of the panel and dawn to the right. The concentric circles represent magnetic latitude in 10° intervals and magnetic local time is displayed in 1 hour intervals. The ionospheric footprints of Van Allen Probes A and B are shown in red and orange respectively. Latitudinal chain of magnetometers used for substorm location in purple and the longitudinal chain in red.

latitudinal and longitudinal extent of the perturbations in the magnetometer data due to the substorm current wedge, which will be discussed later.

Wave activity was observed in the line of sight velocity as measured by the Christmas Valley East (CVE) and Christmas Valley West (CVW) radars between 10:00 and 12:00 UT on 14^{th} November 2012. Figure 7.3 shows the variations in the Doppler velocity as measured by the CVE (a) and CVW (b) radars against magnetic longitude and universal time, where blue represents the flow towards the radar and red is away. Both of these plots are made up from the data obtained from a series of range gate and beam cells covering a range of longitudes along a constant latitude.

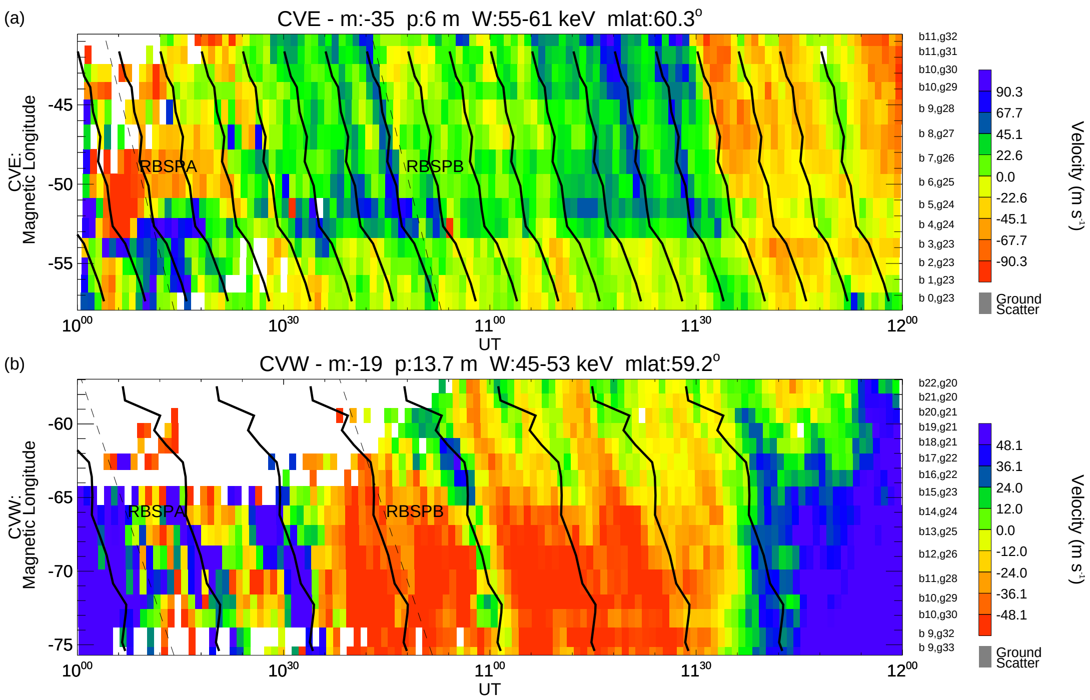

Figure 7.3: Wave observations - Radar line of sight velocity as measured by Christmas Valley East (top panel) and Christmas Valley West (bottom panel) in universal time - magnetic longitude coordinates. Each panel uses a string of range gate/beam cells along a constant longitude in order to provide a longitudinal view of the waves. Wave activity in the measured velocity is present in both panels, solid black lines represent the Fourier phase of the waves. Slanted dashed lines show the estimated trajectory of the particles that would have been observed by both Van Allen Probes.

Figure 7.4 shows the Fourier phases for the CVE wave in panel (a) and the CVW wave in panel (b). Both waves exhibit westward phase propagation and thus have negative m-numbers, suggesting a source in westward drifting ions, though the phase propagation and wave periods in both waves are both very different. The CVE wave has an m of ~-35 and a period of 361 s where the CVW wave exhibits an m number of only ~-19 but has a much longer period of 819 s. The phase fronts shown in this figure are overlaid on the radar data in Figure 7.3 as repeating thick black lines.

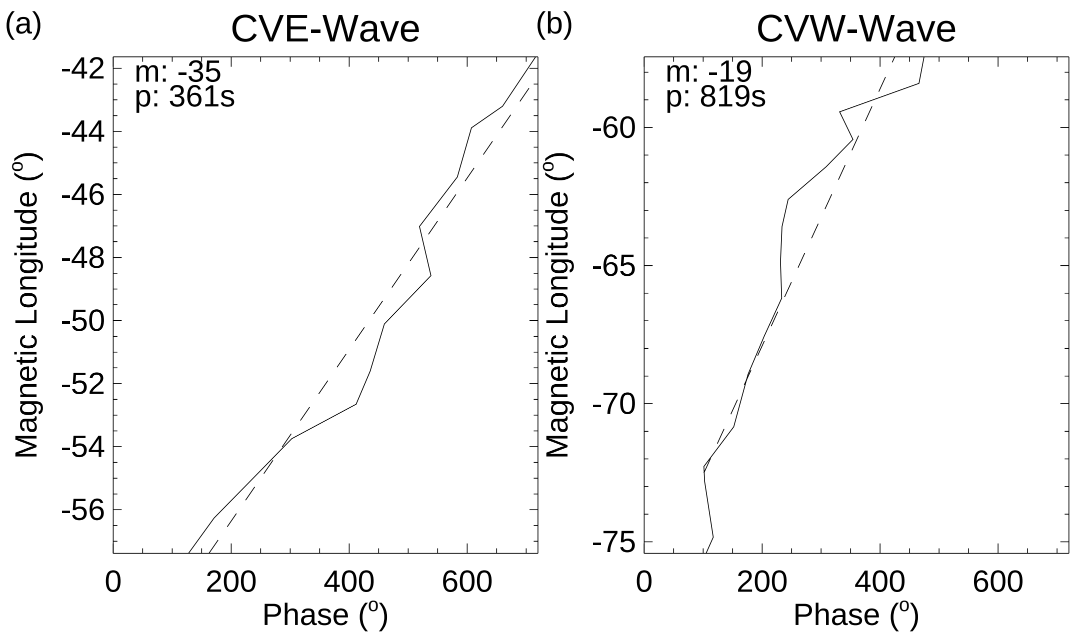

Figure 7.4: Fourier phase profiles - Fourier phase profiles derived for waves observed by CVE (a) and CVW (b) as a function of magnetic longitude. The dashed line is a linear fit to the phase gradients.

The periods of both of these waves appear to be typical of a drift-resonant interaction with a cloud of energetic particles when compared to the wave periods shown in Figure 5.7. This means that Equation 5.1 can be used to find the angular drift frequencies of the waves and therefore the angular drift frequency of the particle populations responsible for driving the waves. Even though the periods and wave numbers exhibited by the CVE wave and the CVW wave are quite different, they exhibited similar angular drift frequencies of 0.5×10^{-3} rad s^{-1} and 0.4×10^{-3} rad s^{-1} respectively.

The angular drift frequency of the particles is directly related to their energy by Equation 2.73. The approximate energy range predicted for the particles responsible for driving the CVE wave is 55 - 61 keV and the range for CVW is slightly lower at 45 - 53 keV.

7.3.2 Substorm Location

The auroral electrojet indices (AE, AL, AO and AU) can be used to help determine whether these waves may be related to substorm activity. The indices are a measure of global electrojet activity derived from the H component of the magnetic field (*Davis and Sugiura*, 1966). During a substorm, the AL index should decrease in response to the westward electrojet that forms part of the substorm current wedge (see Section 1.2.4.1 on page 18).

Figure 7.5 shows the AU and AL indices in panel (a) and the AE and AO indices in panel (b) where it is evident that there are a number of substorm activations prior to the onset of the two waves mentioned above. There is a clear, sharp onset to this period of substorm activity, marked on both panels at 8:30 UT, characterised by a large decrease in the AL index associated with a strong increase in the strength of a westward electrojet.

The significant amount of substorm activity present on that morning comes as no surprise when looking at the D_{st} index for the few days surrounding the event in Figure 7.6. This figure shows that the event being studied occurred shortly after the end of the main phase of a moderately intense geomagnetic storm (see Section 1.2.4.2 on page 20).

In order to locate the substorms it was necessary to use the method described in Chapter 6 by using ground magnetometers. Figure 7.7 shows the perturbations in the magnetic field as measured by the longitudinal (panel (a)) and latitudinal (panel (b)) magnetometer chains.

Figure 7.7a shows the perturbations in the D component of the magnetic field as a function of magnetic longitude (x-axis) and UT (y-axis) where a positive perturbation is represented by red and a negative perturbation is represented by blue. The horizontal dot-dashed line at 8:30 UT represents the estimated onset time of the substorm found using the AE indices, the curved dotted lines represent the longitude of the Van Allen Probes with time and the vertical dashed lines show the longitudes of the magnetometer stations used. Using the method described in the previous chapter, the approximate

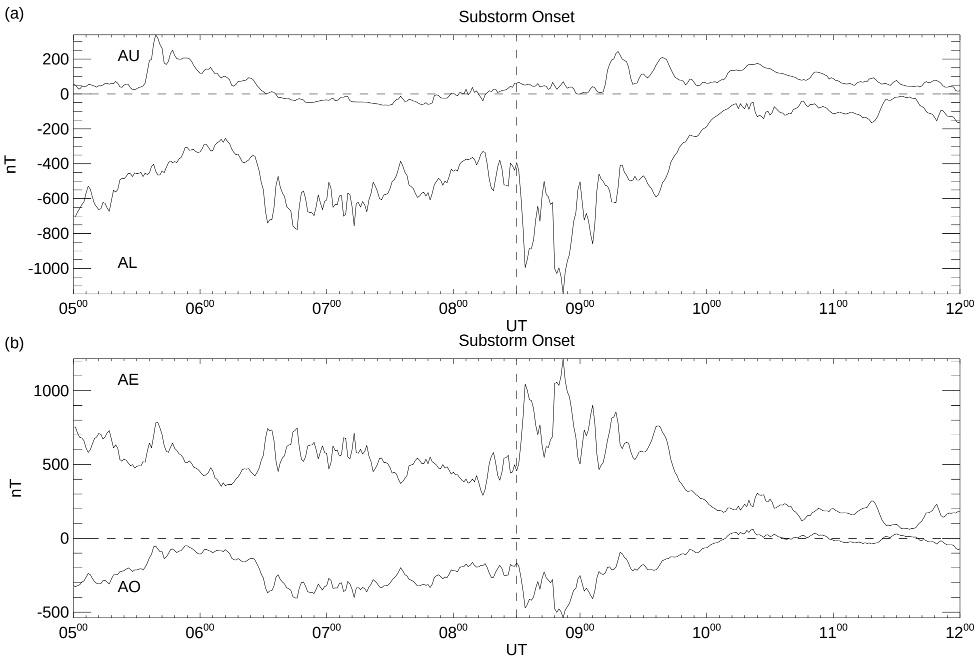

Figure 7.5: Auroral Electrojet indices - The auroral electrojet indices show that there was substorm activity prior to the substorm being studied and that this substorm started around 8:30 am.

longitudinal extent and central point of the substorm has been derived from the positive and negative bays and is represented by three solid black lines.

Figure 7.7b shows the perturbations in the Z component of the magnetic field as a function of magnetic latitude (y-axis) and UT (x-axis). The vertical dot-dashed line at 8:30 shows the substorm onset time, the curved dotted lines show the latitude of the Van Allen Probes ionospheric footprints with time and the horizontal dashed lines show the latitudes of each magnetometer station. The latitudinal extents and central latitude of the substorm are represented by the solid black lines and are also derived using the method from the previous chapter. Here, the magnetometer bays caused by the SCW are not obvious enough for the algorithm to detect until ~9:20 UT, this is most likely due to the SCW initially existing to the east of the latitudinal magnetometer chain, where the bays in Z can only be seen when the electrojet passes directly over the chain. As is observed in Figure 7.7a, the upward field-aligned current spread west with time and eventually passes the latitudinal chain, causing the bays to become present.

Figure 7.8 shows the H component of the raw magnetometer data obtained from

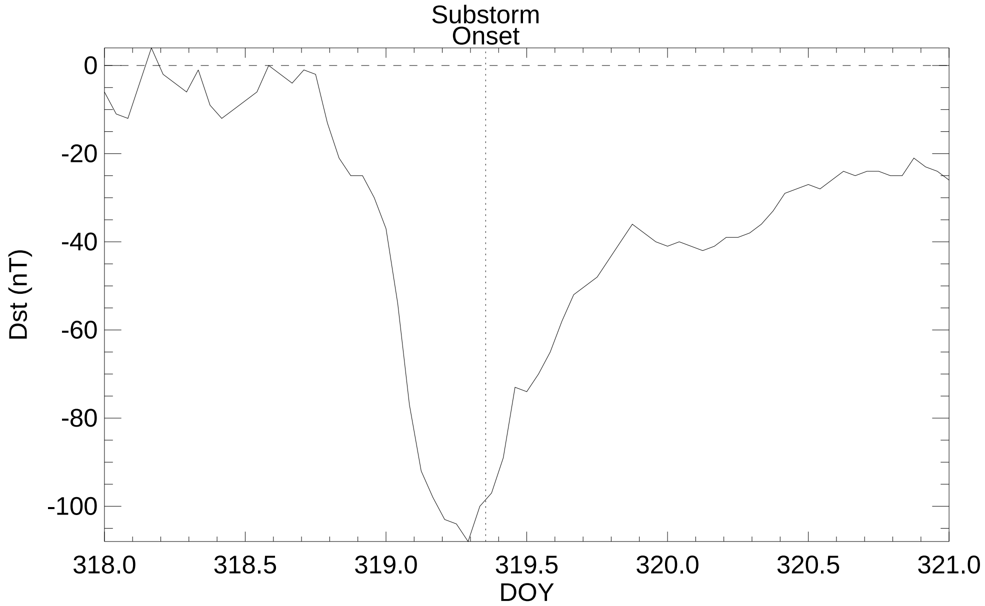

Figure 7.6: D_{st} **index** - The D_{st} index around the time of the event indicates the onset of a geomagnetic storm prior to the event being studied.

the latitudinal chain between 7 and 12 UT where the first data point in each plot is set to zero. Sharp drops of up to 400 nT are observed in the H component by the Baker Lake (BLC), Fort Churchill (FCC) and Weyburn (WEYB) magnetometers around the onset time at 8:30 UT. The large drops in the H component indicate the presence of a nearby westward electrojet forming part of the substorm current wedge. The local drops in H arrive a little later than the onset of the substorm, as with the bays in Z and are likely to be late for the same reason.

The largest extent in magnetic latitude and magnetic longitude is shown in Figure 7.2 as a black box. The substorm appears to be very much skewed towards dawn. The approximate centre of the substorm at onset is around 4.4 MLT, where usually substorm onsets occur close to midnight. It appears that the SCW centre is located to the east of the location of both westward-propagating wave observations which would be expected from the results of Chapters 5 and 6. The location of this substorm onset can be compared to other substorm onsets to see just how unusual it is.

Figure 7.9a shows a histogram of the magnetic local times of the substorms that appear on the list of substorms provided by *Frey et al.* (2004). Included on this plot

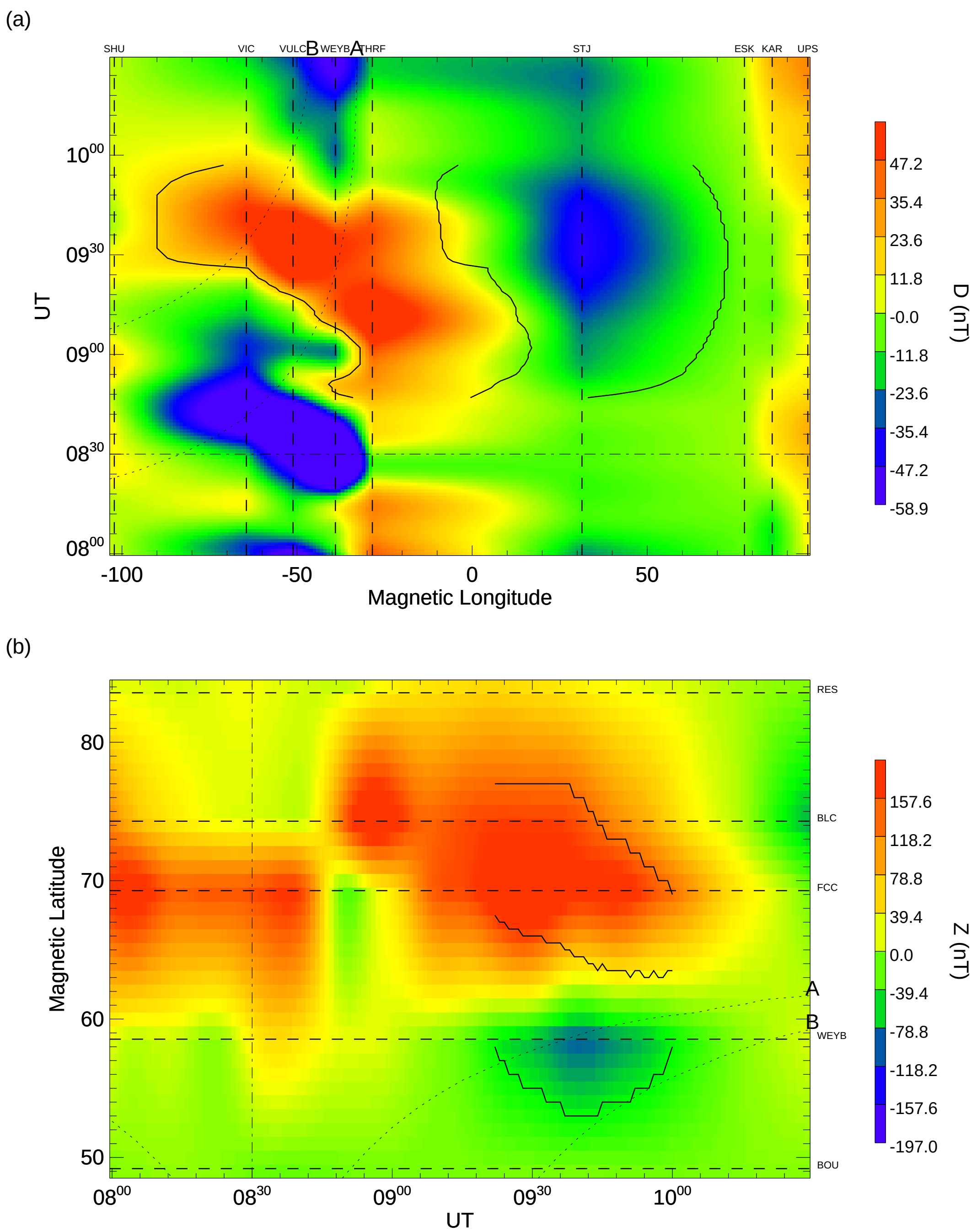

Figure 7.7: Magnetic perturbations due to substorm current wedge - Top panel shows magnetic perturbations in the D component of the magnetic field as a function of time and magnetic longitude, indicating where the substorm current wedge existed. The bottom panel shows the perturbations in the Z component of the magnetic field as a result of the substorm current wedge nearby.

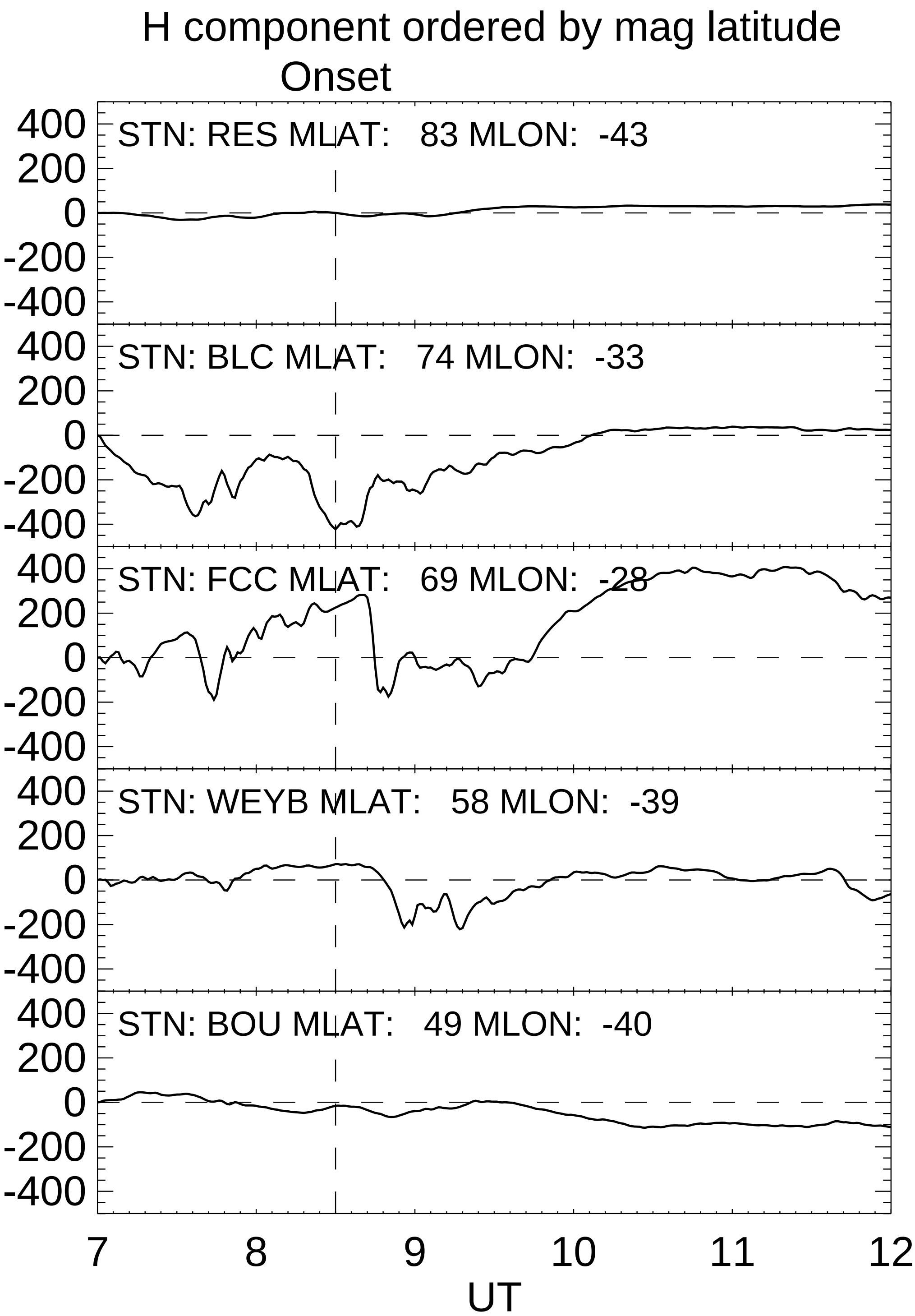

Figure 7.8: H **component of magnetic field data** - Raw H component data measured by the latitudinal chain of magnetometers where the first data point is set to zero in each plot. Drops in H are observed near to the onset time at ~8:30 UT.

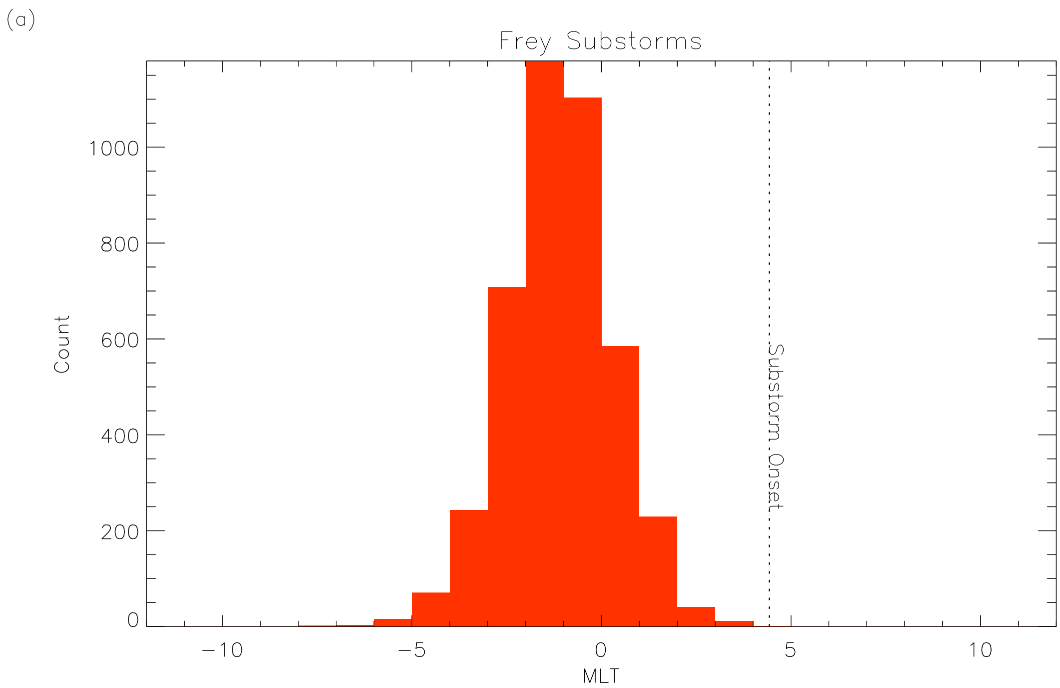

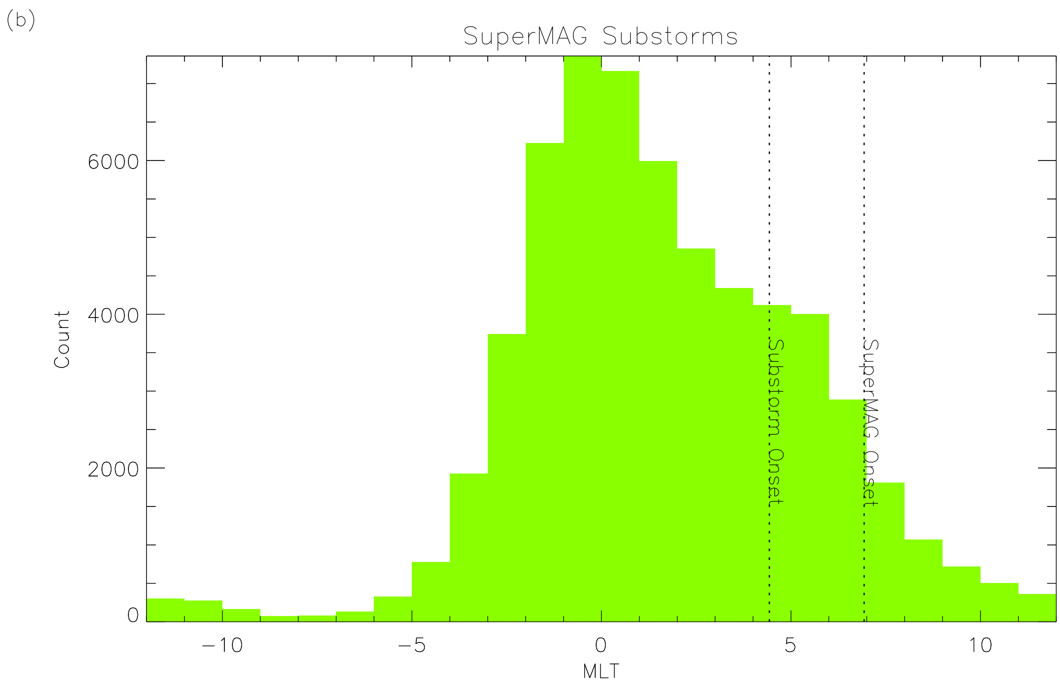

Figure 7.9: Substorm local times - Histograms of the magnetic local times of substorms in the Frey list (a) and the SuperMAG list(b). Vertical dashed line in each plot labelled 'Substorm Onset' shows the local time of the centre of the substorm as determined by the technique described in Section 6.4 for this event, also another line shown in the SuperMAG plot shows the location of the substorm onset as detected automatically by SuperMAG using the SML index.

is a vertical dash line to represent the approximate location of the substorm associated with this event. On this list of substorms, most of the substorms observed appeared in the two hours of MLT prior to midnight and very few substorm onsets occurred as far as 4 MLT. It is possible that the reason that no substorms were observed past 4 MLT was due to dayglow obscuring auroral features caused by substorms at such locations.

SuperMAG provides a list of substorm onsets detected using their own SuperMAG indices SME, SMU and SML (*Newell and Gjerloev*, 2011a,b). The SME, SMU and SML indices are equivalent to the AE, AU and AL indices, however instead of using only 10-13 magnetometers, more than 100 stations may be used to create the SuperMAG indices. The conditions required for the onset to be counted by SuperMAG are that there must be at least a 45 nT drop in SML over a 3 minute time period and it must be a sustained drop so that the first 30 minutes after onset must average 100 nT below the initial value before onset.

Figure 7.9b shows a similar plot for the 59249 substorm onsets detected between 1^{st} January 1981 and 6^{th} July 2013. The peak in this distribution of substorms occurs just before midnight similar to panel (a), though this distribution is far more spread out. It is unlikely that the onsets detected close to noon are substorm related, but there are a lot of potential substorm onsets around 4-5 MLT unlike the distribution of Frey substorms.

Also shown in Figure 7.9 is a vertical line with the label 'SuperMAG Onset' which refers to a substorm onset detection potentially related to the event being discussed in this chapter. This onset occurred at 8:26 UT at around 6.9 MLT, which is much further east of the centre of the substorm as determined in Figure 7.7 but lies close to the eastern edge of the substorm as measured using that technique.

7.3.3 Van Allen Probe Location

The exact location of the Van Allen Probes during this event is important to know because it affects whether the particle instruments will be able to detect any relevant particle injections for this event. Figure 7.2 shows that both of the spacecraft have ionospheric footprints in the general vicinity of both waves. Probe B even crosses the location of the CVE wave directly, but both need to be near enough in both latitude and longitude to potentially detect the particles responsible for driving both waves.

It is expected that the particles that drive each wave will originate on the same L-shell as that which the waves exist upon, so if the Van Allen Probes were to detect these particles it would have to be at the time when they cross this particular L-shell. As both waves exist at slightly different latitudes, it is necessary to look at the particle data at two points in time for each spacecraft. The times of interest when probe A crosses the latitude of the CVW wave and the CVE wave are 9:45 and 10:00 UT respectively. As the orbit of probe B is slightly behind that of probe A the equivalent times are 10:30 and 10:45 UT respectively.

Figure 7.10 shows the orbital configuration of the probes between 8:30 and 12:00 UT plotted in Solar Magnetic coordinates, where Z is along the dipole axis, the XZ plane contains the Earth-Sun line and Y points in the dusk direction. Panel (a) shows that for the majority of this time, the probes are located in the post-midnight sector, while rapidly increasing in radial distance from the Earth. Panels (b) and (c) show that the probes remain very close, but not completely in the magnetic equatorial plane.

It is important to know where the probes are located along a given field line as this affects whether the probes will experience particles of all equatorial pitch-angles. Figure 7.11 shows the field line that each probe is on when they cross the latitudes of each wave projected on the XZ plane as found using the T96 field model. The top row relates to probe A and the bottom relates to probe B while the left column is for the CVW latitude crossings and the right is for the CVE latitude crossings. The red dot in each plot shows the location of the probes along the field line, and the horizontal dashed line shows the magnetic equator.

In each of the panels of Figure 7.11 the probes are shown to be slightly north of the equator, which means that particles with 90° equatorial pitch angles, α_{Eq}, will not be observed by the HOPE and MagEIS instruments. As the largest local pitch angle to the field line at the location of the probes would be 90° and the strength of the field can be calculated using a T96 model field, the first adiabatic invariant (see 2.14) can be used to find out what equatorial pitch angle a particle must have in order to mirror at this location. This estimate of the maximum equatorial pitch angle is presented in each panel and varies between ~76 – 83°. This range of α_{Eq} has been taken into account when calculating the particle energies expected for the above waves using Equation 2.73.

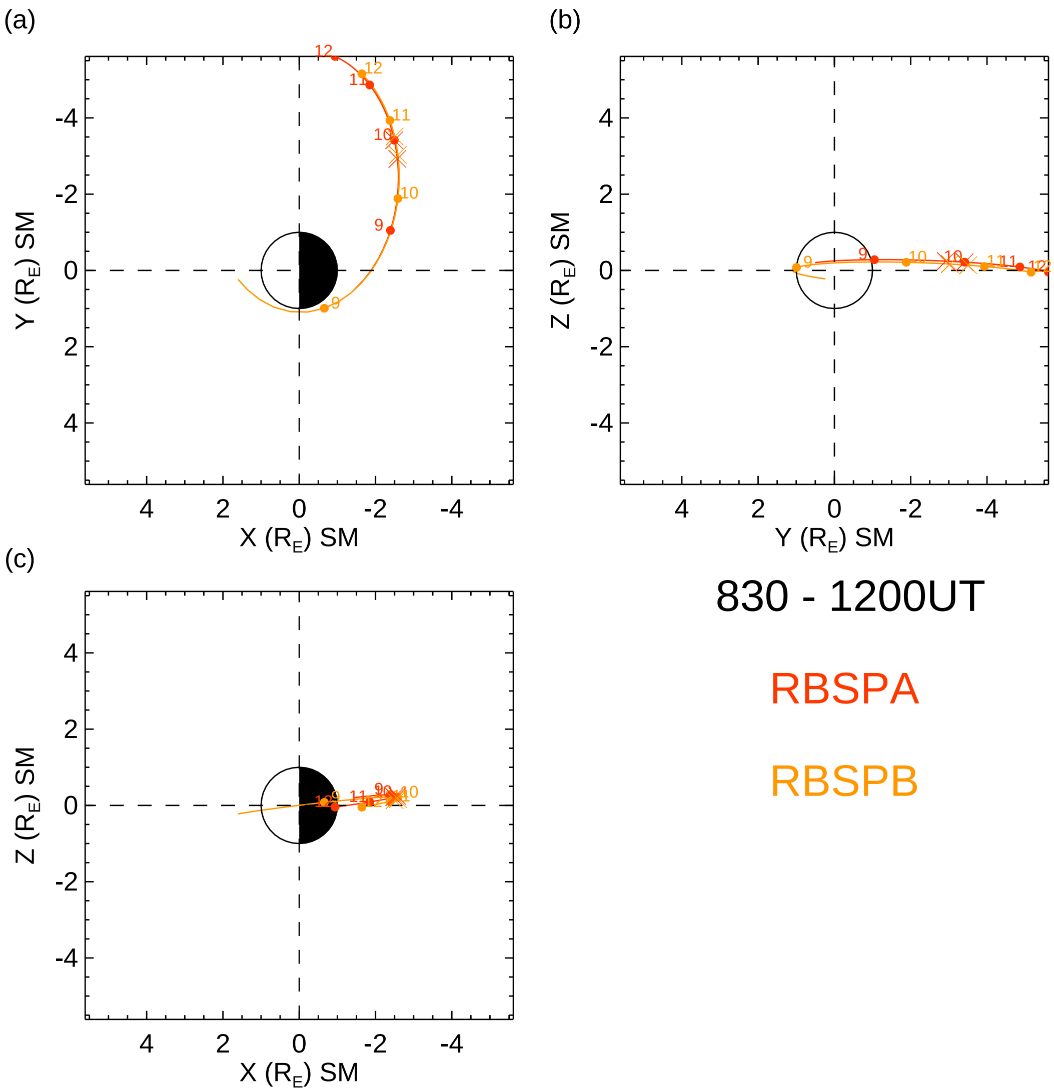

Figure 7.10: Van Allen Probe orbital configuration - The eccentric orbit of the Van Allen Probes lies close to the magnetic equatorial plane are plotted in Solar Magnetic (SM) coordinates. The four times of interest where the probes cross the latitudes of the waves are represented by crosses, all four of these times occur when the probes are near to 3:00 MLT.

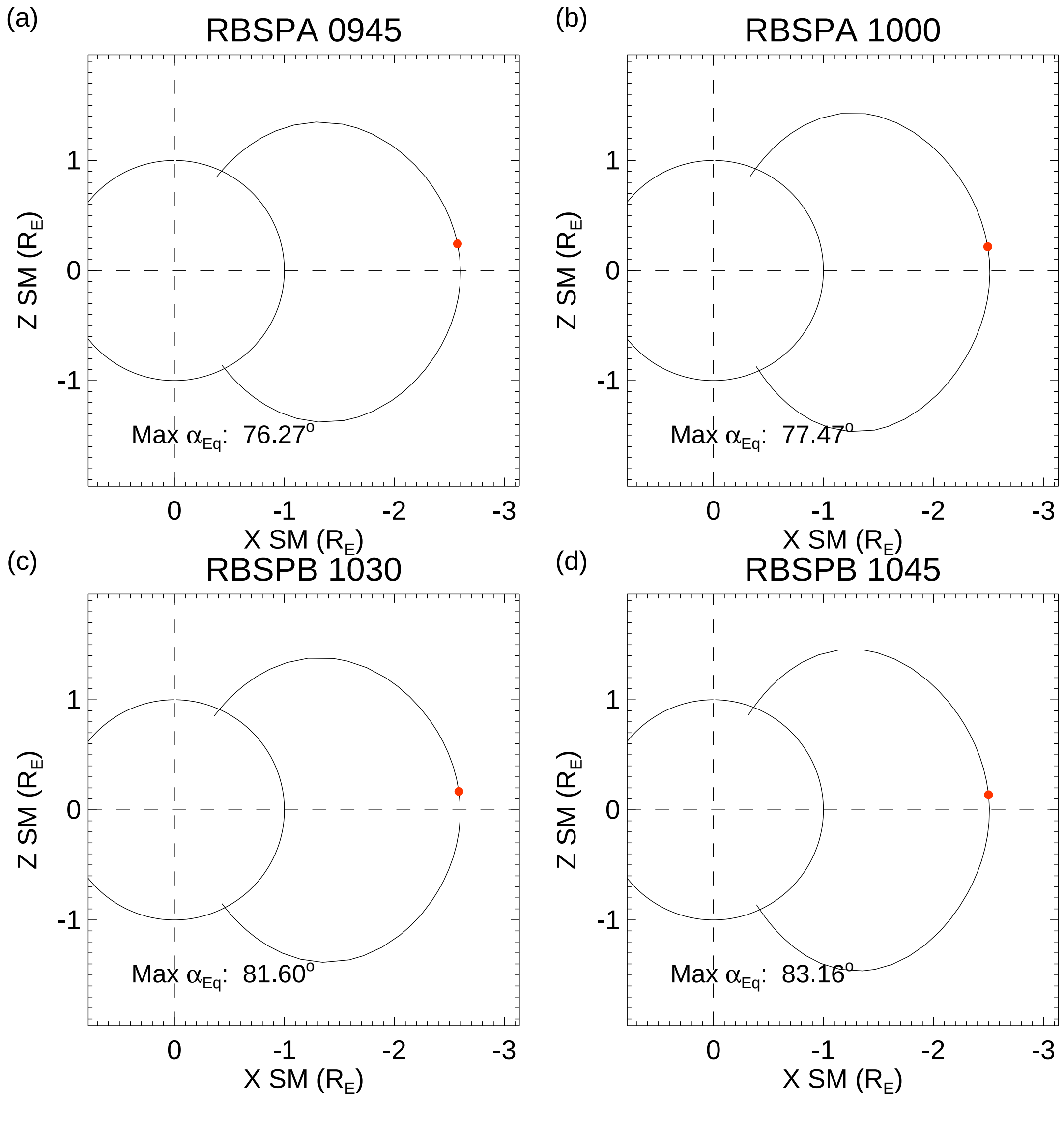

Figure 7.11: Field line locations - Each panel shows the field lines that the probes existed on when their footprints crossed the latitude of both waves. The model field can then be used to calculate an approximate estimate of the maximum equatorial pitch angle for particles that could reach the spacecraft.

7.3.4 Particle Data

Figure 7.12 shows the spin-averaged differential proton flux as measured by probe A in panel (a) and B in panel (b) between each probes times of interest - 9:45-10:00 UT and 10:30-10:45 respectively. The colour scale is plotted on a log scale as there are orders of magnitude of difference between the lower energy bins and the higher energy bins.

The differential proton flux in these plots was then converted to ion distribution functions (IDF) using the method described in Section 4.5. Figure 7.13 shows these ion distribution functions as a function of UT (x-axis) and energy bin (y-axis). In both plots, there are increases in the IDF at energies close to those predicted by the waves, where the horizontal lines represent these energies.

In order for there to be free energy available to drive a wave in the IDF, there must be a positive gradient at the same energy as the particle energy required to drive the wave. In other words, the positive gradient around this energy would mean that there are more particles with a higher energy than that required to drive the wave than there are particles with less energy such that energy can be taken from those higher energy particles and transferred to the wave leading to wave growth as discussed in Chapter 2.

Figure 7.14 shows the gradients in the IDFs shown in Figure 7.13 against time (bottom axis) and L-shell (top axis). Red represents negative gradients responsible for wave damping and green represents positive gradients responsible for wave growth. The IDFs had to be smoothed using a boxcar algorithm to create these plots as there is a small amount of jitter between the bins. Both panels show that there are positive gradients present at similar energy ranges to that predicted by the waves indicating that particles observed by the Van Allen Probes are in fact potential candidates for the driving particles for these ULF waves. The energy level at which there is potential for wave growth reduces very gradually over the ~0.25 L-shells (~1°) that the probes move through in these plots.

Figure 7.15 shows the IDFs for each of the four times of interest, with the two IDFs produced by probe A in the top row and those produced by probe B in the bottom and the IDFs related to the CVW wave latitude are in the left column and those related to the CVE wave latitude are in the right column. In each panel the energy ranges predicted for the driving particles of the appropriate waves are shown as two vertical

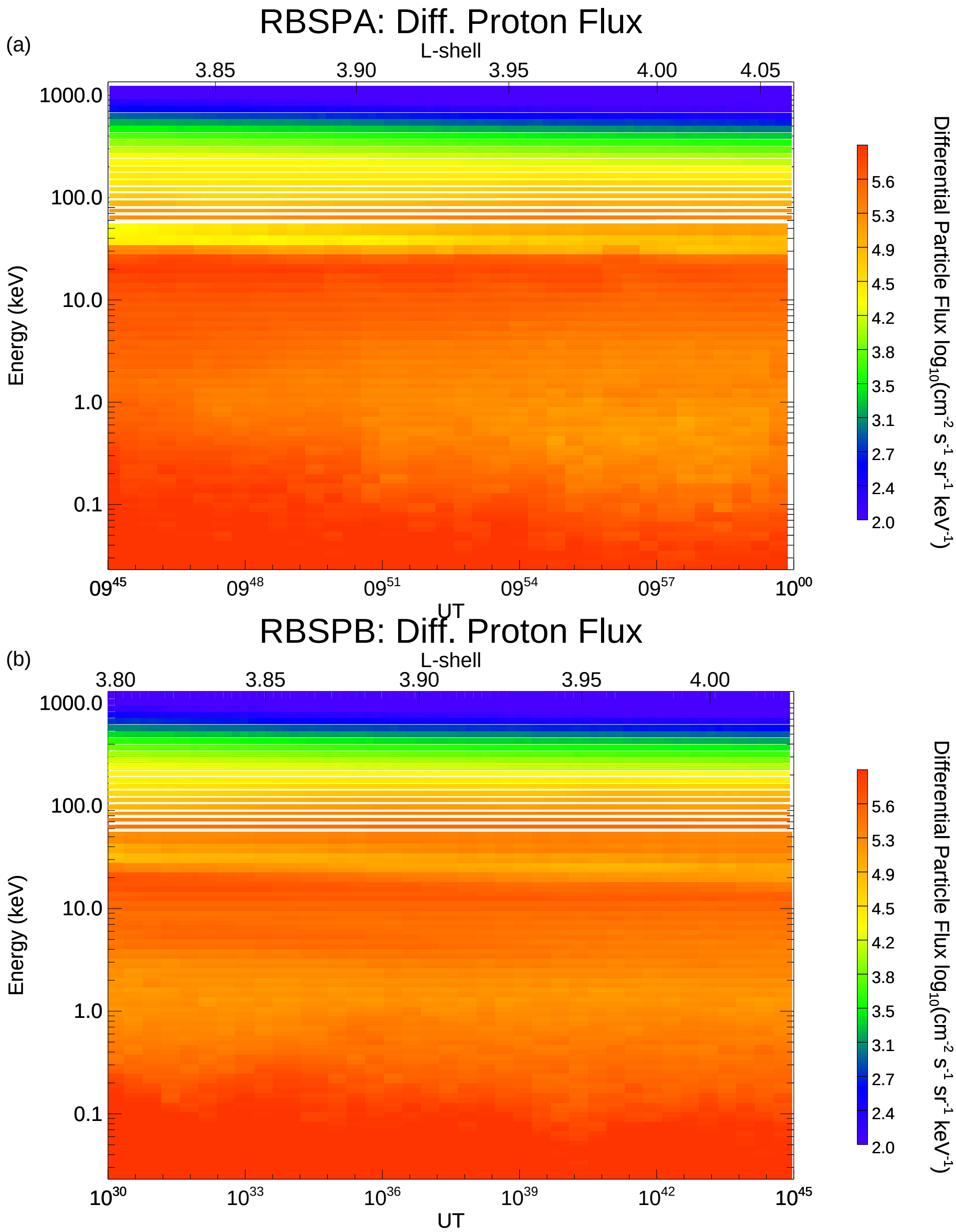

Figure 7.12: Differential particle fluxes - Differential particle flux as measured by HOPE and MagEIS on probes A (a) and B (b) between the times at which each probe crosses the latitude of each of the waves.

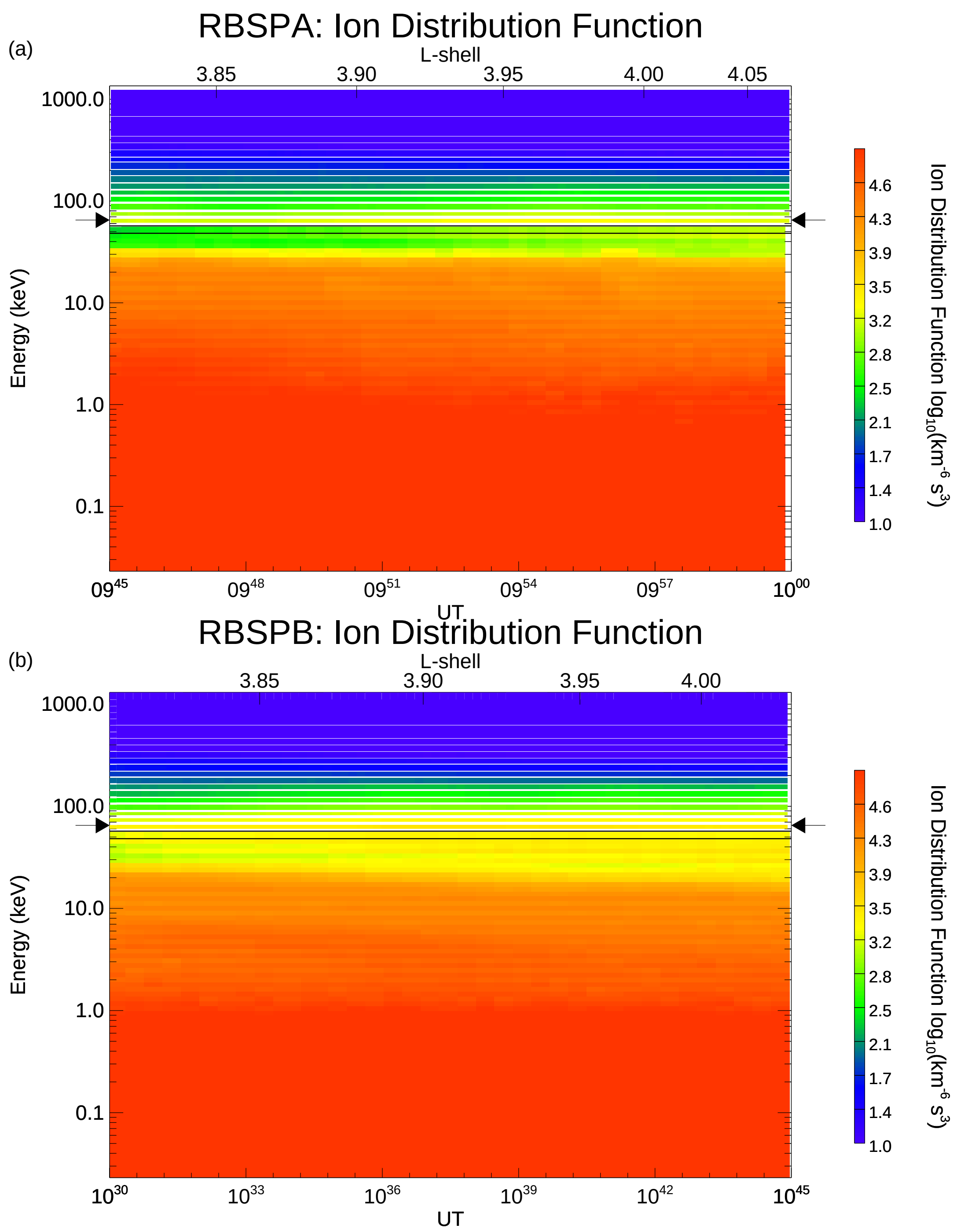

Figure 7.13: IDF as a function of time - IDFs as a function of time for both spacecraft between the times of both latitude crossings where a bump around the energy of the waves is marked with arrows.

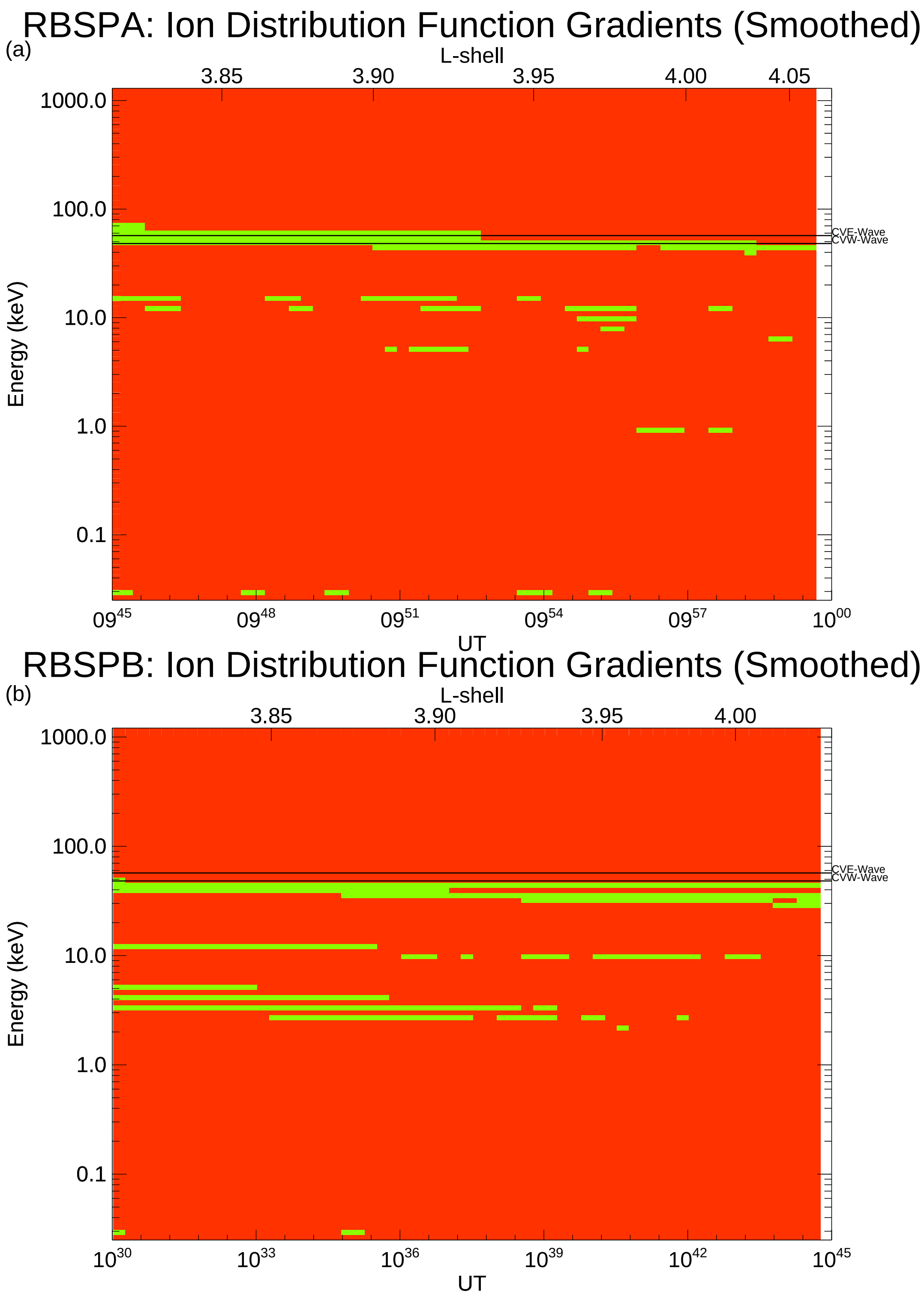

Figure 7.14: IDF gradients - Gradients of the IDFs displayed in Figure 7.13 where green is positive and red is negative.

lines. The parts of the IDF derived from HOPE data are shown in blue and those derived from MagEIS are shown in red.

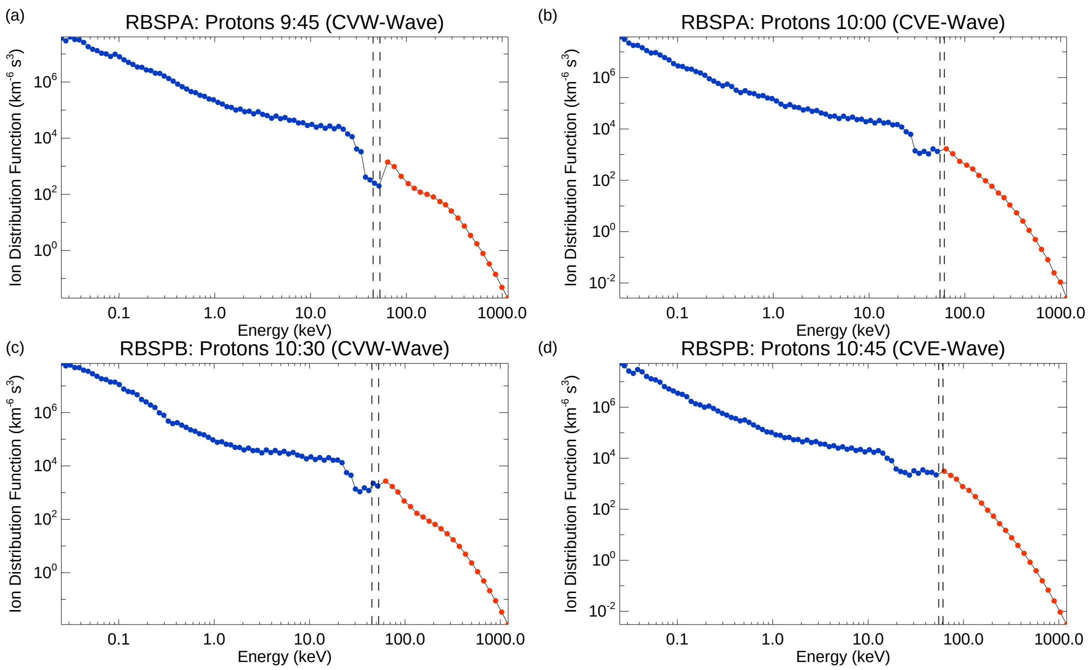

Figure 7.15: IDFs for times of interest - Ion Distribution Functions (IDF) for each spacecraft at both of the waves latitudes where blue denotes the portion of the IDF calculated using HOPE data and red is that derived from MagEIS data..

In each panel of Figure 7.15, there is a notch in the IDF present around the energies predicted from the waves. In at least panels (b) and (c) there appears to be free energy available for each of the waves. Panel (d) isn't so clear as to whether there is still free energy within this IDF and it is difficult to tell whether the the positive gradient in panel (a) between the HOPE and MagEIS data is a genuine indicator of available energy, or just an artefact created by the use of two different instruments.

It is clear from the IDFs that there was free energy available in velocity space at the required energy level to drive the waves, Figure 7.16 considers the spatial aspect of the IDFs. Panels (a) and (b) show the IDFs of several energy bins between 20 and 75 keV as probes A and B sweep out, away from the Earth, through a number of L-shells between 8:30 and 12:00 UT . As discussed in Chapter 2, wave energy can be sourced from the spatial gradient in the IDF, where the IDF must increase closer to the

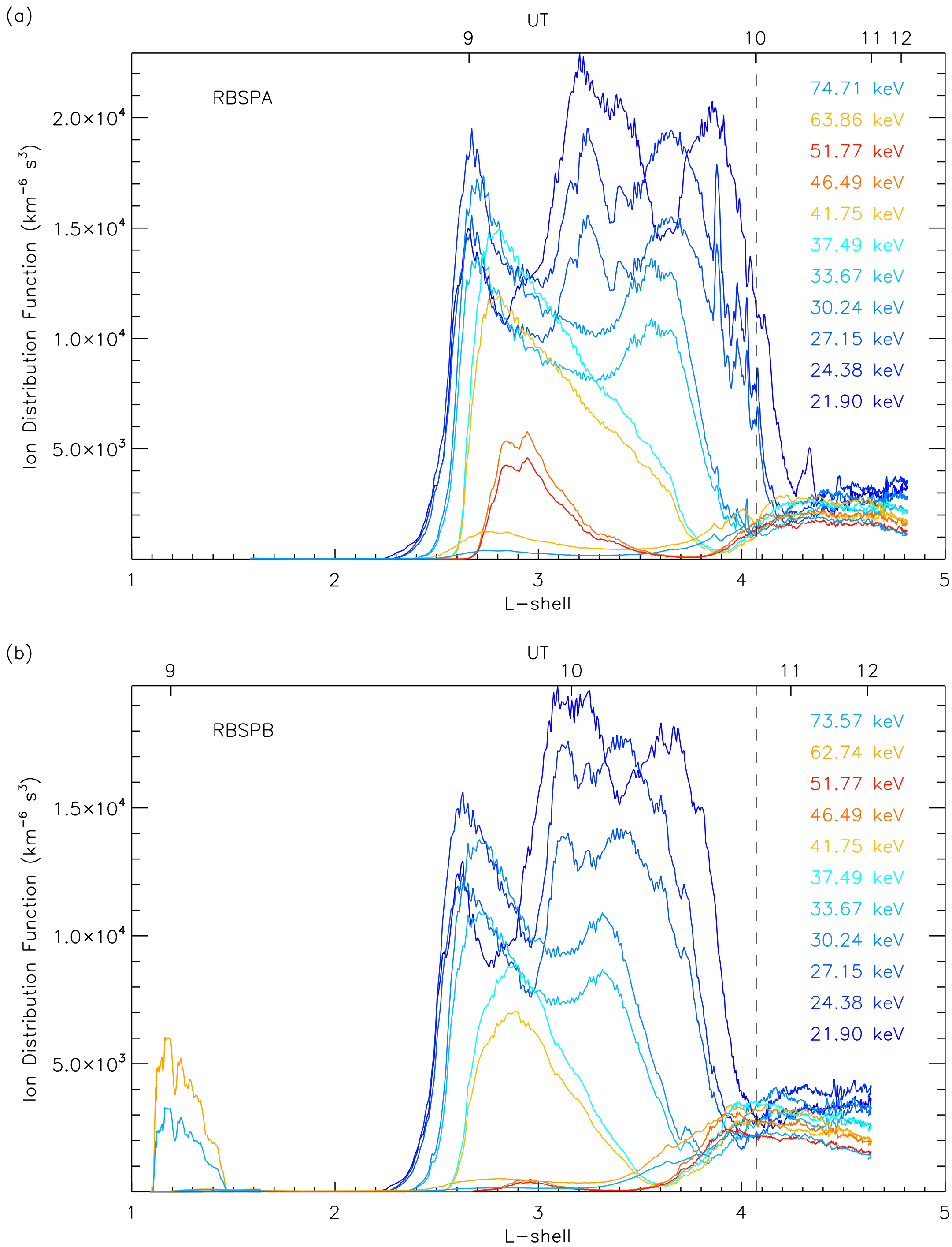

Figure 7.16: IDF variation with L-shell - Ion distribution functions calculated for the energy bins between 20 and 75 keV for RBSPA (a) and RBSPB (b) as a function of L-shell as the probes traverse away from the planet in their orbits. The energy bins closest to the energy range of the driving particles are coloured red and those further away are more blue. Dashed vertical lines represent the four times of interest shown in Figure 7.15.

Earth. The inward gradients in the IDFs appear to be present in the data from both probes, but those which exist at the energy levels required to drive the waves discussed in Section7.3.1 aren't at the same L-shell as either wave, and those which are on the same L-shell as the waves are at much lower energy levels.

In both panels of Figure 7.16, the ion distribution functions at all levels, including those within the energy range of the waves, show an increase in the vicinity of the waves beyond $L = 3.5$. It is unclear whether the variations shown in Figure 7.16 are spatial or temporal as both spacecraft appear at different L-shells at different times. This increase in the IDF may be consistent with an injected cloud of particles acting as a seed for the waves as suggested by *Mager and Klimushkin* (2007, 2008) which becomes further amplified by the free energy in the velocity space distribution observed in Figure 7.15.

7.4 Discussion

7.4.1 Particle Origins

In the previous chapters, the angular drift frequency of the particles inferred from the properties of the waves have been used to determine whether they were likely to originate from within the vicinity of a substorm by tracing their position back in time from the time and location of the start of the wave. This was done assuming that the angular drift frequency remained constant from the point of injection until they had reached the wave. If the particles passed through the longitudinal extent of the substorm while it was present then this would support the idea that the particles driving that particular wave had originated from the substorm in question.

A similar procedure must be done for this event, not only to check that the waves could have been driven by this substorm, but to be sure that the particles observed by the Van Allen Probes both had originated from this substorm and would have subsequently arrived in an appropriate location to have driven part of the ULF waves observed. The assumption that ω_d is constant still stands.

Figure 7.17 shows a visual representation of this analysis. Each plot is a magnetic longitude (x-axis) against UT (y-axis) plot similar to that used in Figure 7.7a where panel (a) relates to the CVE wave and panel (b) relates to the CVW wave. The

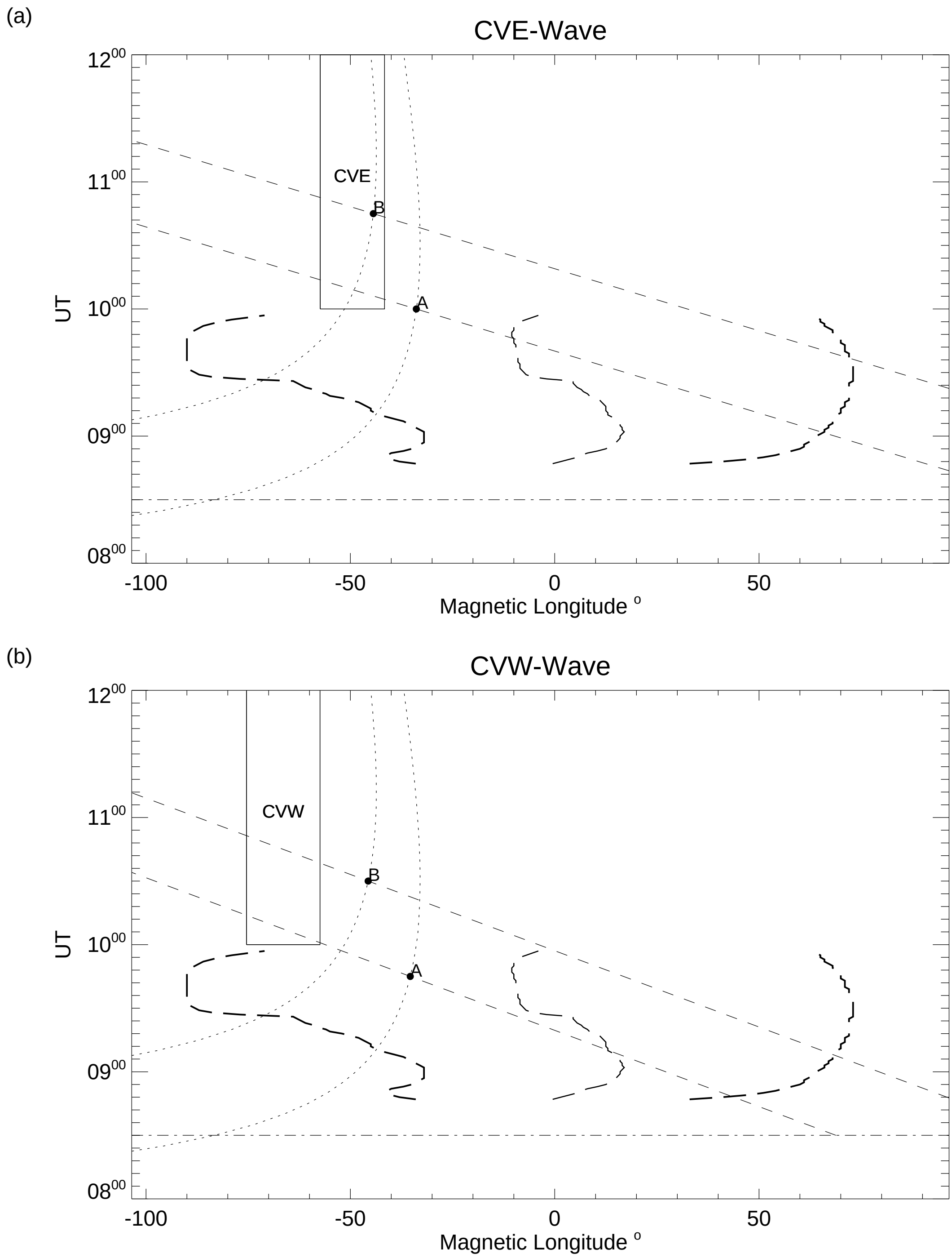

Figure 7.17: Particle origins - Both panels show the longitudinal extent of the substorm as two thick dashed lines as derived in Figure 7.7a with the time and longitude of the wave observations represented by a solid rectangle. The spacecraft positions when they cross the latitude of the waves are represented by a black dot. Using the angular drift frequency determined by each wave, the particle trajectories that would have intercepted the spacecraft before or as they reached the wave observations are shown as the diagonal dashed lines.

horizontal dot-dashed line at 8:30 UT represents the onset of the substorm and the longitudinal limits of the substorm determined from the magnetometer data are presented as two bold long-dashed lines. The location and duration of each wave is represented by the solid-lined box in each figure. The longitude of the Van Allen Probes as a function of time is overlaid as a dotted line where the time and location at which the probes cross the latitude of the wave is signified by a bold dot.

In both panels of Figure 7.17, the trajectory of the particles that were observed in the positive gradient region of the Van Allen Probe IDF data, and are candidates for both injection during the substorm and driving the observed waves, are represented by a diagonal dashed line, where the gradient of the line is determined using ω_d. It appears that in all four cases, the particles that were measured by the probes would have gradient-curvature drifted at the appropriate velocity to pass through the location of the wave and driven the oscillations that were presented in Figure 7.3. The times at which the particles would have crossed the wave are represented by dashed lines in both panels of Figure 7.3. Also, looking back in time before the particles had reached the probes, it appears that they would have originated from some location within the extent of the substorm current wedge.

7.4.2 Pitch Angle Distributions

As mentioned in 4.5, it is possible to obtain pitch angle distributions for certain data. The HOPE instrument can provide this data for the ions and therefore see which pitch angles are most likely to drive the waves observed above.

Figure 7.18 shows the HOPE part of the IDFs in Figure 7.15 separated into pitch angle bins. Unfortunately, the energy range provided by the CVE wave is slightly above the scope of HOPE, so panels (b) and (d) don't show the relevant parts of the IDF. It appears that the the IDFs all peak around the 90° pitch angle, possibly due to particles with pitch angles closer to 0 or 180° falling within the loss cone.

The positive gradient present in each panel of Figure 7.15 is also detectable in the pitch-angle separated data throughout the entire range of pitch angles. The location of the notch appears to change with pitch angle, such that the notch covers lower energies at pitch angles closest to 90°.

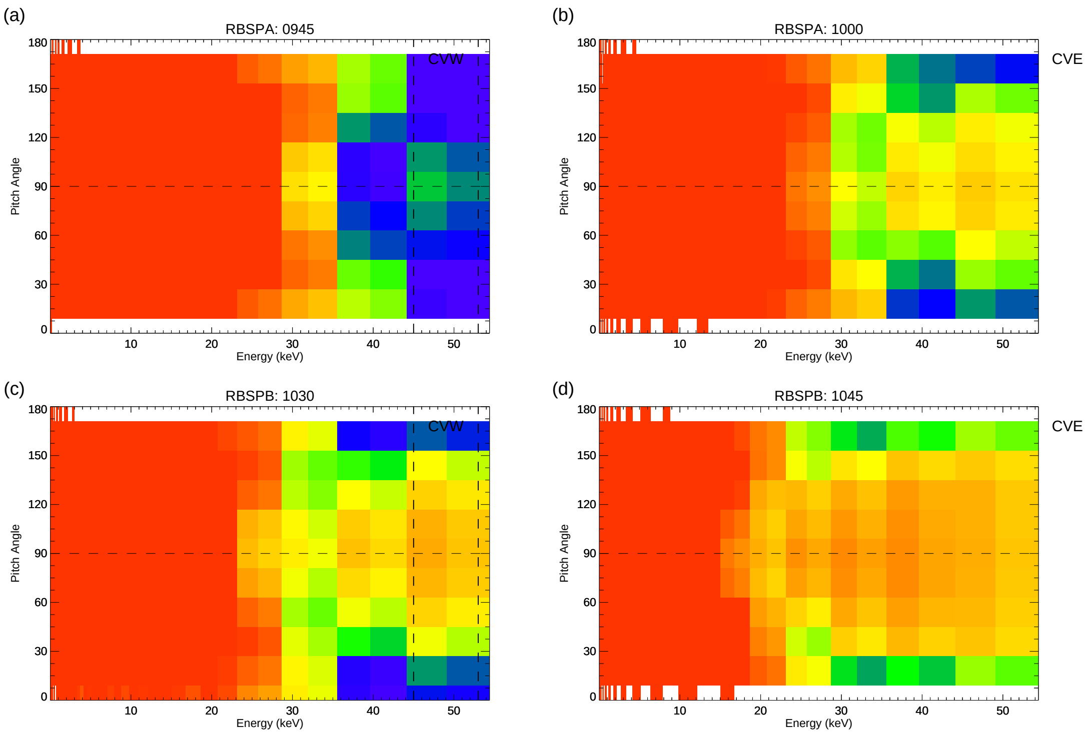

Figure 7.18: IDFs split into pitch angle bins - The IDFs as presented in Figure 7.15 split into their pitch angle distributions.

Figure 7.19 shows the gradients of Figure 7.18 on the same set of axes. The IDFs had to be smoothed slightly to remove most of the jitter in the data so that the gradients could be seen clearly. Panels (a) and (c) show that there is a positive gradient in the IDFs in the energy range of the wave, though in (a) this is very much limited to pitch angles close to 90° and a small range of energy, where the positive gradients present in panel (c) are spread over a much larger range of energy and pitch angle.

Even though the energy range of the CVE wave is beyond what HOPE is capable of measuring, the gradients observed in (b) and (d) follow a similar pattern to those in (a) and (c). The later observation sees the positive gradients spread over a larger range of particle energies.

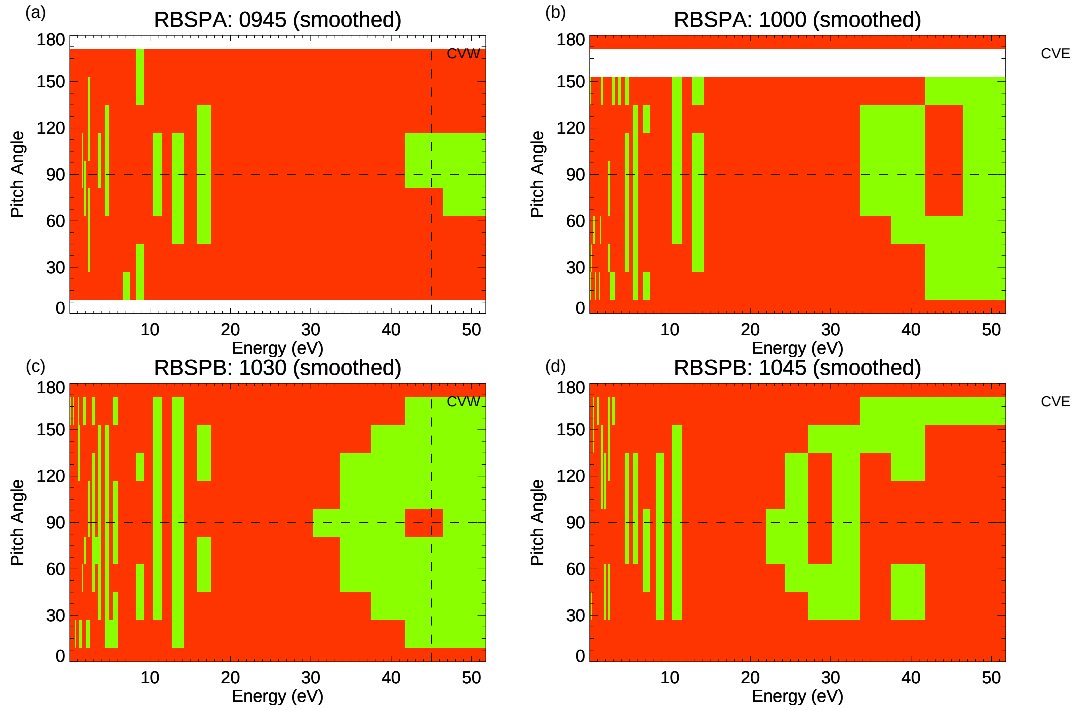

Figure 7.19: Pitch angle IDF gradients - Gradients of the IDFs shown in Figure 7.18 where green represents a positive gradient and red represents a negative gradient.

7.4.3 Comparison to Previous Results

Figure 7.20 shows a comparison of the current results with those obtained from the previous two chapters. In red is the CVE wave, in blue is the CVW wave, in grey are the waves from Chapter 5 and in black are those from Chapter 6. Panel (a) is the comparison of the azimuthal wave numbers, panel (b) is the comparison of the angular drift frequencies and (c) is the comparison of the particle energies calculated using Equation 2.73. Each panel shares a common x-axis where wave events are plotted against their azimuthal location relative to the centre of the substorm, wave observations to the west of the substorm are on the left of the plots and wave observations to the east of the substorm are on the right of the plots. The centre of the substorms for the grey points are all determined using IMAGE data, the centre of the substorm is defined using magnetometer bays for the coloured points and the black points are a mixture of the two.

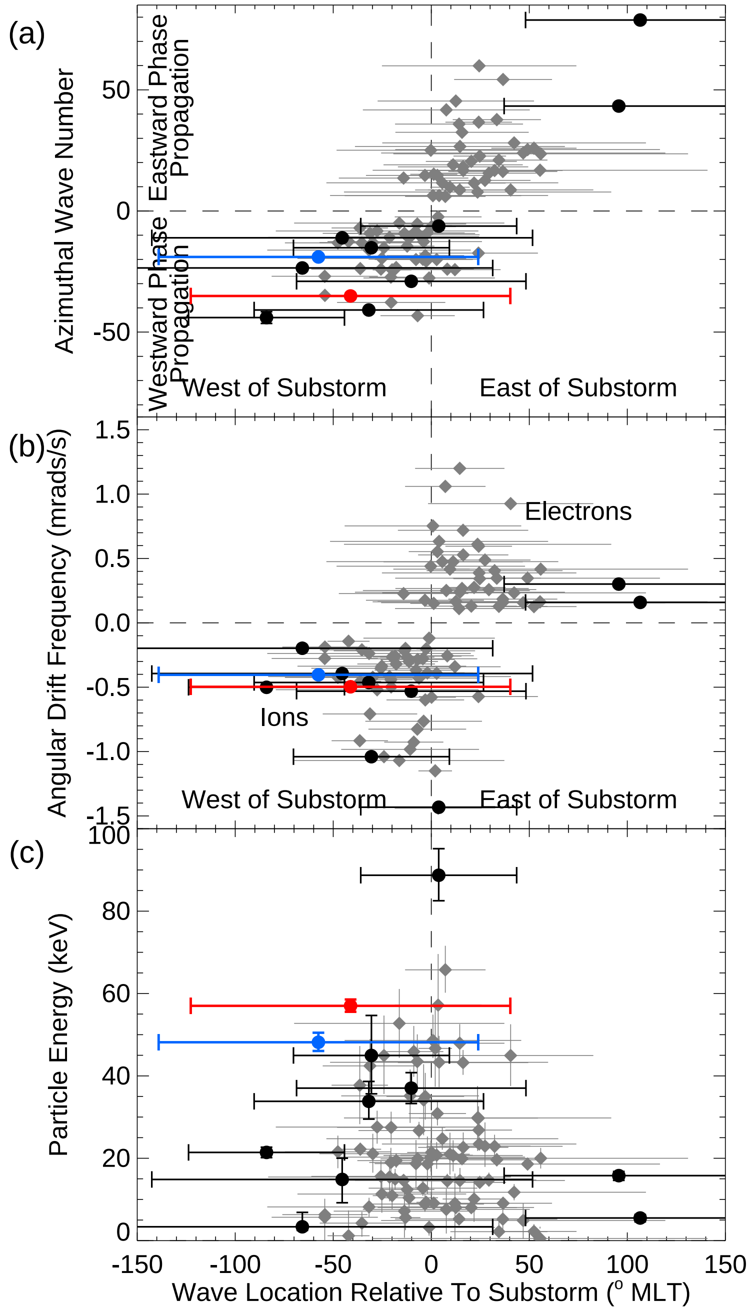

Figure 7.20: Comparison to previous results - Comparison of results obtained in this chapter to those from the previous chapters. Panel (a) shows the azimuthal wave numbers, (b) shows angular drift frequencies, and (c) shows inferred particle energies all plotted against the wave location relative to the substorm, events to the left of the plot are waves which occurred to the west of the substorm and events to the right were to the east. Results from Chapter 5 are in grey, results from Chapter 6 are in black while the red and blue correspond to the CVE and CVW waves from this chapter respectively.

Panel (a) shows that while the CVE wave is closer to the epicentre of the substorm, it also has a higher azimuthal wave number than the CVW wave. This is unusual when compared to the earlier results as they show that there is typically an increase in m with distance from the substorm, though they are still both well within the general spread of the previous results.

Panel (b) shows that the angular drift frequencies of these two waves follow the expected trends found in the previous chapters, where the waves closer to the substorm typically have larger angular drift frequencies than those farther out. Even though the m numbers don't increase with distance from the substorm, the large difference in the periods of the two waves has meant that the CVE wave still has a large angular drift frequency than that of the CVW wave.

As with the angular drift frequencies found in panel (b), the particle energies inferred from the wave parameters also follow the expected pattern. The CVE wave predicts particles of a higher energy as the source than the CVW wave does as it is closer to the substorm. The main difference between these results and the previous ones are that, overall, the energies found for these two waves are slightly higher than the rest of the population. This is likely due to the waves being observed at lower magnetic latitudes using the mid-latitude array of SuperDARN radars whereas the previous results were obtained from the higher latitude main-array.

7.5 Summary

The primary aim of this chapter was to observe particle populations using in-situ data as they drift around the Earth driving ULF waves, allowing for a comparison with the energies calculated using the method described in 5.6.3. It was also of interest to find an appropriate range of pitch angles to include in the calculation of particle energy.

Two waves observed using SuperDARN radars were associated with the injection of westward drifting energetic ions from a nearby substorm. The particle populations responsible for driving these waves appear to have been detected using the HOPE and MagEIS instruments aboard the Van Allen Probes.

An initial look at the ion distribution functions created from the spin-averaged differential particle flux measured by the Van Allen Probes reveals that there is a notch in the distribution where the waves are being driven. This notch contains the positive gradients indicative of energy available for growth of the waves at the expected energy ranges.

A closer look at the ion distribution functions using pitch angle distribution data shows that this notch is present over all of the pitch angles observed and that its location in energy increases slightly as α departs from 90° although the particle distribution functions become less significant as they move away from 90° pitch angles due to the lower count rates available in those regions.

It was found that the maximum equatorial pitch angle that the Van Allen Probes could detect in each IDF ranged from 76 - 83°, so not all of the particles that could have potentially driven these waves were observable. Due to the significant peak in the IDF around 90° observed in Figure 7.18 and how little the particle energy predictions change with estimates of α_{Eq}, values between ~75 and 90° are likely to be important for wave growth in this example.

When the results of this chapter are compared to those of the previous chapters, the parameters such as m, ω_d and W of the two waves observed in this study appear to be very consistent. The azimuthal wave numbers and period of the waves observed in this chapter are very different to each other but are fairly typical of waves of this type. The unusual behaviour of m may be explained by the difference in local eigenfrequencies between the two wave locations - in order for there to be resonance between the waves and the driving particles, m must be modified to satisfy the drift-resonance condition (see Equation 5.2). The angular drift frequencies and energies are larger in magnitude closer to the substorm as expected. The main difference is that the energies are in general slightly higher than the previous results, most likely due to the observations taking place at lower latitudes.

Chapter 8

Conclusion

This thesis has set out to investigate the properties of substorm-driven ULF waves. Previous studies of such waves were discussed in Chapter 3 and were determined to be driven by drifting clouds of energetic particles that are injected into the nightside magnetosphere due to substorm activity. This class of waves is likely to be excited by one of two possible mechanisms: the first being the excitement due to drift-resonant particles as part of a bump-on-tail instability (*Southwood et al.*, 1969), the other being that the cloud of particles produces an alternating current which excites the waves (*Mager and Klimushkin*, 2007, 2008) which was the mechanism suggested for the events studied by *Zolotukhina et al.* (2008); *Yeoman et al.* (2010, 2012). It is likely that a mixture of these two mechanisms may be the cause, where the alternating current driven by the drifting particles acts as an oscillation seed which becomes amplified by the particle instability.

Yeoman et al. (2010) made the suggestion that the proximity of the wave observation to the substorm may be a controlling factor in the phase propagation of these waves. Chapter 5 investigates this suggestion with a statistical study of ULF waves observed by HF radars nearby and shortly after the onset of substorms visible in IMAGE FUV data. This study was then taken further with Chapter 6 which looked in detail at three case study events where multiple waves at various azimuthal locations were associated with individual substorms. In both Chapters 5 and 6, driving particle energies were estimated using Equation 2.73 but there were no direct observations of the responsible particle populations. Chapter 7 used in-situ data to find the particle distributions relevant to a single case study event where two waves were observed to the west of a substorm.

8.1 Spatio-temporal Characteristics of Substorm-Driven ULF Waves

Chapter 5 investigated the properties of 83 poloidal ULF waves that were associated with nearby substorm activity. The waves were observed using the Doppler velocity measured by five SuperDARN radars in the northern hemisphere. The waves were observed at various azimuthal separations from the substorm location both to the east and to the west.

The waves exhibited azimuthal wave numbers with magnitudes from 2 - 60, with a mixture of eastward and westward phase propagations. The azimuthal wave numbers were directed such that waves with positive m (eastward phase propagation) typically occurred to the east of the substorm and negative m (westward phase propagation) to the west. The magnitude of m appeared to generally be larger for those waves observed farthest from the substorms and smallest for the closest, for both eastward and westward phase propagations.

The source for this population of waves was suggested to be a drift-resonant interaction with a cloud of gradient-curvature drifting energetic particles. Due to the drift-resonance condition being invoked as the mechanism for wave growth, the drift speed of the particles had to match the phase speed of the waves. The angular drift frequencies of the waves were similar to the m numbers such that positive ω_d was mostly observed to the east of the substorm and negative ω_d to the west, but unlike the azimuthal wave numbers, the magnitude typically reduced with distance from the substorms. The waves which exhibited positive wave numbers and angular drift frequencies were associated with a source in eastward drifting electrons and waves with negative wave numbers and angular drift frequencies were associated with westward drifting protons.

As the angular drift frequency calculated using the wave parameters would match the angular drift frequency of the clouds of particles and the azimuthal separation of the waves and substorms was known, it was possible to estimate an expected time lag between substorm onset and wave onset. This estimated time lag was typically very similar to the actual observed time lag supporting the theory that the waves were related to those substorms.

Using Equation 2.73, it was possible to estimate the particle energies responsible for driving each of the waves with the use of the measured angular drift frequency of the waves. These predicted particle energies appeared to be much higher for those waves observed closest to the substorm location and lowest for those furthest away, with no apparent difference between the eastern, electron driven waves and the western, proton driven waves. This trend in particle energies implies that, as the clouds of energetic particles gradient-curvature drift away from the point of injection, higher energy particles are lost relatively quickly leaving lower energy particles to drive higher-m waves farther from the source. The higher energy particles could be falling within the loss cone quicker than lower energy particles and being lost to the atmosphere, or they could be losing their energy to the waves that they drive.

The latitudinal phase propagation of these waves was also studied, with unclear results. The majority of the population of these waves exhibited equatorward phase propagation typical of this class of waves (e.g., *Yeoman et al.*, 2010). The rate of latitudinal phase propagation, l, hinted at a possible relationship to the waves location in latitude relative to the substorm though this remains uncertain. One of the things that could be studied in more detail in future would be the latitudinal dependence of the wave and particle characteristics such as equatorward phase propagation and energy. The trends noted by *Yeoman et al.* (2008) where the azimuthal wave numbers and predicted particle energies were suggested to be related to the L-shell of the waves could be elucidated with the use of both StormDARN and main array SuperDARN radars in order to cover a larger range of latitudes, and also a larger range of latitudinal separations from the substorm.

It is clear from this study that the phase propagation of the ULF waves associated with substorm injection is related to their proximity to the substorm as suggested by *Yeoman et al.* (2010). The phase propagation of these waves all appear to propagate away from the source of the energetic particles. This study is unique in that there were a large number of electron-driven waves which are rare in previous publications (*Eriksson et al.*, 2006; *Zolotukhina et al.*, 2008; *Yeoman et al.*, 2010). Another interesting result of this study is that, amongst the high-m and intermediate-m waves observed, there were a number of low-m waves which would usually be associated with sources external to the magnetosphere.

8.2 Multi-Radar Observations of Substorm-Driven ULF Waves

The study in Chapter 5 investigated 83 events in which a single ULF wave was observed for each substorm. The aim of Chapter 6 was to study substorm events where multiple wave observations associated with the substorm at various different locations relative to the substorm. With multiple wave observations at different locations relative to the substorm it is possible to tell whether the trends observed in Chapter 5 would hold for each individual substorm and to study how the particle populations evolve as they drift away from their source.

This study was focused on three substorm events. For events 1 and 2, the substorms were located using IMAGE FUV data as in Chapter 5, but due to the limited lifetime of IMAGE the substorm of event 3 had to be located using other means. The IMAGE FUV data and ground magnetometer data simultaneously available during a number of substorms was used to determine an algorithm that would allow the bays in the magnetometer data caused by the substorm current wedge to be used as a proxy for the auroral FUV data provided by IMAGE. This enabled the use of ground magnetometers to locate the substorm involved for event 3.

Event 1 included the observation of three westward drifting ULF waves all observed to the west of the substorm. For event 2 two other westward propagating ULF waves associated with a single substorm were observed. In event 3 there were four ULF waves associated with one substorm, two of which were observed with negative m to the west of the substorm and two with positive m to the east. The phase propagations for each of these waves appear to fit with the observations in Chapter 5 where westward phase propagation was associated with westward drifting ions and eastward propagation was attributed to eastward drifting electrons.

The waves in this study were all analysed in the same manner to those in Chapter 5, where the drift resonance condition was invoked as the source and the particle energies were estimated using Equation 2.73. These waves exhibited $|m| = 2$ to 79 where in each event the magnitude of the azimuthal wave number increased with distance from the particle source. Both the angular drift frequencies and estimated particle energies (2 to 95 keV) in all three events was reduced for waves observed farthest from the substorm and highest for the closest waves. The values for m, ω_d and W were similar to those observed in the previous study, where the trends in these values also remained similar to those predicted by the previous chapter.

The large range of particle energies estimated from the wave characteristics in each event suggest that in any given substorm, the injected particles may contain a large range of energies. Also, the variation in energies predicted from event to event suggest that the range of energies present in this population of injected particles is likely to vary from substorm to substorm.

8.3 Van Allen Probe Observations of Particle Distributions During Substorm-Driven ULF Waves

In both Chapters 5 and 6, the wave parameters, wave location and geomagnetic activity are used to predict the energy of the particle populations required to drive them. The aim of Chapter 7 was to use in-situ particle data aboard the Van Allen Probes to be able to observe these particle populations injected by the substorms as they drive ULF waves. This would allow for a comparison between the energy levels at which there is free energy available within the particle distribution functions and the predicted particle energies, while investigating the importance of the particle pitch-angle.

Chapter 7 concentrated on a single substorm event which coincided with the observation of two nearby ULF waves. This substorm event was detected and located with the use of ground magnetometer data using the method described in Chapter 6. The two waves appeared to the west of the substorm, both with negative m numbers and were associated with westward drifting ions. The azimuthal wave numbers of these two waves were -19 and -35 where the largest m was observed closest to the substorm (unlike the previous Chapters). The two wave also has very different wave periods, but were both still typical of the distribution observed in Chapter 5.

The vastly different wave periods and m numbers combined to predict angular drift frequencies which followed the same trend as previous results where they reduced with distance from the substorm. The estimated energies for the waves, $45 - 53$ keV and $55 - 61$ keV, also reduced with distance from the location of the substorm as expected. All of the wave parameters and the derived angular drift frequencies and energies fit reasonably well with the results from the previous chapters. The exception to this was that the energies observed seemed slightly higher for the observed azimuthal separations, possibly due to the waves being observed at lower latitudes using the StormDARN radars.

This particular event was chosen due to the conjunction with both Van Allen Probes. Both probes crossed through the paths of the particles that drove the waves. The HOPE and MagEIS instruments onboard the probes were used to find the local ion distribution functions to each of the crossings.

The spin-averaged data revealed a notch in the IDFs in the relevant energy ranges for both of the waves. Inside these notches existed positive gradients indicative of the availability of free energy for wave growth. These IDFs were also created for pitch-angle distribution data and showed the same structure, though the location of the positive gradient increased in energy with the departure of the pitch angle from $90°$. The maximum equatorial pitch angles that could be observed by the probes were also estimated between 76 and $83°$ due to the spacecraft locations being slightly away from the magnetic equator. The conclusion of this part of the study was that particles with equatorial pitch angles of the order $\sim 75 - 90°$ were likely to be the most important to wave growth.

8.4 Future Work

The phase characteristics of substorm-driven ULF waves and particle energies required to drive those waves have been shown to be related to the proximity of the wave to the substorm that drives it, though there are still other dependencies that remain unclear. The dependence on wave properties such as the latitudinal phase propagation and azimuthal wave number may have some dependence upon the latitude or L-shell that the wave is excited at. Given many more events like the three investigated in Chapter 6, future work may also enable us to determine the range of particle energies injected during the substorm which can lead to wave growth, and what the conditions are which determine whether wave growth will occur.

This study could be taken further with a statistical study of substorm driven ULF waves and the associated particle fluxes with spacecraft like the Van Allen Probes in order to determine whether these results are typical. It is still to be determined whether a bump-on-tail distribution function is required, or whether enhanced particle fluxes without the positive gradient would be enough to drive such waves as suggested by *Mager and Klimushkin* (2007, 2008). The possibility that these waves are driven by spatial instabilities such as the event in *Dai et al.* (2013) as opposed to velocity space instabilities (bump-on-tail) could be studied in more detail using the Van Allen Probe data. It may be the case that the class of waves studied in this thesis source their energy from both instabilities, or that substorm driven waves are predominantly amplified by one particular instability. Further conjunctions with substorm-driven ULF waves may be able to disambiguate the spatial and temporal variations observed in the IDFs as a function of L-shell to determine whether the bump observed in Figure 7.16 at $L > 3.5$ could be the enhanced particle flux seeding the ULF waves as suggested by *Mager and Klimushkin* (2007, 2008).

References

Agapitov, A. V., and O. K. Cheremnykh (2011), Polarization of ULF Waves in the Earth's Magnetosphere, *Kinematics and Physics of Celestial Bodies*, *27*, 117–123. 62, 64, 65, 66

Agapitov, O., et al. (2009), Surface waves and field line resonances: A THEMIS case study, *J. Geophys. Res.*, *114*, A00C27, doi:10.1029/2008JA013553. 51, 61

Akasofu, S. I. (1964), The development of the auroral substorm, *Planet. Space Sci.*, *12*, 273–282, doi:10.1016/0032-0633(64)90151-5. 15, 16, 120

Allan, W., and E. M. Poulter (1992), ULF waves-their relationship to the structure of the Earth's magnetosphere, *Reports on Progress in Physics*, *55*(5), 533. 59, 61, 62

Allan, W., E. M. Poulter, and E. Nielsen (1982), STARE observations of a Pc 5 pulsation with large azimuthal wave number, *J. Geophys. Res.*, *87*(A8), 6163–6172, doi:10.1029/JA087iA08p06163. 67

Allan, W., E. M. Poulter, K.-H. Glassmeier, and E. Nielson (1983a), Ground magnetometer detection of a large-M Pc 5 pulsation observed with the STARE radar, *Journal of Geophysical Research: Space Physics*, *88*(A1), 183–188, doi:10.1029/JA088iA01p00183. 67, 72

Allan, W., E. M. Poulter, and E. Nielsen (1983b), Pc5 pulsations associated with ring current proton drifts: STARE radar observations, *Planet. Space Sci.*, *31*(11), 1279–1289, doi:10.1016/0032-0633(83)90065-X. 72, 73, 112

Anderson, B. J., M. J. Engebretson, and S. P. Rounds (1990), A statistical study of Pc 3-5 pulsations observed by the AMPTE/CCE magnetic fields experiment, 1. Occurrence distributions, *J. Geophys. Res.*, *95*(A7), 10,495–10,523, doi:10.1029/JA095iA07p10495. 69, 71

Baddeley, L. (2003), Wave-Particle Interactions in the Terrestrial Magnetosphere, PhD Thesis, University of Leicester. 106

Baddeley, L. J., T. K. Yeoman, and D. M. Wright (2005a), HF doppler sounder measurements of the ionospheric signatures of small scale ULF waves, *Ann. Geophys.*, *23*(1), 1807–1820, doi:10.5194/angeo-23-1807-2005. 78, 108, 123

Baddeley, L. J., T. K. Yeoman, D. M. Wright, K. J. Trattner, and B. J. Kellet (2005b), On the coupling between unstable magnetospheric particle populations and resonant high m ULF wave signatures in the ionosphere, *Ann. Geophys.*, *23*, 567–577, doi:10.5194/angeo-23-567-2005. 81, 108, 123

Baker, D. N., T. I. Pulkkinen, V. Angelopoulos, W. Baumjohann, and R. L. McPherron (1996), Neutral line model of substorms: Past results and present view, *Journal of Geophysical Research: Space Physics*, *101*(A6), 12,975–13,010, doi:10.1029/95JA03753. 13

Baker, D. N., et al. (2013), The Relativistic Electron-Proton Telescope (REPT) Instrument on Board the Radiation Belt Storm Probes (RBSP) Spacecraft: Characterization of Earth's Radiation Belt High-Energy Particle Populations, *Space Sci. Rev.*, *179*, 337–381, doi:10.1007/s11214-012-9950-9. 105

Banks, P. M., and T. E. Holzer (1969), High-latitude plasma transport: The polar wind, *Journal of Geophysical Research*, *74*(26), 6317–6332, doi:10.1029/JA074i026p06317. 10

Baumjohann, W., and R. Nakamura (2001), Updating the near-earth neutral line model, *eprint arXiv:physics/0111145*. 13

Baumjohann, W., G. Paschmann, and C. A. Cattell (1989), Average plasma properties in the central plasma sheet, *Journal of Geophysical Research: Space Physics*, *94*(A6), 6597–6606, doi:10.1029/JA094iA06p06597. 8

Belakhovsky, V. B., and V. A. Pilipenko (2010), Excitation of Pc5 Pulsations of the Geomagnetic Field and Riometric Absorption, *Cosmic Research*, *48*, 319–334. 109, 132

Belmont, G., R. Grappin, F. Mottez, F. Pantellini, and G. Pelletier (2013), *Collisionless Plasmas in Astrophysics*, Wiley. 11

Bittencourt, J. (2013), *Fundamentals of Plasma Physics*, Elsevier Science. 32

Blake, J. B., et al. (2013), The Magnetic Electron Ion Spectrometer (MagEIS) Instruments Aboard the Radiation Belt Storm Probes (RBSP) Spacecraft, *Space Sci. Rev.*, *179*, 383–421, doi: 10.1007/s11214-013-9991-8. 90, 105

Burch, J. L. (2000), IMAGE Mission Overview, *Space Sci. Rev.*, *91*, 1–14, doi:10.1023/A:1005245323115. 90, 95

Carbary, J. F., K. Liou, A. T. Y. Lui, P. T. Newell, and C. I. Meng (2000), "blob" analysis of auroral substorm dynamics, *J. Geophys. Res.*, *105*(A7), 16,083–16,091, doi:10.1029/1999JA000210. 120

Chang, T., and A. G. Union (1986), *Ion Acceleration in the Magnetosphere and Ionosphere*, Geophysical Monograph Series, Wiley. 8

Chapman, S., and J. Bartels (1940), Geomagnetism. Vol. I. Geomagnetic and related phenomana. Vol. II. Analysis and physical interpretation of the phenomena. By S. Chapman and J. Bartels. The International Series of Monographs on Physics. London (Sir Humphrey Milford, Oxford University Press), 1940, 8°. Pp. xxviii+1049; illustrations. 3 guineas, *Quarterly Journal of the Royal Meteorological Society*, *67*(288), 63–66, doi:10.1002/qj.49706728810. 5

Chapman, S., and V. C. A. Ferraro (1931), A new theory of magnetic storms, *Terrestrial Magnetism and Atmospheric Electricity*, *36*(2), 77–97, doi:10.1029/TE036i002p00077. 4

Chisham, G. (1996), Giant pulsations: An explanation for their rarity and occurrence during geomagnetically quiet times, *J. Geophys. Res.*, *101*(A11), 24,755–24,763, doi: 10.1029/96JA02540. 53, 78, 79, 80, 164

Chisham, G., D. Orr, and T. K. Yeoman (1992), Observations of a giant pulsation across an extended array of ground magnetometers and on auroral radar, *Planet. Space Sci.*, *40*(7), 953–964, doi:10.1016/0032-0633(92)90135-B. 76, 78, 108, 109, 132

Chisham, G., et al. (2007), A decade of the Super Dual Auroral Radar Network (SuperDARN): scientific achievements, new techniques and future directions, *Surv. Geophys.*, *28*, 33–109, doi: 10.1007/s10712-007-9017-8. 90, 109, 135

Claudepierre, S. G., et al. (2013), Van Allen Probes observation of localized drift resonance between poloidal mode ultra-low frequency waves and 60 keV electrons, *Geophysical Research Letters*, *40*(17), 4491–4497, doi:10.1002/grl.50901. 72, 76

Clauer, C. R., and R. L. McPherron (1974), Mapping the Local Time-Universal Time Development of Magnetospheric Substorms Using Mid-Latitude Magnetic Observations, *J. Geophys. Res.*, *79*, 2811 – 2820, doi:10.1029/JA079i019p02811. 17, 145

Dai, L., et al. (2013), Excitation of poloidal standing Alfvén waves through drift resonance wave-particle interaction, *Geophysical Research Letters*, *40*(16), 4127–4132, doi:10.1002/grl.50800. 76, 77, 201

Davis, T. N., and M. Sugiura (1966), Auroral electrojet activity index ae and its universal time variations, *J. Geophys. Res.*, *71*, 785 – 801, doi:10.1029/JZ071i003p00785. 18, 171

Dungey, J. W. (1961), Interplanetary Magnetic Field and the Auroral Zones, *Phys. Rev. Lett.*, *6*, 47–48, doi:10.1103/PhysRevLett.6.47. 10

Dungey, J. W. (1963), The structure of the exosphere or adventures in velocity space, in *Geophysics: The Earth's Environment*, edited by C. Dewitt, Gordon and Breach. 49

Engebretson, M. J., D. L. Murr, K. N. Erickson, R. J. Strangeway, D. M. Klumpar, S. A. Fuselier, L. J. Zanetti, and T. A. Potemra (1992), The Spatial Extent of Radial Magnetic Pulsation Events Observed in the Dayside Near Synchronous Orbit, *J. Geophys. Res.*, *97*(A9), 13,741–13,758, doi:10.1029/92JA00992. 75

Erdélyi, R., and I. Ballai (2007), Heating of the solar and stellar coronae: a review, *Astronomische Nachrichten*, *328*(8), 726–733, doi:10.1002/asna.200710803. 2

Eriksson, P. T. I., L. G. Blomberg, and K. H. Glassmeier (2006), Cluster satellite observations of mHz pulsations in the dayside magnetosphere, *Adv. Space Res.*, *38*, 1730–1737, doi:10.1016/j.asr.2005.04.103. 81, 132, 197

Fenrich, F. R., J. C. Samson, and R. A. Sofko, Gand Greenwald (1995), ULF high- and low-m field line resonances observed with the Super Dual Auroral Radar Network, *J. Geophys. Res.*, *100*, 21,535 – 21,548, doi:10.1029/95JA02024. 82, 83, 109, 116

Finn, J. M. (2006), Magnetic Reconnection: Null point, *Nat. Phys.*, *2*, 445 – 446, doi:10.1038/nphys353. 11

Frey, H. U. (2007), Localized aurora beyond the auroral oval, *Reviews of Geophysics*, *45*(1), n/a–n/a, doi:10.1029/2005RG000174. 9

Frey, H. U., S. B. Mende, and V. Angelopoulos (2004), Substorm onset observations by IMAGE-FUV, *J. Geophys. Res.*, *109*(A10304), A10,304, doi:10.1029/2004JA010607. 2, 99, 110, 111, 112, 113, 116, 132, 135, 137, 145, 147, 173

Funsten, H. O., et al. (2013), Helium, Oxygen, Proton, and Electron (HOPE) Mass Spectrometer for the Radiation Belt Storm Probes Mission, *Space Sci. Rev*, *179*, 423–484, doi:10.1007/s11214-013-9968-7. 90, 105

Galand, M., and D. Lummerzheim (2004), Contribution of proton precipitation to space-based auroral FUV observations, *Journal of Geophysical Research: Space Physics*, *109*(A3), n/a–n/a, doi:10.1029/2003JA010321. 96

Gallagher, D., P. Craven, and R. Comfort (1988), An empirical model of the earth's plasmasphere, *Advances in Space Research*, *8*(8), 15 – 24, doi:http://dx.doi.org/10.1016/0273-1177(88)90258-X. 8

GFZ Potsdam (), K_p Index, `http://www.gfz-potsdam.de/forschung/ueberblick/departments/department-2/erdmagnetfeld/daten-dienste/kp-index/theorie/`, [Online; accessed 04-December-2014]. 20

Gjerloev, J. W. (2012), The SuperMAG data processing technique, *J. Geophys. Res.*, *117*, 1–19, doi:10.1029/2012JA017683. 102, 103

Gjerloev, J. W., R. A. Hoffman, M. M. Friel, L. A. Frank, and J. B. Sigwarth (2004), Substorm behavior of the auroral electrojet indices, *Annales Geophysicae*, *22*(6), 2135–2149, doi:10.5194/angeo-22-2135-2004. 19

Gosling, J. T., D. N. Baker, S. J. Bame, W. C. Feldman, R. D. Zwickl, and E. J. Smith (1985), North-south and dawn-dusk plasma asymmetries in the distant tail lobes: ISEE 3, *Journal of Geophysical Research: Space Physics*, *90*(A7), 6354–6360, doi:10.1029/JA090iA07p06354. 10

Grant, I. F., D. R. McDiarmid, and A. G. McNamara (1992), A class of high-m pulsations and its auroral radar signature, *J. Geophys. Res.*, *97*(A6), 8439–8451, doi:10.1029/92JA00434. 82

Greenwald, R. A., W. Weiss, and E. Nielsen (1978), STARE: A new radar auroral backscatter experiment in northern Scandinavia, *Radio Sci.*, *13*(6), 1021–1039, doi:10.1029/RS013i006p01021. 61, 67, 72

Greenwald, R. A., et al. (1995), DARN/SUPERDARN A Global View of the Dynamics of High-Latitude Convection, *Space Sci. Rev.*, *71*, 761–796, doi:10.1007/BF00751350. 90, 91, 109, 135

Hamilton, D. C., G. Gloeckler, F. M. Ipavich, W. StÃijdemann, B. Wilken, and G. Kremser (1988), Ring current development during the great geomagnetic storm of February 1986, *Journal of Geophysical Research: Space Physics*, *93*(A12), 14,343–14,355, doi:10.1029/JA093iA12p14343. 20

Hanslmeier, A. (2007), *The Sun and Space Weather*, Springer Science & Business Media, 2007. 2

Huang, C. Y., and L. A. Frank (1994), A statistical survey of the central plasma sheet, *Journal of Geophysical Research: Space Physics*, *99*(A1), 83–95, doi:10.1029/93JA01894. 8

Hughes, W. (1983), Hydromagnetic Waves in the Magnetosphere, in *Solar-Terrestrial Physics*, *Astrophysics and Space Science Library*, vol. 104, edited by R. Carovillano and J. Forbes, pp. 453–477, Springer Netherlands, doi:10.1007/978-94-009-7194-3_18. 49, 51, 52, 53, 59

Hughes, W. J., R. I. Mcpherron, J. N. Barfield, and B. H. Mauk (1979), A compressional Pc4 pulsation observed by three satellites in geostationary orbit near local midnight, *Planet. Space Sci.*, *27*, 821–840, doi:10.1016/0032-0633(79)90010-2. 67, 70, 123

IMAGE (), IMAGE Map, `http://www.geo.fmi.fi/image/stations.html`, [Online; accessed 16-June-2014]. 100

INTERMAGNET (a), INTERMAGNET, `http://www.intermagnet.org/index-eng.php`, [Online; accessed 16-June-2014]. 90

INTERMAGNET (b), INTERMAGNET Magnetic Observatories, http://www.intermagnet.org/imos/imomap-eng.php, [Online; accessed 16-June-2014]. 101, 102

Jacobs, J. A., Y. Kato, S. Matsushita, and V. A. Troitskaya (1964), Classification of geomagnetic micropulsations, *Journal of Geophysical Research*, *69*(1), 180–181, doi:10.1029/JZ069i001p00180. xii, 36

Kivelson, M. G., and C. T. Russell (1995), *Introduction to Space Physics*, Cambridge University Press. 3, 6, 7, 8, 10, 12, 14, 24, 33, 37, 41, 42, 44, 48

Kletzing, C., et al. (2013), The Electric and Magnetic Field Instrument Suite and Integrated Science (EMFISIS) on RBSP, *Space Science Reviews*, *179*(1-4), 127–181, doi:10.1007/s11214-013-9993-6. 105

Klimushkin, D. Y., and P. N. Mager (2012), Coupled Alfvén and drift-mirror modes in non-uniform space plasmas: a gyrokinetic treatment, *Plasma Phys. Control. Fusion*, *54*(015006), doi:10.1088/0741-3335/54/1/015006. 123

Klimushkin, D. Y., P. N. Mager, and K.-H. Glassmeier (2012), Spatio-temporal structure of Alfvén waves excited by a sudden impulse localized on an L-shell, *Ann. Geophys.*, *30*(7), 1099–1106, doi:10.5194/angeo-30-1099-2012. 60, 119

Laundal, K. M. (2010), Auroral Imaging as Tracer of Global Magnetospheric Dynamics, PhD Thesis, University of Bergen. 96

Leonovich, A. S. (2001), A theory of field line resonance in a dipole-like axisymmetric magnetosphere, *J. Geophys. Res.*, *106*(A11), 25,803–25,812, doi:10.1029/2001JA000104. 125

Liou, K., and J. M. Rouhoniemi (2006), A case study of relationship between substorm expansion and global plasma convection, *Geophys. Res. Lett.*, *33*, doi:10.1029/2005GL024736. 120

Lühr, H. (1994), The IMAGE magnetometer network, *STEP International Newsletter*, *4*, 4–6. 90, 135

Mager, P. N., and D. Y. Klimushkin (2005), Spatial localization and azimuthal wave numbers of Alfvén waves generated by drift-bounce resonance in the magnetosphere, *Ann. Geophys.*, *23*, 3775–3784, doi:10.5194/angeo-23-3775-2005. 108

Mager, P. N., and D. Y. Klimushkin (2007), Generation of Alfvén Waves by a Plasma Inhomogeneity Moving in the Earth's Magnetosphere, *Plasma Phys. Rep.*, *33*, 391–398, doi:10.1134/S1063780X07050042. 84, 85, 108, 109, 123, 124, 125, 132, 187, 195, 201

Mager, P. N., and D. Y. Klimushkin (2008), Alfvén ship waves: high-m ULF pulsations in the magnetosphere generated by a moving plasma inhomogeneity, *Ann. Geophys.*, *26*, 1653–1663, doi:10.5194/angeo-26-1653-2008. 74, 84, 85, 108, 109, 123, 124, 125, 132, 133, 187, 195, 201

Mager, P. N., D. Y. Klimushkin, and N. Ivchenko (2009), On the equatorward phase propagation of high-m ULF pulsations observed by radars, *J. Atmos. Sol.-Terr. Phys.*, *71*, 1677–1680, doi:10.1016/j.jastp.2008.09.001. 74, 84, 108, 124, 133

Mann, I., and G. Chisham (2000), Comment on "Concerning the generation of geomagnetic giant pulsations by drift-bounce resonance ring current instabilities" by K.-H. Glassmeier et al., Ann. Geophysicae, 17, 338/350, (1999), *Annales Geophysicae*, *18*(2), 161–166, doi:10.1007/s00585-000-0161-4. 58

Mann, I. R., et al. (2008), The Upgraded CARISMA Magnetometer Array in the THEMIS Era, *Space Sci. Rev.*, *141*, 413 – 451, doi:10.1007/s11214-008-94576. 90, 101, 135, 145

Mauk, B. H., N. J. Fox, S. G. Kanekal, R. L. Kessel, D. G. Sibeck, and A. Ukhorskiy (2013), Science Objectives and Rationale for the Radiation Belt Storm Probes Mission, *Space Sci. Rev.*, *179*, 3–27, doi:10.1007/s11214-012-9908-y. 90, 104

Mazur, J., et al. (2013), The Relativistic Proton Spectrometer (RPS) for the Radiation Belt Storm Probes Mission, *Space Science Reviews*, *179*(1-4), 221–261, doi:10.1007/s11214-012-9926-9. 105

Mazur, V. A., and D. A. Chuiko (2011), Excitation of a magnetospheric MHD cavity by Kelvin-Helmholtz instability, *Plasma Phys. Rep.*, *37*, 913–934, doi:10.1134/S1063780X11090121. 61

McPherron, R. L. (1991), Physical Processes producing magnetospheric substorms and magnetic storms, *Geomagnetism*, *4*, 593–739. 13

McPherron, R. L. (2005), Magnetic pulsations: Their sources and relation to solar wind and geomagnetic activity, *Surv. Geophys.*, *26*, 545–592, doi:10.1007/s10712-005-1758-7. 59

McPherron, R. L., and R. H. Manka (1985), Dynamics of the 1054 UT March 22, 1979, substorm event: CDAW 6, *Journal of Geophysical Research: Space Physics*, *90*(A2), 1175–1190, doi:10.1029/JA090iA02p01175. 19

McPherron, R. L., C. T. Russell, M. G. Kivelson, and P. J. Coleman (1973), Substorms in space: The correlation betweeen ground and satellite observations if the magnetic field, *Rad. Sci.*, *8*(11), 1059–1076, doi:10.1029/RS008i011p01059. 13, 15, 136, 145

Mende, S. B., et al. (2000a), Far ultraviolet imaging from the IMAGE spacecraft. 2. Wideband FUV imaging, *Space Sci. Rev.*, *91*, 271–285, doi:101023/A:1005227915363. 90, 94, 110, 135

Mende, S. B., et al. (2000b), Far ultraviolet imaging from the IMAGE spacecraft.1. System design, *Space Sci. Rev.*, *91*, 243–270, doi:10.1023/A:1005271728567. 90, 94, 95, 96, 110, 135

Milan, S. E., T. K. Yeoman, M. Lester, E. C. Thomas, and T. B. Jones (1997), Initial backscatter occurrence statistics from the CUTLASS HF radars, *Ann. Geophys.*, *15*, 703–718, doi:10.1007/s00585-997-0703-0. 91, 93

Mitchell, D., et al. (2013), Radiation Belt Storm Probes Ion Composition Experiment (RBSPICE), *Space Sci. Rev.*, *179*(1-4), 263–308, doi:10.1007/s11214-013-9965-x. 105

NASA (), Heliospheric Current Sheet, `http://lepmfi.gsfc.nasa.gov/mfi/hcs/HCS.gif`, [Online; accessed 03-July-2014]. 4

National Geophysical Data Center, NOAA (), K_p Index, `http://www.ngdc.noaa.gov/stp/geomag/kp_ap.html`, [Online; accessed 04-December-2014]. 20

Nedie, A. Z., R. Rankin, and F. R. Fenrich (2012), SuperDARN observations of the driver wave associated with FLRs, *J. Geophys. Res.*, *117*, A06,232, doi:10.1029/2011JA017387. 61

Newell, P. T., and J. W. Gjerloev (2011a), Evaluation of SuperMAG auroral electrojet indices as indicators of substorms and auroral power, *J. Geophys. Res.*, *116*, 1 – 12, doi:10.1029/2011JA016779. 177

Newell, P. T., and J. W. Gjerloev (2011b), Substorm and magnetosphere characteristic scales inferred from the SuperMAG auroral electrojet indices, *J. Geophys. Res.*, *116*, 1 – 15, doi:10.1029/2011JA016936. 177

Nielson, E., W. Guttler, E. C. Thomas, C. P. Stewart, T. B. Jones, and A. Hedberg (1983), SABRE - A new radar auroral backscatter experiment, *Nature*, *304*, 712 – 714, doi:10.1038/304712a0. 76

Parker, E. N. (1958), Dynamics of the Interplanetary Gas and Magnetic Fields., *Astrophys. J.*, *128*, 664, doi:10.1086/146579. 3

Pilipenko, V., N. G. Kleimenova, O. V. Kozyreva, M. J. Engebretson, and O. Rasmussen (2001a), Long-period magnetic activity during the May 15, 1997 storm, *J. Atmos. Sol.-Terr. Phys.*, *63*, 489–501, doi:10.1016/S1364-6826(00)00189-9. 74, 108, 124, 125

Pilipenko, V. A., J. Watermann, V. A. Popov, and V. O. Papitashvili (2001b), Relationship between auroral electrojet and Pc5 ULF waves, *J. Atmos. Sol.-Terr. Phys.*, *63*, 1545–1557, doi:10.1016/S1364-6826(01)00031-1. 74, 81

Pilipenko, V. A., O. V. Kozyreva, M. J. Engebretson, D. L. Detrick, and S. N. Samsonov (2001c), Dynamics of long-period magnetic activity and energetic particle precipitation during the May 15, 1997 storm, *J.Atmos. Sol.-Terr. Phys.*, *64*, 831 – 843. 124, 125

Pisacane, V. (2005), *Fundamentals of Space Systems*, Applied Physics Laboratory series in science and engineering / The Johns Hopkins University, Oxford University Press. 8

Pokhotelov, O. A., V. A. Pilipenko, and E. Amata (1985), Drift anisotropy instability of a finite-β magnetospheric plasma, *Planet. Space Sci.*, *33*, 1229–1241, doi:10.1016/0032-0633(85)90001-. 123

Radoski, H. R. (1971), A note on the problem of hydromagnetic resonances in the magnetosphere, *Planetary and Space Science*, *19*(8), 1012 – 1013, doi:10.1016/0032-0633(71)90152-8. 45

Radoski, H. R. (1974), A theory of latitude dependent geomagnetic micropulsations: the asymptotic fields, *J. Geophys. Res.*, *79], pages = 595 – 613, doi = 10.1029/JA079i004p00595.* 125

Reistad, J. P. (2012), Non-conjugate aurora and interhemispheric currents, Masters Thesis, University of Bergen. 96, 97, 98

Rishbeth, H. (1988), Basic physics of the ionosphere: a tutorial review, *Journal of the Institution of Electronic and Radion Engineers*, *58*, S207 – S223, doi: 10.1049/jiere.1988.0060. 21, 22, 23

Robinson, T. R., T. K. Yeoman, R. S. Dhillon, M. Lester, E. C. Thomas, J. D. Thornhill, D. M. Wright, A. P. van Eyken, and I. W. McCrea (2006), First observations of SPEAR-induced artificial backscatter from CUTLASS and the EISCAT Svalbard radars, *Annales Geophysicae*, *24*(1), 291–309, doi:10.5194/angeo-24-291-2006. 82

Rosenbauer, H., H. GrÃijnwaldt, M. D. Montgomery, G. Paschmann, and N. Sckopke (1975), Heos 2 plasma observations in the distant polar magnetosphere: The plasma mantle, *Journal of Geophysical Research*, *80*(19), 2723–2737, doi: 10.1029/JA080i019p02723. 10

Russell, C., and R. McPherron (1973), The magnetotail and substorms, *Space Science Reviews*, *15*(2-3), 205–266, doi:10.1007/BF00169321. 13

Saka, O., T. Iijima, H. Yamagishi, N. Sato, and D. N. Baker (1992), Excitation of Pc 5 pulsations in the morning sector by a local injection of particles in the magnetosphere, *J. Geophys. Res.*, *97*(A7), 10,693–10,701, doi:10.1029/92JA00441. 125

Saka, O., O. Watanabe, and D. N. Baker (1996), A possible driving source for transient field line oscillations in the postmidnight sector at geosynchronous altitudes, *J. Geophys. Res.*, *101*(A11), 24,719–72,426, doi: 10.1029/96JA02039. 125

Samson, J. C., B. G. Harrold, R. A. Ruohoniemi, R. A. Greenwald, and A. D. M. Walker (1992), Field Line Resonances Associated With MHD Waveguides In The Magnetosphere, *Geophys. Res. Lett.*, *19*(5), 441–444, doi:10.1029/92GL00116. 118

Southwood, D., and W. Hughes (1983), Theory of hydromagnetic waves in the magnetosphere, *Space Science Reviews*, *35*(4), 301–366, doi:10.1007/BF00169231. 58

Southwood, D. J. (1974), Some features of field line resonances in the magnetosphere, *Planet. Space Sci.*, *22*, 483–491, doi:10.1016/0032-0633(74)90078-6. 45

Southwood, D. J., and M. G. Kivelson (1982), Charged particle behavior in low-frequency geomagnetic pulsations, 2. Graphical approach, *Journal of Geophysical Research: Space Physics*, *87*(A3), 1707–1710, doi:10.1029/JA087iA03p01707. 52, 53

Southwood, D. J., J. W. Dungey, and R. J. Etherington (1969), Bounce resonant interaction between pulsations and trapped particles, *Planet. Space Sci.*, *17*, 349–361, doi:10.1016/0032-0633(69)90068-3. 51, 123, 132, 140, 195

Takahashi, K., P. R. Higbie, and D. N. Baker (1985), Azimuthal Propagation and Frequency Characteristic of Compressional Pc 5 Waves Observed at Geostationary Orbit, *J. Geophys. Res.*, *90*(A2), 1473–1485, doi:10.1029/JA090iA02p01473. 67, 68, 69

Takahashi, K., R. W. McEntire, A. T. Y. Lui, and T. A. Potemra (1990), Ion Flux Oscillations Associated With a Radially Polarized Transverse Pc 5 Magnetic Pulsation, *J. Geophys. Res.*, *95*(A4), 3717–3731, doi:10.1029/JA095iA04p03717. 75, 123

Takahashi, S., and T. Iyemori (1989), Three-dimensional tracing of charged particle trajectories in a realistic magnetospheric model, *J. Geophys. Res.*, *94*(A5), 5505–5509, doi:10.1029/JA094iA05p05505. 129

Vaivads, A. W., W. Baumjohann, E. Georgescu, G. Haerendel, R. Nakamura, M. Lessard, P. Eglitis, L. Kistler, and R. Ergun (2001), Correlation studies of compressional Pc5 pulsations in space and Ps6 pulsations on the ground, *J. Geophys. Res.*, *106(A12)*, 29,797 – 29,806, doi:10.1029/2001JA900042. 125

VT-SuperDARN (), Virginia Tech Field of View Tool, `http://vt.superdarn.org/tiki-index.php?page=radarFoV`, [Online; accessed 02-July-2014]. 91

Walker, A., R. Greenwald, W. Stuart, and C. Green (1979), Stare auroral radar observations of Pc 5 geomagnetic pulsations, *Journal of Geophysical Research: Space Physics*, *84*(A7), 3373–3388, doi:10.1029/JA084iA07p03373. 61, 63, 82

Walker, A. D. M., R. A. Greenwald, W. F. Stuart, and C. A. Green (1978), Resonance region of a PC5 micropulsation examined by a dual auroral radar system, *Nature*, *273*, 646–649, doi:10.1038/273646a0. 82

WDC Kyoto Observatory (), D_{ST} Index, http://wdc.kugi.kyoto-u.ac.jp/dstdir/dst2/onDstindex.html, [Online; accessed 04-December-2014]. 20

Wing, S., and P. T. Newell (1998), Central plasma sheet ion properties as inferred from ionospheric observations, *Journal of Geophysical Research: Space Physics*, *103*(A4), 6785–6800, doi:10.1029/97JA02994. 8

Wing, S., et al. (2005), Kp forecast models, *Journal of Geophysical Research: Space Physics*, *110*(A4), n/a–n/a, doi: 10.1029/2004JA010500. 20

Woch, J., G. Kremser, and A. Korth (1990), A comprehensive investigation of compressional ULF waves observed in the ring current, *J. Geophys. Res.*, *95*(A9), 15,113–15,132, doi:10.1029/JA095iA09p15113. 69, 70, 82

Wright, D. M., T. K. Yeoman, and P. J. Chapman (1997), High-latitude HF Doppler observations of ULF waves . 1. Waves with large spatial scale sizes, *Ann. Geophys.*, *1556*, 1548–1556, doi: 10.1007/s00585-997-1548-2. 72

Wright, D. M., et al. (2000), Space Plasma Exploration by Active Radar (SPEAR): an overview of a future radar facility, *Annales Geophysicae*, *18*(9), 1248–1255, doi:10.1007/s00585-000-1248-7. 82

Wright, D. M., T. K. Yeoman, I. J. Rae, J. Storey, A. B. Stockton-Chalk, R. J. L, and K. J. Trattner (2001), Ground-based and polar spacecraft observations of a giant (Pg) pulsation and its associated source mechanism, *J. Geophys. Res.*, *106*, 10,837–10,852, doi: 10.1029/2001JA900022. 78, 108, 132

Wu, Q., T. J. Rosenberg, L. J. Lanzerotti, C. J. Maclennan, and A. Wolfe (1991), Seasonal and Diurnal Variations of the Latitude of the Westward Auroral Electrojet in the Nightside Polar Cap, *J. Geophys. Res*, *96*(A2), 1409–1419, doi:10.1029/90JA02379. 145, 147

Wygant, J., et al. (2013), The Electric Field and Waves Instruments on the Radiation Belt Storm Probes Mission, *Space Science Reviews*, *179*(1-4), 183–220, doi: 10.1007/s11214-013-0013-7. 105

Yeoman, T. K., and D. M. Wright (2001), ULF waves with drift resonance and drift-bounce resonance energy sources as observed in artificially-induced HF radar backscatter, *Ann. Geophys.*, *19*, 159–170, doi:10.5194/angeo-19-159-2001. 82, 127, 141, 164

Yeoman, T. K., M. Tian, and M. Lester (1992), A study of Pc5 hydromagnetic waves with equatorward phase propagation, *Planet. Space Sci.*, *40*(6), 797–810, doi:10.1016/0032-0633(92)90108-Z. 82, 83, 116

Yeoman, T. K., D. M. Wright, and P. J. Chapman (2000), High-latitude observations of ULF waves with large azimuthal wavenumbers, *J. Geophys. Res.*, *105*(A3), 5453–5462, doi:10.1029/1999JA005081. 72, 73, 76

Yeoman, T. K., L. J. Baddeley, R. S. Dhillon, T. R. Robinson, and D. M. Wright (2008), Bistatic observations of large and small scale ULF waves in SPEAR-induced HF coherent backscatter, *Ann. Geophys.*, *26*, 2253–2263, doi:10.5194/angeo-26-2253-2008. 82, 85, 109, 112, 128, 197

Yeoman, T. K., D. Y. Klimushkin, and P. N. Mager (2010), Intermediate-m ULF waves generated by substorm injection : a case study, *Ann. Geophys.*, *28*, 1499–1509, doi:10.5194/angeo-28-1499-2010. 2, xii, 24, 81, 84, 85, 86, 87, 88, 109, 116, 117, 118, 121, 122, 124, 126, 127, 128, 130, 132, 133, 195, 197

Yeoman, T. K., M. James, P. N. Mager, and D. Y. Klimushkin (2012), SuperDARN observations of high-m ULF waves with curved phase fronts and their interpretation in terms of transverse resonator theory, *J. Geophys. Res.*, *117*, A06,231, doi:10.1029/2012JA017668. 132, 195

Zolotukhina, N. A., P. N. Mager, and D. Y. Klimushkin (2008), Pc5 waves generated by substorm injection: a case study, *Ann. Geophys.*, *26*, 2053–2059, doi:10.5194/angeo-26-2053-2008. 74, 75, 81, 108, 124, 132, 195, 197